Electronic Structure and Electro-optical Properties of Silicon/Germanium Strained Layer Superlattices

Alexander Charles Churchill, BSc ARCS

A thesis submitted to the University of London for the degree of Doctor of Philosophy and the Diploma of Imperial College.

September 1990

Solid State Experimental Group
Blackett Laboratory
Prince Consort Road
South Kensington
London SW7 2BZ
England



Abstract

In the hope of one day changing the band gaps of silicon and germanium structures from indirect to direct, novel semiconductor structures containing layers of Si and Ge have been investigated.

The optical properties of crystals in the visible region of the electro-magnetic spectrum are determined primarily by the electronic band structure. Specific features in, for example, the reflectivity arise as a consequence of large densities of transitions between valence and conduction electron bands. Electro-reflectance spectroscopy is very sensitive to these 'van Hove' singularities and has been put to use in determining the new band structure of the novel Si/Ge structures.

The thesis contains a brief introduction on the motivations behind $Si_{1-x}Ge_x$ epitaxy and possible electro-optical device applications. A review then follows, describing the structural and electronic properties of strained $Si_{1-x}Ge_x/Si_{1-y}Ge_y$ layers grown in register with $Si_{1-z}Ge_z$ substrates. These consist of quantum well structures made from layers of $Si_{1-x}Ge_x/Si$ and short-period superlattices containing only 4 monolayers of Si and 4 monolayers of Ge in their period. A calculation for the electron density of states in Si/Ge short-period superlattices is also presented.

Two chapters contain experimental results from the multiple quantum well and short-period superlattice samples which were investigated. The samples were characterised structurally by Raman scattering from phonons, allowing layer quality, periodicity, inbuilt strain and material composition to be determined. Comparisons are made between samples measured before and after post-growth annealing. Electro-reflectance and electro-transmission spectroscopies were used to characterise the samples optically. In addition photo-current spectroscopy was used to compare the band edge absorption of superlattice samples with that in bulk crystals.

Finally a summary gives an overview of the experimental findings and discusses future work that could be undertaken on Si/Ge layered structures.

Acknowledgements

I would like to thank my supervisor, Dr Philip Klipstein for his endless help and enthusiasm and Dr Michael Gell for many theoretical insights and concepts for the work presented.

Thanks also go to Dr Robert Woolley and Dr Andrew Shields for setting up the Raman laser and collecting optics and Electro-reflectance data collection systems respectively. Additional technical help was given for equipment construction and cryogenic practise by Mr S Cussell and Mr D Podger.

Samples were grown for me by Dr Chris Gibbings (BTRL).

Financial support for this work came from the Science and Engineering Research Council (UK) and British Telecommunications plc.

Finally thanks to my Mother for preparing some excellent figures from scrappy drawings and Miss Victoria Cripps for doing likewise with the text.

Abstract. 2

Acknowledgements. 3

Chapter 1 Introduction. 7

Chapter 2 Review of the properties of silicon/germanium systems. 14

2.1 Structural properties. 15
2.1.1 Critical thickness of Si/Ge layers and structural problems of epitaxy. 16
2.1.2 Techniques for layered growth. 24
2.1.3 Methods of structural characterisation. 27

2.2 Electronic properties. 30
2.2.1 Properties of elemental silicon and germanium. 30
2.2.2 Alignment of valence bands in heterojunctions. 42
2.2.3 Electronic states in multiple quantum well structures of Si and Ge. 43
2.2.4 Electronic states in superlattices of Si and Ge. 50
1 Symmetry considerations. 51
2 Kronig-Penney model solutions. 54
3 Full band structure calculations. 56
2.2.5 Prediction for a direct gap Si/Ge structure. 61
2.2.6 Effects from the density of states. 64
2.2.7 Experimental techniques for observing electronic structure. 65
2.2.8 Evidence for new electronic states in Si/Ge systems. 69

Chapter 3 Description of experimental procedures. 72

3.1 Optical characterisation using Raman scattering 73
3.1.1 Optical equipment. 75
3.1.2 Typical results for silicon and germanium. 77

3.2 Electro-modulation spectroscopy. *78*
3.2.1 Electro-reflectance and electro-absorption techniques. *78*
3.2.2 Photo-current spectroscopy techniques. *82*
3.2.3 Electrical contacts to silicon and germanium. *84*

3.3 Description of sample growth and list of samples. *87*

3.4 Computational techniques. *89*

Chapter 4 Density of states of electrons in Si/Ge short-period superlattices. *92*

Chapter 5 Structural analysis by Raman scattering spectroscopy. *100*

5.1 Multiple quantum well $Si_{1-x}Ge_x$/Si samples. *104*
5.1.1 Strain dependence of optic phonon energies. *107*
5.1.2 Folded acoustic phonon modes. *112*
5.1.3 Concluding remarks on Raman charaterisation of quantum well smaples. *122*

5.2 Short-period superlattices. *124*
5.2.1 Optic phonon mode strengths and energies. *124*
5.2.2 Resonant effects on scattering cross-section. *137*
5.2.3 Effects of sample annealing. *142*
5.2.4 Concluding remarks on the structural properties of Si/Ge superlattices. *148*

Chapter 6 Optical analysis. *150*

6.1 Multiple quantum well samples. *152*

6.2 Short-period superlattices (4 monolayer Si: 4 monolayer Ge). *166*
6.2.1 Epitaxial layer thickness effects. *169*

6.2.2 Evidence for superlattice related electronic critical points. *175*
6.2.3 Summary of results for Si/Ge (4:4) superlattice samples. *183*

6.3 Short-period superlattices (2 monolayer Si: n monolayer Ge). *186*
6.3.1 The Si/Ge (6:4) Superlattice. *187*
6.3.2 Electro-reflectance measurements. *189*
6.3.3 Electro-transmission measurements. *195*
6.3.4 Conclusions *206*

Chapter 7 Conclusions from electro-optic and Raman measurements. *208*

7.1 Multiple quantum well and indirect band gap superlattice structures. *209*

7.2 Direct band gap superlattice structures. *211*

7.3 Further work required. *211*

References. *214*

List of publications. *220*

Chapter 1 Introduction.

1 Introduction.

The formation of layered semiconductor structures from silicon and germanium in an age when novel structures are already made from materials such as gallium-arsenide might seem like a step backwards in time, so any thesis devoted to the study of these structures requires some overall review of the motivations behind silicon-germanium epitaxy.

From an industrial view point the investigation of silicon (Si) and germanium (Ge) superlattice structures consisting of atomic layers of Si and Ge, stem from a need for the most popular semiconductor material to perform better when made into optical devices.

Si has been used in the micro-electronic industry for many years, and the technology exists for device manufacture from large crystal wafers. This is because of the physical properties of Si, most of which are notable above those of other crystals; examples are mechanical strength and a useful insulating oxide of high quality. It is also the second most abundant material on earth. When considering Si as a semiconductor, long minority carrier lifetimes make bipolar devices feasible. However the electron energy band structure that makes direct recombinations of minority carriers improbable stops efficient luminescence and absorption of light at near band gap energies and thus limits optical device applications. In recent years III-V semiconductors, consisting of equal ammounts of group III and group V elements to form zinc-blende structures, have appeared in electrical devices instead of Si. Semiconductors such as these eg. GaAs and InP, have direct energy gaps so good detectors and emitters in the infrared and visible light regions have been developed. Unfortunately such devices are hard to integrate with existing Si integrated technologies due to different thermal expansion rates of the materials and to constituent elements having suitable valence to diffuse through and dope the silicon. The converse case is also true and Si is capable of doping III-V material (Bean 1985). Hence separate optical and electronic devices must be made and integrated with corresponding manufacturing difficulties and reduction in operational speed.

The incompatibilty of Si with other semiconductors thus limits its usefulness. As a consequence epitaxial growth of Si has been considered, which could allow the possiblilty of integrating Si technology with electro-optical devices, with the advantage of sharp doping profiles available with epitaxial growth. By also considering growth of Ge on Si substrates, the different lattice constant of Ge opens avenues of control by incorporating strain (Osborn (1985)). Any strain in the unit cell will affect the electron energy levels. For example a reduction in bandgap energy can be achieved by introduction of uniaxial strain for two of the indirect conduction band valleys of a SiGe alloy; this can be achieved by growing epitaxial SiGe alloy in register with a Si substrate, to form a strained layer. In contrast to

group III and V elements, Ge does not form an electrically active impurity in Si as it has the same valence. The next section reviews proposed electro-optic devices which make use of SiGe epitaxy instead of III-V semiconductors. The section following this, then describes the possibilties of making direct band gap semiconductors from layered Si/Ge structures, which could completely replace existing direct band gap semiconductors.

1.1 Current device structures realising $Si_{1-x}Ge_x$/Si technology:

The first working device structures realised in SiGe epitaxy were based on original device concepts but used epitaxial layers grown on Si substrates. This showed the feasibility of integrated opto-electronic devices with existing Si technology.

(i) The Ge p-i-n Photo-Detector proposed by Luyri et al. (1984).

This consisted of a pn Ge junction diode with an intrinsic doped region at the junction where light is absorbed. Initially the Ge structure was grown on a thick SiGe alloy buffer of graded composition matching the lattice constants of the Si (100) substrate at one side and Ge layers at the other. It was found that threading dislocations went through the the entire structure which were associated with the change in the lattice spacing of the buffer grown on Si. A poor diode behaviour resulted. The device was improved with the inclusion of a compositional modulated superlattice in the buffer region, made from SiGe alloys. The additional modulation of composition of these layers was able to turn threading dislocations from the growth direction towards the wafer edge. The final quantum efficiency achieved was 40% at 1.55μm and compares well with commercial Ge photo-detectors. Figure 1.1 shows the band alignment for the device.

(ii) The SiGe MQW photo-detector.

The band gap for uniaxially strained $Si_{1-x}Ge_x$ alloys of various compositions was calculated by R People (1986a and 1985) and was found to be significantly below the gap of a relaxed alloy of a similar composition. An optical device which made use of this idea was made by Temkin et al. (1986). $Si_{1-x}Ge_x$ layers were grown in register with Si cladding layers to form strained quantum wells (QW) for electrons and holes, this resulted in an absorption response which was moved to longer wavelengths than in the equivalent $Si_{1-x}Ge_x$ alloy detector. The device was made with MBE growth of a $Ge_{0.6}Si_{0.4}$ multiple QW with Si barriers, in a Si pn diode junction. Figure 1.2 shows a band schematic with

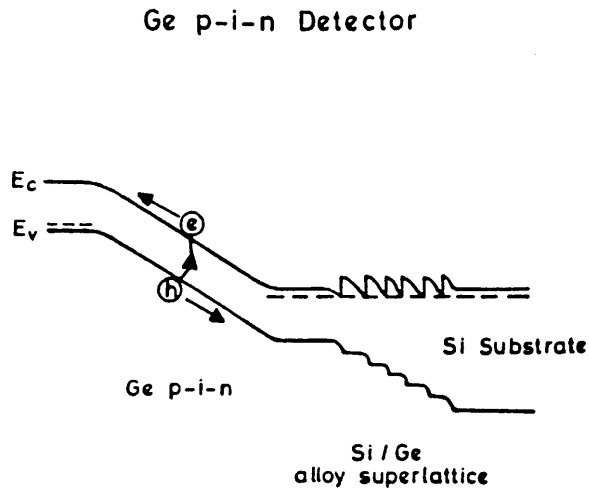


Figure 1.1 The electron energy band alignment for a conventional Ge p-i-n photo-diode detector integrated on to a silicon substrate, using SiGe epitaxy, (after Luyri et al. (1984)).

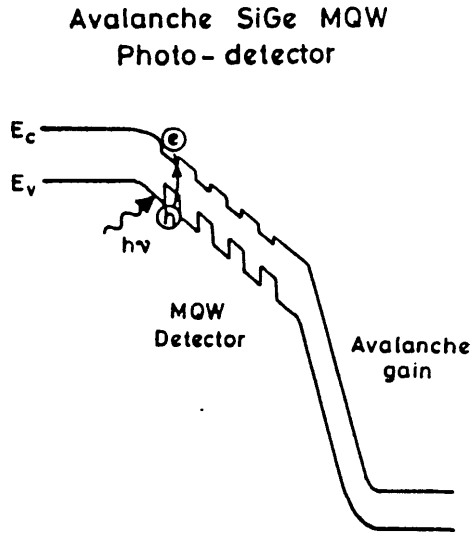


Figure 1.2 The electron energy band alignment for a SiGe strained layer photo-diode. The uniaxial strain lowers the alloy conduction valleys in the growth plane, allowing a lower absorption edge, (after Temkin et al. (1986)).

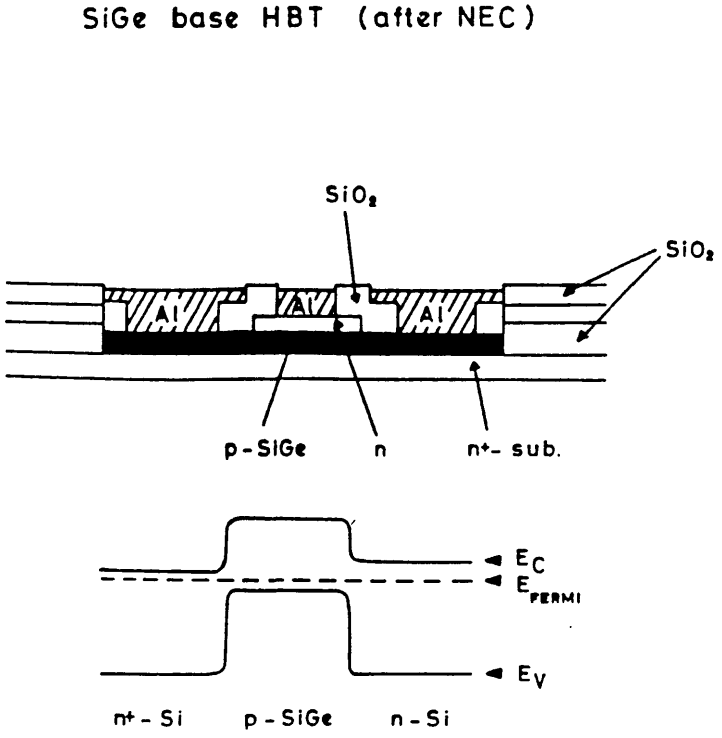


Figure 1.3 A schematic of a heterojunction bipolar transistor including band alignments and wafer structure, proposed by Tatsumi et al. (1989).

quantum wells and Si cladding layers. As the absorption only takes place in the QW regions which are only 60Å in thickness, the light was coupled in to the plane of the QWs which increased the absorption cross-section. In addition a 'single mode' diffraction grating was placed on the top of the device; absorption at 1.3μm was achieved with an overall quantum effeciency of 10.2% Although the structure had many disolcations (approximately 10^{4}), leakage currents were such that reverse bias voltages of 35-40V could be attained. An intrinsic region of Si was added below the QW absorber to give avalanche gain of up to 50. The detector then operated at speeds of 800Mbits/sec with 25km of optical fibre and had an error count rate of less than 10^{-9}. The absorption at the band edge is still indirect in nature and hence it is small.

(iii) Transport Devices.

To demonstrate the possibilities of $Si_{1-x}Ge_x$/Si epitaxy for the electronics industry several types of transistor have been made. Initial devices were based on buried channel Field Effect Transistors (FET), where the different band gaps of the alloys and the different conduction and valence band alignments with bulk Si are used to confine carriers in the channel (People (1985)). Although the devices demonstrated how $Si_{1-x}Ge_x$ epitaxy could be applied in principle, no exceptional device performance was achieved due to some parameters remaining unoptimised.

Using $Si_{1-x}Ge_x$ epitaxy in bipolar circuits is expected to give enhanced performance. World wide, several groups are investigating the possibilities of making Heterojunction Biploar Transistors (HBTs). In this device the base region of a normal bipolar transistor is made from an epitaxial layer of $Si_{1-x}Ge_x$ alloy. Figure 1.3 shows a device proposed by Tatsumi et al. (1988). In addition to the conduction and valence band alignment for the transistor, the device design makes use of the planar technology of epitaxial crystal growth. The band offsets promote electron injection into the base region but reduce hole injection into the emitter region for a given base and emitter doping (People (1986b)). Thus to increase the speed of the device, the base resistance can be reduced by increasing the doping in the $Si_{1-x}Ge_x$ region. This is not possible in normal bipolar devices due to excessive hole injection. Frequencies of operation up to 100GHz have been predicted. The epitaxial design concept also gives inherent speeds due to the thin base region.

First reports of $Si_{1-x}Ge_x$ device performance were from Manasevit et al. (1982), which related to the electrical properties. Unstrained $Si_{1-x}Ge_x$ layered structures of various compositions were studied. The mobility measured as a function of carrier density, was shown to be greater than in bulk Si or $Si_{1-x}Ge_x$ random alloy, but lower than in bulk Ge.

1.2 The Possibility of Direct energy gap systems with Si and Ge.

The devices so far discussed have attempted to use the advantages of epitaxial growth, such as the ability to grow thin layers, to improve existing devices. The work presented in this thesis uses the ability of epitaxial growth to make structures on an atomic scale and thus change the crystal structure and atomic potentials, so creating new semiconductors.

Samples investigated contain a periodic sandwich structure of Si and Ge layers a few monolayers in thickness and the resultant structure is called a superlattice. These superlattices are grown commensurately (ie. in register with the lattice constant of the substrate). Theory predicts that the atomic potentials of the short-period superlattice of Ge and Si modify the bulk crystal properties, effectively tailoring the length of the bulk Brillouin Zone in the growth direction. This can lead to a folding of two of the conduction band valleys to the zone centre (to give so called Zone Folding, Esaki and Tui (1973)). Such a scheme removes the need for momentum conserving phonon assisted transitions between the conduction band valleys and the valence band maxima, thereby increasing the probability of optical transitions.

1.3 Experiments on Si/Ge Quantum wells and Superlattices.

Since epitaxy of Si/Ge layers displays some differences from III-V epitaxy, chapter 2 is split into two sections. The first is devoted to a review of the growth and structural properties of Si/Ge layers. The second section contains a review of the electronic properties of Si/Ge layered structures, using the bulk properties to describe electron states in quantum well and superlattice structures.

Chapter 3 describes experimental and computational procedures used for the analysis of structural and electronic properties of the various Si/Ge samples studied in this thesis. Chapter 4 is devoted to calculations of the density of electron states within a specific Si/Ge layered structure which was typical of the samples investigated.

The Si/Ge samples were characterised optically with Raman scattering spectroscopy and electro-reflectance spectroscopy, to determine their structural and electronic properties. Chapters 5 and 6 contain experimental results; initially on samples of $Si_{1-x}Ge_x$/Si layers 10 to 20nm thick are investigated followed by the properties of superlattices containing very thin Si/Ge layers only a few monolayers in thickness.

A final chapter reviews the current state of Si/Ge epitaxial structures and concludes the studies presented in the thesis.

Chapter 2 Review of the properties of silicon/germanium systems.

2 Review of the properties of silicon/germanium systems.

This chapter contains a review which is split into two sections. The first section considers the structural properties of strained layers of $Si_{1-x}Ge_x$ on various substrates and the techniques of epitaxial growth.

The second section reviews the electronic properties of Si/Ge layered systems. Firstly outlining bulk Si and Ge electronic properties and the perturbation effects of stress and strain. The electron band alignment for abrupt Si and Ge interfaces is then discussed which allows the electronic states in strained quantum well and superlattice samples to be described. Predictions for strengths and energies of optical transitions in superlattices which are measured are listed. A following part then explains the relationship between band structures and measured optical properties. The final part of the chapter includes a brief review of some experimental evidence for electronic transitions within Si/Ge superlattices.

2.1 Structural properties.

In consideration which semiconductors might be grown on Si without problems of cross-doping between substrate and epitaxial layer, the most sensible choice would seem to be Germanium. As Ge is in the same group in the periodic table as Si it has the same orbitals as Si and thus bonding between Si and Ge occurs easily. Random alloys over a large compositional range between Si and Ge can be formed in a diamond structure. Such alloys take an average lattice parameter, because crystalline Ge has a lattice constant which is 4% larger than that of Si.

The electronic properties of a semiconductor are determined significantly by its crystallinity and thus it is important to grow any epitaxial layer pseudomorphically. Epitaxial growth of pure Ge or SiGe alloys on a Si substrate can only be achieved pseudomorphically with very thin layers. When this occurs the growth-plane lattice constant of the epitaxial layer is essentially equal to the substrate lattice constant. The cubic crystal of the epitaxial layer then distorts to become tetragonal, due to the Poisson effect. For epitaxial Ge on a Si substrate the initial cubic lattice of Ge extends in the growth direction. The energy gained by bonding with the substrate is balanced by the stored energy in the strained bonds of the epitaxial layer (Bean (1985)). As the layer thickness increases this strain energy will eventually overcome the epitaxial interface bonding energy, and will be released by forming dislocations. The layer then becomes incommensurate, with random domains of relaxed micro-crystallites separated by dislocations.

From the preceding discussion the idea of a Critical Thickness, hc below which the epitaxial layer is completely strained is formulated. Growth of a layer beyond the Critical Thickness then produces partly strain-relaxed layers.

2.1.1 Critical thickness of Si/Ge layers and structural problems of epitaxy.

If an epitaxial layer of different lattice spacing to the substrate grows pseudomorphically, forming a commensurate layer, there is built-in strain in the layer. For simplicity, consideration will only be given to epitaxial layers that would normally form cubic crystals. The strain due to the change in lattice spacing, a is:

$$\varepsilon_{Strain} = 1 - \frac{a_{Epi}}{a_{Subst}} \qquad [2.1]$$

The strain has a mixture of hydrostatic and uniaxial components as the cubic crystal of the epitaxial layer distorts due to the Poisson Effect, (Poisson ratio ν)

$$\frac{a_{//}}{a_{\perp}} = 1 - \frac{1-\nu}{1+\nu}\varepsilon_{Strain} \qquad [2.2]$$

The increased energy stored in distorting the lattice of course will depend on the layer thickness t. A value of the strain energy is given by Kasper (1989) for a Young's modulus μ

$$E_h = 2\mu\frac{1+\nu}{1-\nu}\varepsilon^2_{Strain} \qquad [2.3]$$

In the initial stages of growth, this energy is balanced by a reduced energy in the interface bonds. As the layer increases in thickness the stored strain energy will also increase. There will be a 'critical thickness' h_c, when misfit dislocations will form, either from existing dislocations or from some nucleating source. The layer will then relax and regain the lattice spacing of a bulk crystal. The energy required to form a misfit dislocation gives rise to a potential barrier thus allowing metastable

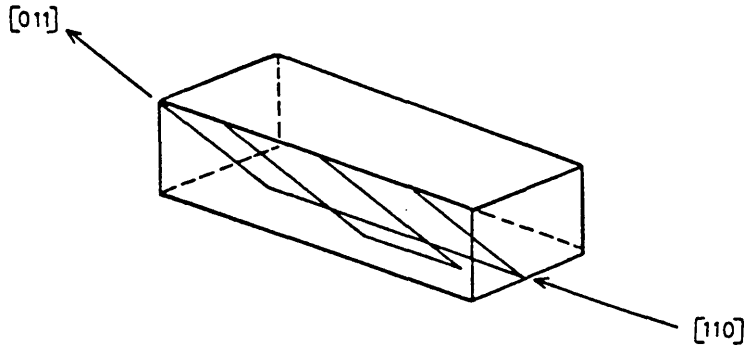


Figure 2.1 A half loop dislocations along [110] directions in a diamond lattice, thought to be responsible for relaxing strained layers caused by epitaxial lattice misfit with the substrate (after Tuppen et al. (1989)).

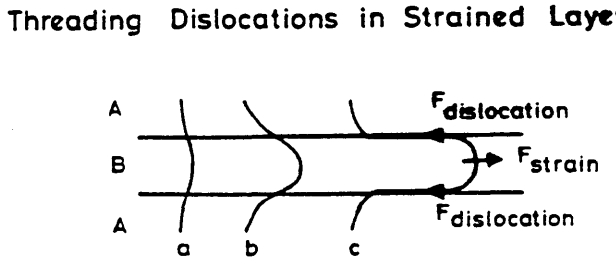


Figure 2.2 Threading dislocation which can relieve strain in tetragonally distorted epitaxial layers. a) shows a coherent dislocation in which no strain is relaxed, b) shows the critical limit for the inbuilt strain and c) shows a full relaxed layer where the lattice mismatch is accommodated by the dislocation Burger's vector (after Matthews and Blakeslee (1974)).

strained layers to be grown, providing they have a thickness below the critical thickness.

To predict the critical thickness for an epitaxial layer, it is necessary to understand the type of misfit dislocations formed in strained layers. Misfit dislocation types were considered by Frank and Van der Merwe (1949) for metals and later in a Transmission Electron Micrograph (TEM) study for semiconductor epitaxial layers by Matthews and Blakeslee (1974). It is not clear which theoretical prediction of hc should be used Kasper (1975) suggests that the thermodynamics of molecular beam epitaxy grown samples favour the Frank and Van der Merwe calculation. However recent experimental results by People and Bean (1985) and Houghton et al. (1990) support the approach taken by Matthews and Blakeslee which is now briefly described below.

In the Matthews and Blakeslee (1974) theory of misfit dislocations it is asserted that lattice mismatch of epitaxial layers will be accommodated up to a value 7%, until the thickness of the strained layer reaches the critical thickness. For strained (001) orientation layers trapped commensurately between a substrate and a capping layer, typical misfit dislocations are observed in two pairs having two sets of Burger's vectors: $\pm a/2[101]$ or $\pm a/2[101]$ and $\pm a/2[011]$ or $\pm a/2[011]$, having a corresponding total Burger's vector: $\pm[110]$, which is stable in fcc lattices.

Hence the Burger's vector is inclined 45° to the (100) direction and 60° to the dislocation lines.

Such a formation can be explained in terms of half loops forming at the growth surface of the strained layer, (see figure 2.1). Having identified the type of dislocations present in strained layers, Matthews and Blakeslee were able to derive a formula balancing a misfit force from the strained layer and tension in the dislocation. Essentially a strained layer within cladding layers has a 'critical thickness' h_c, at which threading dislocations become incoherent at the layer interfaces and propagate along the interfaces forming misfit dislocations. Hence strain within the epitaxial layer is relaxed.

The critical thickness is calculated from balancing the forces that act on the threading dislocation;

$$h_c = \frac{b}{2\pi\varepsilon} \frac{(1-\nu\cos 2\alpha)}{(1+\nu)\cos 2\lambda} \left[\ln \frac{h_c}{b} + 1 \right] \qquad [2.4]$$

b = magnitude of Burger's vector associated with the lattice misfit

ε = misfit strain

ν = Poisson's ratio

α = angle between the misfit dislocation and the layer orentation.

λ = slip angle

This concept is illustrated in figure 2.2

The expression given by [2.4] is valid for layers which have cladding of the substrate material around them. Thus it could be expected that a different value of critical thickness may be found for strained layers without capping layers to retain the epitaxial strain. The Matthews and Blakeslee theory currently gives the best fit to experimental data, although the theory neglects the nucleation of dislocations in the strained crystal and the effects of point defects and surface steps at the strained layer interfaces. Dislocations are assumed to exist in the threading form and are converted to misfit dislocations by the strained layers. Another problem is that when trying to fit theories like this one with experimental results, it is necessary to take into account the experimental detection thresholds.

Recent results from People and Bean (1985) suggest that the critical thickness of SiGe strained epitaxial layers grown on Si or Ge (001) substrates may be significantly larger than the current theories predict. In this work a Transmission Electron Microscope was used to detect the presence of misfit dislocations. A stochastic model was derived to explain the anomalous results, but since that work Fritz (1987) has shown that the results of People and Bean can be fitted to the standard Matthews and Blakeslee formalism providing some changes are made; these changes allow for the fact that standard TEM and X-ray analyses used to detect misfit dislocations may not be sensistive to all misfit dislocations. Hence some measurements may suggest that the samples are more strained than they actually are.

Fritz defines a ratio accounting for the resolution of a measuring technique:

$$R = \frac{\Delta a}{a} \qquad [2.5]$$

where a is the lattice constant of the crystal and a is the change produced by the presence of a misfit dislocation, observed in X-ray topography or TEM. Typically R is 10^{-3} for X-ray diffraction techniques. Also a scaling factor Q, is introduced related to the number of dislocation present for a layer thickness above the critical thickness, so that R is scaled accordingly to R/Q to reduce the measurement sensitivity. Typically Q is less than one, between 1% and 30%, several mechanisms have been proposed for reasons why there are sometimes less dislocations present than expected (Fritz (1987)).

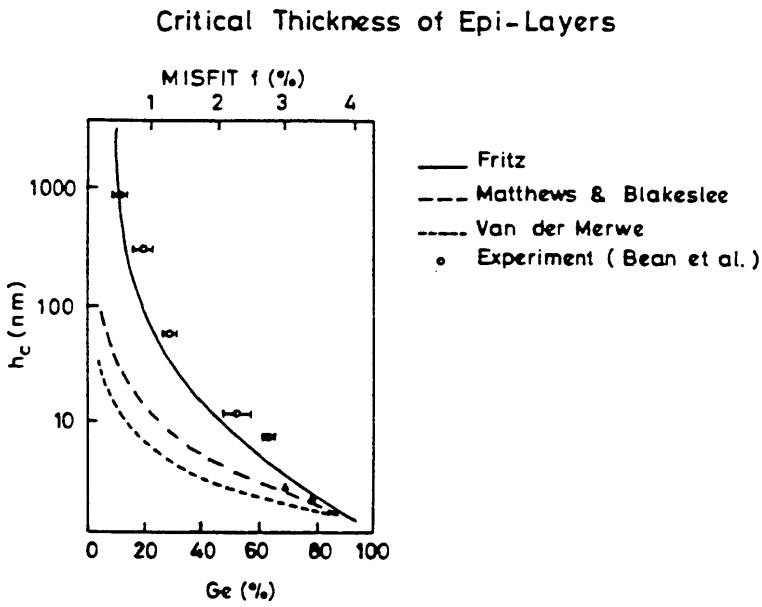


Figure 2.3 Plot of three critical thickness theories for strained epitaxial layers and results of studies performed by Bean and co-workers. The critical thickness for 50% alloy will be 100Å, for pure Ge on silicon the thickness is reduced to 10Å

Q relates a metastable critical thickness observed by People and Bean and the proposed equilibrium critical thickness h_c, of Matthews and Blakeslee. Both Kohama et al. (1988) and Tuppen et al. (1989) investigate critical thicknesses beyond that which equilibrium predicts, highlighting the problems that still exist with the definition of critical thickness.

The strain ε as a function of thickness is defined to be equal to the lattice misfit f, for a thickness h_c

$$f = \varepsilon(h_c), \qquad [2.6]$$

replacing [2.6] with the experimental resolution R
gives:

$$f\text{-}R = \varepsilon(h_c) \qquad [2.7]$$

finally the scaling factor Q, is introduced to take account of the less than expected number of dislocations present, thus [2.8] is obtained

$$Q(f\text{-}\varepsilon) = R. \qquad [2.8]$$

rearranging [2.4]:

$$f - \frac{R}{Q} = \frac{b}{2\pi h_c} \frac{(1-\nu\cos 2\alpha)}{(1+\nu)\cos 2\alpha}\left[\ln\frac{h_c}{b} + 1\right] \qquad [2.9]$$

Figure 2.3 shows predictions for the Frank and Van der Merve, Matthews and Blakesee and Fritz theories together with the experimental data obtained by People and Bean for SiGe layers on Si(001) substrates measured with conventional X-ray diffraction techniques. In this case $R/Q = 7.5 \times 10^{-3}$, which is reasonable for the measurements made by People and Bean.

Symmetrically Strained Systems.

Considering growth of pseudomorphic elemental Ge on Si (001) substrates (a 4% strain), it is found that the maximum thickness of Ge which can possibly be grown is six monolayers before dislocations

relax the strain and destroy the crystallinity of the layer. For alloys of composition between elemental Si and Ge the critical thickness for the epitaxial layer can be read off figure 2.3. An empirical rule states that for an entire superlattice or set of quantum wells, the total thickness for a pseudomorphic structure must not exceed the critical thickness for the average composition of the entire structure. For example if a structure is grown with repeated alternating layers of Si and Ge of similar thickness on a substrate having a composition of 50% SiGe alloy then the structure can have an infinite length, provided each alternating layer has a thickness less than its critical thickness if grown directly on the substrate.

For the samples considered later the substrate is a Si (001) crystal face and for an 8 monolayer period superlattice containing equal thickness of 4 monolayers of Ge grown on 4 monolayers of Si, the strain is contained only in the Ge layers. The period can be repeated 5 times before dislocations occur. The total thickness for the entire structure is 50Å, which is just under the critical thickness for a 50% alloy grown on a Si (001) surface.

To make optical devices however, it will be necessary to have much thicker structures if the properties of the epitaxial layer are going to be exploited rather than those of the substrate. Because of this problem the technique of symmetrically strained systems has been developed by Kasper (1989), in which the strain in the superlattice or quantum well is spread evenly throughout the repeated period and thus extendined superlattice structures can be grown. This is done by growing on a substrate or buffer with a composition the same as the average composition of the repeated structure. This is accomplished by growing on a buffer layer of the right composition. (Unfortunately there are no commercial $Si_{1-x}Ge_x$ alloy substrates available.) Two options are feasible. Firstly, a buffer layer is grown to a thickness far beyond the critical thickness and thus dislocations relax the growing surface; however this leaves a poor surface for subsequent growth and a considerable thickness of relaxed buffer layer material is required before a dislocation density is attained which is below the threshold where reliable devices can be fabricated. The second option is that of one proposed by Kasper (1989); a 'virtual substrate' is grown, consisting of a partially relaxed buffer with a much smaller thickness. The partially relaxed buffer has a lattice constant equivalent to the strain symmetrised superlattice but with the layer thickness and dislocation defect density much reduced.

For example a virtual substrate of $Si_{0.75}Ge_{0.25}$ would require either of the following buffers:

250Å of $Si_{0.45}Ge_{0.55}$ or 1500Å of $Si_{0.65}Ge_{0.35}$

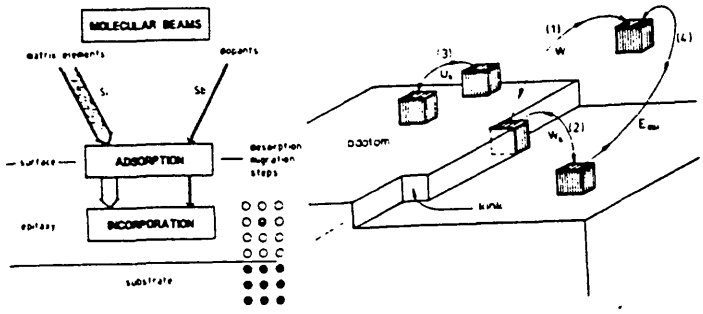


Figure 2.4 A schematic taken from Kasper (1989), showing the Molecular Beam Epitaxy process. A combination of absorption and incorporation processes, silicon adatoms migrate to surface steps to complete the growth surface. The process is shown in a flow diagram on the left and represented in a schematic on the right. Atoms absorb or desorb from the growth front (1) or sample surface (4), migrate on the sample surface (3) and be captured by the growth front (2).

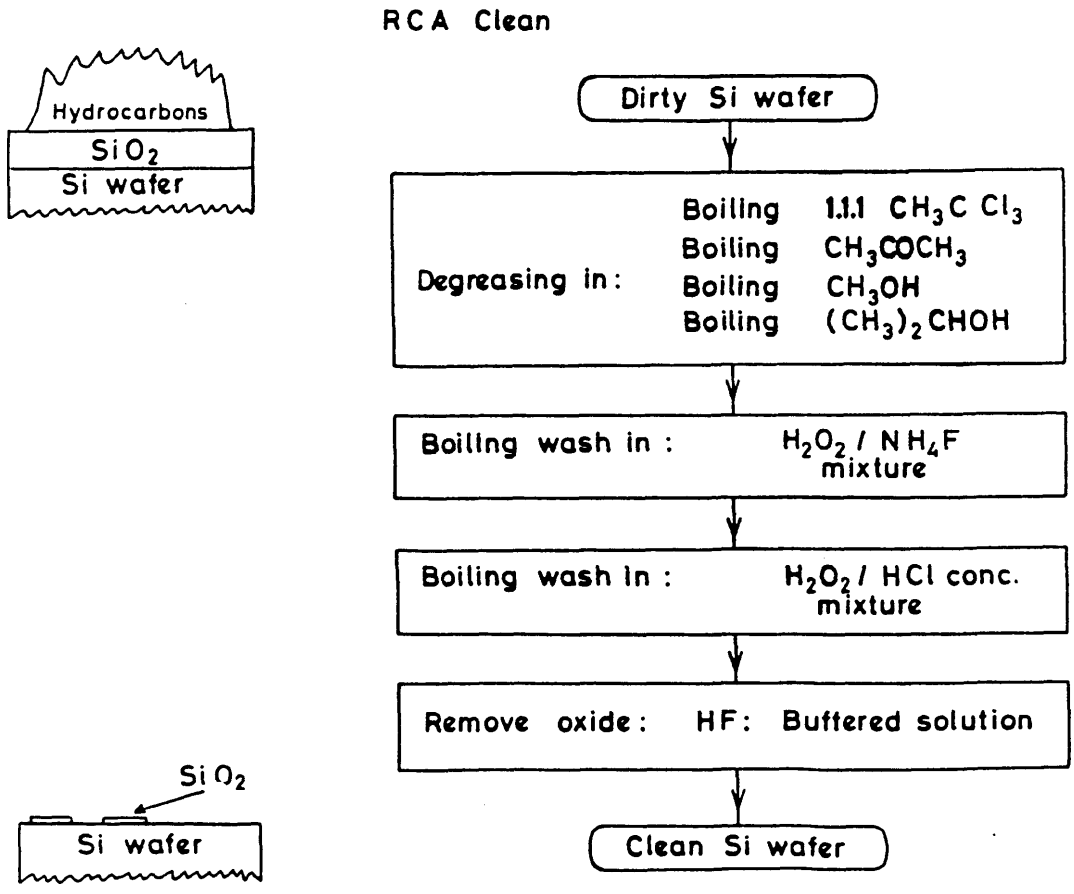


Figure 2.5 A Flow diagram showing the RCA cleaning procedure for cleaning silicon substrates.

2.1.2 Techniques for layered growth.

To grow thin layers of Si that are useful for electronic devices we must be able to control the growth to reduce the inclusion of impurities and defects, such as dopants and dislocations that affect optical and transport properties. A bulk crystal can be refined after pulling from a melt, but an epitaxial layer must be perfect to start with. Two methods for epitaxial growth have emerged:

Low Pressure Chemical Vapour Deposition (LPCVD)
and Molecular Beam Epitaxy (MBE).

LPCVD involves the pyrolysis of a gas eg. $SiCl_4$ to deposit on to a Si substrate, which is at elevated temperatures. Usually the gas is in continuous flow through the growth chamber.

MBE is an extended evaporation technique, carried out under ultra high vacuum. Non-interacting beams of Si atoms and molecules impinge on a heated substrate, at which non-equilibrium thermo-dynamic processes compete to produce an epitaxial layer. Figure 2.4 shows a schematic of the MBE process.

Both methods have their own problems such as elevated growth temperatures and consequently high growth rates in the case of LPCVD and finite volume of source material resulting in machine down time for replenishment for MBE.

For growth of pure Si we must remove the sources of impurities. Listed here are the three main sources of defects found in epitaxial Si.

a) The source of Si for deposition can itself contain many doping impurities, (SiH_4 or $SiCl_4$ gas for Vapour Phase Epitaxy (VPE) or solid Si for MBE). It is left to the suppliers of the chemicals for growth to reduce contamination as the grower has little or no control over this.

b) The growth chamber has a large surface area from which contaminents can de-sorb. Current LPCVD systems use a quartz vessel which usually has a low number of contaminants. MBE by necessity of an ultra high vacuum usually utilises a stainless steel vessel which can have considerable Carbon contamination.

Hydro-carbon sources must be carefully placed to reduce contamination. Most systems use cryopumps but initial pumping is often carried out with diffusion pumps with neoprene 'O'-rings, both containing

carbon.

c) The Si substrate can form a source for doping impurities and nulceation of structural defects. The substrates can often be obtained polished 'ready' for growth but the surface is by no means clean. A typical cleaning procedure to remove most hydro-carbons, transition metals and oxides is called the 'RCA cleaning procedure'. Figure 2.5 shows a schematic of the process. The clean involves a series of baths, each aimed at removing different contaminants. The wafer is then placed directly in to the growth chamber for the final removal of any oxide.

Solid state diffusion of dopants from the substrate during growth can form a problem in itself and the solution is described in a following description of LPCVD.

There now follows a short discussion of Chemical Vapour Deposition for growth of epitaxial layers. Highlighted are essential differences between normal III-V CVD and Si CVD.

Normal chemical vapour epitaxy is carried out at atmospheric pressure, and involves the pyrolysis at an elevated temperature of a gas, typically a metal-organic. The chemistry involved in growth is a mixture of homogeneous (gas phase) and heterogeneous (surface) chemistry. For Si growth the precursor gas has the typical form SiH_xCl_{4-x} and in most cases, unfortunately, is highly inflammable. The Si substrates for growth are heated by a radio frequency coil, to temperatures (900°C) that will allow the precursor gas to strip any contaminants from the surface of the Si. Water vapour is particularly harmful if present in the growth chamber, forming good oxides on the samples at these temperatures, however typically the oxides and carbon impurities react with H_2 in the precursor gas.

At these temperatures dopants can be released from the substrate and flow across the growth surface, via solid state diffusion, to dope the epi-layer anisotropically. This process is known as auto-doping and makes doped hetero-structures virtually impossible, if grown at such elevated temperatures.

A technique known as Reduced Pressure Chemical Vapour Deposition (RPCVD) has been developed by Meyerson (1989) and is used to overcome this problem. Auto-doping can be almost eliminated by growing at low temperatures (650 - 750°C). However the stripping quality of the precursor gas to clean the substrate is reduced and as in the case of MBE it is necessary to reduce the growth pressure to remove the water vapour in the chamber. Typical pressures in RPCVD are 10 - 80 Torr. The reduced temperature growth also allows heterojunction structures to be formed from materials that would normally inter-diffuse at higher temperatures. The pyrolysis of the carrier gas becomes proportional to the pressure and hence the growth rate can also be substantially reduced.

An alternative method of epitaxial growth that yields low impurity and defect incorporation is molecular beam epitaxy. The ability to produce abrupt doping profiles and junctions of high quality comes from the fact that the growth temperature is much below the temperatures of solid state diffusion for adatoms and dopants. Physically we have a condensation of molecular beams on a heated substrate (The typical temperature for MBE growth of Si is 550°C, with a corresponding growth pressure of 10^{-8} Torr to reduce oxygen content). A two dimensional gas of adatoms is formed on the substrate which then orders itself by surface diffusion to form an atomic layer. The Si atoms migrate to surface steps, where they 'stick'. Thus layered growth is a process of lateral motion of surface steps. No carrier gas is involved.

The wafers are also cleaned with the RCA technique before insertion into the Ultra High Vacuum (UHV) chamber for growth. The absence of carrier gas means the native oxide will not be automatically stripped. The wafer can be cleaned in-situ by ion bombardment, however surface damage caused by this technique is usually considered too high. Another technique used utilises amorphous sputtered Si which causes Si dioxide to change to a monoxide phase which is easily desorbed at 900°C in UHV.

The matrix and doping sources for conventional MBE growth are mainly thermal sources. However, thermal effusion cells such as Knudsen cells which are usually used on MBE systems are impracticable as Si sources, as the cell temperature needs to be very high to get any appreciable vapour pressure. Electron beam evaporators are therefore used, where an electron beam locally evaporates Si from a water cooled pure crystal. The material sources have shutters to open and close the molecular beam from the substrate, thus heterojunctions can be made from different materials. To reduce carbon contamination other parts of the MBE machine such as source shutters and shields are also made of pure Si crystals.

The usual advantages of MBE are the availablity of in-situ analysis techniques. Low energy electron diffraction (LEED) and Reflection high energy electron diffraction (RHEED) can be used to check the surface orientation and morphology. The normal technique of using RHEED to check the growth phase in III-V growth cannot be used as it is not easy to observe the diffraction due to Si, due to the extra electrons from the e-beam evaporators. However some studies have been made on highly polished substrates by Sakamoto (1986); the following observations have been recorded:

i) Oscillations of spot intensities due to the rotating surface (2x1) and (1x2) orientation during growth, fade out as a function of time.
ii) Strength of such oscillations is strongly dependant on growth temperature.

LEED has been used by De Jong (1983) to study growth temperatures. A range of temperatures is found for good growth. For temperatures below this window disordered growth is found. It is important to note that the temperature range for good growth with MBE does not overlap the normal temperatures for LPCVD growth. One possiblity could be due to the difference in condensation coefficient, a measure of adatom sticking, which is unity for MBE and about 0.15 for LPCVD. Also the LPCVD process contains a high activation energy for creating bonds at the surface. Kasper proposes that such a difference in growth mechanisms could be due to carrier gas and chemical reaction products absorbed on the growth surface in LPCVD, which are absent in the MBE process.

Although the growth temperature for MBE is much below temperatures for solid state diffusion, it is found that many dopants segregate on the surface and do not incorporate, leaving a weakly doped epi-layer and a large doped surface. Ion implantation is used for n-type doping where the high energy atoms incorporate after recoiling from one collision. It can be noted that:

i) Antimony (Sb) is completely incorporated substitutionally,
ii) Sb atoms are not sputtered significantly by incoming Si atoms.
iii) Electron mobilities are comparable to bulk values.

Arsenic can also be used as a n-type dopant, but growth temperatures have to be carefully controlled if hetero-epitaxy is also required.

For the opposite p-type dopant Boron (B) is normally used. However as B has a high melting point, B_2O_3 oxide effusion cells are used. It has been shown with SIMS analysis that with carefully set conditions there is little or no incorporation of the oxygen (Bean (1987)).

2.1.3 Methods of structural characterisation.

There are various methods for post-growth characterisation of semiconductor layered structures. In chapter 5 Raman scattering from phonons is used to probe the different kind of bonds found in Si/Ge structures which can be used to determine microscopic ordering and strain on a macroscopic scale. In this section however, a brief review is presented of some techniques that were made use of, but were not performed directly by myself.

Most characterisation techniques used to test structural properties rely on the semiconductor having a crystalline form. For example a technique known as Rutherford Back Scattering uses channelling of Helium atoms, so that any scattering can indicate the presence of strain or incommensurate layering.

The most popular techniques use coherent scattering or in other words diffraction of electrons or X-rays to determine the crystallinity of the samples.

One common practise is to thin samples parallel to the growth direction so that electrons can be transmitted through the cross-section of the epitaxial layers. One or many of the diffracted beams can be imaged to produce what is known as a Transmission Electron Micrograph (TEM). This picture can give information about the ordering within superlattice layers. Care has to be taken when analysing these pictures. For example any roughness at layer interfaces is averaged over the entire thickness of the sample, and if the image is produced only by a beam diffracted by the periodicity of the superlattice then the interfaces of course will appear very sharp.

X-ray analysis uses Bragg diffraction (Kittel (1976)). For topographical studies an image is formed in an object plane from diffracted beams. The intensity of the diffracted beams are modulated by changes or distortions of the Bragg plane which occur when a layer contains dislocations or tetragonal deformation due to strain. The resolution is essentially determined by the photographic limits, the finest nuclear emulsions have a grain size of 1μm, thus the resolution for dislocations and defects is about $10^6 cm^{-2}$.

From straight diffraction studies, lattice constants can be determined and hence alloy concentration and lattice distortion can be found. In general monochromatic X-rays are diffracted from a reference crystal to the sample the collected by an ionisation detector. Thus the sample is compared to the reference crystal. This technique produces various diffracted beams as a function of crystal angle giving what is known as a Rocking Curve. The theory of diffracted waves in crystals is well understood and determination of crystal quality and structure is then a matter of fitting theoretical rocking curves to the experimentally observed curves. (Tanner (1976)). From diffraction various parameters can be found:

i) layer thickness and lattice mismatch with substrate,
ii) tetragonal distortion because of inbuilt strain,
iii) superlattice period and average lattice constant.

Another technique used was secondary ion mass spectroscopy (SIMS). An ion beam is focused on the the crystal surface and sputters semiconductor ions from a 1nm deep region near the surface. These ions are collected and analysed by a mass spectrometer. The total sensitivity can be 1 impurity atom in 10^5 and depth profiling can be undertaken by etching away the crystal with the ion beam. Once calibrated, accurate depth profiles can be obtained. (Prutton (1983)).

If defects and dislocation densities are very low, optical microscopy techniques can be used. Preferential chemical etches can highlight surface defects related to threading dislocations from lattice misfits, which are then counted under a microscope to give defect density values.

2.2 Electronic Properties.

The second section of chapter 2 is devoted to electron behaviour in layered Si/Ge heterosystems. Firstly a review on bulk electronic properties of Si and Ge semiconductors is given. Electronic states within a crystal directly affect the optical properties of the crystal, for example optical reflectivity and transmission. Following from a description of bulk states the concept of band offsets between heterojunctions of Si and Ge is defined and electronic states in layered structures forming 'quantum wells' are discussed. Some typical parameters are used to calculate the electronic transitions one might expect in quantum wells and these results will be used for comparisons with experiments in chapter 6.

The next section describes electronic transitions formed by making very short-range changes in the crystal potential by making layered structures a few monolayers in thickness from Si and Ge. Comparisons with bulk crystals and confined states found in Kronig-Penney models (Kittel (1976) are made and the symmetry groups of superlattice structures are given. The band structure for a particular superlattice consisting of 4 monolayers of Si and 4 monolayers of Ge is discussed and finally electronic transitions in a proposed superlattice which has a direct energy gap are described. Predicted strengths and energies of optical transitions are tabulated for use in later experimental chapters.
Sections 2.2.6 and 2.2.7 describe how the electronic band structure is related to the optical properties of semiconductors, and how these properties are experimentally observed.

Finally a brief historical review of the optical investigations in Si/Ge systems is given.

2.2.1 Properties of elemental silicon and germanium.

The electronic states in semiconductor layered superlattice and quantum well structures are mainly determined by the electronic states in the bulk constituent semiconductors.

Si and Ge both have very similar band structures; this is a consequence of both semiconductors being uni-polar with hybridized s^2p^2 covalent bonding orbitals which form a diamond unit cell structure (Kittel 'Theory of Solids' (1987)). (Diamond structures have face-centred-cubic Bravais lattices with two atoms per basis unit.)

As Chelikowsky and Cohen (1976) point out the major differences between Si and Ge stem from the

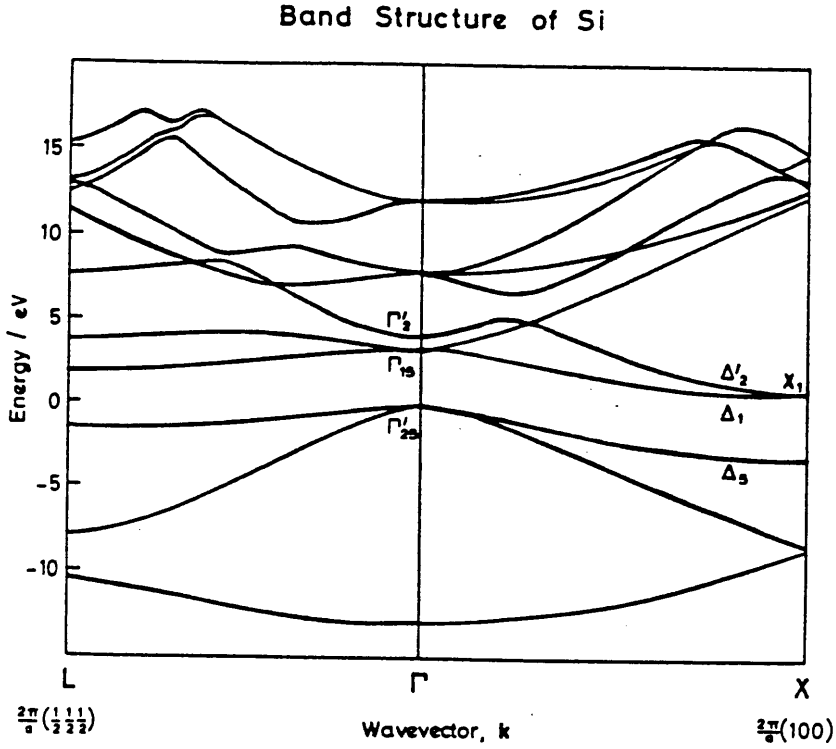


Figure 2.6 Calculated band structure of silicon, the lowest part of the conduction band occurs at Δ, no spin effects are included but two effective masses are observed for the valence band structure.

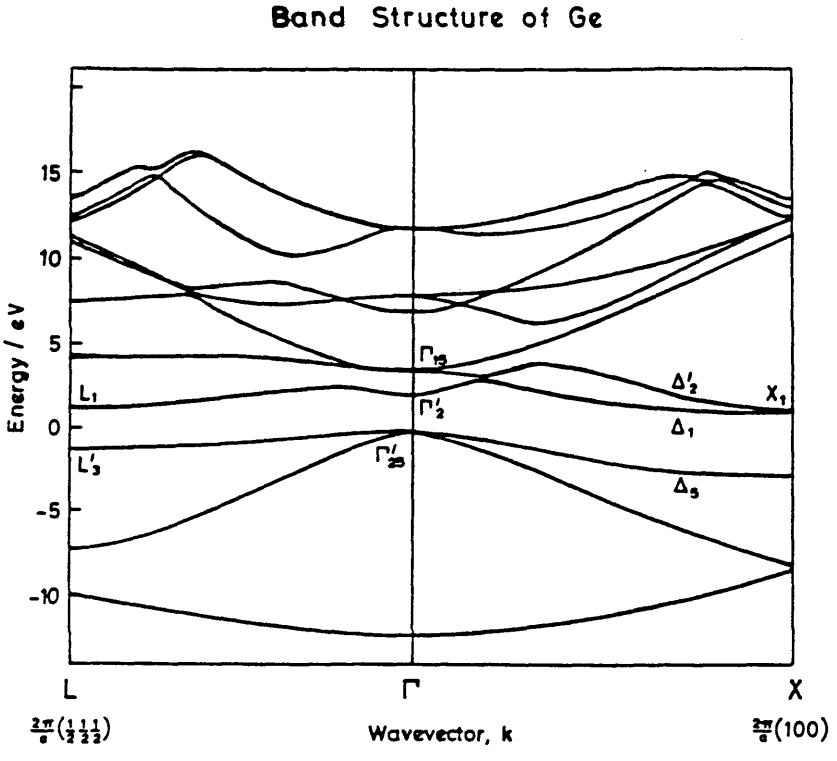


Figure 2.7 Calculated band structure of germanium, the lowest part of the conduction band occurs at L, no spin effects are included but two effective masses are observed for the valence band structure.

different atomic masses (Si:28.086 and Ge:72.59) and lattice constants (Si:10.2611au. and Ge:10.6921au.). Neglecting spin-orbit coupling the valence and conduction bands can be described with a ns^2np^2 electron basis set, ignoring effects from core electrons, where n is either 3 or 4 depending on the period of the element. Figures 2.6 and 2.7 show the two band structures which have been calculated on a small computer using the procedures of Press et al (1987) and using local pseudopotentials in a 50 plane wave basis OPW scheme (Bassani and Parravicini (1975)). The pseudopotential form factors have been taken from tabulated data found in Cohen and Heine (1971). Notice the similarity of the valence bands, only the ordering of the conduction bands is different between Si and Ge.

Considering the symmetry of the bands at the Brillouin zone centre, it is found that the lowest valence band has Γ_1 representation, that is s like symmetry. The upper most valence band is Γ'_{25}, being triply degenerate when spin-orbit coupling is neglected. The overall symmetry of these bands corresponds to covalent p like bonding electrons in the lattice. The inclusion of spin-orbit coupling is represented by 4 fold Γ^+_8 band and 2 fold Γ^+_7 band. The valence bands have different curvature and correspondingly different effective masses. It is convenient to label these bands using an angular momentum representation $|J,M_j>$, where J is the angular momentum quantum number and M_j is the magnetic quantum number. Thus the heavy hole (hh) band is labeled |3/2,3/2> and the light band (lh) |3/2,1/2>. The presence of spin interactions split the six fold degenerate band to form another double degenerate band |1/2,1/2>, the split-off band (so). The justification of these representations can be found by considering the decomposition of the Γ'_{25} band into the free space p orbitals (Bassani and Paravachini (1976)).

The conduction bands consist of anti-bonding orbitals and thus their symmetry reflects this. In the case of Si the lowest conduction band has a Γ_{15} representation, a mixture of p and d like electrons, dispersing down in the Δ direction to form a minimum in energy at about 0.8X. This minimum is six fold degenerate in momentum space and is a mixture of s, p and d like in character.

In Ge, the s like Γ'_2 band which lies above the Γ_{15} band in Si has been pushed down to form the lowest conduction band. This band then disperses to a minimum energy at L, this point having 8 fold degeneracy in momentum space.

In the dipole approximation the optical transition matrix operator, which determines the allowed transitions and their strength is represented by **r** which has a Γ_{15} representation in the O_h group. (Tables of Tinkham (1968) and Bassani and Paravachini (1976)). For transitions from the upper most valence band to conductions band states the following bands have symmetry allowed transitions (ie. by

Table 2.1 Si and Ge Mechanical and Physical Constants.

	Si	Ge	
b	-2.35	-2.55	eV
Δ	0.044	0.292	eV
c_{11}	1.657	1.292	10^{12} dyn/cm^2
c_{12}	0.639	0.479	10^{12} dyn/cm^2
a_{Si}	5.431	N/A	Å
a_{Ge}	N/A	5.657	Å
δPE_0	-	12.5×10^{-6}	eV/Kgcm^2

This table shows physical parameters for crystal and band deformation of Si and Ge. b, Δ and δPE_0 are the valence band deformation potential, s-o splitting and E_0 critical point hydrostatic deformation, c_{11} and c_{12} are the irreducible lattice compliance parameters and a_{Si} and a_{Ge} the Si and Ge lattice constants.

The parameters are taken from papers of Pollak and Cardona (1968), Chandrasekar and Pollak (1977) and tabulated results in Neuberger (1971) and Brantley (1973).

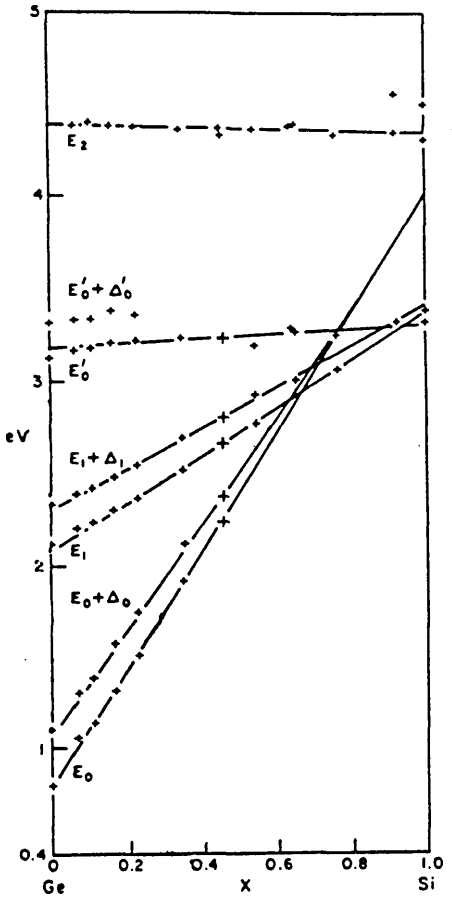


Figure 2.8 Critical point energies for $Si_{1-x}Ge_x$ alloys of various compositions, determined by electro-reflectance spectroscopy. (After Kline, Pollak and C ardona (1968)).

considering the decomposition of $\Gamma_{15} x \Gamma'_{25}$):

Γ'_{25} to Γ'_2 labelled E_0
Γ'_{25} to Γ_{15} " E'_0
Γ'_{25} to Γ_{25}
Γ'_{25} to Γ_{12}

E_0 and E'_0 label critical points. The strength of the opitcal transitions depends strongly on the local density of states in the bands participating in the optical transition. For a critical point the joint density of states is high, and thus the measured optical signal will be enhanced over other allowed transitions. There are other allowed critical points away from Γ, where the band symmetries are compatible and joint density of states are high. For example along L'_3 to L_1 is labelled E_1. Kline et al. (1968) have measured critical point energies for these high symmetry points in a range of $Si_{1-x}Ge_x$ relaxed alloys. Their results are shown in figure 2.8. The lowest direct optical transitions are 3.34eV E_1 transition in Si and 0.889eV E_0 transition in Ge. The smallest conduction to valence band transition assisted by phonons is 1.17eV for the Si Γ'_{25}-Δ_1 and 0.7eV for the Ge Γ'_{25}-L_1. The purpose of the superlattice described below is to allow the lowest indirect transitions to behave like direct transitions. Before considering electronic states in strained epitaxial layers it is necessary to consider the effects on bulk bands when external stress and strain is applied.

Hydrostatic pressure does not change the symmetry of the unit cell but only the size and consequently the perturbation does not lift any degeneracies. However the hydrostatic pressure moves all the bonding orbitals closer together, hence increasing their overlap and increasing the width and gaps of the bands.

The E_0 critical point changes due to hydrostatic deformation as

$$\Delta E_0 = \frac{\delta P E_0}{3} (c_{11} + 2 c_{12}) |\varepsilon| \qquad [2.10]$$

where $\delta P E_0$ is the hydrostatic deformation of the E_0 gap, c_{11} and c_{12} are compliance parameters and ε the strain, values are defined in table 2.1.

Uniaxial stress changes the symmetry of the unit cell and hence will cause some splittings of degenerate bulk bands for directions in the lattice which become inequivalent. Considering a compression in the z-direction, the bonding orbitals in this direction will be compressed together, the xy or in-plane bonds

will be pulled apart. **s** like bands will be unaffected, the **p** like states however will lose their degeneracy. Thus for Si or Ge the **p** like conduction valleys will split in energy and the upper most doubly degenerate valence band will split into two bands.

Considering the valence bands first, a description in terms of a **k.p** expansion can be used. (Luttinger and Kohn (1955)). Following a reduced form by Pollak and Cardona (1968) the valence band Γ_{25}' can be written in terms of the basis set: $|J,M_J>$. The perturbation effects of uniaxial deformations being described by the following matrix:

$$\begin{array}{ccc} |\frac{3}{2},\frac{3}{2}> & |\frac{3}{2},\frac{1}{2}> & |\frac{1}{2},\frac{1}{2}> \\ \begin{vmatrix} E_s & 0 & 0 \\ 0 & E_s & E_s\sqrt{2} \\ 0 & E_s\sqrt{2} & \Delta+E_s \end{vmatrix} & & \end{array} \qquad [2.11]$$

when diagonalised matrix [2.11] gives new energies for the strained perturbed valence bands:

$$E(1) = E_s$$

$$E(2) = -E_s/2 + \Delta/2 - \frac{1}{2}(\Delta^2 + 2\,\Delta E_s + 9E_s)^{\frac{1}{2}}$$

$$E(3) = -E_s/2 + \Delta/2 + \frac{1}{2}(\Delta^2 + 2\,\Delta E_s + 9E_s)^{\frac{1}{2}} \qquad [2.12]$$

where $E_s = 2b(\varepsilon_{||} - \varepsilon_{\perp})$ [2.13]

Where $\varepsilon_{//}$ and $\varepsilon_{\perp}$ are the strains in the crystal for parallel and perpendicular directions respectively, defined by

$$\varepsilon_{||} = 1 - \frac{a_{||}}{a}$$

[2.14]

$$\varepsilon_{\perp} = 1 - \frac{a_{\perp}}{a}$$

Equation [2.15] relates z-direction and in-plane lattice constants.

$$a_{\perp} = a\left(1 - \frac{2c_{12}}{c_{11}}\left(\frac{a_{\parallel}}{a} - 1\right)\right) \qquad [2.15]$$

b is the valence band deformation potential and Δ is the spin-orbit splitting for the bulk bands, c_{11} and c_{12} are stiffness factors defined in table 2.1.

Matrix [2.11] arises from Luttinger's (1956) general **k.p** expansion for the upper valence bands. The momentum operators **p**, are expressed in terms of the angular momentum operators, with the $|J,M_J>$ basis set. The operators become inequivalent when uniaxial strain is applied to the system.

It can be seen that at the Brillouin zone centre, the light and heavy hole bands split by the uniaxial stress component $3/2E_s$, but also mixing of the light and split-off bands occurs. Away from the zone centre mixing of all three valence bands occurs and if effective masses of the new bands are required then the full **k.p** formalism of Luttinger and Kohn away from Γ is required, (Luttinger and Kohn (1955) and Luttinger (1956), see also Hensel and Feher (1963) and Hessagawa (1963) for a more detailed analysis of strain perturbation effects).

The precise deformation of the conduction band valleys away from Γ is not needed for the measurements presented later which concentrate on direct transitions and involve states only at Γ (Pearsall et al (1986)). The effects of both hydrostatic and uniaxial deformations are depicted in figure 2.9 comparing deformed $Si_{1-x}Ge_x$ against cubic Si.

For $Si_{1-x}Ge_x$ strained layer epitaxy, the tetragonal distortion contains a mixture of both hydrostatic and uniaxial components. Considering growth of pure Si on to a Ge substrate (ie. the in-plane lattice constant is constrained to take the value of Ge that of 5.657Å) then the Si will be compressed in the growth direction due to the Poisson effect and extended in the in-plane directions (Equation [2.15]). This has the effect of decreasing the direct band gap, lowering the in-plane Δ conduction valleys and raising the z-direction Δ conduction valley. The opposite effects will occur when Ge is grown tetragonally distorted to take the Si substrate lattice constant. For this case it is found that the L conduction band valleys lie above the degenerate Δ valleys in the in-plane directions.

When looking at the tetragonal distortion effects on the valence bands, it is found that the ordering of the masses is reversed for the nonequivalent directions. For compressional stress ie. tetragonlly distorted Si on a Ge substrate, the upper valence band has a light hole character in the stress direction

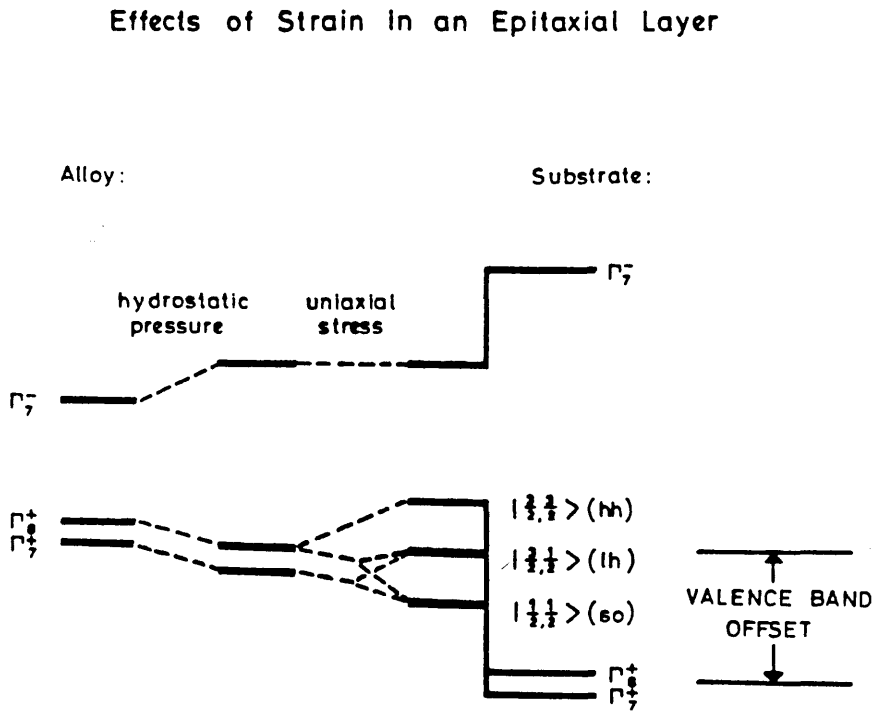


Figure 2.9 The effect of tetragonal distortion on the zone centre conduction and valence states of a SiGe alloy grown on Si. The structure is Type I, and the top valence band is heavy hole in character in the growth direction.

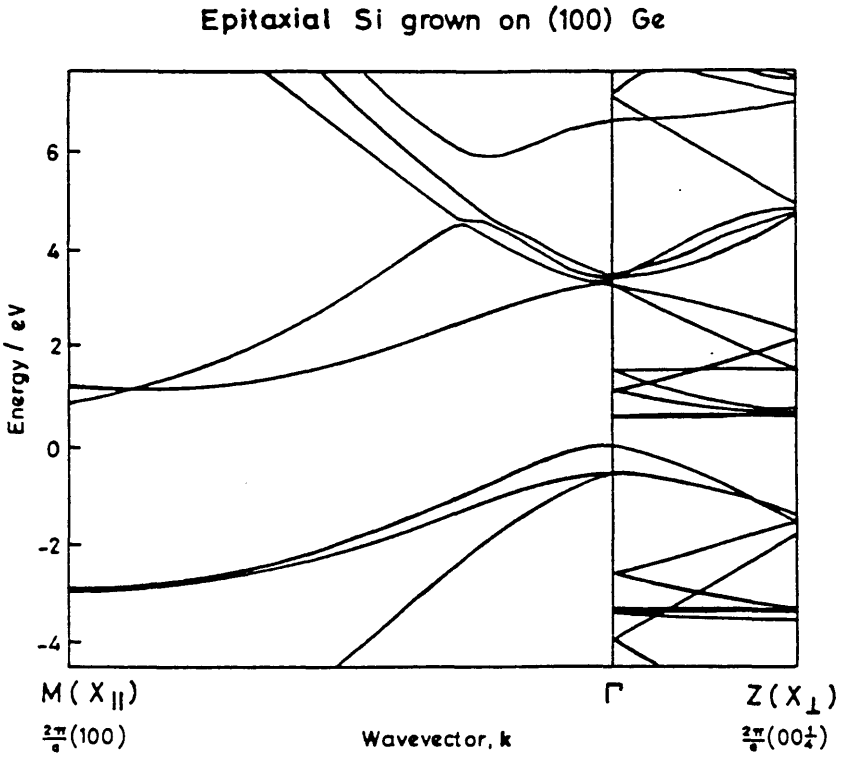


Figure 2.10 Calculated band structure of tetragonally distorted silicon grown on a germanium (001) surface. Z and M represent the growth and in-plane layer directions respectively, the conduction band valleys are now split, the lowest is in the growth direction. The valence band degeneracy at the zone centre has been lifted, with a light hole like state in the growth direction and a heavy hole like state in the layer plane.

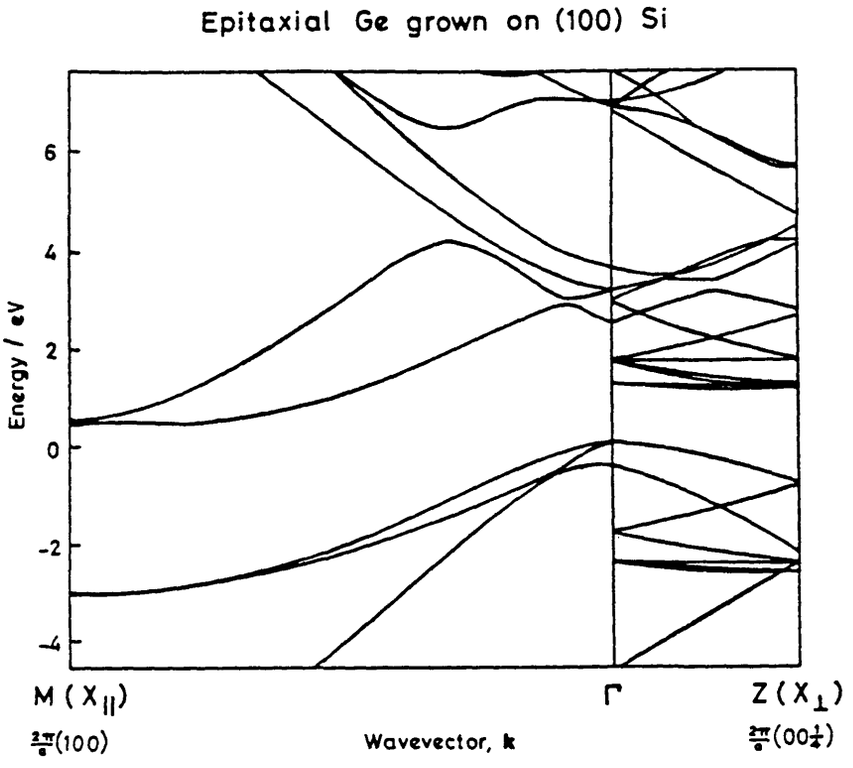


Figure 2.11 Calculated band structure of tetragonally distorted germanium grown on a silicon (001) surface. Z and M represent the growth and in-plane layer directions respectively, the conduction band valleys are now split, the lowest is in the M direction. The valence band degeneracy at the zone centre has been lifted, with a heavy hole like state in the growth direction and a light hole like state in the layer plane.

(z-direction) but is heavy in character for the in-plane directions. Conversely the masses reverse for tensional stress, (that is Ge distorted to a Si substrate). This 'hole ordering' is really a consequence of the decomposition that makes up the light and heavy hole bands. Neglecting spin, the light hole consists of p_z, and some (p_x+ip_y) orbitals, the heavy hole consists only of p_x+ip_y (Bastard and Brum (1985)). After strain has been applied substantial mixing of these states will have occured at momentum values away from k=0.

Figures 2.10 and 2.11 show the band structures for Si and Ge however, the crystals have been distorted tetragonally to have in-plane lattice constants of each other. Form factors are taken from the previous calculations, but the unit cell and final crystal potential have been distorted using equation [2.15]. In this figure the z-direction has been folded into the zone centre by a Bloch symmetry operation, this symmetry operation represents a reduction in translational symmetry of four times the original unit cell of the fcc lattice. Such a reduction would occur if a superlattice were constructed having a repeat period of 8 monolayers. For example this construction is useful when considering the repeated 4 monolayer: 4 monolayer Si/Ge short-period superlattices in section 2.3.

2.2.2 Alignment of valence bands in heterojunctions.

In an epitaxial system, semiconductors having different atomic potentials are allowed to come together with abruptly. Thus it is important to know how the electronic states align at the crystal interfaces. One consequence of band misalignment may result in the electrons being energetically confined to one of the semiconductors.

Alignment of the bands occurs on an atomic scale; once the alignment of atomic states is known then the alignment of the valence band can be found. The valence band offset may be used in semi-empirical superlattice band structure calculations or effective mass approximations to calculate new valence and conduction states for electrons and holes in heterojunction systems.

Experimentally the valence band offsets may be found from comparing optical transitions from the valence to vacuum states of the various semiconductors using X-ray Photoemission Spectroscopy (Prutton (1983)). Unfortunately this method has the disadvantage of large systematic errors in experimental energies being subtracted to find the valence band offset. Another method using photoluminescence, that relies on the alignment of deep level impurities (associated with dislocations), can also yield the band offset (Weber (1990)).

When calculating valence band offsets it is important to realise that the calculated valence bands, although derived from atomic potentials bear no energy reference to them. Lining up the atomic potentials at the semiconductor interface does not immediately give the valence band offset for the two materials. Thus a more ellaborate scheme is needed. The most widely quoted and first published predictions for the Si/Ge valence band offset have come from the calculations of Van der Walle and Martin (1986). Their calculations use a self-consistent formalism in a Local Density Framework and are thus ab-initio.

Since uniaxial stress significantly alters the positions of the atoms at the interface (the Poisson effect is a bulk manifestation of this), the valence band offset was calculated for the Si/Ge system either with the Si tetragonally strained to Ge or vice versa. A linear interpolation can be used between the two extreme distortions of the lattice. If a $Si_{1-x}Ge_x$ alloy is used for one of the sub-lattice instead of pure Ge or Si then a virtual crystal approximation can be used to calculate the final valence band offset.

The predicted results compare well with the experimental values of Yu et al. (1990) and other calculations using Linear Combinations of Muffin-tin Orbitals of Cardona and Christensen (1989). The photoluminescence results of Weber (1990) also confirm these predictions. Van der Walle's and Martin's results together with some experimental results are summarised in the following table **2.2**.

2.2.3 Electronic states in multiple quantum well structures of Si and Ge.

In this section the effect of how electronic states are altered when a weak potential over a large range is considered; such a change is produced by changing the Ge concentration in thick quantum well layers.

Considering one band it can be assumed that the electron with an effective mass m^* will experience an additional potential due to the change in Ge content as a function of position. As the quantum well structure is large compared to the atomic scale, the potential can be modelled by the band offset and the effective mass parameter at the band edge. This is called the effective mass approxiamtion (Bastard and Brum (1985)). New electron states of increased energy will be formed in the well region due to the barrier confinement potential. Multiple quantum well electronic states can be calculated by the Kronig-Penney formalism. From Kittel (1976) the expression for the Kronig-Penney model, equation No.20 Chapter 7 is modified to allow different effective masses for well and barrier bands.

The following transcendental equation must be solved for the electronic confinement energy **E**:

Table 2.2 Valence band offsets for Si/Ge heterojunctions.

	Si/Ge strained to Si(001) (relative to Si VB) eV	Si/Ge strained to Ge(001) (relative to Si VB) eV
Theory (average of all 3 bands)		
Van der Walle & Martin	0.54	0.51
Cardona & Christensen	0.27	-
Experiment (upper most valence band)		
Mahowald et al. (1985)	0.4 +/- 0.1	-
Yu et al. (1989)	0.83 +/- 0.11	0.22 +/- 0.13
Lang et al. (1985)	0.8	
Abstrieter et al. (1985)	0.4	
People (1986b) references therein	0.74	0.24

$$\cos K(a+b) = \frac{(q^2m_1^2 + k^2m_2^2)}{2m_1m_2qk} \sin ka \,.\, \sinh qb + \cos ka \,.\, \cosh qb$$

[2.16]

where $q = \frac{(2m_2(U-E))^{\frac{1}{2}}}{\hbar}$ $\qquad$ $k = \frac{(2m_1E)^{\frac{1}{2}}}{\hbar}$

u is the potential imposed by the quantum well, K an arbitrary wavevector of the 'superlattice' made from the repeated quantum wells of barrier length a and well length b. m_1 and m_2 are the effective masses for the bands in the barriers and wells respectively, which modify the free electron wave and where h is Planck's constant.

If E is greater than u then hyperbolic functions replace the trignometric functions and the electronic states sit above both well and barrier band edges (Bastard and Brum (1986)).

The following sections describe the confining effects on electronic states within multiple quantum wells consisting of $Si_{1-x}Ge_x$/Si strained layers.

Figure 2.9 shows how the conduction and valence bands would be aligned for pseudomorphic $Si_{1-x}Ge_x$ alloys grown on Si (Van der Walle and Martin (1986)). For both Γ'_2 electrons and Γ'_{25} holes in the alloy the Si regions represent forbidden barriers, thus both electrons and holes are confined to the same part of the semiconductor crystal. Such a heterojunction system is denoted a type I structure. Providing the electrons maintain their symmetry ie. they remain in the same band throughout the heterostructure, a confining effect will increase the energy of the electronic states within the $Si_{1-x}Ge_x$ layers and not allow states within the Si layers of the structure.

In considering the lowest energy optically allowed direct transitions in bulk Si and $Si_{1-x}Ge_x$ alloys it is noted that although in Si the E_1 critical point has the lowest energy, for alloys of 30% Ge or more the E_0 critical point moves down and becomes the lowest energy transition. For the calculation of quantum confined conduction band states the Γ'_2 band, corresponding to the conduction band involved in the E_0 critical point in Si and Ge, is used.

Firstly, the effects of deformation are considered. The equations for uniaxial and hydrostatic deformation from the preceeding section have been used for the bands involved in the E_0 transition. Figure 2.12 shows the collective effects of strain and alloy composition on these bands. Band gap energies for alloys were taken from Kline et al. (1968).

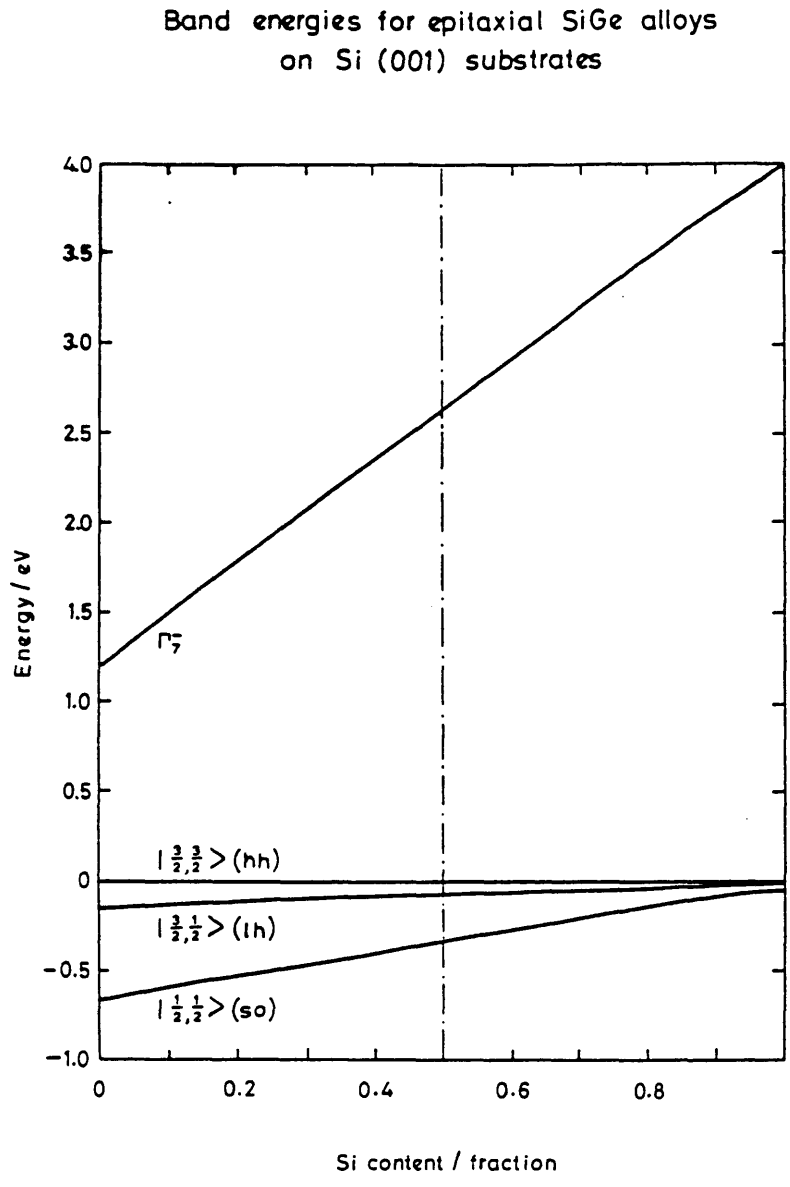


Figure 2.12 Energies for the Γ'_2 conduction band and upper most valence bands in tetragonally distorted $Si_{1-x}Ge_x$ grown on Si(001), as a function of composition.

Table 2.3 Parameters for Effective Mass Calculations of $Si/Si_{0.5}Ge_{0.5}$ quantum well samples.

	Well mass	Barrier mass
e	0.11	0.18
lh	0.23	0.16
hh	0.27	0.5
so	taken as approx. to hh	

ΔE_v (valence band offset, average over the 3 bands.)	:	0.26 eV
ΔE_c (conduction band offset for Γ^-_7/Γ'_2)	:	0.95 eV

Table 2.4 Transition energies of multiple quantum well samples of section 6.

Well width (Å) $Si_{0.5}Ge_{0.5}$	10	20	40
Barrier width (Å) Si	60	120	240
hh - Γ_2 (eV)	3.34	3.01	2.79
lh - Γ_2 (eV)	3.37	3.14	2.89
so - Γ_2 (eV)	3.86	3.33	3.11

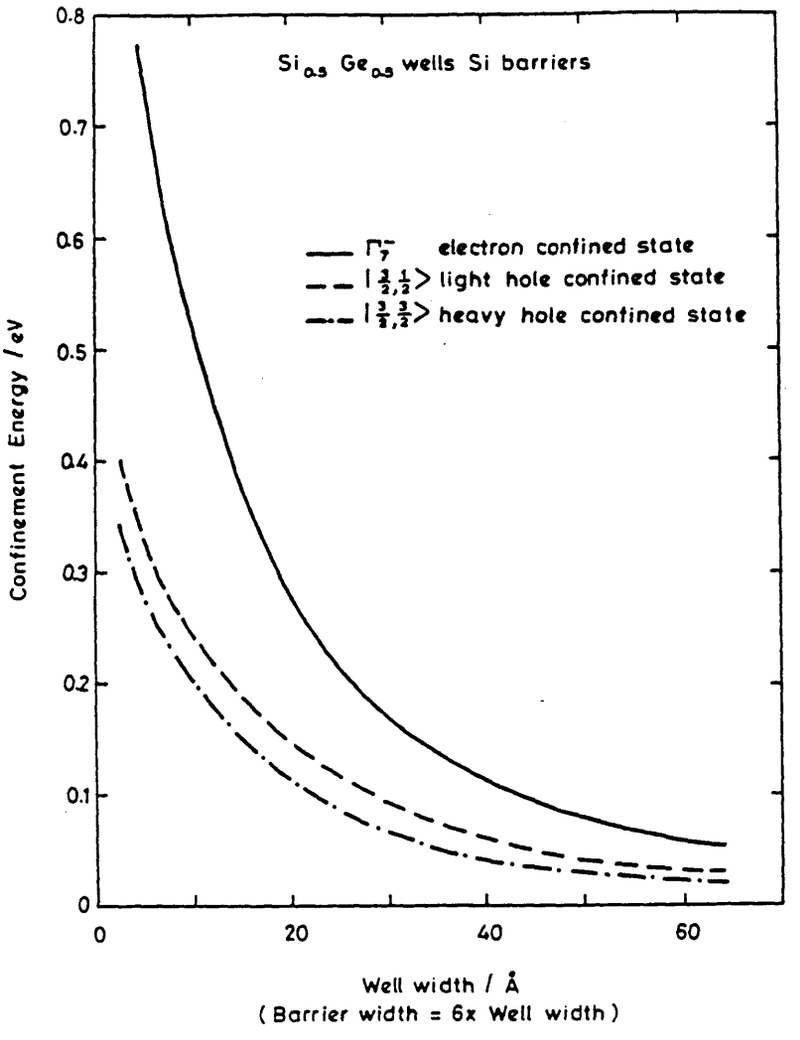


Figure 2.13 Confinement energies for electrons, light and heavy holes in $Si_{0.5}Ge_{0.5}$/Si multiple quantum wells as a function of $Si_{0.5}Ge_{0.5}$ well width. The Si barrier width is set at 6 times the well width. The mass parameters and barrier heights are defined in table 2.2.

BIBL. LONDON UNIV.

For the calculation of the confinement effects on these bands, an alloy composition of 50% is chosen, which is the composition of the samples discussed in the experimental chapter.

Equation [2.16] is then solved for Γ_2' and strain split Γ_{25}' bands of the $Si_{0.5}Ge_{0.5}$/Si quantum well system. Using the virtual crystal approximation an average valence band offset of 0.26 eV is found from the results of Walle and Martin (1986), thus the conduction band offset for Γ_2' is 0.95 eV. These band offset values represent the potentials u for the valence and conduction bands.

Although the results are less sensitive to effective mass parameters than to length parameters, the effective masses have been calculated using the effective mass sum rule (Gell (1990b)), and are given in table 2.3.

The lowest confined state relating to Γ_2' and strain split Γ_{25}' bands are plotted as a function of confining width in figure 2.13 for a strained $Si_{0.5}Ge_{0.5}$ quantum well confined with Si layers. The final optical trnasitions within the quantum wells are the sums of both strain and confinement effects.

The symmetry of the bulk bands chosen for the calculation is such that optical transitions are allowed. Confinement effects of the quantum well will modify the electronic wave functions and give rise to a new set of states, conventionally numbered by index n, in ascending order of confinement energy E. The symmetry of the new pseudo-wavefunctions gives rise to a new selection rule for optical transitions. For conduction and valence band representations c and v that are compatible via the dipole representation; the allowed sub-band transitions have the same index:

$$n_{\Gamma_c} = n_{\Gamma_v} \qquad [2.17]$$

The calculated transitions for n = 1 are listed in table 2.4.

2.2.4 Electronic states in superlattices of Si and Ge.

As the well and barrier widths of a quantum well structure are reduced the electronic states which were isolated in the wells will extend and mix with each other. The resulting structure is called a superlattice.

Another way to view a superlattice however, is to view it as an artificial periodicity brought about by an ordering of consituents of a random alloy. The composition of the alloy being the average composition over the superlattice period. This alloy is appropriately denoted the host crystal of the superlattice. Thus an approach for calculating the electron states in a superlattice is to impose a weak ordering potential on the random alloy. This is particularly useful if the period of the superlattice is very short and comparable with the inter-atomic spacing of the bulk crystals.

.1 Symmetry considerations.

A superlattice in this context is defined to consist of a periodic structure made from small numbers of monolayers (2 to 8) of elemental semiconductors. This structure is somewhat smaller than other superlattices currently made with III-V semiconductors, see for example Shields et al. (1990). The length is such that electronic states of each semiconductor overlap and are extended over the entire period.

Here superlattices made from two types of atomic species are considered. The superlattice is denoted: A/B (n:m) C(001), indicating a period of n+m monolayers containing n monolayers of semiconductor A and m monolayers of semiconductor B. The whole structure is grown on the (001) surface of semiconductor C, thus the in-plane lattice constant is constrained to take that of semiconductor C.

For superlattices orientated to the (001) direction, the superlattice point group can be described by one of three subgroups of O_h, obtained by inspection (for example see Satpathy et al. (1988), however their inspection misses a special case of n=m=1 which produces the T_d subgroup). The subgroup depends on the number of monolayers of Si or Ge and is given in table 2.5. Only the superlattice having a group D_{2d} lacks inversion symmetry and thus electro-optical effects may occur (Yariv (1985)).

As previously discussed in the introductory chapters the substrate lattice constant has the ability to shift the strain throughout the unit cell of a Si/Ge short-period superlattice. As the Ge content of a $Si_{1-x}Ge_x$ alloy substrate is increased, the strain shifts from the extreme of (i) purely strained Ge, to (ii) equally compressed Ge and tensile stressed Si, to (iii) purely tensile stressed Si.

The samples considered in this work were nominally specified as Si/Ge (4:4) or Si/Ge (2:6,8 or 10) superlattices grown on a variety of $Si_{1-x}Ge_x$ (001) substrates.

Considering the 8 monolayer period superlattice, a new unit cell is found. Here it is expressed in terms

Table 2.5 Symmetry Groups of the Si/Ge (n:m) superlattices.

Subgroup	number of layers			Example
O_h	n	or	m	
T_d	1		1	Si/Ge (1:1) on Si(001) (a zinc-blende crystal structure)
D_{4h}	odd		even	Si/Ge (3:4) on $Si_{0.5}Ge_{0.5}$(001)
D_{2d}	odd		odd	Si/Ge (5:5) on Ge (001)
D_{2h}	even		even	Si/Ge (4:4) on Si (001) Si/Ge (2:6) on $Si_{0.3}Ge_{0.7}$(001)

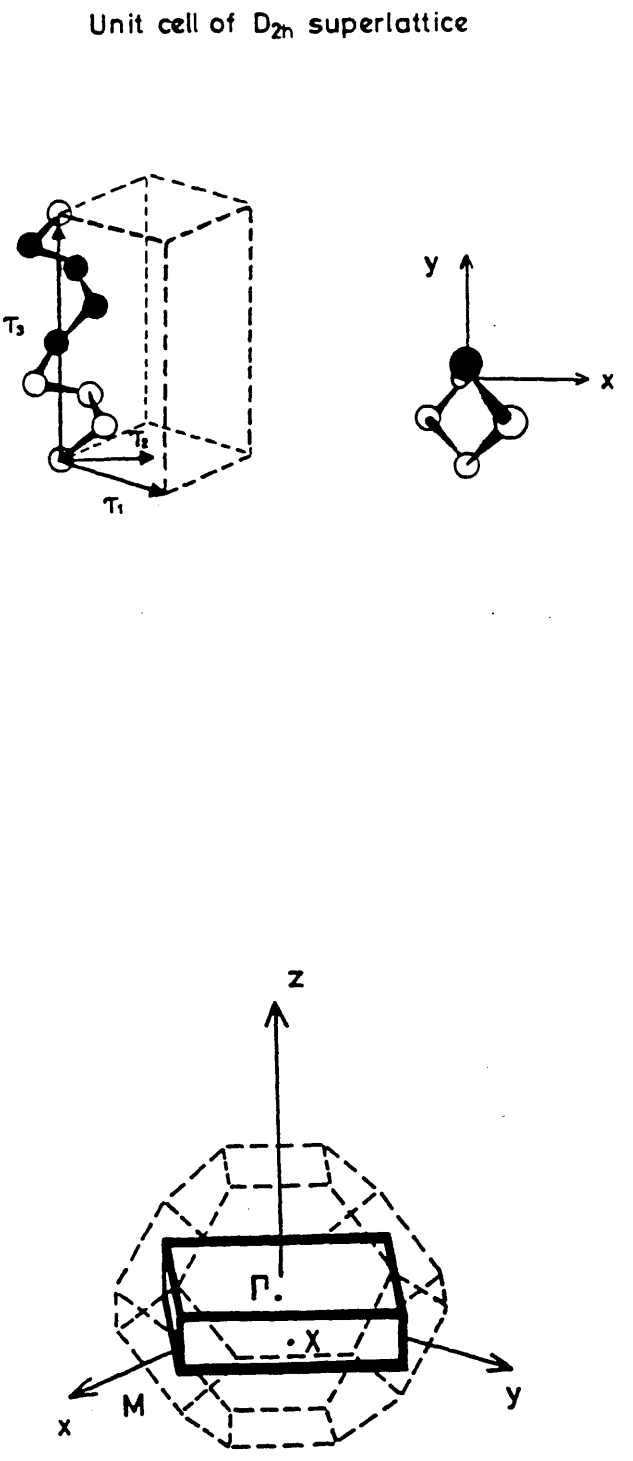


Figure 2.14 The unit cell for a D_{2h} superlattice and corresponding Brillouin zone, within the fcc Brillouin zone. The atomic positions for the Si/Ge (4:4) superlattice are shown.

of the diamond fcc unit cell length a, figure 2.14 shows the unit cell with vectors indicated.

$$a(1\,0\,0) \qquad \frac{a(1\,1\,0)}{2} \qquad a(0\,0\,2)$$

It can be seen that the reciprocal lattice is defined by:

$$\frac{2\pi(2\,0\,0)}{a} \qquad \frac{2\pi(1\,1\,0)}{a} \qquad \frac{\pi(0\,0\,1)}{a}$$

Figure 2.14 shows the corresponding Brillouin zone where special symmetry points have been labelled according to Gell and Churchill (1989).

By comparing the new superlattice Brillouin zone with the diamond fcc zone it can be seen that electronic states in the Z direction are derived from folded Δ_z bulk states. The M points are directly related to the in-plane X points in the bulk semiconductor, sitting in the same place for both Brillouin zones. The X and X' positions are related to the L points of the diamond structure. However, these points become inequivalent because of different directions of the interface bonds in the superlattice unit cell. As with the effects of strain in quantum well samples the valence band Γ_{25}' is split.

.2 Kronig-Penney model solutions

(for the Si/Ge (4:4) on Si (001)).

Calculation of the band structure induced by the superlattice is by no means an easy task, for example the (4:4) Si/Ge superlattice unit cell now contains 8 atoms.

However, as with the quantum well structures, sometimes it is possible to model the new electron states by bulk bands in the elemental semiconductors in the effective mass approach. For the case of a Si/Ge (4:4) on Si(001) superlattice this problem was first solved using the effective mass approach by People and Jackson (1987) and subsequently for other Si/Ge superlattice structures by Pearsall (1989).

It is not clear how these calculations determine the lowest lying conduction bands, as the lowest bands in Si and Ge are indirect and zone folding will occur when a superlattice is formed. Poeple and Jackson fold the X_1 Si valleys towards the zone centre and estimate a new effective mass at Γ. This state is then

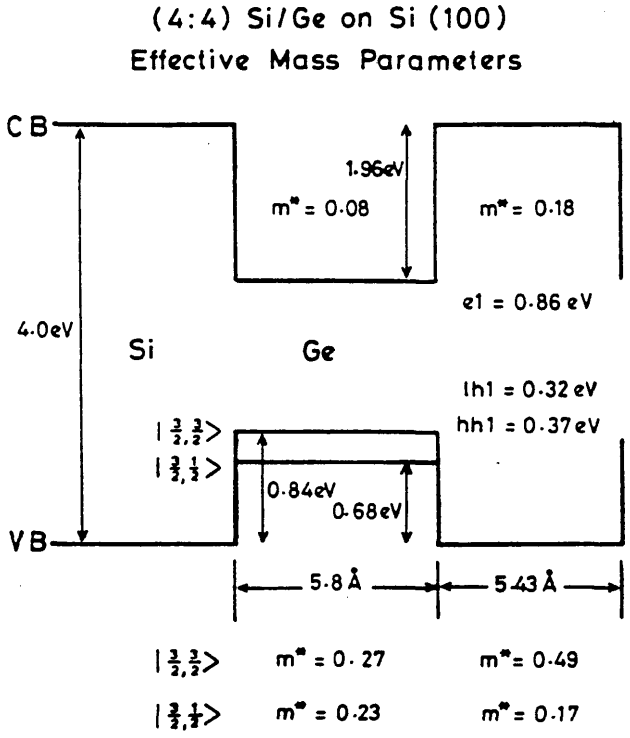


Figure 2.15 The conduction and valence band alignment for a Si/Ge (4:4) superlattice grown on Si (001) substrates. The confinement energies for the electrons and holes within the Ge 'well' regions are indicated.

used with Ge Γ_2' in equation [2.16] and a symmetry arguement to find a new superlattice state, (figure 1 of their paper is wrong as it assumes that the Brillouin zone is twice the actual size in the Z direction, thus this paper misses two transitions in the superlattice). Fortuitously their result compares well with full band structure calculations for the lowest electron states.

Presented here are confined states for the Γ_2' bands in Si and Ge, which can be calculated without any ambiguity. Figure 2.15 shows the band alignment for strained Ge on Si and the dimensions used in the calculation. Hydrostatic and uniaxial deformation potentials were used from the preceeding table (2.1). Equation [2.16] was then solved to give two optical transitions for strain split heavy and light hole respectively:

$$hh - \Gamma_2' = 2.42 \text{ eV}$$
$$lh - \Gamma_2' = 2.53 \text{ eV}$$

As Gell and Herbert (1987) point out when the superlattice period becomes comparable in size with the electron wave functions, an effective mass approach becomes meaningless as the superlattice states are a mixture of many bulk states across the whole Brillouin zone. This puts into question the validity of this type of calculation.

.3 Full Band structure Calculations.

(for the Si/Ge (4:4) Superlattices)

Calculations of the full band structure using atomic potentials have been tackled by a number of authors using different methods: For example local density approximation (LDA) schemes have been used by Satpathy et al. (1988), Froyen et al. (1988), together with quasi-particle theory by Hybertson and Schluter (1988), however calculations of this type can suffer as the methods normally calculate only ground state energies and no band gaps are predicted. Band gaps are calculated by adding extra electrons into the system under study, thus the conduction bands calculated are not truly excited states of the system but ground states of systems with unrealistic numbers of electrons. Other calculations use empirical pseudopotentials, for example Wong et al. (1987), Freidel et al. (1989) and Gell (1988). Also tight-binding schemes have been tried by Brey and Tejedor (1988). An extensive review is outside the bounds of the work however Gell (1988) compares some of the results for various types of calculation.

The reduced Brillouin zone produces a corresponding increase in the number of plane waves required to fully decribe the new electron states formed by the superlattice perturbation. By using a more

appropriate basis set of electron functions, ie. that of the host crystal, the calculation size is reduced to a more managable number of plane waves which can be realistically used for a convergent solution (This method has been exploited by Gell and Herbert (1987)).

It is useful to review this technique, so that it can be seen clearly how electron states in the superlattice are related to the host crystal. Firstly a solution to the alloy host crystal is solved, but over the superlattice unit cell instead of the zinc-blende unit cell.

$$H_0\psi_{nk}(\mathbf{r}) = \varepsilon_{nk}\psi_{nk}(\mathbf{r}) \qquad [2.17]$$

Then a superlattice wavefunction is expressed in terms of the alloy host:

$$\varphi_{sl}(\mathbf{r}) = \sum_n \sum_k A_{nk}\psi_{nk}(\mathbf{r}) \qquad [2.18]$$

then the superlattice eigenvalue equation is solved,

$$(H_0 + V)\varphi_{sl}(\mathbf{r}) = E_{sl}\varphi_{sl}(\mathbf{r}) \qquad [2.19]$$

where V is the difference in atomic potentials for an ordered superlattice and a random alloy, which also contains the minute changes in atomic position within the superlattice period due to strain deformation. Equations [2.18] and [2.19] become:

$$A_{n'k'}(\varepsilon_{n'k'} - E_{sl}) + \sum_n \sum_k A_{nk}\langle\psi_{n'k'}|V|\psi_{nk}\rangle = 0 \qquad [2.20]$$

The matrix element $\langle\psi_{n'k'}|V|\psi_{nk}\rangle$ is considerably simplified by the fact that the ψ_{nk} basis set is a better than plane waves which have been used in other calculations (Gell (1988)).

The technique allows the superlattice states to be easily described with equation [2.18] in terms of the random alloy states formed from the average composition of the superlattice.

The results of Gell (1988) are used to describe the band structure of the (4:4) Si/Ge superlattice. From figure 2.14 it can be seen that the Brillouin zone is reduced by a factor of 4 in one direction, (z - dir), thus a simple picture of the Δ_z valleys of the conduction bands folding in to the zone centre can be used, and the band structures of Si and Ge in figures 2.7 and 2.8 should be compared to the full band structure

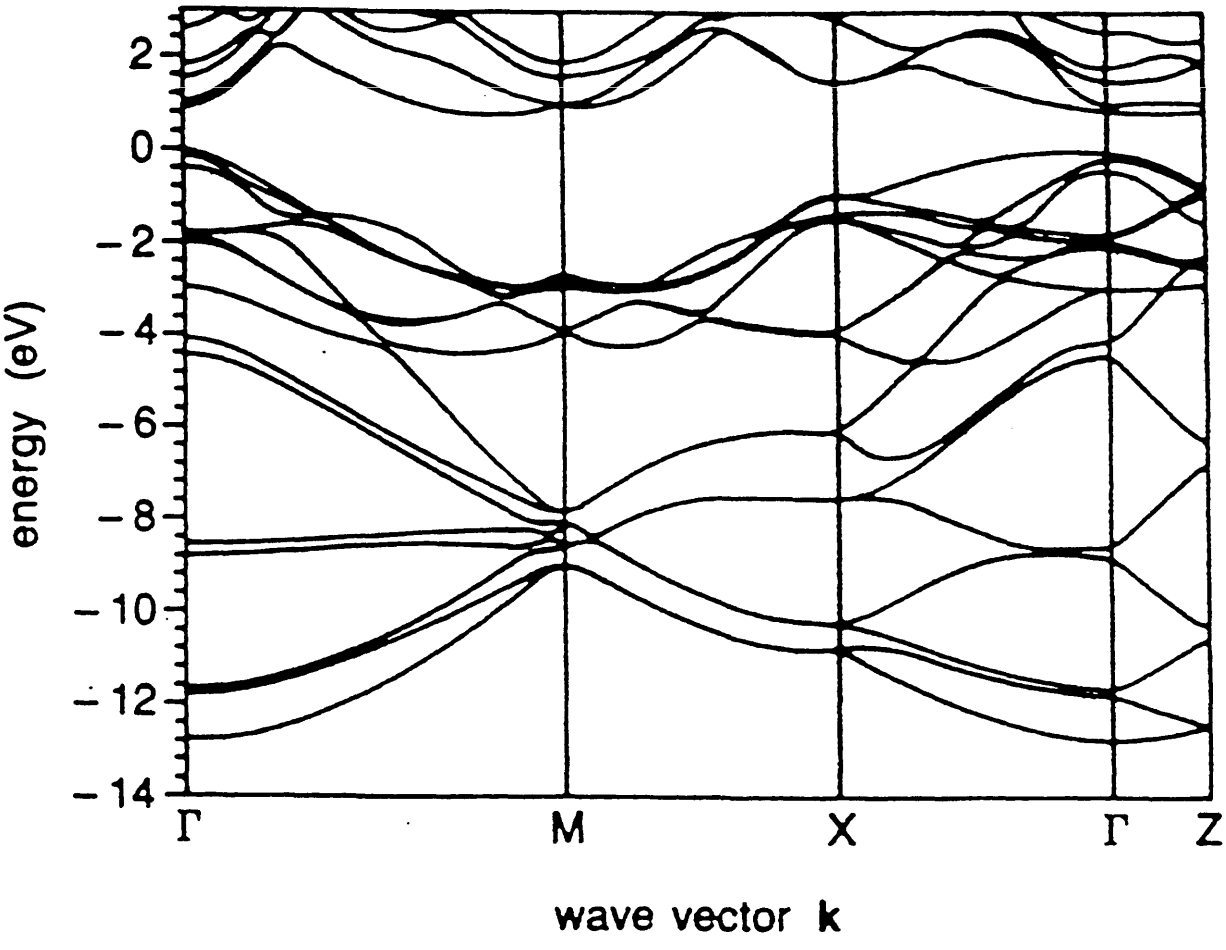


Figure 2.16 Band structure of the Si/Ge (4:4) superlattice on Si(001). The labelling of the high symmetry points in the superlattice is shown in figure 4. 1.

calculations below.

Figure 2.16 shows the full band structure of the (4:4) Si/Ge superlattice on a Si (001) substrate taken from Gell and Churchill (1989). It is instructive to consider the origin of the new bands in the superlattice. The superlattice bands are labelled C1..Cn for conduction bands upwards and V1..Vn for the valence bands downwards.

The essential difference between the host crystal, ie. that of the 50% alloy and the superlattice is the ordering of atomic potentials, which is expressed mathematically by the inclusion of the valence bands offsets of the two materials and the weak difference in atomic potentials of Si and Ge.

For the case of the Si/Ge (4:4) superlattice on Si (001), states C1..C4 originate from the folded Δ_1 states in the growth direction. Valence bands states V1..V4 originate from the Γ region. There is also significant conduction to valence band mixing Gell (1988). The M valley of C1 forms the lowest conduction band, this originates from the in-plane Δ valleys of the host crystal. If the superlattice is grown on Ge (001) the strain is transferred to the Si layers within the unit cell. The lowest conduction band valley is at Z. So for all distributions of strain within the unit cell the (4:4) Si/Ge superlatttice has an indirect bandgap. This reflects the failure of the (4:4) superlattice to fold in the bulk Si min valleys to the zone centre.

The symmetry of C1 at the zone centre is derived from Δ_1 of the host semiconductor, and optical transitions from the valence bands are forbidden. C2 has been mixed with some upper host conduction bands and has significant s like character. The C3 conduction band is evenly distributed thoughout the superlattice layers, however state C4 is confined to the edges of the layers and may be resonant in behaviour (this should be compared to the states found in GaAs/AlGaAs superlattices according to Gell (1988)). The next highest conduction band, C5 is not related to the zone folded Δ states but derived from the Γ'_2 band of the alloy host crystal, having s like character and being confined to the Ge layers. This state can be compared to the one calculated using a Kronig-Penney formalism of the preceeding section. As expected the near gap energy states are derived from states found over almost the entire Brillouin zone of the bulk constituent semiconductors.

Unfortunately even though the atomic potentials in the superlattice have been changed by inclusion on Ge instead of Si, the optical dipole matrix elements expressing the strength of optical transitions between the upper most valence band and lowest conduction bands still reflect the Si indirect band edge. Table 2.6 based on the results of Gell (1988) shows the squared dipole matrix elements, representing optical transition strength for the lowest allowed transitions at Γ in the (4:4) Si/Ge

Table 2.6 (Gell 1988) Optical transitions in the Si/Ge (4:4) superlattice on Si (100).

Valence Band	Conduction Band	Energy eV	Strength (Si $E'_0 = 1$) $\lvert\langle\Psi_{cond}\lvert e.r\rvert\Psi_{val}\rangle\rvert^2$
V1/V2	C2	1.0-1.2	0.0025
V1/V2	C3	1.5-1.6	0.025
V1/V2	C5	2.6-2.8	0.16

superlattice. The Si E'_0 transition is used as a reference and has unit value.

While the distribution of strain in the unit cell can move the lowest superlattice conduction band valley from M to Z, is does not significantly change the optical dipole matrix elements.

An important feature, not found in superlattice band structure calculations based on the Kronig-Penney model, is additional van Hove 'Critical Points' found in the Si/Ge (4:4) superlattice away from the Brillouin zone centre. These transitions have an origin from the E_1 transitions in Si and Ge, which occur at L in the diamond Brillouin zone. These points are mapped to the X and X' points in the superlattice Brillouin zone, giving rise to transitions in the range 2.37-2.45 eV and 2.80-2.89 eV, which have comparable strength to the zone centre transitions, shown in table 2.6. Such transitions are considered by Gell (1988), but not by other full band structure theories based on density functional theory. The Si/Ge (4:4) superlattice is investigated experimentally in chapters 5 and 6.

2.2.5 Predictions for a direct gap Si/Ge structure.

As can be seen above, a Si/Ge (4:4) superlattice does not possess a direct gap; the lowest conduction band always disperses down towards the Brillouin Zone edge, no matter how the strain is distributed in the superlattice period. This is a consequence of the lowest conduction band in the host crystal having a 'camel's back' like structure with a minimum at 0.8X.

As Gell points out (1988) this camel back structure in the lowest conduction band is reduced as the Ge content in the host crystal is increased. By increasing the Ge content to 75% the band disperses upwards away from Γ. Hence keeping the superlattice period of 8 monolayers but considering the (2:6) Si/Ge superlattice, it is found that the lowest point in the conduction band is at Γ. Which is the requirement for a direct band gap. This effect can be seen in figure 2.17, which shows the conduction bands for (6:2), (4:4) and (2:6) superlattice structures dispersing to Z.

Effectively the problem has been changed to one of making Ge direct by the inclusion of a biatomic layer of Si which pushes up the indirect L valleys allowing Γ'_2 to be mixed with the lowest conduction band state, (Gell 1989).

In addition to the superlattice average composition criteria of 75%, carrier confinement effects can be created by cladding the superlattice with $Si_{1-x}Ge_x$ alloys of x=0.6-0.8. This will create a type I band alignment for valence and conduction bands in the superlattice and surrounding substrate and cladding layers which will confine both electrons and holes in the superlattice region of the semiconductor

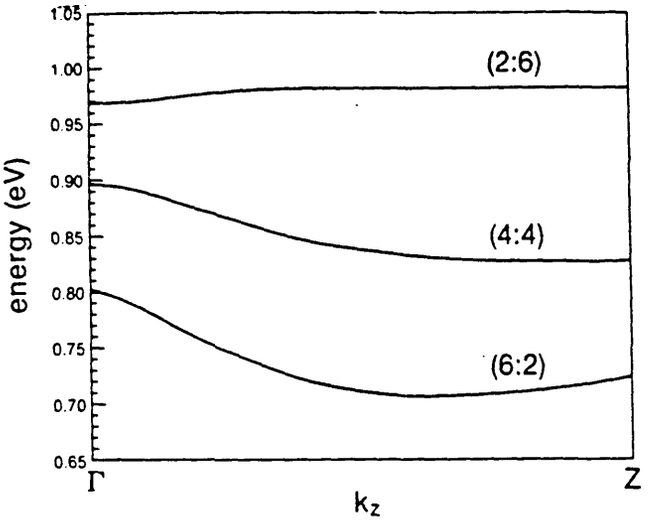


Figure 2.17 The z-direction dispersion for the lowest conduction bands in Si/Ge (2:6), (4:4) and (6:2) superlattices, showing that only the (2:6) superlattice has a direct band gap. (After Gell (1988)).

Table 2.7 Optical transitions for the (2:6) Si/Ge Superlattice

Valence Band	Conduction Band	Energy eV	Symmetry Properties
V1/V2	C1	~0.7eV	allowed
V1/V2	C2	~1.2eV	disallowed
V1/V2	C3	~1.4eV	allowed

heterojunction structure (Gell 1989). The predicted energy gaps from zone folded states are given in table 2.7

The bi-atomic sheet of Si is crucial in mixing bands of the host crystal with the correct symmetry to enhance the optical matrix element of the lowest conduction band at Γ. If one or three monolayers of Si are contained in the superlattice instead of half the unit cell of bulk Si, the **s** like Γ'_2 of Ge can become further mixed with the **p** like folded conduction band valleys, thus reducing the optical transition strengths by more than an order of magnitude (Gell (1988)). Other structures containing bi-atomic layers of Si are predicted to have direct band gaps, for example the Si/Ge (2:8) and (2:10) superlattices, Gell (1989).

Such structures containing biatomic layers of Si in a superlattice period are analysed in the experimental chapters.

2.2.6 Effects from the density of states.

Strengths of optical critical points in semiconductors, do not depend only on the optical dipole matrix element $\langle\Psi_{cond}|e.r|\Psi_{val}\rangle$ between the conduction and valence bands, but on the density of states at the various points on the band structure. This of particular relevance to Si/Ge systems since some of the conduction and valence bands have dispersions parallel to each other in **k**-space and thus have large joint densities of states. In chapter 4 the density of states for Si/Ge (4:4) superlattices on Si(001) and Ge(001) substrates has been calculated, and is compared to experimental values and bulk densities of states.

The optical properties of the semiconductor crystal are related to the electronic band structure by the dielectric response function, given in Ziman (1972). It relates the ability of the electrons in the crystal to move when a force or field is applied to the crystal, hence represents the screening function of the electrons and thus the electron band structure. Here the imaginary part of the dielectric function is given,

$$\varepsilon(E,\Gamma) = 1 + \frac{e^2\hbar^2}{\pi^2 m^2 E^2}\int dE \int dk_1 dk_2 \frac{|e.f_{ncnv}(k_1,k_2)|^2}{|\nabla_k E_{cv}(k_1,k_2)|}\left\{\frac{1}{E_{cv}(k_1,k_2)-E-i\Gamma}\right\} + \left\{\frac{1}{E_{cv}(k_1,k_2)+E+i\Gamma}\right\} \qquad [2.21]$$

Where $E_{c\,v}(k) = E_c(k)-E_v(k)$ corresponding to optical transitions between valence and conduction

bands. The term f_{ncnv} is a function of transition strength and is defined by

$$f_{ncnv} = \langle \psi_{nv} | e.p | \psi_{nc} \rangle \qquad [2.22]$$

It can be seen that the term ∇E in the denominator makes the optical response function [2.21] very sensitive to van Hove singularities or critical points in the band structure, where high densities of states are found and the bands participating in the optical transitions are parallel to each other in reciprocal space. This term appears in the integral of [2.21] as a consequence of the Jacobian transform from the real crystal space to the reciprocal space.

The real part of the dielectric function can be found from the imaginary part by the Kramers Kronig transform (Ziman (1972)).

2.2.7 Experimental techniques for observing electronic structure.

To determine the electronic band structure of a semiconductor it is common to use optical spectroscopy, thus determining the optical transitions within the band structure.

One common technique is photoluminescence spectroscopy. In this technique electrons and holes are created in the conduction and valence bands of the semiconductor by incident light. These carriers then relax to the band edges, where some of them recombine to emit light corresponding to the energy difference from the lowest conduction band and highest valence band (Stradling and Klipstein (1989)). Photoluminescence spectroscopy unfortunately can suffer from poor crystal quality, and measurements sometimes only reveal defects in the crystal rather than the band structure (Davies (1989)).

From the previous section, it can be seen that the dielectric function is related to optical transitions within the semiconductor. Thus optical reflectivity, absorption and transmission measurements can be used to determine the electronic band structure. For example the normal incidence reflectivity of light at a given wavelength is from Maxwell's equations is found as,

$$R = \left[\frac{n-1}{n+1} \right]^2 \qquad [2.22]$$

where the refractive index n, of the semiconductor is related to the dielectric function ε, by,

$$n^2 = \varepsilon \qquad [2.23]$$

Likewise absorption of light within the semiconductor can also be found from manipulating Maxwell's equations. Although ε can be derived from reflectivity and absorption measurements, because it consists of components from many optical transitions, direct observation of single optical transitions within the semiconductor is hard. The reflectivity normally consists of weak inflexions corresponding to the various critical points in the band structure on top of a background originating from lower energy transitions (Cardona (1969)).

The experimental technique usually used instead of reflectivity is modulation spectroscopy. This relies on changing the dielectric function, thus giving the differential of the reflectivity or absorption, removing the background signal and leaving the critical point structure. In the semiconductor samples considered the perturbation is applied in the form of an electric field. There are two significant mechanisms for modulation of the dielectric function by an electric field depending on whether the sample is a quantum well or bulk crystal.

For bulk crystals, electric field modulation of the dielectric function occurs through perturbations of states in the electron band structure. The main perturbation mechanism for atomic electron states in the presence of an electric field is the Stark effect (Merzbacher (1961)). However, for free carriers in a semiconductor this effect turns out to be insignificant in small fields, when compared to a tunnelling effect called the Franz-Keldysh Effect (Franz (1958) and Keldysh (1958)). The perturbation of the electric field allows free electrons and holes for a given optical transition to tunnel into the forbidden energy regions below the optical transition. For energies above the optical transition the electron-hole wave functions oscillate as their wavefunctions follow Airy functions in the presence of the electric field. The optical absorption or imaginary part of the dielectric function ε_i, is a function of the overlap of electron and hole wave functions in the band structure. Aspnes (1966) has calculated ε_r and ε_i for single bands in an electric field to produce the electrooptic functions F and G shown in figure 2.18. These become the basic line shapes observed in electro-reflectance spectroscopy of bulk materials, representing the imaginary and real parts of the dielectric function. Specific representation of ε_r and ε_i to F and G depends on the type of critical point for a given transition (Cardona (1969)). So far the above discussion assumes that optical transitions occur between bands in the electronic band structure. However other optical transitions can occur to produce excitons, hydrogenic type particles consisting of electrons and holes bound by a Coulombic field. Due to the low effective masses and high screening potentials in semiconductors, the ionisation energy for these particles is very low compared to the Hydrogen atom. Duke and Alferieff (1966) show that any significant electric field (~10kV/cm) easily

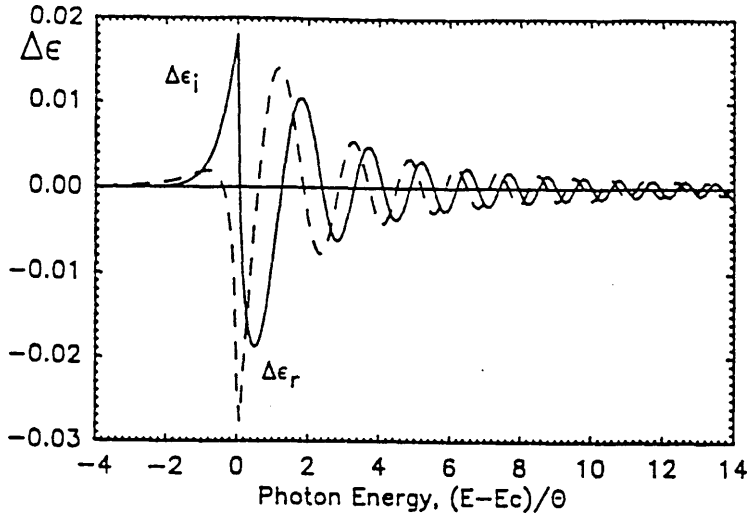


Figure 2.18 Shows the electrooptic functions F and G representing ε_i and ε_r respectively. (Reproduced by A J Shields).

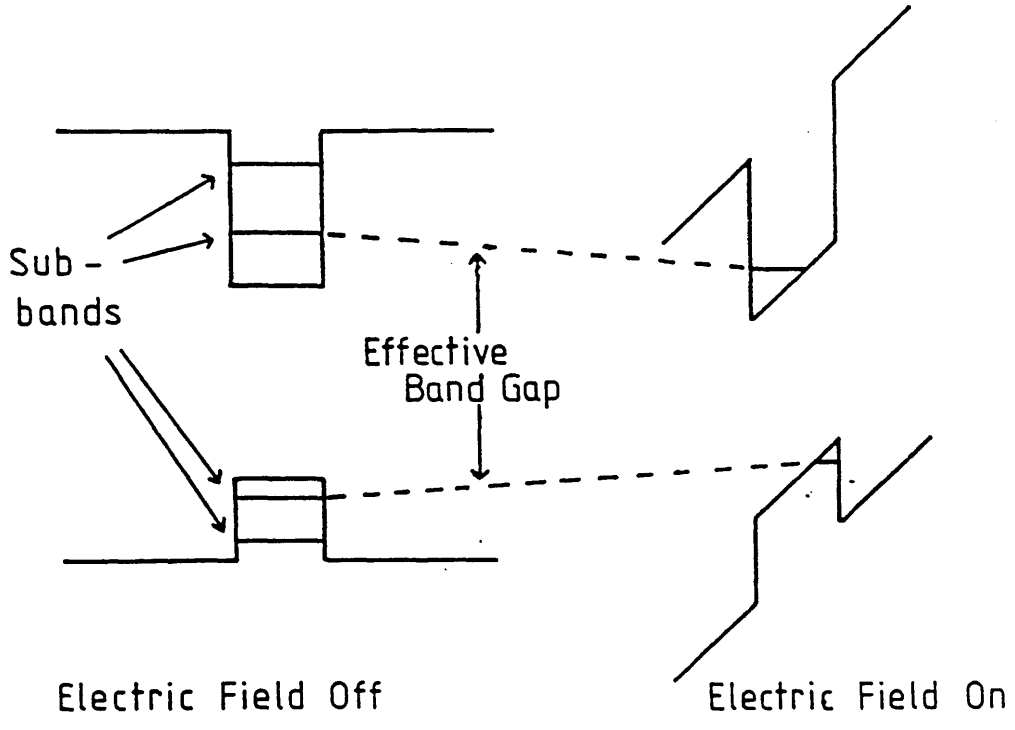


Figure 2.19 A schematic of the conduction and valence bands in a quantum well sample with and without electric field applied, showing the effect of the Quantum Confined Stark Effect.

ionises the exciton and making excitonic effects in electro-reflectance spectroscopy of bulk semiconductors very broad and small. Apsnes (1972) has shown that in low fields the electro-reflectance line shapes follow a third derivative of the dielectric function, instead of the electrooptic functions (F and G) of figure 2.18.

For electric fields in quantum well samples, the electro-modulation mechanism is somewhat different. For fields parallel to the quantum well layer, the main difference from that of the bulk case is the different density of electron states in the two dimensional electron band structure. For fields perpendicular to the quantum well, the band discontinuities significantly alter the free carrier wave functions. The main modulation mechanism for electronic states becomes the Quantum Confined Stark Effect (Miller (1984)). Figure 2.19 depicts this mechanism, the confined electron and hole states reduce their confinement energy, producing a red shift, in the presence of the new confining potential. In this case the band offsets hold the exciton in a bound state increasing its binding energy and making excitonic effects in modulation spectroscopy more important. The electro-reflectance line shape becomes that of a single oscillator often with a first differential Lorentzian or Gaussian line shape (Shields et al (1989)).

The expressions [2.22] and [2.23] relating reflectivity and the dielectric function are valid for light at normal incidence to the crystal. For electro-reflectance, the complete Fresnel expression for reflecticity must be differentiated (Cardona (1969)). Seraphin and Bottka (1966) have shown that this relation reduces to,

$$\Delta R = \alpha \Delta \varepsilon_r + \beta \Delta \varepsilon_i \qquad [2.24]$$

for functions α and β (the Saraphin coefficeints) and the real and imaginary parts of the dielectric function ε_r and ε_i. In all cases at the band edge of bulk semiconductors, β is very small and can be neglected. For optical transitions with higher energy α and β become comparible.

Klipstein and Apsley (1986) have shown that for quantum well samples the dielectric overlayers between the sample surface and the quantum well play an important part in determining the reflectivity formula, and α and β become factors dependent of the overlayer thickness which can have equal importance thoughout the spectral region.

Apsnes and Frova (1967) have also shown that expression [2.24] modifies in the presence of non-uniform electric fields. A non-uniform electric field produces modulated reflectance of different intensity as a function of depth from the front of the sample surface. In some cases ε_r and ε_i can be

completely mixed, such that at the band edge β is the significant coefficient and not α.

2.2.8 Evidence for new electronic states in Si/Ge systems.

Interest in Si/Ge superlattices has been growing since initial experiments by Kasper et al. (1975) showed the possibilty of epitaxial growth of $Si_{1-x}Ge_x$ alloys. Later Bean et al. (1982) showed pseudomorphic growth, which had introduced strain into the system. Samples were characterised with Raman scattering spectroscopy and Rutherford Back Scattering techniques. Bean et al. introduced the idea of low temperature epitaxy, which allowed metastable layers to be grown, and also introduced the concept of critical thickness. Superlattices of Si/Ge were initially predicted to enhance the electron mobility for Si by Moriarty and Krishnamurthy (1983), however it was the calculations of People (1986), which showed a reduction in the band gap of strained $S_{1-x}Ge_x$ epitaxial alloys that prompted optical investigations to begin. Lang et al. (1985) and Pearsall et al. (1986) investigated $Si_{1-x}Ge_x$ samples with photo-current and electro-reflectance spectroscopy respectively, showing effects of reduced bandgaps due to strain deformation effects on the conduction bands and confinement effects in quantum well structures.

Since these investigations, work on Si/Ge has turned towards short-period superlattice structures in the hope of making the indirect semiconductors direct with zone folding. Pearsall et al. (1987) have concentrated on Si/Ge (4:4) structures grown on Si (001). Using electro-reflectance spectroscopy to investigate the electronic states, they observe interesting effects in which the superlattice seems to produce new electronic transitinos below the direct gap of Si at 3.4eV. However Abstreiter and co-workers (Zachai et al. (1988) and Eberl et al. (1987)) have looked at Si/Ge (6:4) structures grown on alloy buffers, using the argument that 10 monolayer periods are required to fold the 0.8X minima of the Si conduction band to the Brillouin zone centre. Abstreiter has been able to use photoluminesence spectroscopy to analyse his samples and observations of a transition at around 0.7eV have been made. Figure 2.20 shows an electro-reflectance spectrum of Pearsall et al., which clearly indicates some spectral activity below the direct gap of Si. In subsequent papers which investigate a wider class of superlattice, that of Si/Ge (n:n, where n=1,2,4 or 6), Hybertson et al. (1988) and Pearsall et al. (1989a) have shown the effects seen in figure 2.18 to be only associated with the (4:4) superlattices. However from the above discussions on the theoretical calculations of band structures in Si/Ge superlattices, it can be seen that only very weak transitions below the direct gap of Si are predicted, thus the

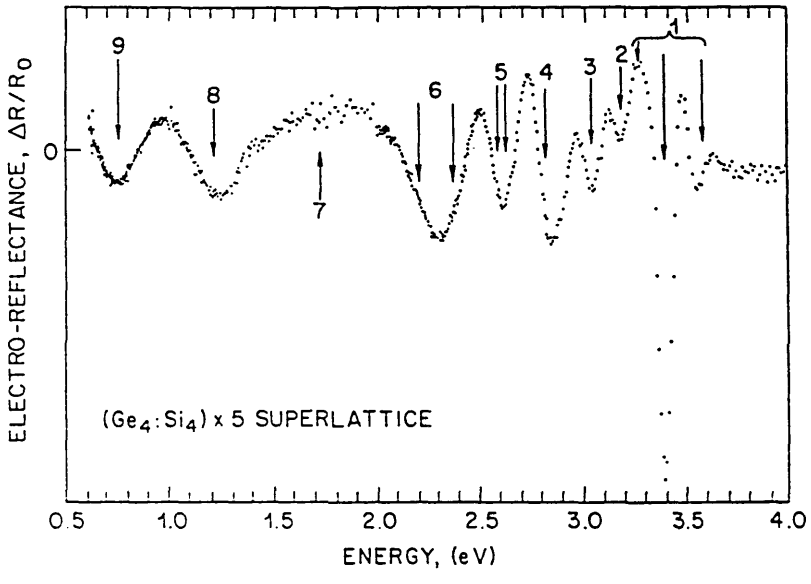


Figure 2.20 An electro-reflectance spectrum of a Si/Ge (4:4) superlattice grown on Si (001) taken by Pearsall et al. (1987). Indicated are proposed super lattice transitions, the features at 3.4-3.8eV are due to the Si cladding layers, a large signal is seen below the indirect band gap of Si at 1.1eV. Reproduced with permission from the author.

experimental results pose an enigma.

The Si/Ge (6:4) samples of Abstreiter et al (1989) have been compared to (3:2) and (12:8) superlattices. Zachai et al. (1990) observe photoluminescence from the (6:4) structure at an energy down to 0.7eV, which they ascribed to the superlattice. It is not clear however that the photoluminescence occurs from electronic states in the superlattice or from defects associated with dislocations within the samples. Pearsall et al. (1989b) have looked at similar samples grown on Ge(001) subtrates, using electro-reflectance spectroscopy, and have observed fine structure on the Ge direct transition. Both Pearsall (1990a) and Abstreiter et al. (1989) have written review articles on the subject of Si/Ge short-period superlattices, which include most of the significant results in the field.

Chapter 3 Description of experimental procedures.

3 Description of experimental procedures.

This chapter summarises the experimental and computational procedures used in the subsequent chapters. Firstly Raman scattering and electro-modulation spectroscopies are described and example spectra are given for bulk silicon and germanium samples. A following section outlines how electrical contacts are made to the epitaxial samples for electro-modulation experiments. Techniques for Photo-current spectroscopy are also described.

Section 3.3 contains a brief description of the techniques used by C J Gibbings when growing the samples, together with a list of measured samples.

The computational techiques are outlined in section 3.4, for line fitting of electro-reflectance spectra and for finding phonon and electron states of Si/Ge structures.

3.1 Optical Characterisation using Raman Spectroscopy

Raman scattering of phonons is a sensitive analytic tool for determining new Physics and sample quality of semiconductors (Klein (1986)). The Raman process observed in the Si/Ge samples investigated in this thesis, involves the inelastic scattering of monochromatic light by phonons. A process that conserves both momentum and energy for the phonon/photon system. The experimental geometry determines the observed momentum wavevector, a spectrometer is then used to measure the energy of the scattered light. Raman intensities can be about 10^{10} smaller than that of the Rayleigh elastically scattered light. In the Raman process phonons can be created or destroyed. For the experiments presented phonon modes corresponding to the more favourable creation of phonons (the Stokes process) are observed. In this case the energy of the scattered light is less than the incident laser light energy.

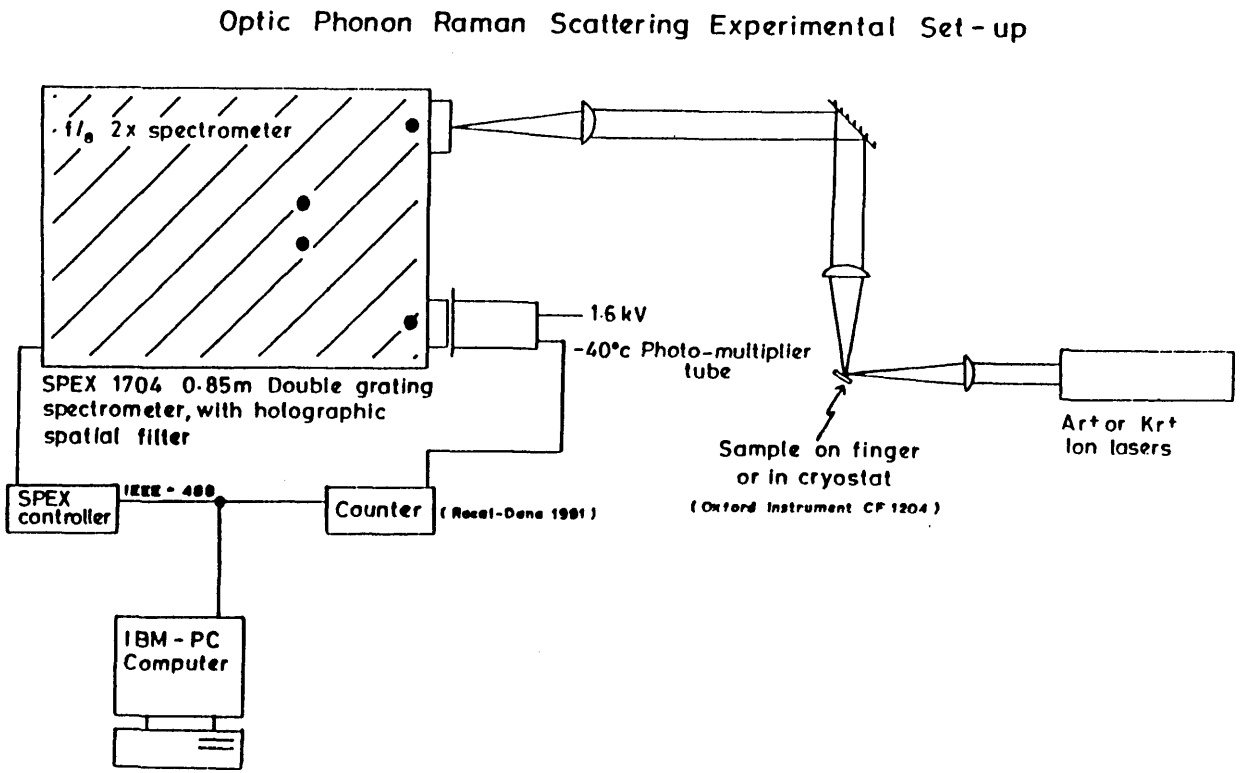


Figure 3.1 A schematic of the Raman scattering spectroscopy experiment. Argon and krypton ion plasma lasers are indicated for the light source, but a single cavity dye laser was also used for Resonant Raman measurements.

3.1.1 Optical Equipment

Raman scattering spectroscopy was carried out using a Coherent 4W Ar^+ ion plasma laser and dye laser system. Most of the experiments were performed at room temperature with the sample on a translational stage with three degrees of freedom. One measurement was performed at liquid helium temperatures in an Oxford Instrument CF1204 continuous flow cryostat with f/2 'Spectrosil' windows.

Figure 3.1 shows a schematic set-up of the Raman scattering system. The laser light was focused on the sample to a small spot of about ~200μm radius, lens aberrations will not allow a smaller spot size. Power densities were kept between 50 and 100Wcm^{-2}. The specular reflection from the front surface was directed away from the collecting optics. The scattered light was collected by f/2 optics and analysed by a single pass f/8 double grating monochromator. (A SPEX Industries 0.85m focal length unit with 1800 graticules/mm gratings and holographic spatial filter between the two gratings.) The detector used was a thermoelectrically cooled photomultiplier tube with a S20 low energy enhanced photo-cathode. The dark count was typically 11 counts/second. An International Business Machines - Personal computer (IBM-PC) and Racal-Dana 1441 nanosecond counter were used to acquire and store the data. The spectrometer had a typical resolution of $1cm^{-1}$ for an entrance and exit slit of 100μm; the resolution used for most experiments was between 1 and $2cm^{-1}$.

Care must be taken to avoid signals from Raman active vibrational modes in the atmosphere surrounding the sample. If these modes are the same intensity and energy as the phonon modes of interest the sample must be placed in a vacuum or atmosphere of Ar to remove their effect. A simple check can be made to see if the Raman signal is from the semiconductor or the surrounding atmosphere. The atmospheric virbational lines are very sharp compared with the phonon lines. Thus their presence can be verified by a simple check: If the phonon modes are fully resolved by the spectrometer; reducing spectrometer slits and hence increasing the spectral resolution further will not affect their width. On the other hand the atmospheric vibrational lines will reduce in width as the spectral resolution is increased. Thus both types of mode can be distinguished.

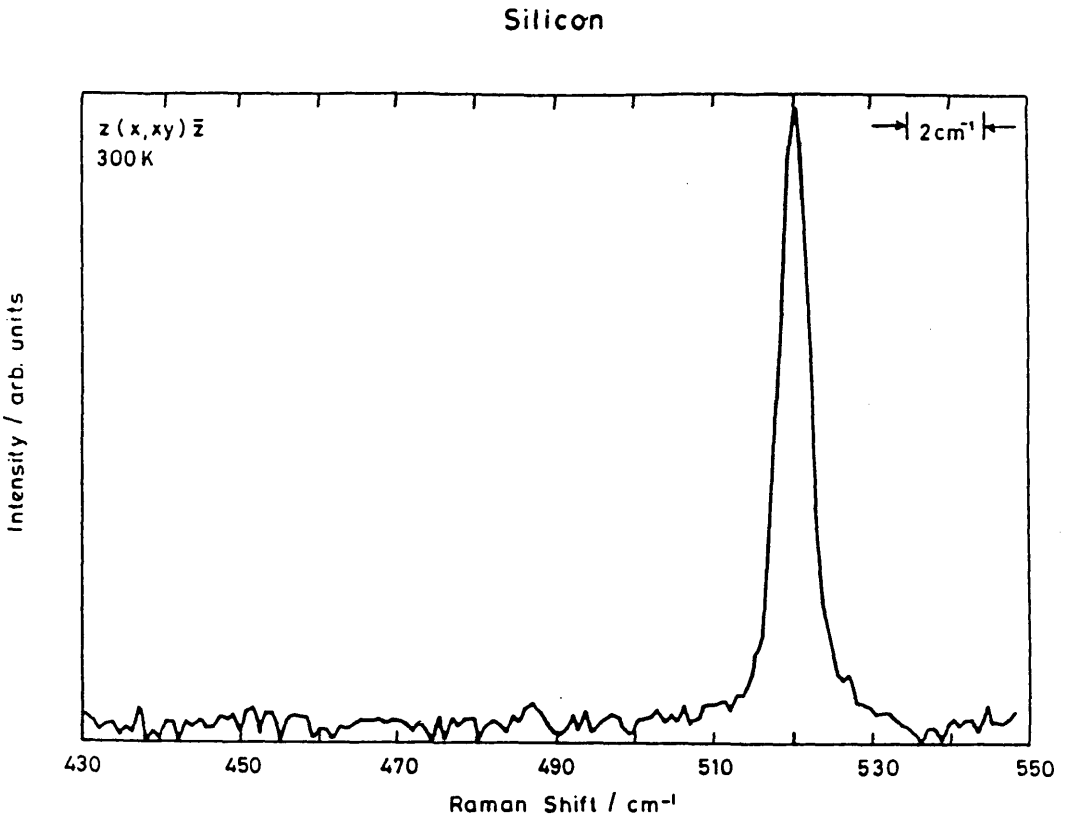


Figure 3.2 Room temperature Stokes Raman scattering spectrum of the LO phonon from bulk Si (001).

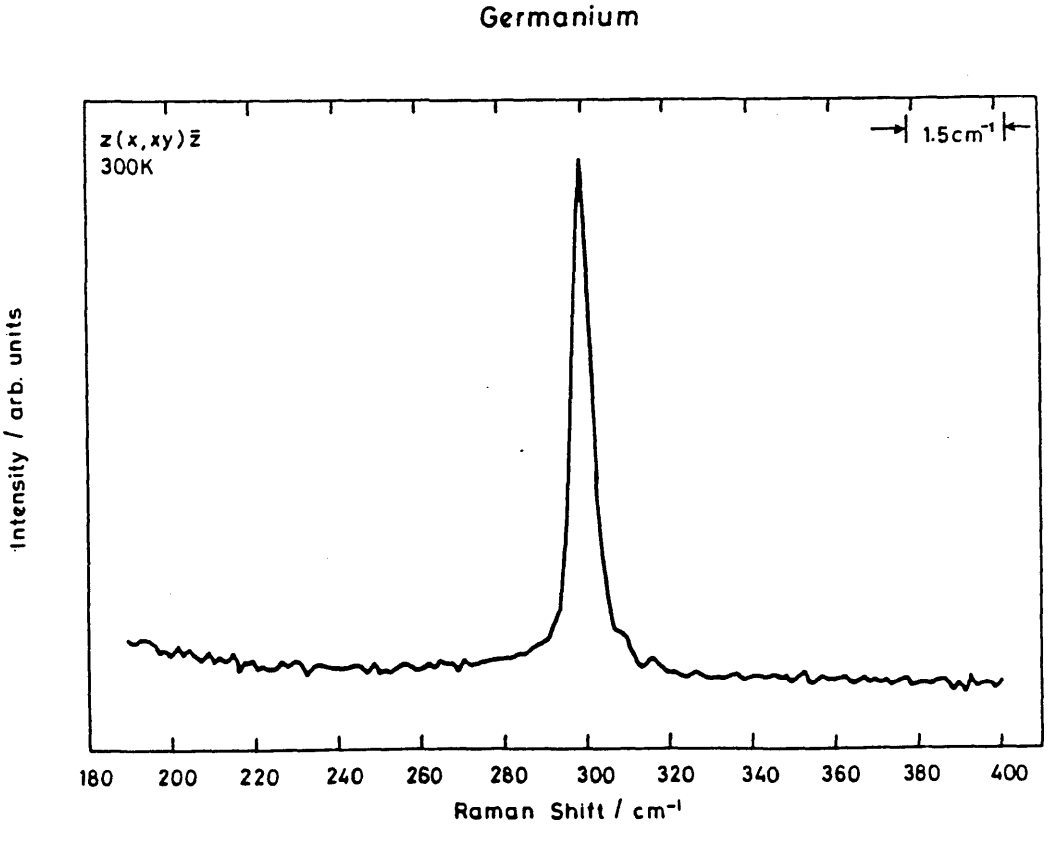


Figure 3.3 Room temperature Stokes Raman scattering spectrum of the LO phonon from bulk Ge (001).

Generally, plane polarised 514.5nm light from the laser was used for Raman Scattering. However, for resonant effects, a Coherent 599 single cavity dye laser was also used. Two types of dye were pumped using all visible lines of the 4W Ar^+ ion plasma laser:

i) DCM usable range 610 to 680nm,
(Exciton Chemical Co. Dayton, Ohio 45431).

ii) Rhodamin 110 (MW 366.8gm) usable range 530 to 580nm.
(Lambda Physik GmbH, D-3400, Gottingen).

The laser light was filtered with a prism before being focused on to the sample. The system was extensively tested with various samples of bulk and epitaxial group IV and III-V semiconductors, all the results comparing well with previously published Raman scattering spectra.

3.1.2 Typical results for Silicon and Germanium

The configuation of optics allows back-scattered light to be collected by the spectrometer. Polarisation is denoted by the expression z(x,xy)z, where x and xy refer to the incident and collected light polarisations with respect to the crystal axes. In this case xy is used to denote unpolarised collection. The incident laser and collecting optics are not in the z-direction but this can be neglected since the high refractive index of the semiconductor means that light in the crystal is only a few degrees off the z-direction for most external incident angles. The symmetry of diamond lattice structures requires that only Longitudinal Optic (LO) phonons can scatter for Γ_{25} Raman active phonons in z-direction for polarisations $z(x,y)\bar{z}$, for example see Cardona (1982). Figure 3.2 and 3.3 show Stokes Raman scattered light for Si and Ge respectively, measured in back-scattering geometry, at room temperature. The ratio of Stokes and anti-Stokes mode intensities was measured to determine the sample temperature (Kittel (1976)), which was found to be below 100°C for samples nominally at room temperature.

For a Ge substrate a single Γ_{25} LO phonon mode was observed at 300cm^{-1}, likewise for Si at an energy of about 519cm^{-1}. No other modes were observed in this spectral region with the equipment and samples that were available.

3.2 Electro-modulation spectroscopy

3.2.1 Electro-reflectance and electro-absorption techniques.

Electro-modulation spectroscopy was used to identify the energy values of new critical points in the band structures of short-period superlattices and quantum well samples. A typical set-up for the spectroscopy usually has the following components:

(i) light source,

(ii) monochromator,

(iii) detector,

(iv) phase sensitive detector/Lock-in amplifier with oscillator

and

(v) a computer for data retrieval and equipment manipulation.

Figure 3.4 shows the typical arrangment which was used for the electro-reflectance measurements. An epitaxial sample has a polished front surface, on which a semitransparent Schottky barrier is placed (see section 3.3). The samples were typically 5mm x 10mm and 0.5mm thick and the Schottky barrier was approximately 2mm in diameter. Light from the monochromator slits is focused to an image about 0.25-0.5mm in diameter on the Schottky barrier. The specularly reflected light is detected with a photo-detector as a function of wavelength. The reflectivity is modulated by the application of an electric field across the Schottky barrier. This modulation is detected by a Lock-in amplifier and the resulting change in reflectivity due to the modulation is recorded by an IBM-PC as a function of wavelength or photon energy. The measurement is very sensitive to van Hove singularities in the band structure of the semiconductor under investigation, as described in section 2.2.7.

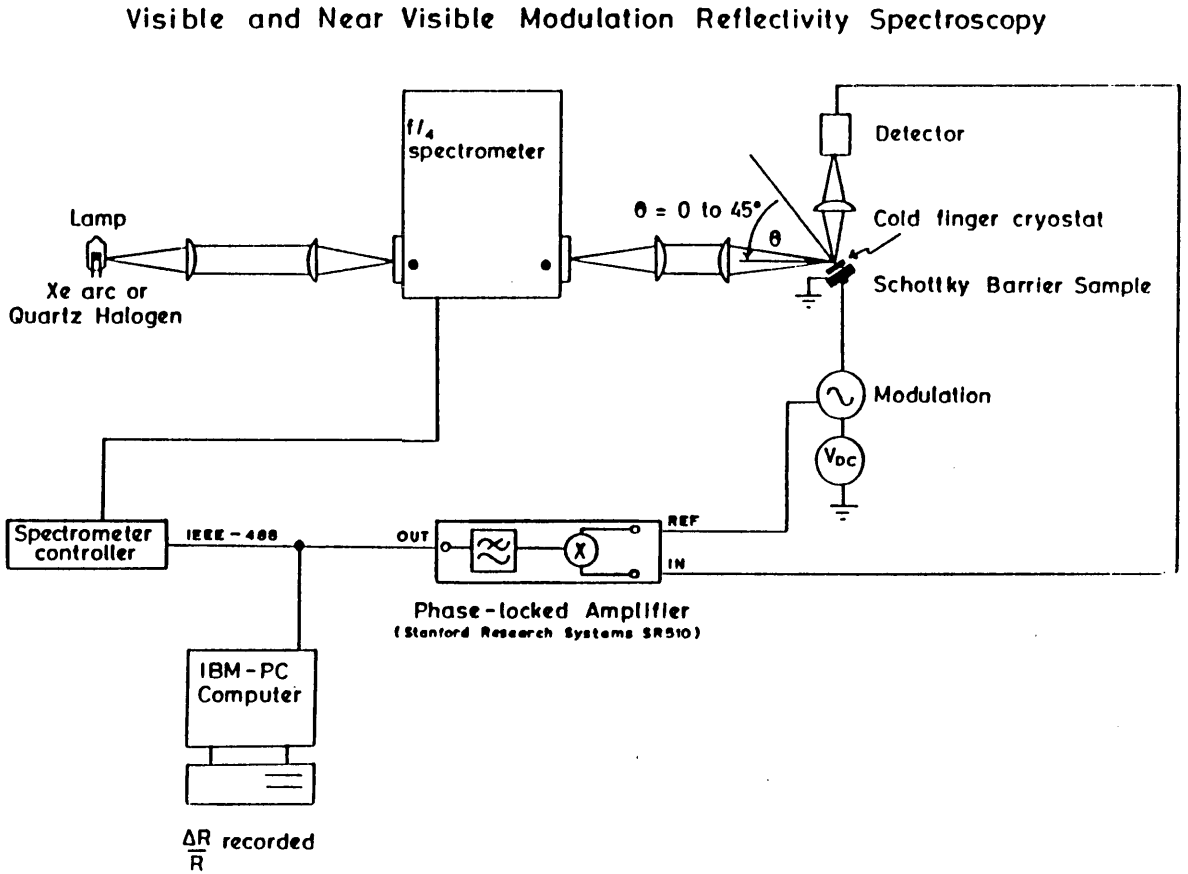


Figure 3.4 A schematical representation of an experimental set-up for electro-modulation spectroscopy. Monochromatic light from the spectrometer is reflected from a Schottky barrier on the sample. The light is collected and the signal analysed with a lock-in amplifier and computer.

Providing the sample is moderately transparent, modulated transmission measurements can be undertaken. However, the absorption of light in the vicinity of a critical point is high and the intensity of the transmitted light therefore very low, making modulated transmission measurements difficult. Transmission measurements were restricted to very thin samples (in this case epitaxial layers grown on Si) and to photon energies near the band edge of the sample. If the light detected has passed only once through the sample and has not suffered multiple reflections then the transmitted light is proportional to the absorption, and thus modulated transmission is proportional to modulated absorption.

It is usual to normalise the resultant spectrum by dividing by the non-modulated reflectivity or transmission response of the sample. This is obtained by seperately taking a spectrum but chopping the incident light instead of modulating an electric field across the sample, thus giving the DC reflectivity or transmission. Subsequently the electro-reflectance or electro-transmission spectrum is divided by the DC spectrum for normalisation. Unless otherwise specified all modulation spectroscopy results presented in the thesis are normalised.

The light source for modulation spectroscopy is required to be broad band. For ultra violet and near visible light (2 - 4 eV) a Xe arc lamp was used (Wotan XBE 250W/O ozone free lamp). This lamp has a number of spectral lines around 800nm (1.55eV), and so for the energy region 0.6 - 2 eV a Tungsten filament lamp was used (Philips 7724 EVA M/28). Although having a lower luminosity than an arc lamp, the filament lamp a smoother black body spectral response. For some transmission measurements a more intense light source was needed for the 0.6 - 1 eV region and a 0.25mm arc Mercury lamp was used (Wotan HBO 100 W/2).

The monochromator was a 0.3m focal length Czerny-Turner f/4.2 type with either 1800 graticule/mm or 600 graticule/mm gratings with a typical energy resolution of 8 meV for 1mm wide slits. The photon energy range covered was 0.6 to 3.8 eV, suitable filters were used to remove second order diffracted light emitted from the spectrometer. The spectral resolution was kept between 2 and 10meV for the measurements described.

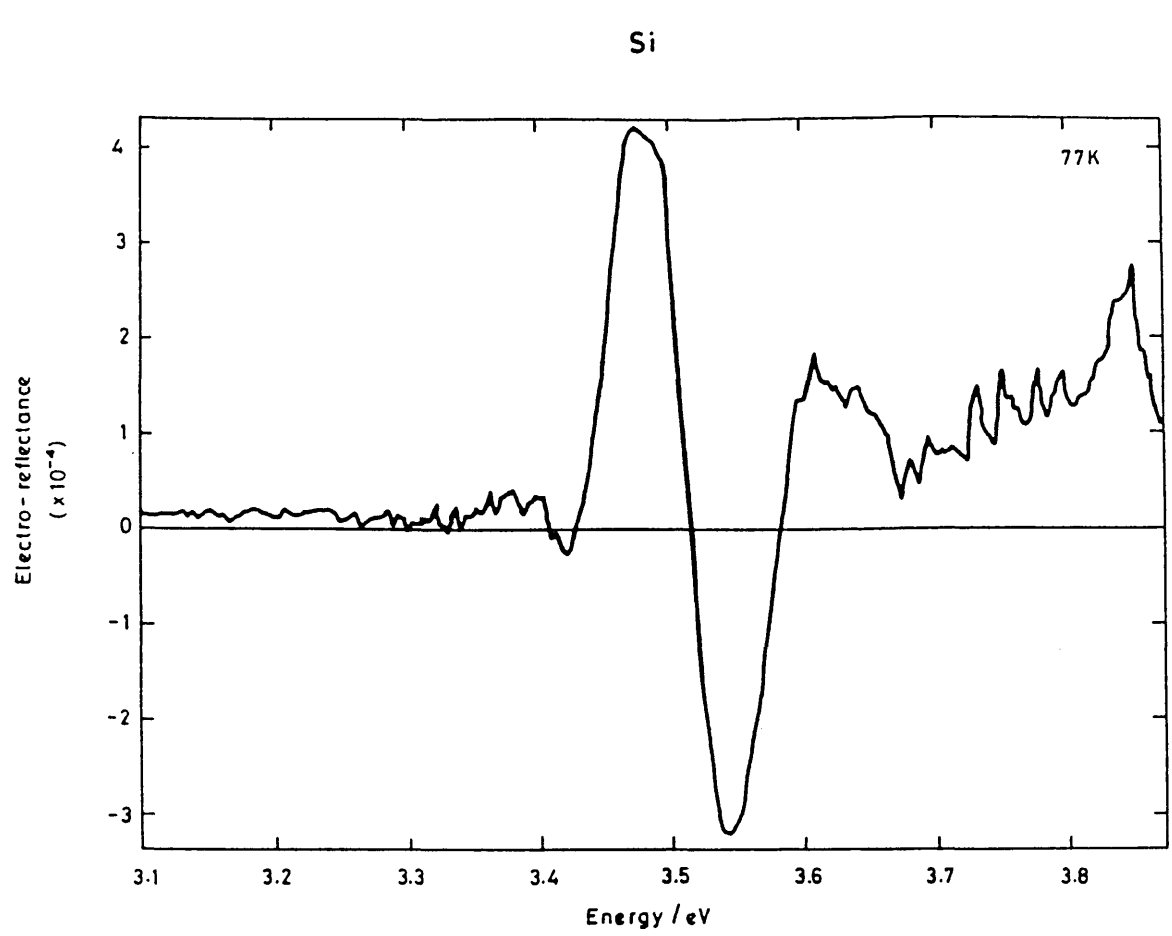


Figure 3.5 Electro-reflectance spectrum of n-type bulk Si(001) at 77K, showing the lowest direct energy transitions E_1 and E'_0.

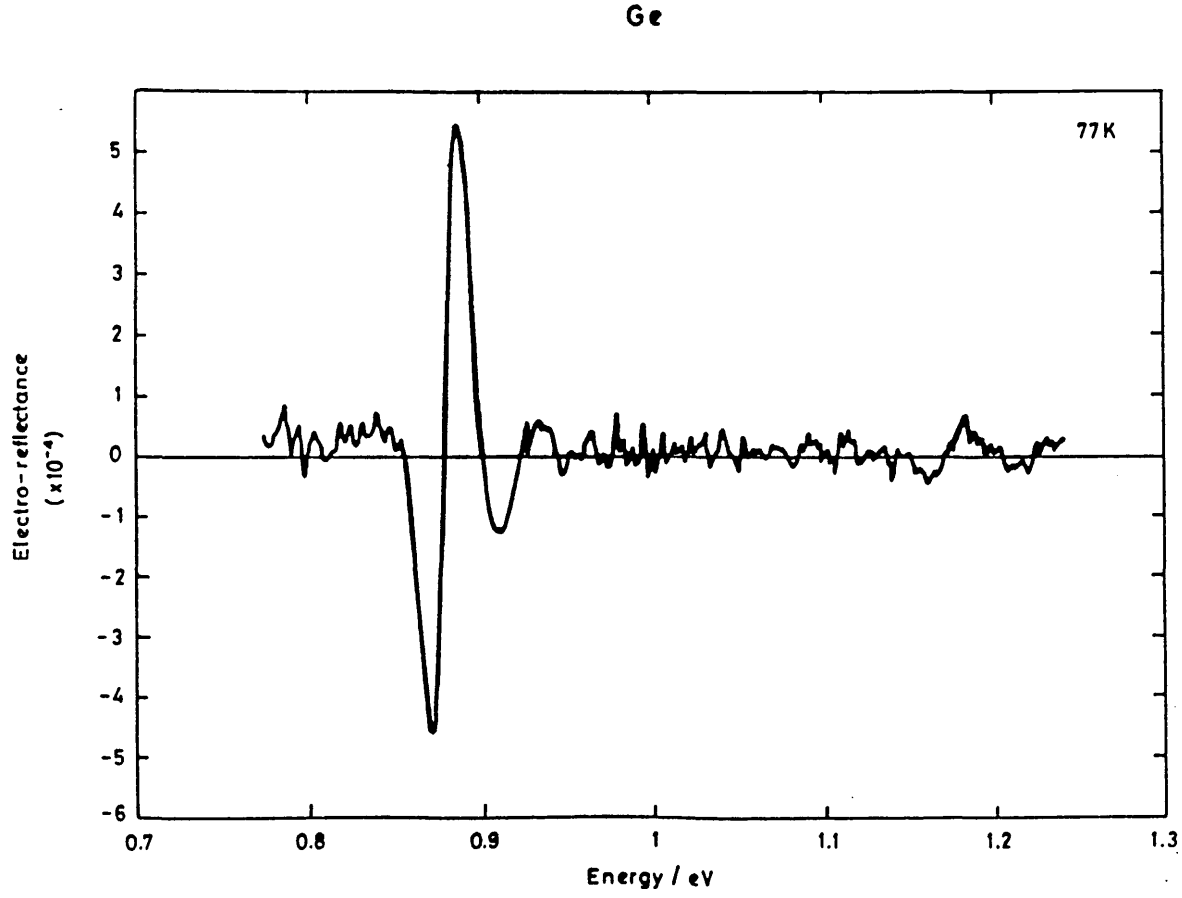


Figure 3.6 Electro-reflectance spectrum of n-type bulk Ge(001) at 77K, showing the lowest direct energy transitions E_0 and $E_0+\Delta_0$

The detectors, operated at room temperature, were a photo-multiplier tube (EMI 6558Q) for energies between 2 and 3.8 eV, a Si photo-diode between 1 and 3.8 eV and a PbS photo-conductor between 0.6 and 1.5 eV. Care was needed to make sure that the photomultiplier was operating in a linear region of its gain curve. The phase sensitive detector amplifier was a Stanford Research Systems SR510, which had a dynamic range of over 110dB.

The electric field was applied perpendicular to the epitaxial layers by means of a semi-transparent Schottky barrier which allowed light to pass through to the semiconductor. Section 3.2.2 outlines the procedure for making such contacts. The Schottky diode was reversed biased and an additional modulation field applied in the form of a square wave, see Cardona (1969). The amplitude of the square wave was typically the same as the applied bias. The modulation frequencies used were around 200-230 Hz.

Figure 3.5 and 3.6 show typical spectra for the lowest energy transitions for Si and Ge. The Ni Schottky barriers for these particular samples were placed on (001) surfaces, and no special polarisation effects were observed. The results for the Si E_1/E'_0 transitions compare well with previously published results of Kondo and Moritani (1977) and others. The Ge E_0 and $E_0+\Delta_0$ spectrum compares well with results obtained by Gaillard et al. (1973).

3.2.2 Photo-current measurements.

The photo-current of electron-hole pairs produced by incident light on a semiconductor can easily be measured in Schottky barrier diode samples. The electric field from the formation of the Schottky barrier will sweep carriers away from the region where light is absorbed and carriers were created, thus the sample acts like a photo-detector. The same equipment as for electro-reflectance/transmission measurements was used. However, the sample leads were connected to a current amplifier feeding the lock-in amplifier and the incident light was modulated with a light chopper. The photo-current measured as a function of photon energy is an analogue to absorption in the absence of carrier transport anomalies (Rogers et al. (1984)). Figure 3.7 shows the photoconductivity for the band edges of a Si substrate and an epitaxial $Si_{0.5}Ge_{0.5}$ alloy grown on Si (001) both with Ni Schottky barriers. In general no normalisation is

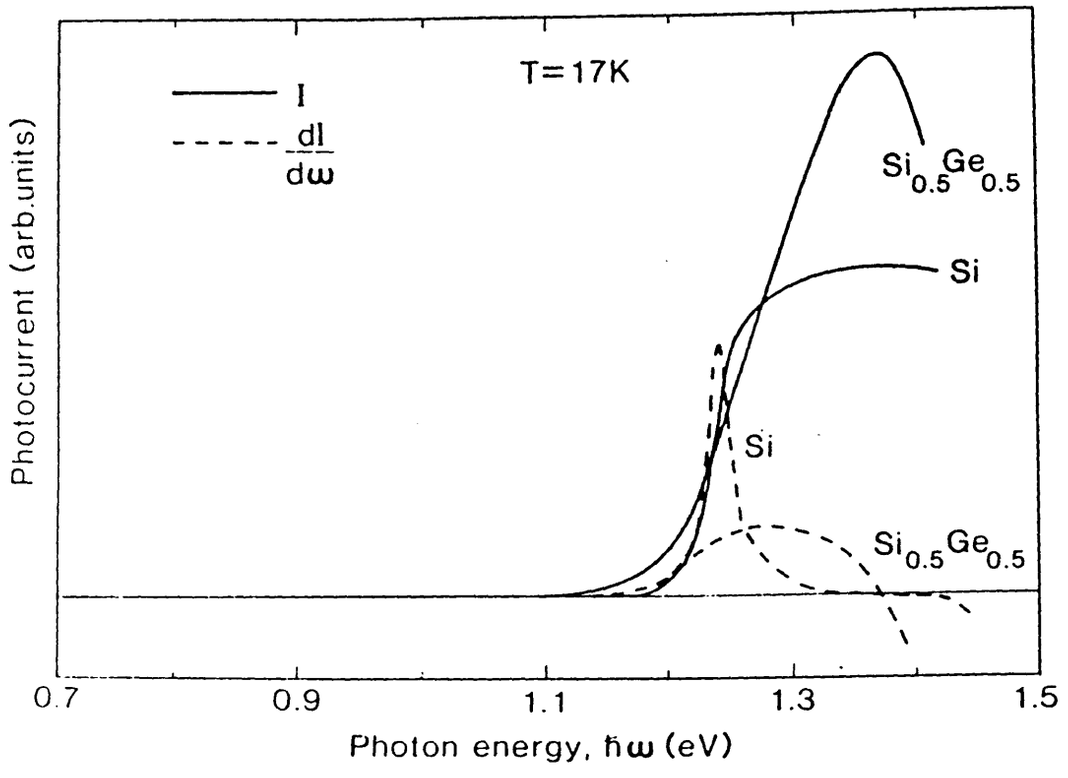


Figure 3.7 Photo-current spectra of bulk n-type Si and epitaxial $Si_{0.5}Ge_{0.5}$ grown on Si(001) (sample ALY50), performed at 17K. No photo-current response is observed for either samples below the indirect band edge of Si (Γ'_{25}- Δ_1) or $Si_{0.5}Ge_{0.5}$ (Γ'_{25}- Δ_1).

carried out for photo-current measurements. The light source used was the Tungsten filament lamp and which was shown to have a broad featureless spectrum with a Ge photo-diode dectector.

Both electro-modulation spectroscopy and photo-current measurements were carried out with the sample attached to a cold finger of a closed cycle compressed Helium cryostat with a base temperature of 17K and with a horizontal plane of 3 orthogonal f/1 Calcium Fluoride windows. The sample temperature was measured by a diode attached to the sample finger, in an 'oxygen free' copper block. A forward bias of 10μA was passed through the diode, and a corresponding voltage drop measured in a four terminal fashion. The voltage drop across the diode was tabulated with the resistance of a calibrated Rhodium-Iron resistor as a function of temperature. The samples were mounted on fibre-glass squares attached to the cold finger with Cryo-Con copper loaded grease.

3.2.3 Electrical contacts to silicon and germanium.

The electric field for electro-modulation spectroscopy is applied by means of a reversed biased Schottky barrier diode, which is semi-transparent to enable light to be transmitted through to the semiconductor. To form a diode structure it is necessary to have two contacts to the semiconductor: an ohmic contact (with low resistance), and a Schottky metal-semiconductor contact. Sample preparation, before evaporation of the contact, requires no special procedures for either of the two semiconductors used, although the surface oxide of Si is a very good insulator and must be removed for an effective contact. The procedure for making the two types of contacts on Si and Ge now follows.

Surface contamination can be very damaging to contacts on semiconductors, so a systematic cleaning procedure must be used. Surface cleaning started with a primary degreasing of the sample in a series of ultra-sonic baths of 15 minutes each, containing 'Analar' pure reagents of:

i) Tri-chloroethane,

ii) Acetone,

iii) Methanol,

The cleaning procedure is finally completed by removal of the surface oxide with a bath of buffered Hydrofluoric acid mixture for 2-3 minutes. The sample is then washed in Methanol before being placed immediately in an 'Edwards Cold Trap' diffusion pumped evaporator.

To form a low resistance contact to a semiconductor it is usual to lower the metal-semiconductor interface electron work function by locally increasing the extrinsic doping near the contact (Sze (1985)). The samples were grown on a substrate which was doped n-type to a level of 10^{15}-$10^{18}cm^{-3}$. The 'ohmic' contact consisted of Gold doped with 2% Antimony (Johnson Matthey Special Product). Using the method of Holland (1956) and a Molybdenum filament, about 2000Å of metal was evaporated to form two 1mm diameter spots on the sample at 10^{-6} torr. Two contacts allowed the resistivity of a single contact to be tested. Immediately after the evaporation the sample was placed in a Bio-rad Polaron annealing furnace and heated to 500°C within 30 seconds, it was then kept at 500°C for 1 minute under an atmosphere of H_2 cracked with N_2. (An alternative method used involved a rapid anneal to 460°C within 2 seconds also under a forming gas atmosphere.) The contact resistance was generally less than 30Ω in a temperature range of 15 to 300K.

Following a successful formation of a low resistance contact the sample was then recleaned by the above procedure and a Schottky barrier formed on the epitaxial surface which was to be spectroscopically investigated. The epitaxial surface was already polished to optical quality and required no preparation other than the cleaning procedure outlined above. The Schottky barrier was made by evaporating a Nickel film, 50Å in thickness and about 2.5mm in diameter, from a Tungsten filament at 10^{-5} torr. The Ni film has no optical features in the wavelength region of interest. The Ni forms a silicide on the surface (Zhang et al. (1982)), although Auger depth profiling of a 'test' Schottky barrier showed little evidence for Ni diffusion (Rohlfing (1988)). All the samples investigated had capping layers of about 200Å of Si to protect any Si/Ge heterostructure burried beneath the surface. Wires were bonded to the contacts using Silver loaded glue or paint. Occasionally a Gold pad 0.5μm in thickness was also evaporated on top of part of the Schottky contact so that bonding did not damage the contact. Figure 3.8 and 3.9 show the prepared sample with wires attached and a current voltage characteristic of a sample. The reverse bias condition is indicated with a typical voltage applied for electro-modulation spectroscopy.

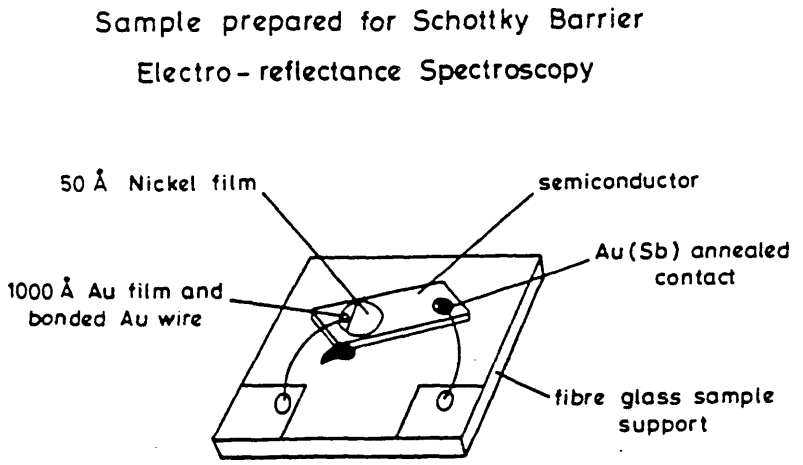


Figure 3.8 Diagram of a sample prepared for electro-reflectance spectroscopy.

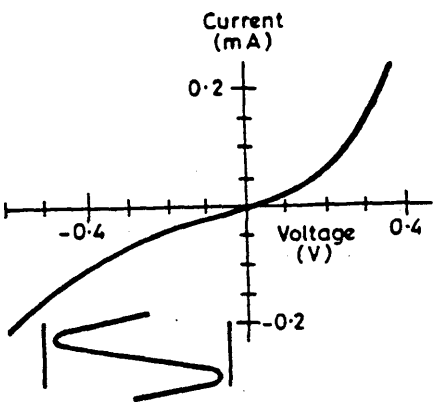


Figure 3.9 A typical current-voltage charateristic for a nickel Schottky barrier contact on a Si-epitaxial layer sample. A voltage region which would be used for electro-modulation spectroscopy is indicated.

3.3 Description of Sample Growth.

The dimensions and specifications of the individual samples measured are specified in the relavent chapters. The samples were all grown by molecular beam epitaxy in a VG Semicon MBE system by Dr C J Gibbings of British Telecommunications Research Laboratories. Si and Ge were evaporated from two Airco Temescal electron beam hearths on to Wacker Si (001) n^+ type doped substrates. The molecular beam fluxes were controlled by an Inficon Sentinel III flux controller (Tuppen et al. (1989)) with typical growth rates of 10Å/s for $Si_{1-x}Ge_x$/Si structures and 0.5Å/s for Si/Ge short-period superlattices. Generally the doping in the substrates was on the order of $10^{18}cm^{-3}$ active n-type electrical dopants and the epitaxial layer left undoped, unless specified. Residual doping levels of $10^{14}cm^{-3}$ n-type were measured by electro-chemical C-V profiling. A B_2O_3 cell was used for p-type doping of the epitaxial layer, and an As ion beam was used for n-type doping.

Deposition of Si/Ge superlattices took place at temperatures between 350 and 500°C. In general, the wafers were loaded into the vacuum system without chemical cleaning. In the vacuum system the remaining surface oxide was desorbed by creating a monoxide at 850°C with a flux of Si. During growth partial pressures of H and CO_2 were below 10^{-8} and 10^{-10} Torr respectively. In most cases the samples consisted of heteroepitaxy of either pure Si or Ge. However a few control samples were grown with $Si_{1-x}Ge_x$ alloys of various compositions, such alloys are assumed to be random, having a diamond lattice but no ordering. After growth some samples were checked for structural defects using a X-ray diffractometer at Britich Telecom Research Labs.

The samples used in the thesis are listed as follows; full desciptions of layer dimensions and compositions are given in chapters 5 and 6 with the characterisation results.

Quantum Wells on Si(001)

QWA QWD

QWB QWE

QWC

Si/Ge (4:4) superlattices on Si(001)

S44A	S44B	S44C
S44D	S44E	S44M

Alloy control samples

ALY50 (x=0.5 $Si_{1-x}Ge_x$ alloy) 0.2μm thick

ALY25 (x=0.75 $Si_{1-x}Ge_x$ alloy) ~0.6μm thick

GEEPI (1μm of Ge grown on a Si(001))

SIEPI (0.7μm of Si grown on a Si(001))

bulk Si:	Si-n doped (001) substrate
bulk Ge:	Ge-n doped (001) substrate

Si/Ge (6:4) superlattices on 60% alloy

S64	S64CL (control sample with alloy replacing superlattice)

Si/Ge (2:n = 6,8, and 10) superlattices on 75% alloy

S26A	S26CL1(control)	S26D
S28B	S26E	S26CL2(control)
S210C		S26CL3(control)

3.4 Computational Techniques.

Various computer algorithms are used throughout the study of Si/Ge layered systems. In Chapter 2, sections 2.2.3 and 2.2.4.2 a Pascal program was used, running on a Digital Equipment Corporation (DEC) Rainbow MSDOS computer, to solve Kronig-Penney model with the expression given in equation [2.16]. The program simply stepped through values of energy until the right hand side of the equation had a value of either +1 or -1, thus locating the band edges respectively at the superlattice Brillouin zone centre or edge.

Chapter 4 contains a calculation of the density of electron states in a Si/Ge superlattice, the code was written in FORTRAN and the calculation performed on a DEC microVAX, details of the techniques used are indicated in that chapter.

In chapter 5, phonon energies measured in short-period superlattices with Raman scattering spectroscopy were modelled with a linear chain model. The technique models phonons in the crystal as one dimensional vibrations; the model consists of a line of atoms seperated with bonds of a given compliance. This method has yielded good values for the dispersion in reciprocal space of phonons when compared to neutron scattering experiments from phonons. Linear chain parameters were taken from Kunc and Gomes-Dacosta (1985) for Ge and Yin and Cohen (1982) for Si. These parameters have been calculated with ab-initio pseudo-potential models, they have been compared to neutron scattering experiments and are given in Table 5.6 chapter 5. The concept behind the calculation is found in Kittel (1976) p107: equations of motion are derived for individual atoms us of mass M separated by bonds of compliance C_p along the chain,

$$M\frac{d^2u_s}{dt^2} = \sum_p c_p(u_{s+p} - u_s) \qquad [3.1]$$

by assuming a periodic solution in time, the solution $u_s \sim e^{-i\omega t}$ is found for frequency ω. The translational symmetry implies a space group representation of e^{ikzs}, the individual displacements can

then be found easily. Equation [3.1] assumes one atom per unit cell of the chain. For a Si/Ge (4:4) superlattice there are 8 atoms per unit cell, and thus 8 coupled equations of the type [3.2] are found:

$$m_i u_i - c_i(u_i - u_{i-1}) + c_{i+1}(u_{i+1} - u_i) = 0 \qquad [3.2]$$

where u_i is the individual displacement of the ith atom m_i and c_i are the corresponding atomic mass and compliance of the bond connecting the ith and i+1th atoms. Again by assuming a periodic displacement in time and length along the chain it is found that:

$$u_j = u_j e^{i\omega t} \qquad [3.3]$$

$$u_{j-1} = u_{j+8} e^{ika} \qquad [3.4]$$

Where a is the unit cell length of the superlattice along the chain and **K** the reciprocal lattice vector. [3.3] is then divided by $m_j^{1/2}$. After subsituting [3.3] and [3.4] in equation [3.2] a determinantal equation is solved. Equation [3.2] only contains interactions between nearest neighbours, to obtain a better fit with experimental neutron scattering results, other elements in the matrix [3.2] corresponding to interactions between atoms further apart need to be considered (Yin and Cohen (1982)). The more general determinental equation becomes:

$$\left[\omega^2 - \frac{1}{\sqrt{m_i m_j}}\left(\sum_{ij} c_i \delta_{ij} + c_{i-j}\right)\right] = 0 \qquad [3.5]$$

where c_{i-j} is the interaction between i and jth atom of the chain and Σc_i is the sum of all interactions for a given atom between all others. After inclusion of [3.4] the procedures of Press et al. (1987) on an IBM-PC were used to find the eigen-energies and eigenfunctions for the atomic displacements.

One of the figures in chapter 6 for an electro-reflectance spectrum showing two new critical points in a Si/Ge superlattice has a line fitted theoretically to the experimental data. Two transitions were considered each using a line shape model described by Aspnes (Cardona (1969)):

$$\frac{\delta R}{R} = A\Gamma^{-n}e^{i\varphi}(E - E_g + i\Gamma)^{-n} \qquad [3.6]$$

Where E_g is the transition energy and Γ a broadening parameter. A and φ are additional fitting parameters. n is related to the dimensionality of the critical point associated with the transition. For example, for a three dimensional critical point such as GaAs E_0, n = 5/2. In the case of the superlattice little is known about the critical points and all parameters are taken to be free. As the superlattice in the modelled sample has a capping layer the reflectivity is closer to the quantum well samples considered by Klipstein and Apsley (1986) than bulk cases considered by Aspnes, and therefore the arbitrary phase φ should be related for both transitions. This was not found to be the case and two independent phases were used in the fit. The fit was performed using experimental data stored in the IBM-PC and procedures of Press et al. (1987).

Chapter 4 Density of states of electrons in Si/Ge short-period superlattices.

4 Density of states of eletrons in Si/Ge short-period suplerattices.

The strength of optical signals eg. reflectivity and transmission, in semiconductors do not depend solely on the optical dipole matrix element $\langle\Psi_{cond}|e.r|\Psi_{val}\rangle$. The main features observed in optical signals, arise from critical points in the band structure where the densities of electron states in the bands are large. The joint density of states is not considered here thus it will not be possible to predict the absorption coefficient. However, the density of electron states in valence and conduction bands has been calculated and will be compared with experimental photo-emission results and bulk silicon and germanium densities of states.

The density of electron states has been calculated in short-period Si/Ge (4:4) superlattices as a function of strain within the unit cell. The technique used was similar to those proposed by Gilat (1972) and Stukel (1971). In this technique a Monte Carlo integration is performed thoughout the crystal Brillouin Zone on the superlattice band structure, and a histogram representing the density of electron states within the various bands is built up. The parameters for this calculation defining the band structures were those of Gell (1988).

A momentum vector **k**, is picked randomly from a Monte Carlo set and the electron energy band structure evaluated at that point. The integration is performed by filling histogram 'bins' corresponding to the electron energies of the band structure for each **k** point; this produces the density of states function. The total histogram value is normalised by the number of **k** points used, giving the density of states on a scale of states/eV atom as a function of energy, eV. Calculation of the electron energy band structure at a specific **k** value is time-consuming and it is usual to only calculate the band structure at a discrete set of mesh points within an irreducible segment of the Brillouin zone. Energies of random **k** points are then interpolated from the mesh using a quadratic approximation. The mesh was generated with a full **k.p** expansion from the band structure at the zone centre (Bassani and Parravicini (1975)). The whole Brillouin zone can be represented from this irreducible segment by symmetry operations of the point group of the superlattice unit cell.

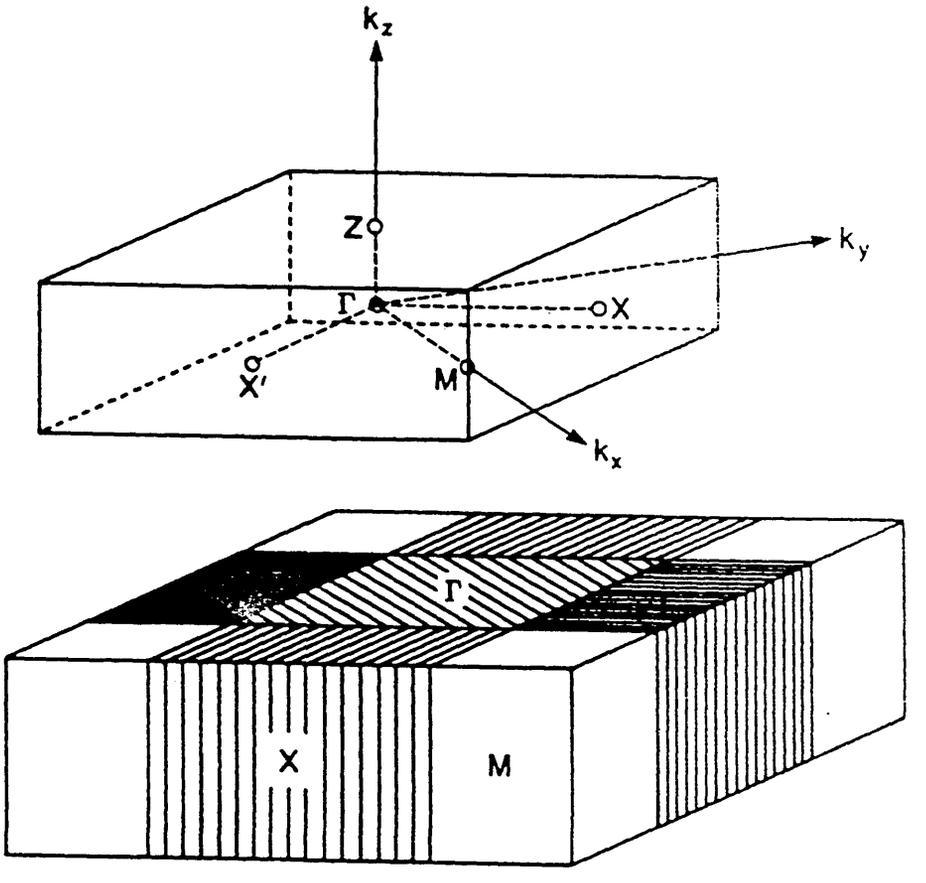


Figure 4.1 Upper part: superlattice Brillouin zone for the (4:4) superlattice showing points of high symmetry. Lower part: definition of the k-space sectors into which the superlattice Brillouin zone is divided for density of electron states calulations.

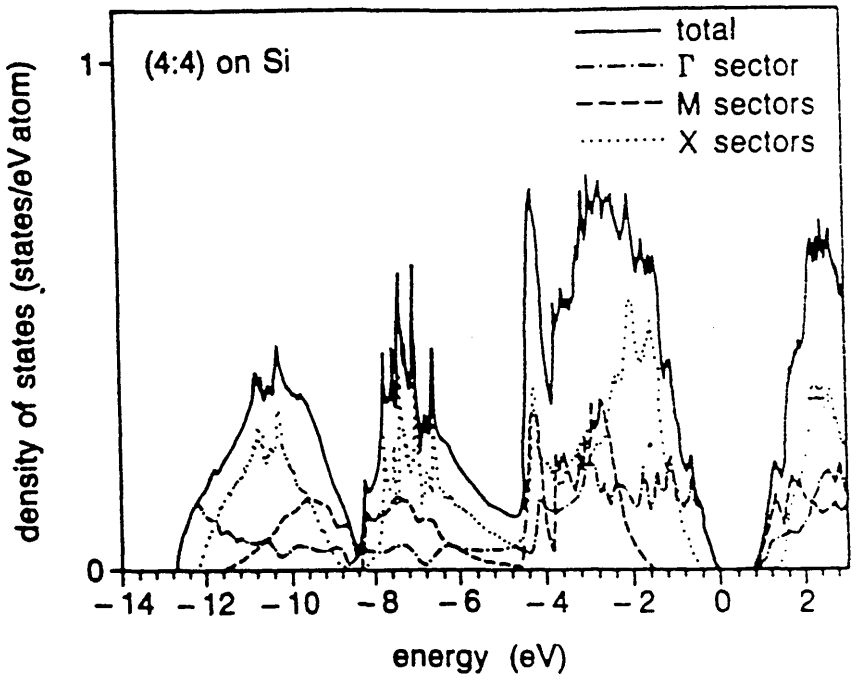


Figure 4.2 Density of states in the Si/Ge (4:4) superlattice on Si(001). The total density of states has been decomposed into contributions derived from t he different k-space sectors defined in figure 4.1.

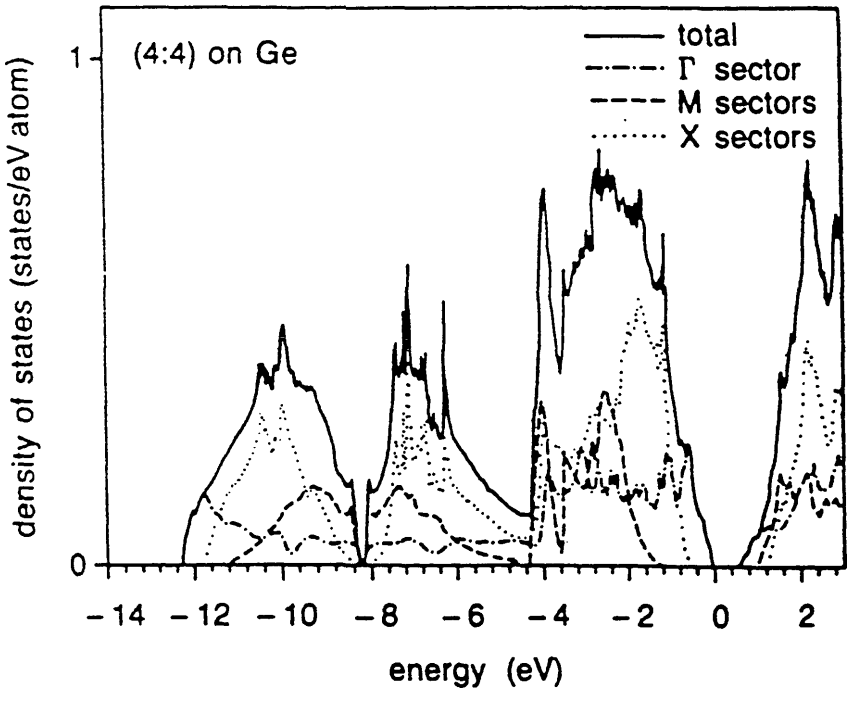


Figure 4.3 Density of states in the Si/Ge (4:4) superlattice on Ge (001).

The Brillouin Zone for the D_{2h} superlattice is substantially smaller than those considered by Gilat and Stukel. The band structure also contains considerable mixing between individual bands and thus changes more rapidly as a function of position in the Brillouin zone than a bulk band structure. Thus a point generation on a cubic spline instead of Gilat's quadratic interpolation was necessary. In all other respects the calculation was similar to those computed by Gilat and Stukel. The total number of Monte Carlo points in the D_{2h} Brillouin zone representing the superlattice, was about 20 million and an energy resolution in the historgram of 5 meV was used.

A new feature of this work is to decompose the density of states into various regions of the Brillouin zone. Figure 4.1 shows the Brillouin zone with labelled sectors. Rucker et al. (1988) have used a tight binding approach to calculate a layer by layer density of states in long-period superlattices of Si/Ge. Figures 4.2 and 4.3 show the density of electron states for Si/Ge (4:4) superlattices grown on either Si (001) or Ge (001) substrates respectively. Thus both cases are represented when the built in strain is (i) compressional in the Ge layers and (ii) tensional in the Si layers, within the superlattice period. A further figure shows a comparison of the two different calculations near the band gap in more detail.

Broadly speaking the valence band structure is similar to both bulk Si and Ge (Chelikowsky and Cohen (1976)), which is not surprising given the covalent nature of the components making up the superlattice. However the band width is slightly larger than either Si or Ge and expresses the effect of the valence band offsets in the superlattice. The valence band can be split into three regions, a lower region of mainly s like orbitals, a middle s/p hybridized region and the upper region of p like bonding orbitals. From the decomposition it can be seen that the number of states in the Γ sector envelops the X sector which in turn envelops the M sector, this is a consequence of the band pinching at the zone edges, see figure 2.16. The effect of hole splitting due to strain at the top of the valence band is not resolved in the density of states. Turning to the conduction bands it can be seen that strain distribution within the unit cell of the superlattice plays an important part in determining where the electron states sit in the Brillouin zone. For the case of the superlattice strained to the Si (001) in-plane lattice constant the lowest conduction band states lie in the M sector. As the strain is moved to the Si layers in the superlattice (on the Ge (001) substrate), states in the Γ sector move down about 0.2 eV below the Si (001) case. However it should be noted from the discussion in section 2.2.4, that the superlattice grown on Ge(001) still has an indirect

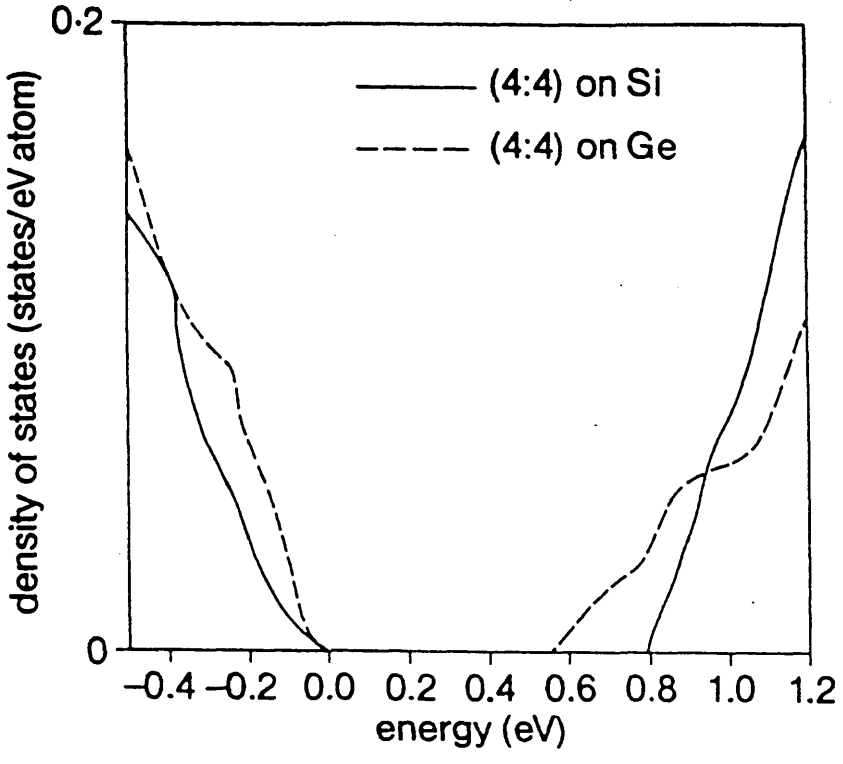


Figure 4.4 Density of states at the valence- and conduction-band edges in the Si/Ge (4:4) superplattice on Si(001) (solid curve) and Ge(001) (dashed curve).

band gap at Z. Figure 4.4 shows weak inflexions in both valence and conduction density of states near the band gap. The energies of -0.4 eV (solid curve) and -0.25 eV (dashed curve) correspond to onsets of the split-off bands, and -0.1 eV in the dashed curve corresponds to the second highest valence band. Inflexions in the conduction band density of states are most pronounced for the superlattice grown on Ge (001): at 0.8 eV corresponding to the second conduction band and 1.07 eV from states of the unfolded Δ minima lying at [100] and [010] directions. In the case for the conduction band edge for superlattices grown on Si (001) substrates, most features are washed out. For example only slight inflexions can be seen in the solid curve at 0.9 eV and 1.0 eV, corresponding to the superlattice C1 and C2 bands at the zone centre.

Experimental verification of the density of electron states can be done, usually with X-ray or ultra-violet photo-emission. For this kind of measurement the superlattice needs to be at the surface of the sample as probing depths are between 1 and 10nm (Hollinger (1987)). In addition, the superlattice must be thicker than the probing depth if substrate effects are to be ignored. Surface density of states effects should also be considered. An ultra-violet photo-emission experiment was carried out at to determine the valence band density of states at British Telecom Research Laboratories. The sample consisted of 5 periods of Si/Ge (4:4) superlattice on a Si (001) substrate. In this case the superlattice was only 5nm thick. The precise structural dimensions are outlined for similar samples in section 6.2.1. However, this sample did not have a Si capping layer. The measured signal was very noisy and no sharp features were observed. Three regions indicated the s, s/p mixed and p regions of the valence band. The overall width of the valence band could be estimated at 13.8 eV, which is larger than both Si and Ge valence band widths and confirms the effect of the band offsets between Si and Ge.

(The work contained in this chapter was carried out in collaboration with Michael Gell of British Telecommunications plc. and has appeared in a publication: Gell and Churchill (1989).)

Chapter 5 Structural analysis by Raman scattering spectroscopy.

5 Structural Analysis by Raman Scattering Spectroscopy.

Raman scattering spectroscopy can be particularly suited to analysing structural properties of Si/Ge samples on a macroscopic scale. Raman scattering spectroscopy does not have the spatial resolution of microscopies such as TEM or X-ray Topography, as the size of the area investigated is determined by the laser spot size which is normally about 200μm and by the laser penetration depth which is determined by the absorption length of the laser light. However the nature of the scattering mechanism relies on the polarisability of bonds in the crystal and this allows atomic investigation (Klein (1986)). Thus Raman scattering can give average structural analysis using atomic parameters. The experimental set-up was the one described in section 3.1, using 514.5 nm laser light from an Ar^+ ion plasma laser. The resonant Raman scattering also used a dye laser system.

The chapter is divided into two sections, each dealing with the different types of samples analysed. The first section considers $Si_{1-x}Ge_x/Si$ quantum well structures, the electronic properties of which were outlined in section 2.3.3. Raman scattering is used to determine the structural quality of the samples to be characterised optically in the next chapter: testing the overall quality of growth of $Si_{1-x}Ge_x$ layers. The next section deals with short-period superlattices, concentrating on the Si/Ge (4:4) superlattice. The isolated layers of pure Ge found in these superlattices allows Raman spectroscopy to be particularly sensitive to layer ordering. However, the samples investigated later in chapter 6.3, contain Si/Ge (2:n=6,8,10) superlattices. These were grown on $Si_{0.25}Ge_{0.75}$ alloy buffers which mask the Raman scattering from the superlattice. Consequently no firm conclusions about the structural quality of the (2:n) superlattices could be gained from Raman scattering spectroscopy.

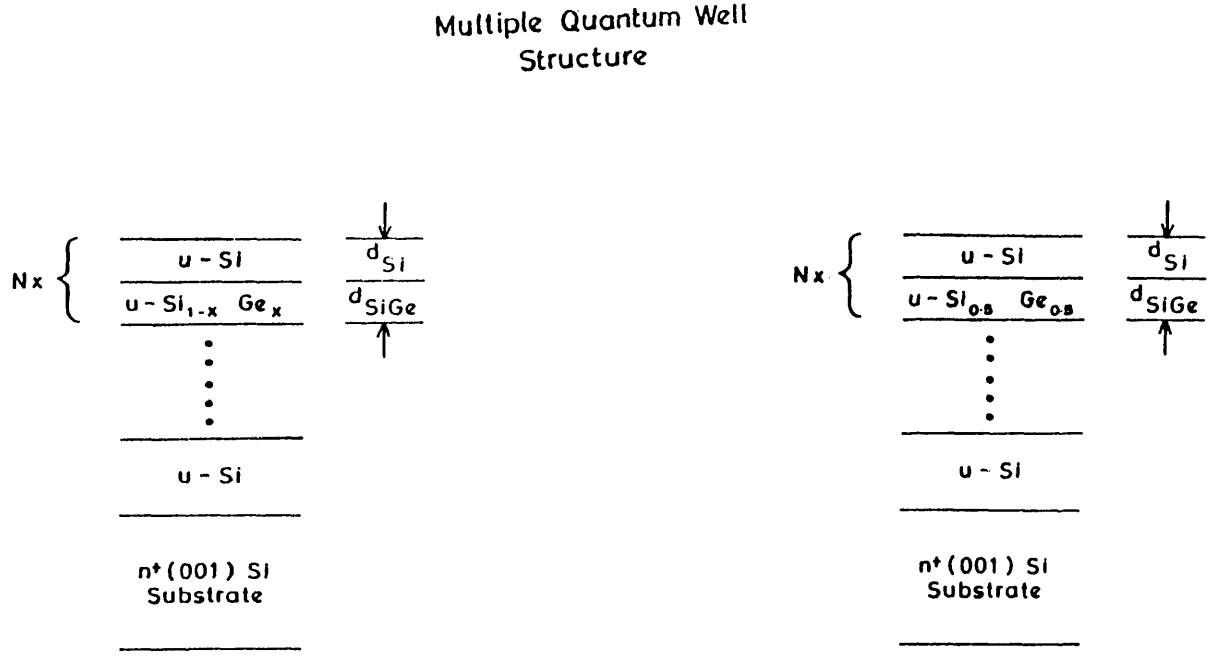


Figure 5.1 A schematic of the epitaxial layers containing quantum well structures, on the right the structure for QWA, QWB and QWC is shown, with wells formed from $Si_{0.5}Ge_{0.5}$ alloys. On the left the structure for QWD and QWE is shown. For the composition and layer thickness refer to table 5.1.

Table 5.1 Nominal Quantum well Sample dimensions

Sample	dSi Å	$dSi_{1-x}Ge_x$ Å	x	Number of wells
QWA	240	40	0.5	15
QWB	120	20	0.5	30
QWC	60	10	0.5	60
QWD	170(120)	30(21)	0.6	15
QWE	170(120)	30(21)	0.4	15

(TEM measured dimensions are given in brackets)

5.1 Multiple Quantum Well $Si_{1-x}Ge_x/Si$ Samples.

This section investigates Si/Ge Quantum Well samples, where the layer thicknesses are upto several orders of magnitude larger than the interatomic spacing. The samples are subsequently investigated optically using electro-reflectance spectroscopy in section 6.1.

Figure 5.1 shows typical layer structures for the samples, the nominal (and actual) dimensions are given in table 5.1. The samples were grown on Si (001) n^+ doped substrates with the procedure outlined in section 3.3. Layer thicknesses were designed so the total thickness of the repeated quantum well system is below the critical thickness for alloys of comparable concentrations on Si (001) substrates, thus the structures are strained, having an in-plane lattice constant of bulk Si. In most cases the alloy concentration and presence of strain was checked with X-ray diffraction at British Telecom Research Laboratories.

Figure 5.2 shows a Stokes Raman Spectrum of light scattered by Longitudinal Optic (LO) phonons from an alloy of $Si_{0.5}Ge_{0.5}$ grown on Si (001) n^+ doped substrate, (sample ALY50). The alloy is 0.2μm thick and thus is grown well above the critical thickness. Hence it has a lattice constant of a bulk alloy and contains virtually no built-in strain.

Four main peaks are observed, which can be identified when the spectrum is compared to the LO Raman scattering spectra of bulk Ge and Si (Figures 3.2 and 3.3). One mode is observed at around $300cm^{-1}$ and can be associated with Ge-Ge bonds. Another is observed at $400cm^{-1}$ which by assuming an average of Si and Ge bond strengths can be associated with Si-Ge bonds. Two modes are observed at around $500cm^{-1}$. The upper of these modes occurs from the substrate, while the lower is associated with Si-Si bonds in the alloy but depressed in energy from the bulk value due to confinement effects; for example see Brya (1973). Other subsidiary modes between the Si-Ge and Si-Si modes occur due to local modes within the $Si_{1-x}Ge_x$ alloy. This is illustrated in figure 5.3, and described by Alonso and Winer (1988). Figure 5.2 compares well to previously published Raman scattering from $Si_{1-x}Ge_x$ alloys by Brya (1973). The equal height of the three main modes indicates a reasonable random alloy of $Si_{0.5}Ge_{0.5}$ when it is

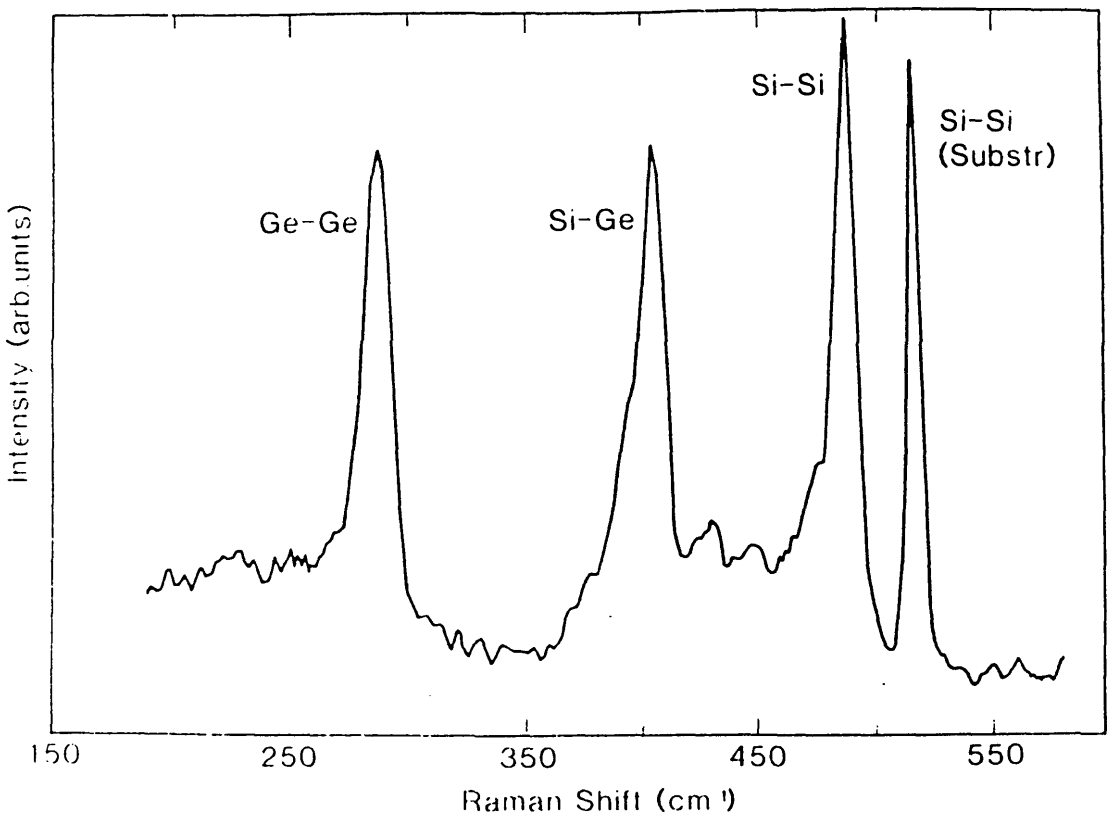


Figure 5.2 Room temperature Raman spectrum of a relaxed $Si_{0.5}Ge_{0.5}$ alloy layer 0.2μm thick grown on Si(001).

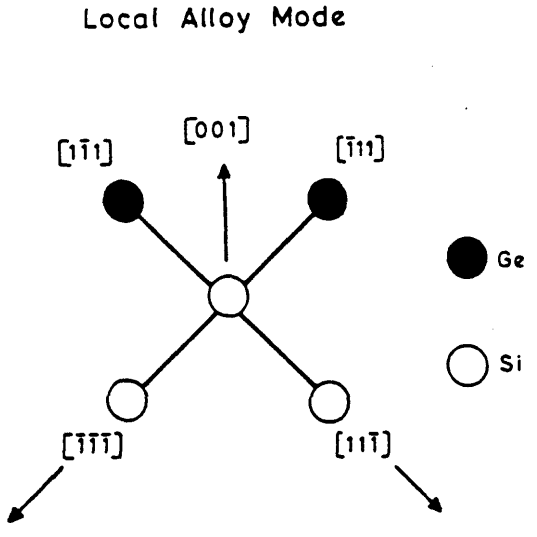


Figure 5.3 A schematic showing how local arrangments of Si-Ge and Si-Si bonds can give rise to local Raman active vibrations, which are observed lying bet ween the Si-Ge and Si-Si modes in the Raman spectrum of bulk alloys (after Alonso and Winer (1989)).

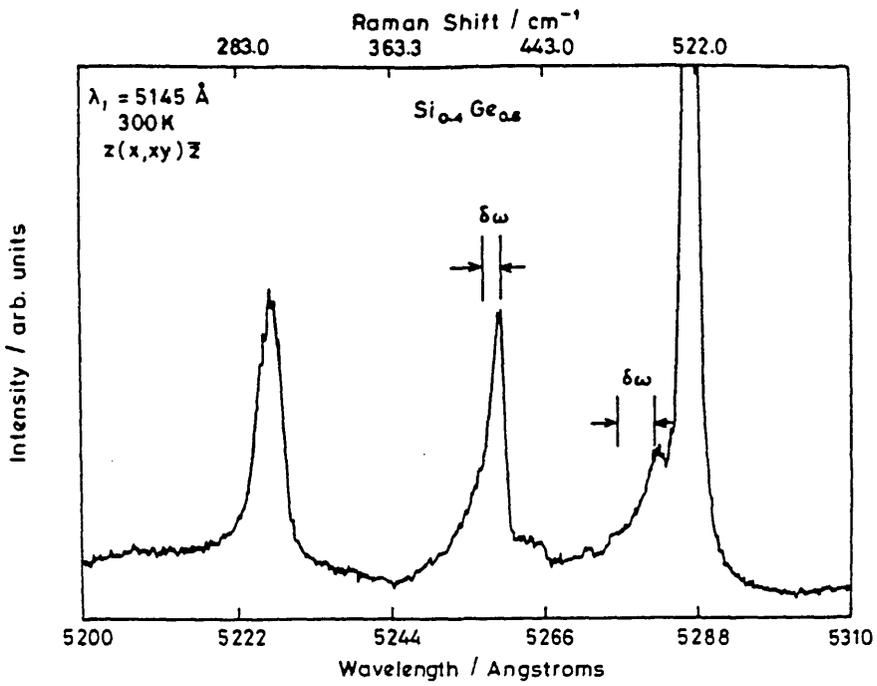


Figure 5.4 A room temperature Stokes Raman spectrum of sample QWD showing scattering from LO phonons.

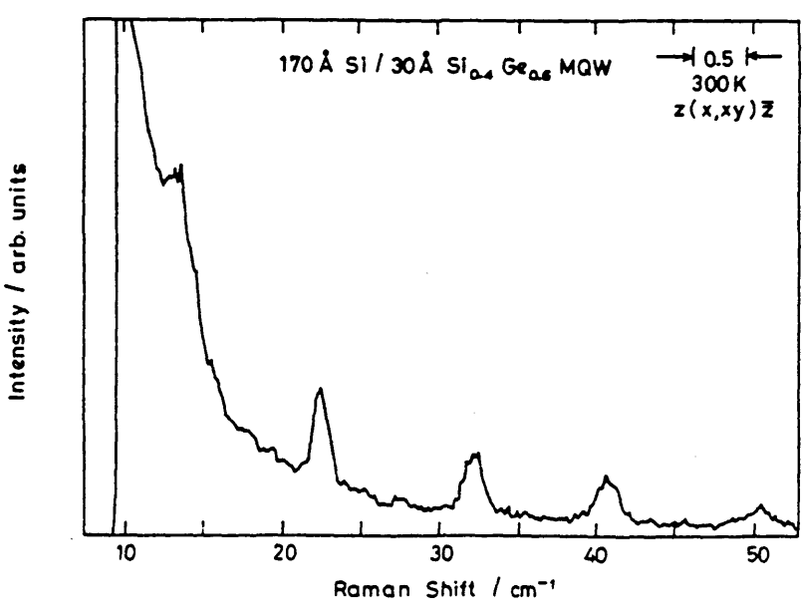


Figure 5.5 A room temperature Stokes Raman spectrum of sample QWD showing scattering from acoustic phonon modes within the quantum wells.

assumed that the Raman intensity in alloys is a function of the number of bonds (Tsang et al. (1989)), No acoustic phonon modes can be resolved in this spectrum as the scattered light for first order momentum conserving Γ_{15} phonons is too near to the laser line for the spectrometer to resolve.

Figures 5.4 and 5.5 show Raman scattering from a typical quantum well sample (QWD), for high and low phonon energies. Two features are observed: repeated periodic modes at low energies (due to folded acoustic phonons) and four optic modes at high energies. The optic modes are similar to the ones observed in the alloy sample but are (i) shifted in energy from both alloy and elemental Si and Ge phonon energies and (ii) have different intensities. Similar observations have been made by Lockwood (1986 and 1987), Brugger et al. (1986) and Cerdeira (1984). The next sections describe how these modes arise.

5.1.1 Strain dependence of optic phonon energies.

Raman scattering by LO phonons can occur in several places within the sample:

i) In the Si substrate, providing the light penetrates to this depth.

ii) In the Si layers in the quantum well structures

iii) In the SiGe layers grown in register with the Si lattice.

The mode energies and intensities from the alloy layers are not only a function of composition but are dependent on the amount of strain in the layers. The energies of phonons in unstrained alloys have been charaterised by Brya (1973) and Renucci et al. (1971), figure 5.6 shows the three optic phonon mode energies as a function of composition, taken from Brya's paper. The additional effect of strain when the alloy is distorted, as it is when grown in register with a Si substrate, can be predicted from results of deforming bulk Si and Ge and SiGe alloys. These results have been well documented by Renucci et al. (1971) for hydrostatic deformation of alloys and by Cerdeira et al. (1972) and Anastassakis et al. (1970) for uniaxial deformation of bulk Ge and Si. A summary of these results suggests that tetragonal distortion of the epitaxial layer, which is a mixture of uniaxial and hydrostatic deformation will give rise

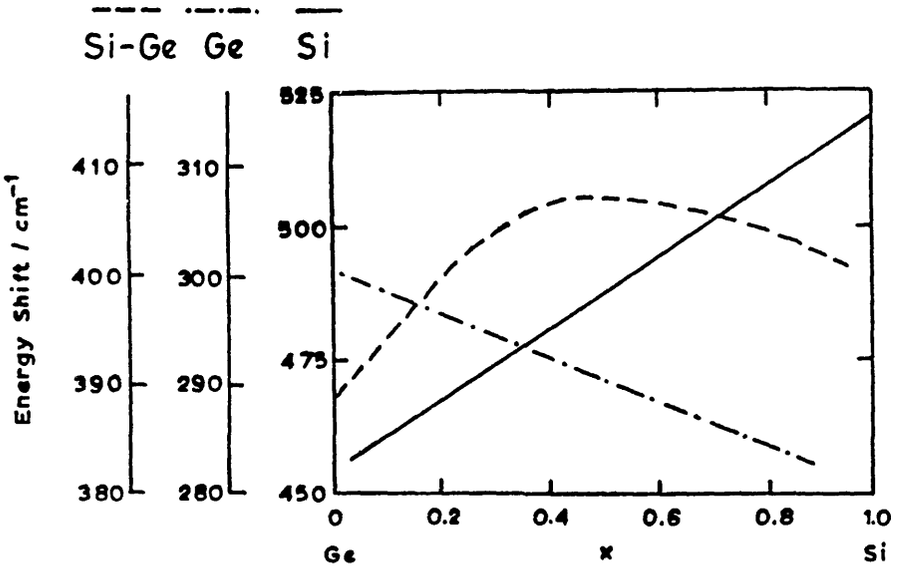


Figure 5.6 Optic phonon mode energies of a $Si_{1-x}Ge_x$ alloy as a function of composition x, measured at room temperature. Three modes are observed corresponding to Ge-Ge, Si-Ge and Si-Si bonds (after Brya (1973)).

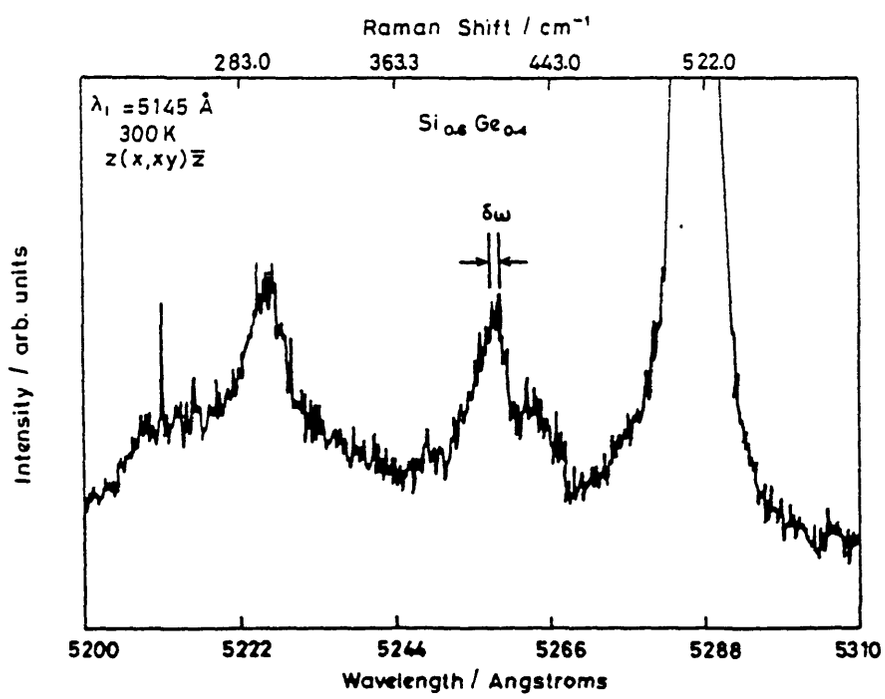


Figure 5.7 Stokes Raman spectrum of scattering from optic phonons within sample QWE, at room temperature.

to an upward shift for Γ'_{25} phonons polarised in the z-direction. The shift is linear in strain for both bulk Ge and Si.

By using the Raman scattering spectrum of optic phonons and precisely determining the optic phonon energies it is possible to either determine the composition or the inbuilt strain in very thin layers of materials. Generally these parameters can be confirmed by the X-ray diffraction techniques described in section 2.1, which makes the combination of Raman scattering and X-ray diffractometry very powerful set of tools for characterisation of the Si/Ge multilayer samples.

Figure 5.7 shows another sample (QWE), with the same dimensional specification as QWD, but only 40% Ge content in the alloy well regions. On the figure the shift of the Si-Ge phonon mode energy has been indicated by subtracting the value for phonons in the bulk alloy. The phonon shifts in sample QWE are less than that of QWD confirming that there is less inbuilt strain in the layers. A plot of strain shifted phonon energies $\delta\omega$ of Si-Si and Si-Ge alloy modes against strain, ε is given in figure 5.8, with samples QWD and QWE indicated. A phenomenological equation from Anatassaki et al. (1970) and Cerdiera et al. (1972) gives the shift in phonon mode energy for a given strain:

$$\delta\omega = p\varepsilon_{zz} + \frac{q}{2\omega_0}(\varepsilon_x,\varepsilon_y) \qquad [5.1]$$

where p and q are constants related to the Gruneisen parameters of compliance and ω_0 is the energy of the phonon investigated.

For the specific case of a uniaxially strained epitaxial layer with a Poisson ratio ν, equation [5.1] becomes:

$$\delta\omega = (\nu p + 2q)\frac{\varepsilon}{2\omega_0} \qquad [5.2]$$

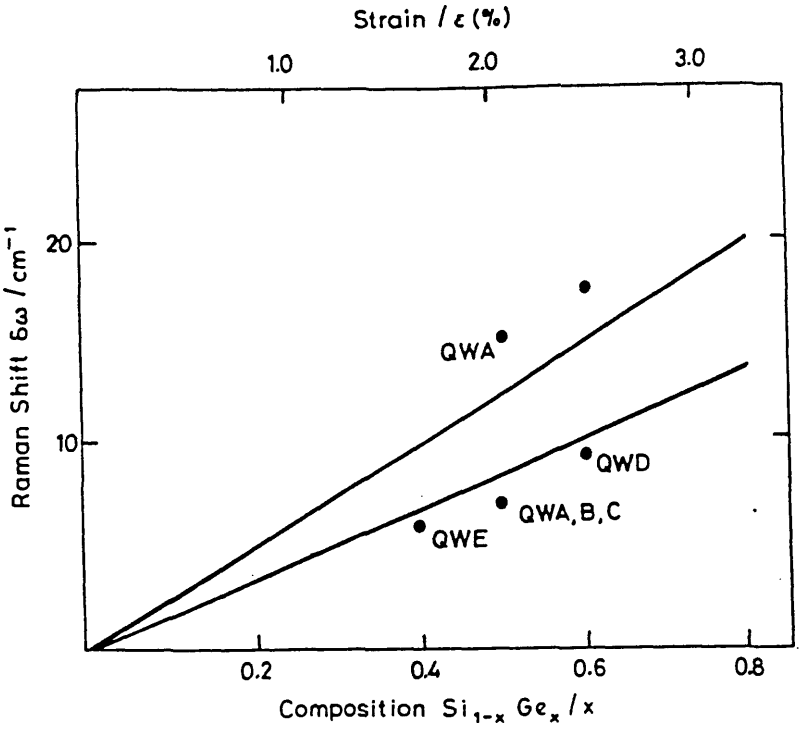


Figure 5.8 Si-Si and Si-Ge optic phonon mode energies measured in strained alloy quantum well samples as a function of composition/strain. The lines indicated are taken from Cerdeira et al. (1985).

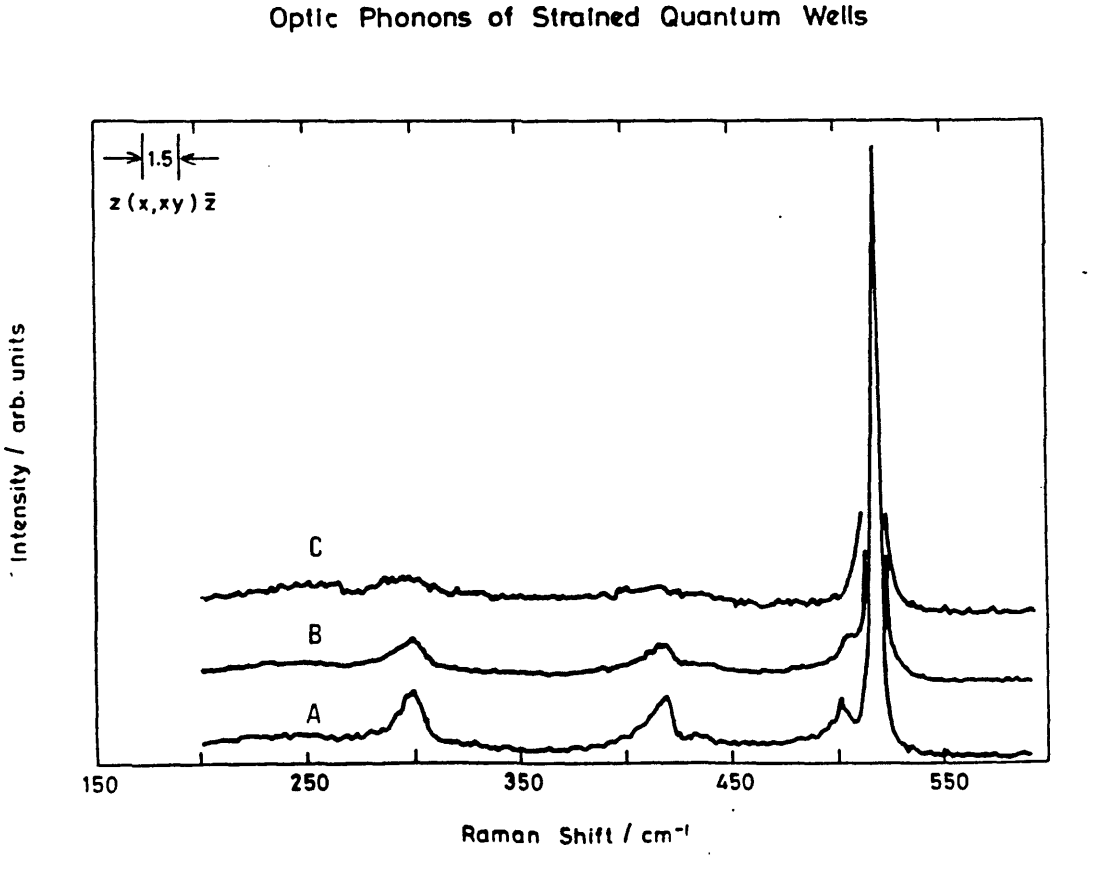


Figure 5.9 A Stokes Raman scattering spectrum of the optic phonon modes from samples QWA, QWB and QWC (bottom to top). The experiment was carried out at room temperature in back scattering geometry, with a spectral resolution of 1.5cm^{-1}.

Table 5.2 Parameters for strain shifted LO phonons.

	ν(Poisson)	p	q
Si	0.77129	-0.4701	-1.3451
Ge	0.7415	-0.6168	-1.9465

where ε is the strain in the epitaxial layer. Parameters derived from Cerdiera's paper are given in table 5.2.

The value of strain ε is linear as a function of the alloy concentration for a given substrate. The strain shifted phonon energies would change quadratically as a function of alloy concentration, if the values of p and q varied linearly from their bulk values for a given alloy concentration. The values plotted on figure 5.8 are fitted well by a straight line. The results of Cerdeira et al. (1985) also support a linear fit. Renucci et al. (1971) report that for various alloys under hydrostatic deformation the Gruneisen parameter -(p+2q) is affected by the whole Brillouin zone and as a consequence the value bows away from a linear interpolation between the bulk values, suggesting that a virtual crystal approximation cannot be used for values of p and q. At best the value of strain shifted optic phonon modes must be determined from the experimental results of figure 5.8 and not the expression given by equation [5.2].

The Raman scattering from strain shifted phonons of three more samples (QWA, QWB and QWC) is shown in figure 5.9. These samples have different layer thicknesses but the same alloy concentration of 50% Ge in the wells. All three show phonons shifted up by the same energy, confirming that the samples contain tetragonally distorted alloy layers. These results are also indicated on figure 5.8.

5.1.2 Folded acoustic phonon modes.

The acoustic branch of the phonon dispersion near the Brillouin zone centre has a slope that follows the speed of sound in the crystal. If the sample is stratified with different acoustic media, as is the case for the quantum well and superlattice samples, not only will the average sound velocity change, but standing waves may be created within the layers, producing a folding of the phonon dispersion.

A model which describes this effect was formulated by Rytov (1956), who originally considered shock waves from earthquakes through layered rock structures. A review of this theory is given by Klein (1986). Restricting the model to phonons allowed by the experimental geometry, (ie. that of scattered light perpendicular to the layers), a new dispersion is found for Longitudinal Acoustic phonons. This is

given by equation [5.3], which is valid for phonons of wavevector K in a repeated layer structure with layers 1 and 2 of thickness a and b:

$$\cos(k(a+b)) = \alpha \,.\, \sin ka \,.\, \sin qb + \cos ka \,.\, \cos qb \qquad [5.3]$$

where $\alpha = \frac{\rho_1 V_1}{\rho_2 V_2} + \frac{\rho_2 V_2}{\rho_1 V_1}$ $\qquad q = \frac{\omega}{V_2}$ $\qquad k = \frac{\omega}{V_1}$

and

$$V_{SL} = (1+\beta)\sqrt{\frac{\beta^2}{V_1} + \frac{1}{V_2} + \frac{\alpha\beta}{V_1 V_2}} \qquad [5.4]$$

where

$$\beta = \frac{b}{a}$$

ρ and V are the densities and sound velocities for the two media 1 & 2. Figure 5.10 shows the solution of this equation. The standing waves in the layered structure give rise to forbidden band gaps in, and a folding of the phonon disperion. These effects occur at the Brillouin zone centre, K = 0 and at a new reciprocal lattice vector at $K = q_{sl} = 2\pi/(a+b)$ formed by the repeated layer structure. However, according to Klein (1986), given that the two layers are similar to each other, these mini-gaps are small and can be neglected. The acoustic phonon dispersion can then be modelled by an average sound velocity given by equation [5.4] and zone folding at $K = q_{sl}$ and K = 0. The folding of the phonon dispersion gives rise to new phonon states which are allowed to scatter in the Raman process. These states are indicated on figure 5.10. In the experiments described here, the wavevector of scattered light is in the z-direction and is always less than the quantum well Brillouin zone, so scattering always occurs in the first Brillouin zone and no umklapp scattering processes take place (Lockwood et al. (1987)).

Hence for a given layered structure, using data from folded acoustic modes, strain shifted optical modes, and the parameters given in table 5.3, the alloy composition (ρ and V), the period (a + b) and period ratio

Table 5.3 Bulk acoustic parameters for Si and Ge. (after Lockwood et al. (1987))

	Si	Ge	
Vsound	8.44	4.9	x 10^5 cm/s
ρ (density)	2.33	5.36	g/cm^3
n (514.5nm)	3.6	4	

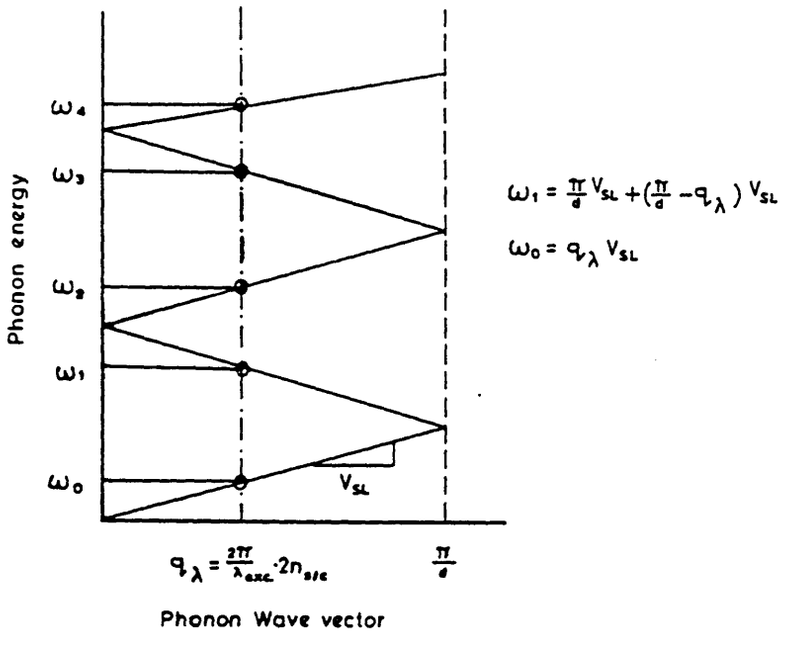


Figure 5.10 The calculated acoustic phonon dispersion in reciprocal space for longitudinal modes within layered multiple quantum well samples.

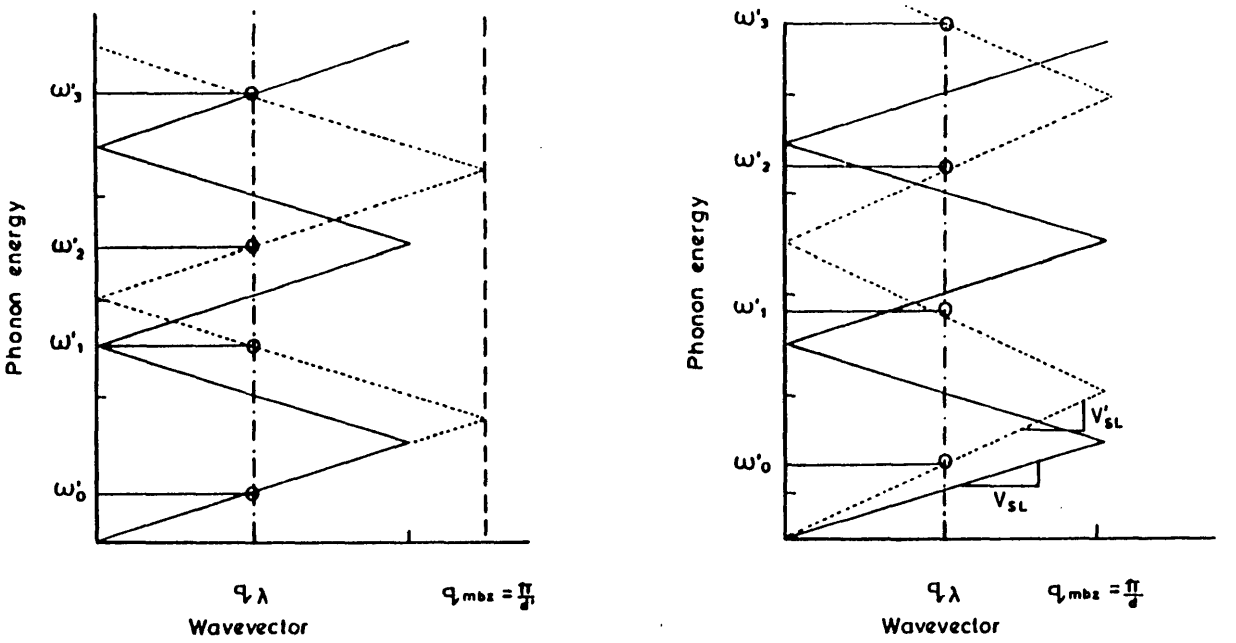


Figure 5.11 The longitudinal acoustic phonon dispersion within multiple quantum well structures showing the effects of changing the well composition (right) and well/barrier repeat length (left).

Table 5.4 Calculated acoustic mode energies for sample QWD

Order	Calculated (cm^{-1}) (Well width)		Measured (cm^{-1}) +/- 1cm^{-1}
	200Å	150Å	
1	4.3	4.3	
	8.8	13.43	13.5
2	17.5	22.08	22.3
	22.0	31.2	32.5
3	30.7	39.78	40.0
	35.29	48.9	50.0

Table 5.5 Acoustic phonons for sample QWA

Order	ω_{expt} cm^{-1}	ω_{calc} cm^{-1}	I_{expt}	I_{calc} (normalised)
0	4.3			
1a	14	13.79	125	125
1b		14.69		
2a	24	23.29	100	85
2b		24.18		
3a	33.5	32.78	56	48
3b		33.68		
4a	42	42.3	15	20
4b		43.19		

β, can be in principle confirmed. Figure 5.11 shows how changing the quantum well repeat period and the alloy composition or well to barrier ratio changes the folded acoustic energies. Determination of β, and period (a + b) is just a matter of fitting the spectrum by equation [5.4] and the zone boundary.

First reports of folded acoustic phonon Raman spectra were by Merlin (1980) in the GaAs/AlGaAs layered system, and subsequently for $Si_{1-x}Ge_x/Si$ by Lockwood et al. (1986 & 1987) and Brugger et al. (1986).

The folded phonons of sample QWD in figure 5.5 cannot be fitted by the dimension parameters given in table 5.1, given the additional results from figure 5.4 which show that the sample contains $Si_{0.4}Ge_{0.6}$ alloys which are fully strained. To obtain a fit with experimental observed phonon energies the sample dimensions must be reduced by about 30% to 149Å total barrier and well thickness, Transmission Electron Microscopy indicates a thickness of 141Å. In this particular case the laser wavelength was 514.5nm giving a back-scattering wavevector of 1.017×10^7 cm^{-1} in the semiconductor (the equations of Lockwood et al. (1987) have been used to determine this wavevector). A further test can be carried out with different laser wavevectors to determine where the quantum well Brillouin zone occurs. In this case a procedure of this type was not necessary in order to find the repeat length of the quantum well structure. Table 5.4 shows the acoustic mode energies calculated for sample QWD, with quantum well repeat periods of 200 and 150Å respectively together with measured phonon energies.

Figure 5.12 and 5.13 show folded phonons from two samples, QWA and QWB. Mode energies for sample QWA are summarised in table 5.5. The phonon modes for QWA are doublets, which are unresolvable experimentally, but in the case of QWB the modes are singlets lying on top of the doublet energies of QWA. Samples QWC and QWE did not show any Raman scattering signal in the energy range of 10 to 300 cm^{-1}.

Care should be taken not to confuse assignment of folded phonons with atmospheric Raman active vibrational modes. The very weak peaks in the spectrum of QWA in figure 5.12 show these vibrational modes.

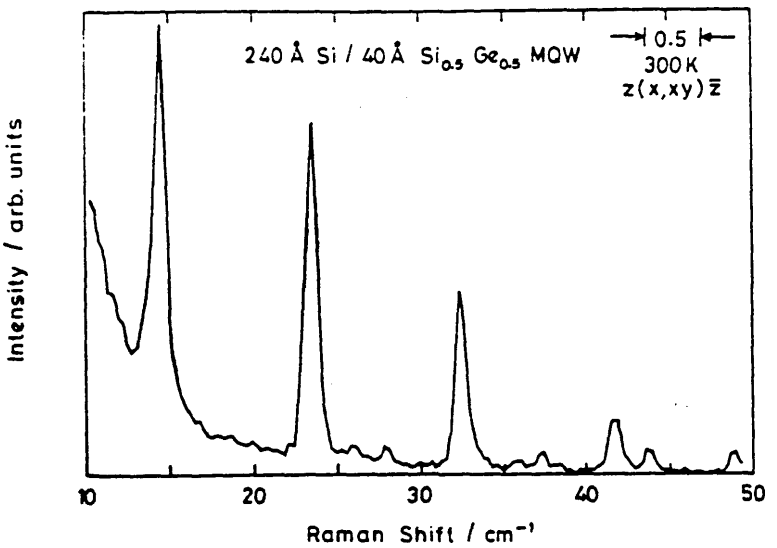


Figure 5.12 A room temperature Raman spectrum of folded acoustic phonons within sample QWA.

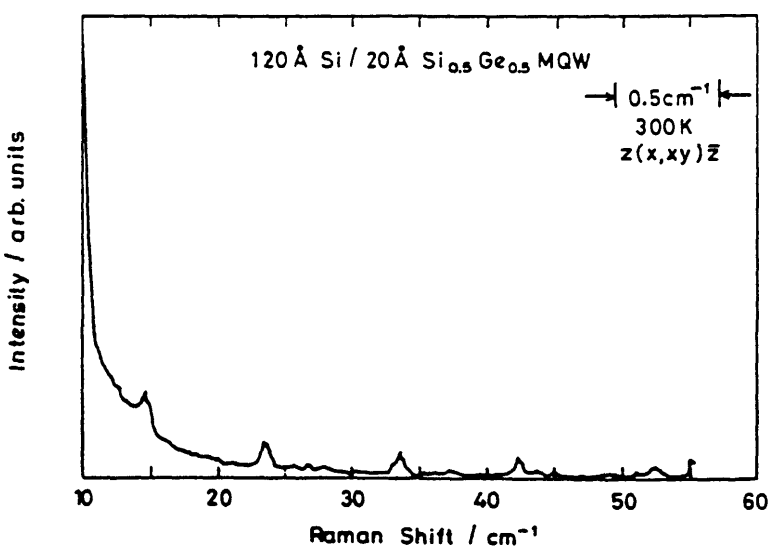


Figure 5.13 A room temperature Raman spectrum of folded acoustic phonons within sample QWB.

In addition to determining the quantum well periodicity and structural dimensions, the intensity of the folded phonon spectrum can also give an indication of the layer composition. In the simplest approximation (when the scattered light is not resonant with any gap in the phonon spectrum) the Raman intensity is proportional to the spectral density $<|d\chi|>_q$ or Raman tensor (Cardona (1982)), where

$$d\chi_q = \int_{SL} e^{-iq} 2P(z) \frac{du(z)}{dz} dz \qquad [5.5]$$

and P(z) is the polarisability of the atoms in the superlattice. This polarisability can, in a simple form, be expressed as a function of atomic concentration. Thus the intensity of the mth mode is:-

$$I_{Raman} = \omega_m (n_m + 1) |P_m(q)|^2 \qquad [5.6]$$

where n_m is a statistical factor for phonons (Bose-Einstein). The polarisability $P_m(q)$ is just the Fourier transform of the concentration profile. Lockwood et al. (1987) give the following polarisability for a quantum well structure as.

$$P_m(q) = \frac{\sin\left[\frac{m\pi a}{a+b}\right]}{m} \qquad [5.7]$$

Normalised phonon intensities have been calculated for sample QWA, which has the least noisy spectrum of all measured folded phonon spectra. Table 5.5 shows predicted and measured folded phonon mode intensities and energies for QWA. In this case a = 6.b where a = 4nm, and the wavelength of the light used for scattering was 514.5nm. The Bose-Einstein factor has been taken to be a constant, because the

phonon energies are small compared to the sample temperature. Good agreement between theory and experiment is found.

5.1.3 Concluding remarks on Raman characterisation of quantum wells.

Quantum well samples (QWA to QWE) have been characterised with Raman scattering. The optic phonon mode energies suggest that for the specified composition all the samples have strained alloys in the quantum well region.

From the folded phonon spectra the periodicity and alloy composition can be verified by using the mode energies and intensities. Samples QWA, QWB and QWD were checked in this way. For sample QWD it was found that the structure has a somewhat smaller dimension than specified, which is probably due to low settings for the Si and Ge fluxes during growth. It can therefore be surmised that although sample QWE showed no folded phonons, it also has slightly smaller dimensions than specified, as it was grown at a similar time to QWD. Samples QWA and QWB had their specified dimensions however QWC showed no folded phonons in its Raman spectrum. Additional information on sample QWA from the intensities of folded phonon modes allowed verification of the alloy conctration in the well region.

It is not clear why samples QWC and QWE did not show any Raman scattering of folded phonons. Since the samples were grown at the same time as other samples there is no evidence to suggest structural defects have reduced the Raman signal intensities. However, it is noted that scattering from optic phonons of the alloy regions was also weak for both samples. The poor scattering intensities from these samples is probably a consequence of small periods and weak alloy concentration. One observation is that as the well width reduces in the series of samples QWA, QWB and QWC, so the folded acoustic phonon intensities reduce, until Raman scattering from folded phonons is not observed in sample QWC. This could suggest that perhaps interface roughness (which would be of the same size for the three samples) becomes comparable to the well width for sample QWC. Raman scattering from folded acoustic phonons relies on the sample having smooth interfaces to 'fold' the phonons, if the interface roughness becomes comparible to the well width then the interfaces no longer appear smooth compared to the

quantum well structure and folding of acoustic phonons no longer takes place. This could perhaps explain why sample QWE, which also has thin wells regions, showed no Raman scattering from folded acoustic phonons.

5.2 Short-period superlattices.

In this section Raman scattering is used to investigate samples which are only a few monolayers in thickness. Figure 5.14 shows a typical structure: a Si/Ge (4:4) superlattice is constructed of 4 monolayers of Ge and 4 monolayers of Si, repeated 5 times, the total period is 11.24Å in thickness (from equation [2.15]) and the the total superlattice structure is therefore 56Å thick. The superlattice was grown with the method described in section 3.3, on Si (001) surfaces and capped with Si. The total structure has a thickness less than the critical thickness for the equivalent $Si_{0.5}Ge_{0.5}$ alloy, so the in-plane lattice constant is that of Si (5.43Å). Samples investigated are denoted S44A to S44E and S44M. Sample S44M has the superlattice repeated nineteen times with suitable buffers between to retain the strain, the others have different buffer thicknesses. The repeated structure allows a compromise to be made between diluting the amount of germanium in the structure to avoid problems with critical thickness and maximising the signal from the superlattice.

5.2.1 Optic phonon mode strengths and energies.

Figure 5.15 shows a Raman scattering spectrum of longitudinal optic (LO) phonons for sample S44M taken at room temperature. A comparison can be made with the alloy spectrum in figure 5.2. The observed modes can be assigned to the following bonds found in the superlattice:

$310cm^{-1}$	Ge-Ge mode,
$400cm^{-1}$	Si-Ge mode,
$520cm^{-1}$	Si substrate mode.

A small shoulder is present to lower energies on the Si substrate mode. At low temperatures (10K) this mode is resolved at $507cm^{-1}$, with another mode appearing at $478cm^{-1}$; figure 5.16 shows a low temperature spectrum of sample S44M. Better examples of these modes can be seen in figure 5.23, discussed in the section on annealing superlattices and in figure 5.22, when the incident light is resonant with superlattice transitions also discussed in the next section.

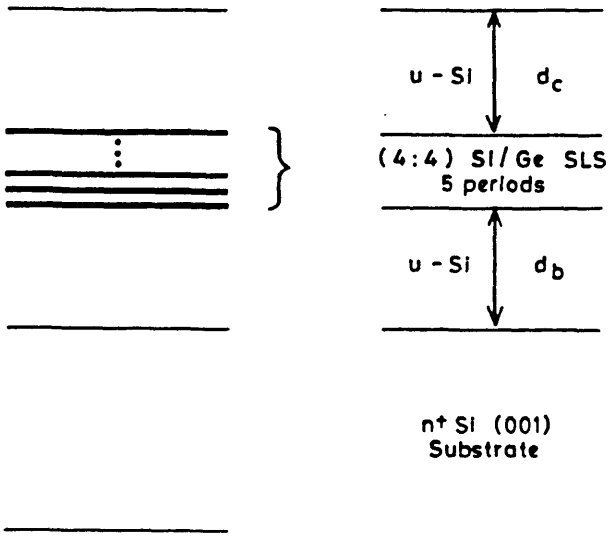


Figure 5.14 Schematic showing the structure dimensions for epitaxial samples containing Si/Ge (4:4) short-period superlattices grown on Si(001), used in the thesis. Samples with this structure type are S44A, S44B, S44C, S44D and S44E.

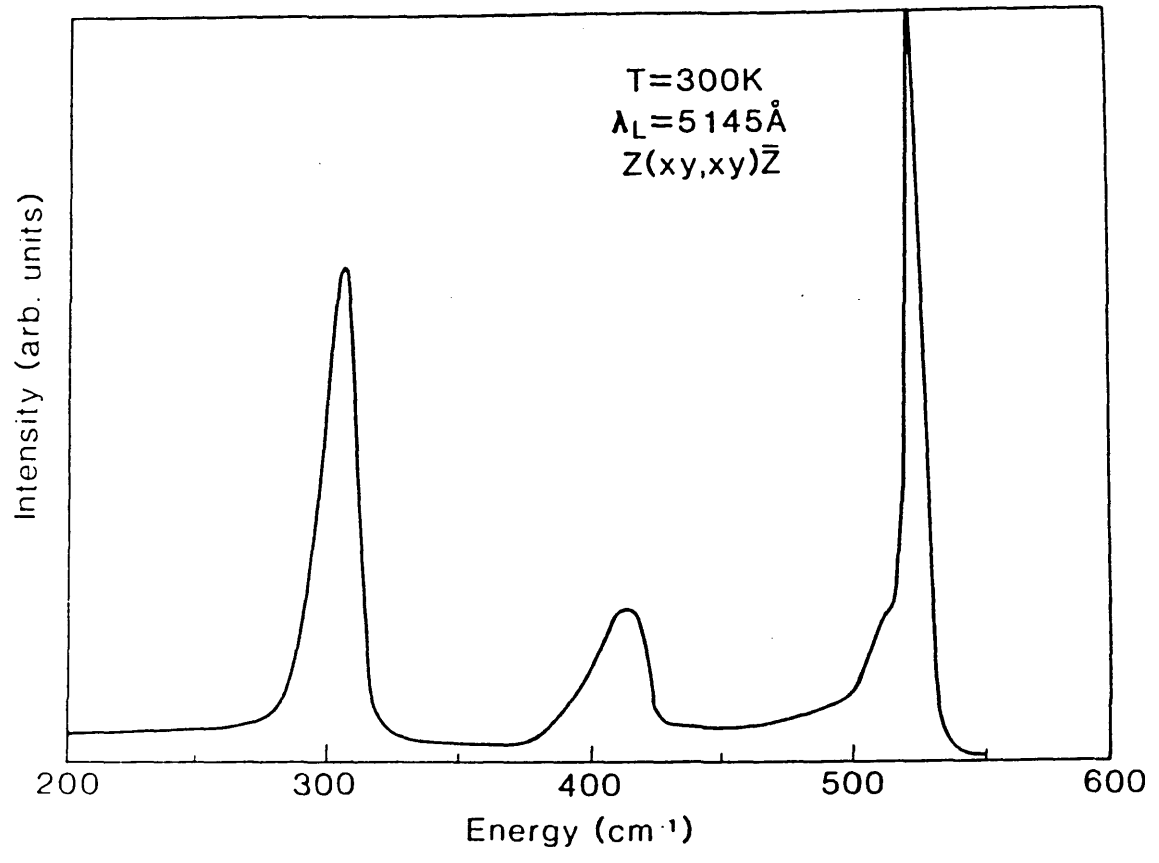


Figure 5.15 A typical room temperature Stokes Raman spectrum for sample S44M, containing 19 repeats of a Si/Ge (4:4) short-period superlattice. Three main modes are observed Ge-Ge (~300cm^{-1}), Si-Ge (~400cm^{-1}) and a Si-Si (~500cm^{-1}).

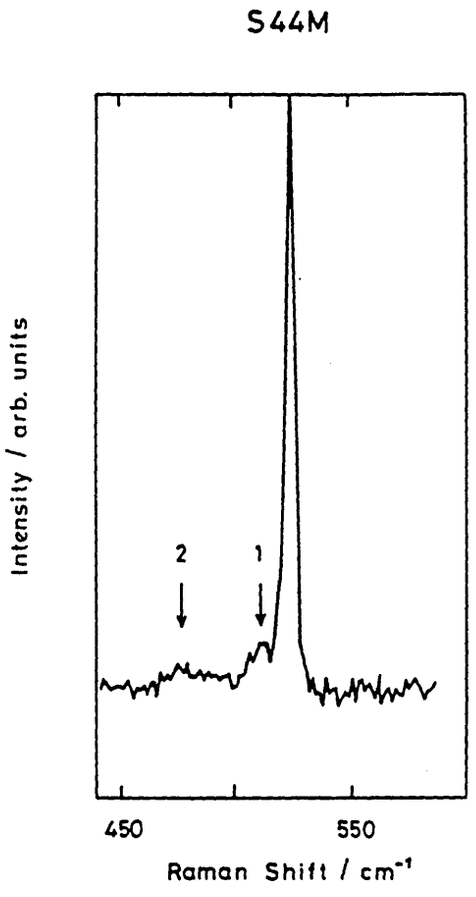


Figure 5.16 A Stokes Raman spectrum of LO phonons in sample S44M, as figure 5.15 but at a temperature of 10K. Two Si-Si confined modes resolved at low temperature are indicated.

It can be noted that the Ge-Ge mode is considerably up shifted in energy compared to modes found in $Si_{0.5}Ge_{0.5}$ alloys ($290cm^{-1}$) and pure Ge ($300cm^{-1}$). Indeed the shift would imply from the results of the preceeding section, shown in figure 5.8, that the Ge layers are highly strained. The quantum well results predict that for a 4% strain this mode should be at $313cm^{-1}$, but as Tsang et al. (1989) point out interaction of the Ge layers with the surrounding Si layers tends to depress the energy upshift of this mode, so quantitive conclusions are difficult.

The Si-Ge mode originates from the Si-Ge bonds which in the superlattices should be at the interfaces. This mode is reminiscent of the interface modes found in GaAs/AlGaAs systems investigated by Sood et al. (1985a) and other workers. However it should be noted that if these modes are truely localised at the interfaces, then they should be transverse modes, which cannot be observed in the back scattering optical geometry used. A longitudinal mode which can be detected by the Raman geometry used, would extend through the entire superlattice period, however the anisotropy of the compliance constants (Yin and Cohen (1982)) allows localised interface modes to occur for transverse motion.

In another paper by Sood et al. (1985b) again investigating GaAs/AlGaAs layered systems, additional modes are observed below the GaAs LO phonon mode. These are described as confined modes, in analogy to confined electron states found in quantum well systems. The modes below the Si substrate mode in figure 5.15 and 5.16 could also be ascribed to the same kind of confinement effect in the superlattice.

The result described above compares well with other reported results of Abstreiter and co-workers (Abstreiter et al. (1989ab), Friess et al. (1989) & (1990)), who have made detailed studies on symmetrically strained short-period Si/Ge superlattices with Raman scattering spectroscopy. Another phenomenon observed in Abstreiter's samples is that of folded acoustic phonons. This is because Absteiter's samples are symmetrically strained and contain large numbers of periods in the superlattice structure (for example Brugger et al. (1988)). Acoustic modes are unfortunately absent from the 5 period superlattices investigated here probably because of the small number of periods.

5.2.1.1 Confined Optic Modes.

In addition to LO confined modes below the Si substrate mode, Friess et al. (1989 and 1990) have reported observations of both LO modes below the Ge mode and the occurrence of confined TO modes when the substrate is orientated to the (110) face. By investigating samples with different superlattice periods, Friess et al. have been able to determine optic phonon mode dispersions from the confined modes.

Phonons that scatter in the superlattice are allowed to have additional energies when compared with bulk scattering because of the extended unit cell in the superlattice, which reduces the Brillouin zone size. The phonon dispersion effectively folds to the zone centre, as in the case of quantum well samples, producing new allowed scattering phonons. However this explanation tells us nothing about where the phonons are in the superlattice layers and other models must be used to describe the phonon modes found in short-period superlattcies. For example the linear chain model, which was discussed in chapter 3.4. This model relies on the approximation that the lattice vibrations of atoms in one direction can be reduced to a one dimensional model of masses separated with compliant springs to form a linear chain. This technique has been widely used to describe phonon modes in both GaAs/AlGaAs and Si/Ge systems, see for example Molinari and Fasolino (1989). Whereas the diamond structure has a primitive cell containing two atoms which leads to two branches in the phonon dispersion, the Si/Ge (4:4) superlattice has 8 atoms per primitive cell and thus leads to 8 branches in its phonon dispersion. Using an extension to the theory of phonons described in Kittel (1976) and the techniques described in chapter 3.4, the phonon dispersions in the growth direction of the (4:4) superlattices have been calculated. The results are shown in figures 5.17 and 5.18. Parameters for the compliance factors are taken from ab-initio calculations of Yin and Cohen (1982) and Kunc and Gomes Costa (1985); use of the virtual crystal approximation was made for Si-Ge bonds. The parameters used for the calculation are tabulated in table 5.6, the masses used were defined in section 2.2. These parameters give very accurate bulk phonon dispersions compared to neutron scattering experiments (Yin and Cohen (1982) and Kunc and Gomes Costa (1985)). The parameters used for the Ge layers were scaled to shift the bulk optic phonon mode energy values upto $310cm^{-1}$, thus including an effect of strain within the calculation.

Table 5.6 Forces constants used in linear chain phonon models

(From Yin and Cohen (1982) and Kunc and Costa Gomes (1985))

	Si (LO)	Ge (LO)	Si (TO)	Ge (TO)
c_{i-j}				
0	+2.614	+2.278	+2.100	+1.855
1	-1.106	-1.050	-1.754	-1.695
-1	-1.106	-1.050	-0.338	-0.203
2	-0.192	-0.083	+0.046	+0.086
-2	-0.192	-0.083	+0.046	+0.086
3	-0.009	-0.006	-0.009	-0.035
-3	-0.009	-0.006	-0.091	-0.094

(units 10^5 dyn/cm)

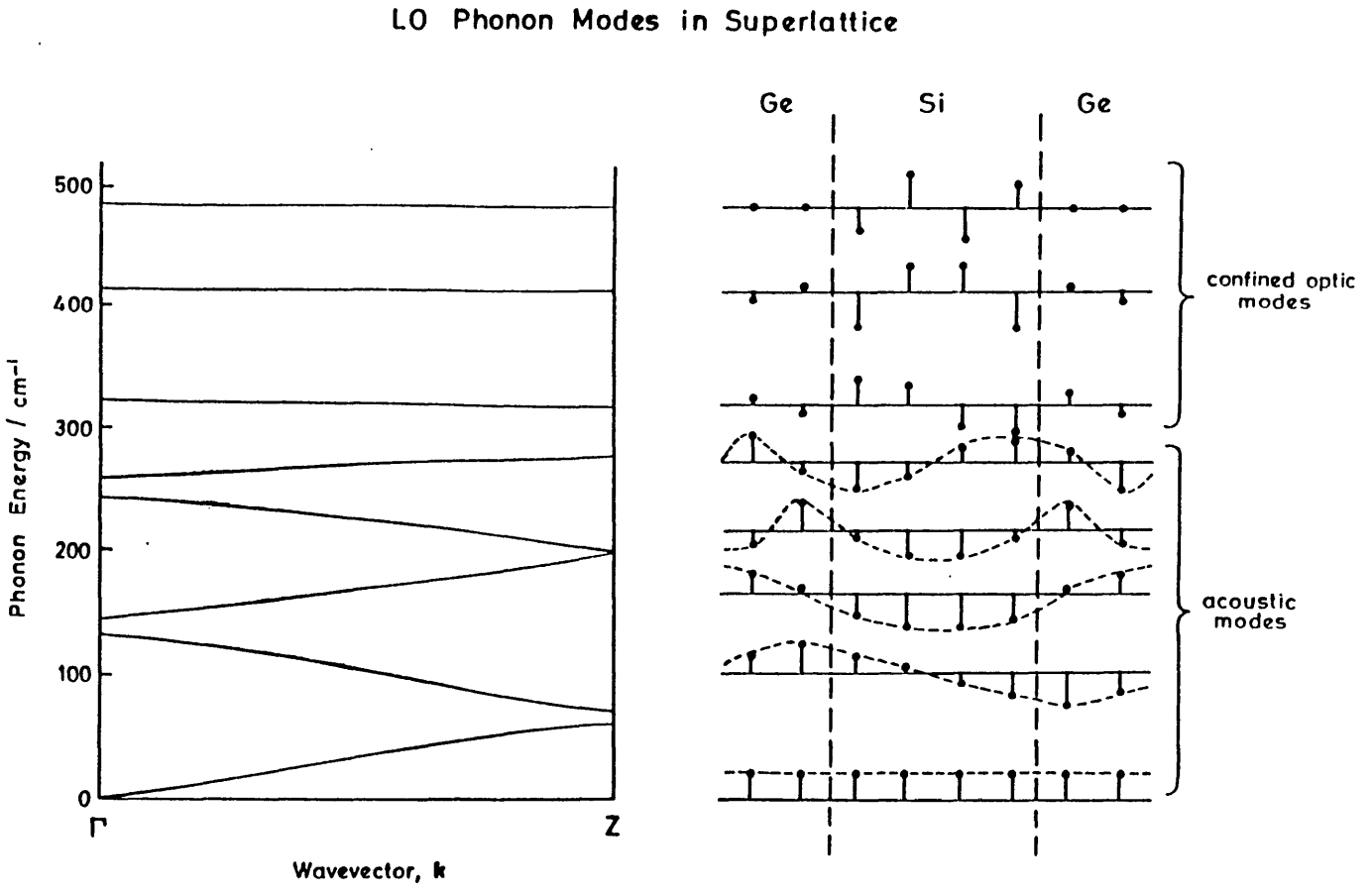


Figure 5.17 The phonon dispersion and atomic eigen-modes for phonons with a longitudinal motion, in the superlattice direction for a Si/Ge (4:4) short-period superlattice, calculated using the linear chain model. Parameters for the calculation are given in table 5.6.

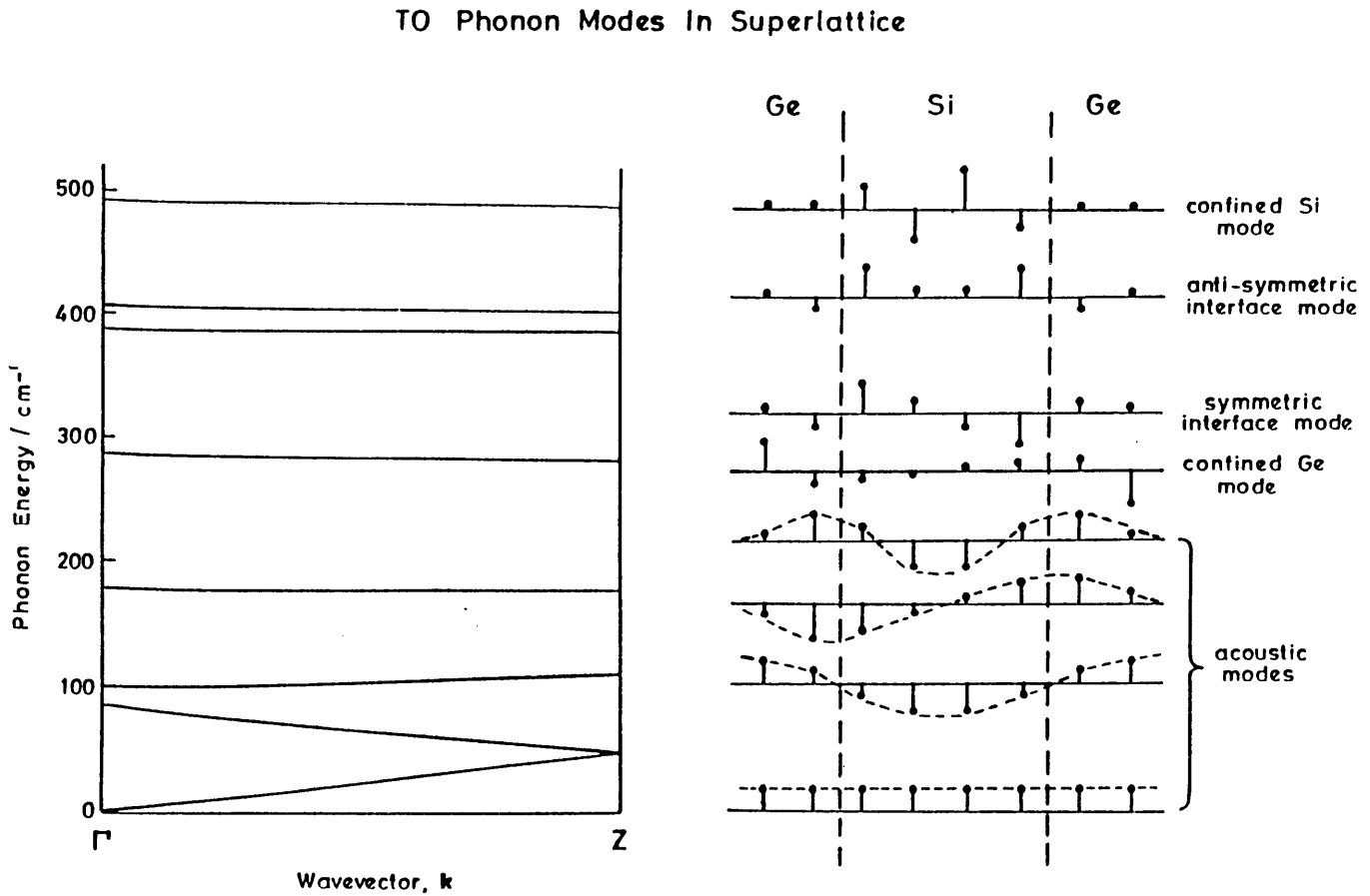


Figure 5.18 The phonon dispersion and atomic eigen-modes for phonons with a transverse motion, in the superlattice direction for a Si/Ge (4:4) short-period superlattice, calculated using the linear chain model. Parameters for the calculation are given in table 5.6.

From the linear chain model of longitudinal phonons in Si/Ge (4:4) superlattices several phenomena can be noted:

i) There are five acoustic modes at low energy with gaps in the dispersion at the zone centre and boundaries. These modes correspond to folded acoustic phonon modes.

ii) An accidental degeneracy occurs in the dispersion at the zone boundary of the acoustic branch due to the bulk Si and Ge dispersion crossing at this point in reciprocal space.

iii) The eigenmodes displayed on the right of figure 5.17 show that there is no true confined Ge mode in the Si/Ge (4:4) superlattice. This is because the optic phonon dispersion branch in Ge is overlapped by the Si acoustic branch.

iv) Two Si confined modes appear, the upper one very much reduced from the bulk Si phonon value of $520cm^{-1}$. This depression is due to a confining effect for the phonon mode, which is rather like the confining effect for electrons in quantum well strutures.

Turning to the transverse modes figure 5.18 again shows that there is no true confined mode in the Ge layers, however two modes forming a doublet are confined to the interfaces of the Si and Ge layers. These are denoted the interface modes and are labelled anti-symmetric and symmetric to describe their eigenmodes.

Unfortunately the energies predicted for LO phonons by the linear chain model do not agree very well with the experimentally observed values, this is because of the lack of crystal structure in the model and because the linear chain model uses only a few parameters. When comparing with experimental results it should also be realised that it is quite possible that the samples investigated are far from ideal 8 monolayer periods.

5.2.1.2 Interfacial phonon modes.

The linear chain model only predicts localised interfacial modes for transverse phonons, and thus the presence of this mode in spectra taken in back scattering geometry suggests some loss of symmetry. Whilst the linear chain model is only one dimensional, the results it predicts are confirmed by more sophisticated models of White et al. (1989) and others for example Dharma-Wandana et al. (1990) and Alonso et al. (1989).

It has been suggested by some workers (Montie et al. (1989), Menendez et al. (1988), for example) that the presence of an interfacial mode is due to relaxation of symmetry, perhaps due to disorder in the layers. Authors Menedez et al. (1988) and Montie et al. (1989b) use linear chain models with disorder parameters to model spectra of (4:4) superlattices, however extension of the linear chain concept to include disorder effects seems optimistic for phenomena that are essentially three dimensional.

Using a three dimensional model for calculating phonon scattering intensities from atomic bond arrangements, Alonso et al. (1989) are able to see an appearance of an interface mode as alloy disorder is introduced at the interfaces. Similar results are reported by Dharma-Wandana et al. (1990), however White et al. (1989) manage to model not only the appearance of a mode but its shape by using a density of phonon states of the entire superlattice Brillouin zone. This density of states effect is typical of amorphous and alloy semiconductors both Albern et al. (1973) and Renucci et al. (1971) reporting effects in Raman scattering from the whole Brillouin zone. The presence of interfacial steps may of course cause enough relaxation of symmetry to allow the interface mode to be observed. The lack of perfect samples leaves the investigator without a control experiment.

Raman scattering of Ge-Ge and Si-Ge optic phonons from other samples S44A, S44B and S44C are shown in figure 5.19, figure 5.20 shows Raman scattering from all three optic modes of sample S44E. As the amount of superlattice probed by the incident light is 20 times less than in sample S44M, experimental integration time was much longer. The confined Si modes are lost in the tail of the Si substrate mode. However the energies and intensities of Si-Ge and Ge-Ge modes indicate that all the samples are strained and relatively ordered compared to a random alloy of $Si_{0.5}Ge_{0.5}$. The Si-Ge modes

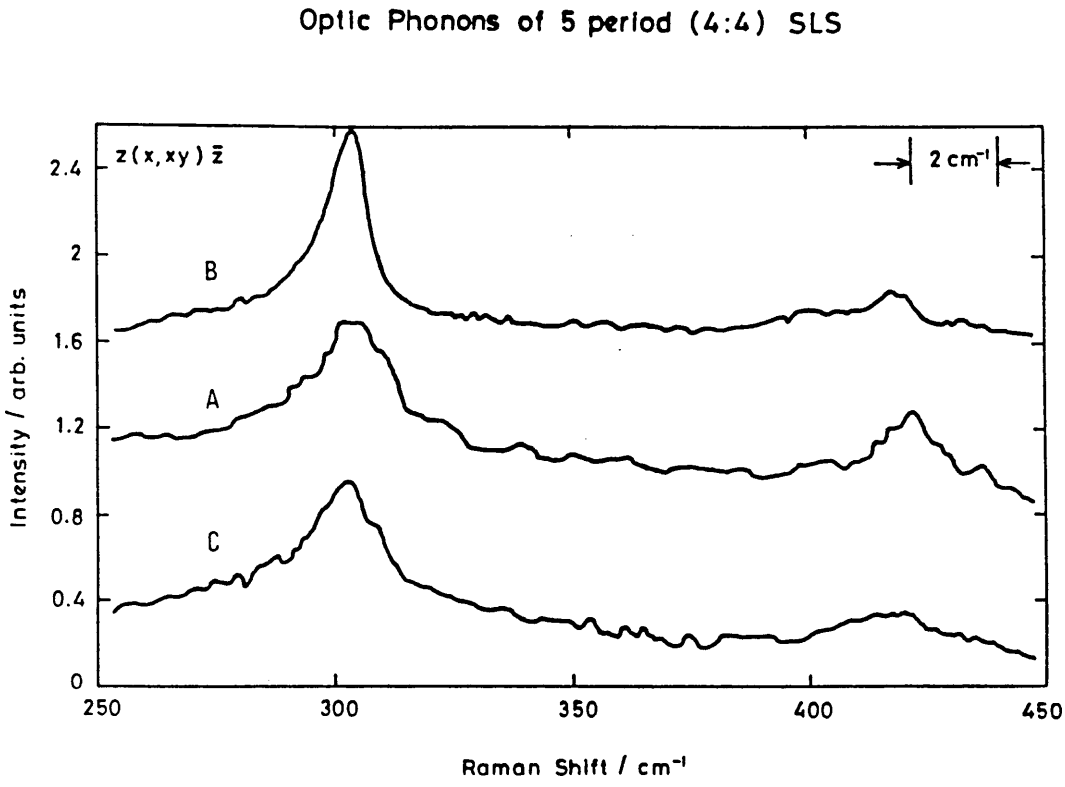


Figure 5.19 Room temperature Stokes Raman scattering spectra of Ge-Ge and Si-Ge optic phonons from samples S44C, S44A and S44B (bottom to top). Si/Ge (4: 4) short-period superlattices grown on Si(001).

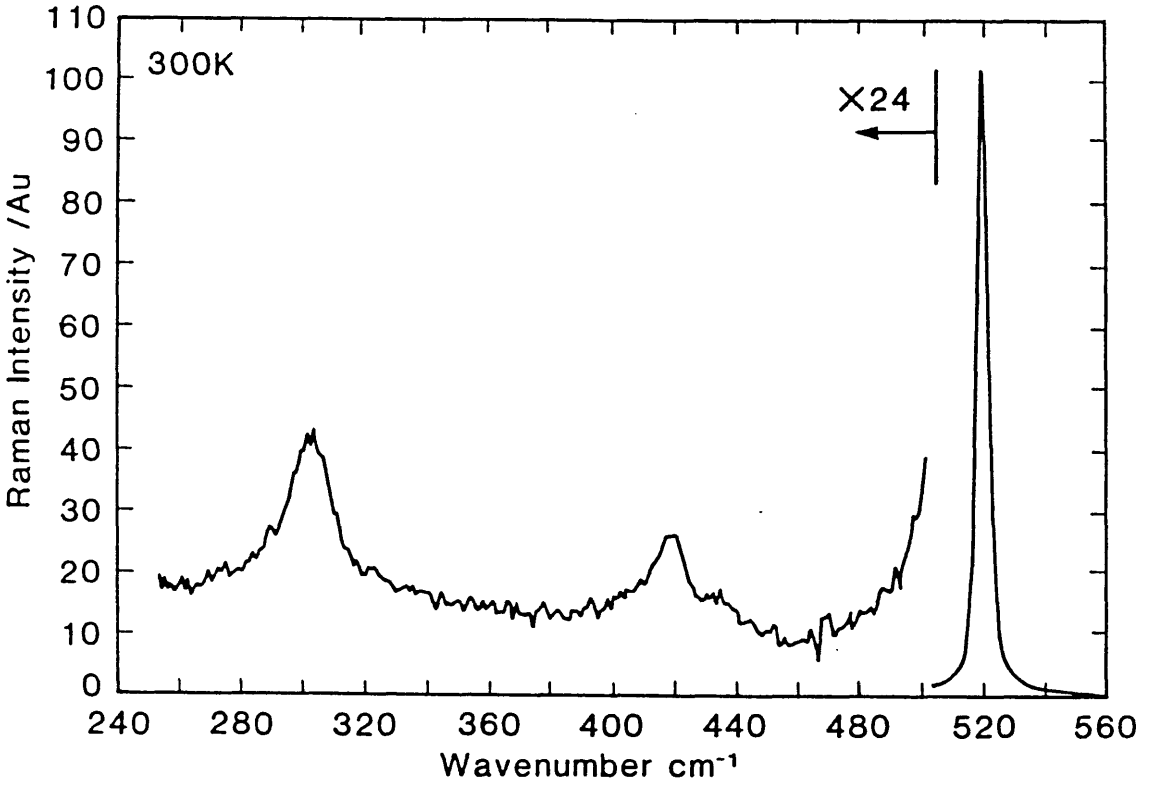


Figure 5.20 A room temperature Stokes Raman scattering spectrum of the optic phonon modes of sample S44E. A Si/Ge (4:4) short-period superlattice grown on Si(001). The signal from the lower Ge-Ge and Si-Ge modes has been scaled by 24.

are also significantly higher in energy (~7cm^{-1}) in the single 5 period superlattices than the multiple superlattice sample, it is not clear why this is, but could be due to a more alloy like mode than an interface mode. An interesting point to note is the dependence of Si-Ge/Ge-Ge mode intensity to Ge-Ge mode energy. Ge-Ge mode energies for samples S44M, S44B, S44E and S44A are 307, 305, 304, and 302cm^{-1} respectively. Whilst the Si-Ge/Ge-Ge intensity ratios are 0.3, 0.33, 0.65, and 0.75. Thus an inverse trend of Ge-Ge mode shift to relative Si-Ge mode intensity is observed.

5.2.2 Resonant effects on scattering cross-section.

The origin and effects of resonant Raman scattering are described, for example in Light Scattering in Solids II by M Cardona (1982). The essential difference between non-resonant and resonant scattering is that in resonant scattering the polarisation of the bond causing scattering includes large effects from the electron-phonon interaction. Obviously deformation of the crystal lattice by a phonon will locally perturb the electron states in the crystal and hence change the total energy of the crystal. However the scattering mechanism is visualised more easily if the electrons are viewed as virtual particles, then the phonon can directly scatter the electron. Virtual electrons and holes are created by the incoming light. The electrons are then scattered by phonons via the electron-phonon interaction and recombine with the holes to form the scattered light. Thus the scattering process depends on the electron-phonon interaction and the properties of the virtual particles present. The Raman efficiency can be written as (Sood et al. (1985b))

$$|\varepsilon_s.\mathbf{R}.\varepsilon_l| \propto \frac{\langle o|r_s|i\rangle\langle i|H_{el}|j\rangle\langle j|r_l|o\rangle}{(\omega_l - \omega_i)(\omega_s - \omega_j)} \qquad [5.8]$$

for laser (l) and scattered (s) light at energies ω, and having polarisations **r**. Hel represents the electron-phonon coupling within the superlattice.

The above paragraph contains a very brief description of resonant Raman scattering phenomena but it is sufficient to say that near critical points in the band structure very enhanced Raman scattering can occur

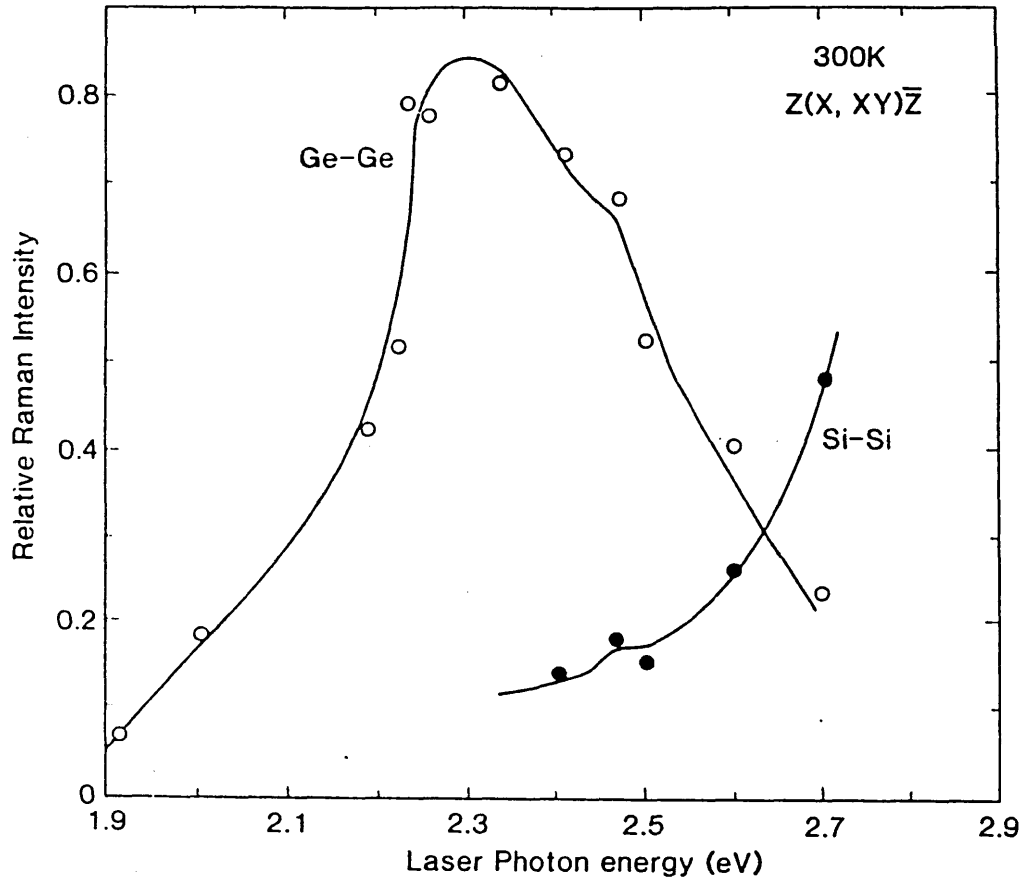


Figure 5.21 The strengths of the Ge-Ge and first confined Si-Si superlattice Raman scattering modes, relative to that of the Si-Si substrate/cladding mode , plotted against photon energy, for sample S44M.

because of the enhanced densities of states. Since the Raman scattering of Si/Ge superlattices contains a spatial element of either Ge-Ge or Si-Si bonds, resonant scattering can tell us not only where the superlattice critical points are but also with which bonds they are predominantly associated.

Cerdeira et al. (1985) used resonant Raman scattering when investigating $Si_{1-x}Ge_x$ alloy quantum wells similar to the ones described in section 1. They observed an increase in scattering from the Ge-Ge phonon mode which demonstrated confined optical transitions in the quantum well region of the sample.

Subsequently Cerdeira et al. (1989) have also studied Si/Ge short-period superlattices, grown symmetrically strained so that large numbers of periods could be investigated. For this kind of experiment it is necessary to measure the absorption depth of the light used for scattering, so that sample volume effects do not affect the Raman intensities measured. Although some resonant behaviour is observed in the short-period superlattices, it was not as strong as the effects in the quantum well samples observed earlier.

The sample investigated here, is S44M having a repeated superlattice structure which when compared with Cerdeira et al. (1989) not only increases the amount of scattered light, but allows scattering from the Si cladding layers to act as a reference line. Since the individual superlattice structures are only 50Å in thickness, the absorption due to any weak superlattice critical point is relatively small when compared to the surrounding Si cladding layers of 120Å.

Figure 5.21 shows the intensities of the first Si-Si confined mode (~507cm^{-1}) and Ge-Ge mode (~307cm^{-1}) relative to the Si cladding layer mode (520cm^{-1}). Although not indicated the Si-Ge mode intensity remained constant with respect to the Ge-Ge mode intensity. A variety of laser wavelengths were used; most of the points used discrete lines of a Ar ion laser however some were obtained using a tunable dye laser with Rhodamin R110 and DCM dyes. The maximum photon energy available was 2.71eV.

The Ge-Ge mode shows a strong resonance near 2.3eV, very close to critical points measured on similar (4:4) superlattices with electro-reflectance, descibed in the next chapter. This resonance corresponds well to theoretical predictions for critical points in Si/Ge (4:4) superlattices; Gell (1988) predicts transitions at

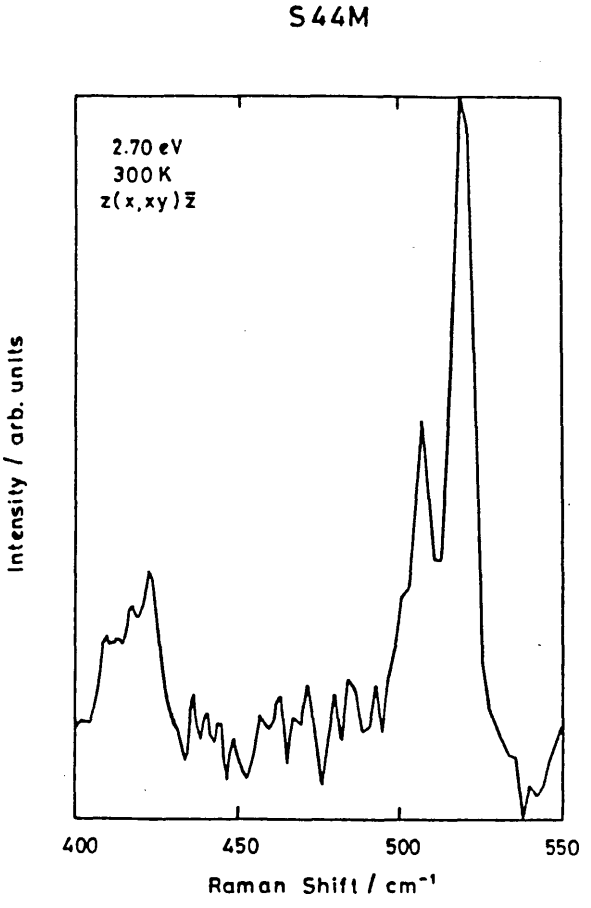


Figure 5.22 Room temperature Raman scattering spectrum of sample S44M with photon energies of 2.7 eV, showing a resonant enhancement of the Si-Si superlattice mode relative to the Si-Si substrate/ cladding mode.

around 2.3eV in the superlattices arising from states near X and X'. Such critical points dervie from the L related E_1 critical point in Ge and Si. The confined Si-Si mode increases in intensity as the scattering photon energy increases towards 2.8eV. Unfortunately the maximum energy of photons from the dye laser system is 2.7eV, so measurements to higher energies could not be carried out. Figure 5.22 shows a Raman spectrum in the vicinity of the Si-Si modes, with an incident photon energy of 2.70eV, the confined Si-Si superlattice mode is very distinct. The enhancement of the Si-Si superlattice mode also is in agreement with electro-reflectance measurements on (4:4) superlattices, which predict another critical point at 2.8eV. This state could correspond to the $\Gamma v1/v2$ to $\Gamma c5$ transitions predicted by Gell (1988). (However, Gell also predicts transitions from other X and X' related states at energies of about 2.8eV.) These results of resonant enhancement due to the superlattice should be compared to resonant scattering from alloys of similar compositions. Cerdeira et al. (1989) have carried out resonant Raman scattering of $Si_{0.4}Ge_{0.6}$ alloys at 100K and show that, in this case all the alloy modes from Ge-Ge, Si-Ge and Si-Si bonds have a maximum intensity near energies of the E_1 critical point, around 2.8eV. Thus the alloy shows different resonant beahviour to the superlattice.

The presence of resonant scattering enhancements in the superlattice sample of the Ge-Ge and Si-Si modes at different energies from the random alloy provide strong evidence for the existence of critical points within the superlattice.

The independent enhancement of the Ge-Ge and Si-Si modes locate the scattering associated from critical points in different parts of the superlattice. However, the corresponding electron charge densities predicted for these critical points are very delocalised, for example see Gell (1988), Froyen, Wood & Zunger (1988). Thus interpretation of resonant Raman based on simple overlap of wavefunctions, to locate the electron states, is rather limited. Symmetry considerations of the superlattice and the electron-phonon interaction must be used before a more complete interpretation is given.

When comparing this result with the results of Cerdeira et al. (1989), account of the strain within the superlattice unit cell must be taken. Cerdeira's sample is symmetrically strained, thus a downshift of about 0.1eV is expected (Gell (1988)) when compared with these results. That is a critical point at around 2.2-2.3eV. Although Cerdeira et al. do not see resonances in these regions for the (4:4) sample,

absorption measurements on the same sample also by Cerdeira et al. (1989) do perhaps suggest critical points at 2.3 and 2.7eV.

5.2.3 Effects of sample annealing.

Whilst the previous two sections have demonstrated structural integrity of the (4:4) superlattice samples, in this section Raman scattering is used to detect disruption of the superlattice by purposely annealing samples to temperatures well above growth temperatures and in some cases above the melting point of bulk Ge.

The sample investigated was S44M, chosen in preference to other (4:4) structures because of the increased Raman scattering due to its repeated structure. Individual samples of S44M were annealed for 3 hours at a specified temperature T_a, in a high vacuum (10^{-6} Torr), then analysed in back scattering geometry with 514.5nm laser light. The light is almost resonant with the predicted X/X' related critical points in the superlattice. The time taken for the furnace to heat up to T_a and cool down to room temperature was less than 30 mintutes.

Several groups have looked at the effects of annealing Si/Ge structures, using X-ray diffraction (Chang et al. (1989)), Raman spectroscopy (Basca et al. (1989)) both techniques (Lockwood, Baribeau and Timbrell (1989)) and photoemission spectroscopy (Hoeven, Aarts and Larsen (1989)). These studies however, do not involve the study of pseudomorphic superlattices with pure Si and Ge layers. Brugger et al. (1988) have looked at symmetrically strained Si/Ge (12:8) superlattices using Raman scattering as a function of annealing. The results presented here however, are complementary to Brugger's since the (4:4) superlattice described here is grown on Si (001) substrates and has all the strain within the Ge layers. Thus two distinct phases are observed (i) relaxation of the strain in the Ge layers below a threshold temperature and (ii) interdiffusion during higher temperature annealing, as opposed to only diffusion in Brugger's case.

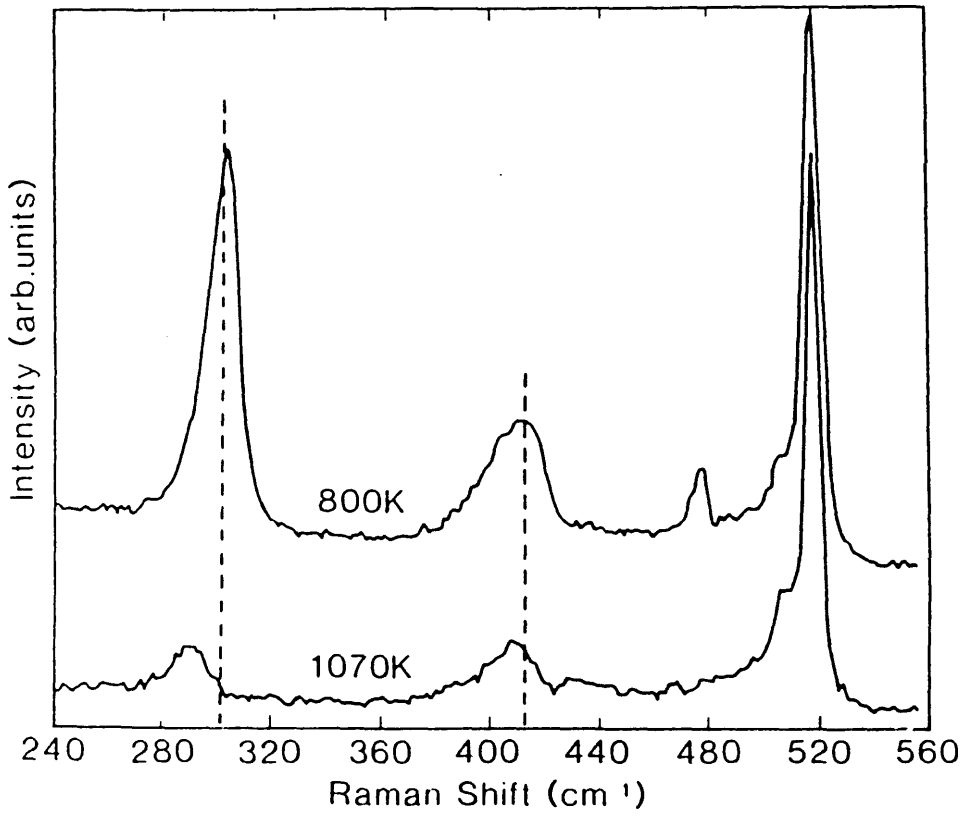


Figure 5.23 Room temperature Raman spectra of two samples of S44M a repeated strained Si/Ge (4:4) short-period superlattice which have been annealed at the temperatures (in Kelvin) indicated.

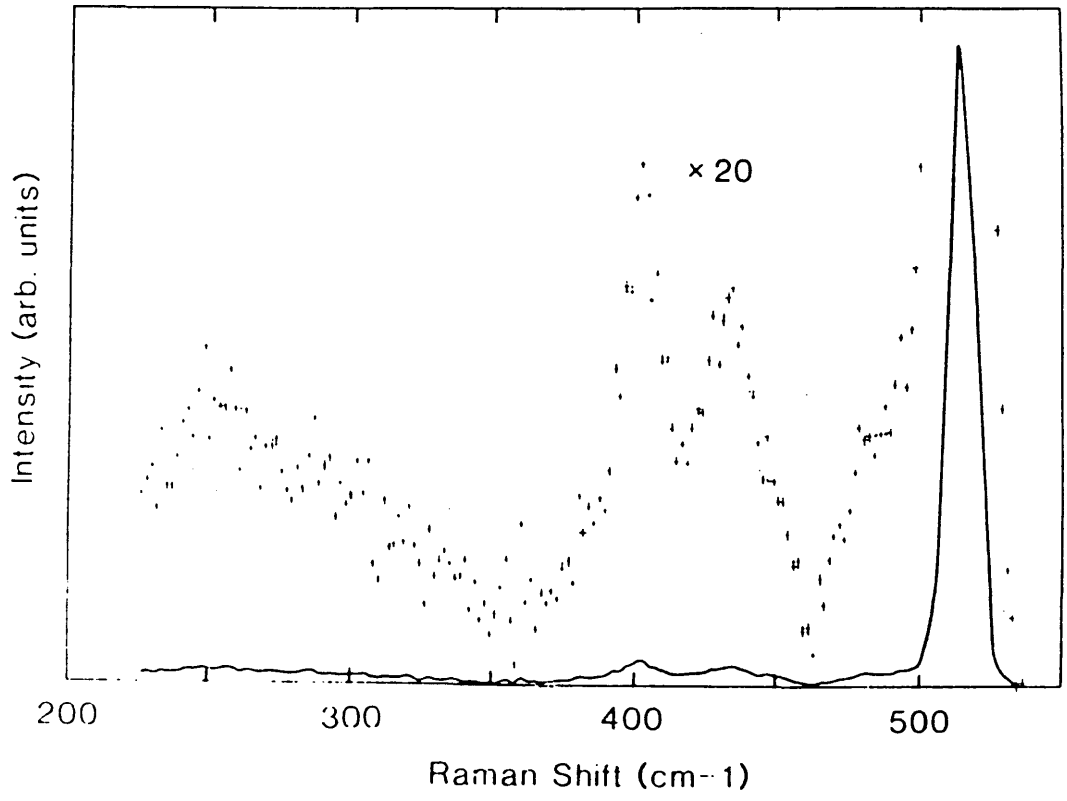


Figure 5.24 Room temperature Raman spectrum of sample S44M, which has been annealed at 1270K.

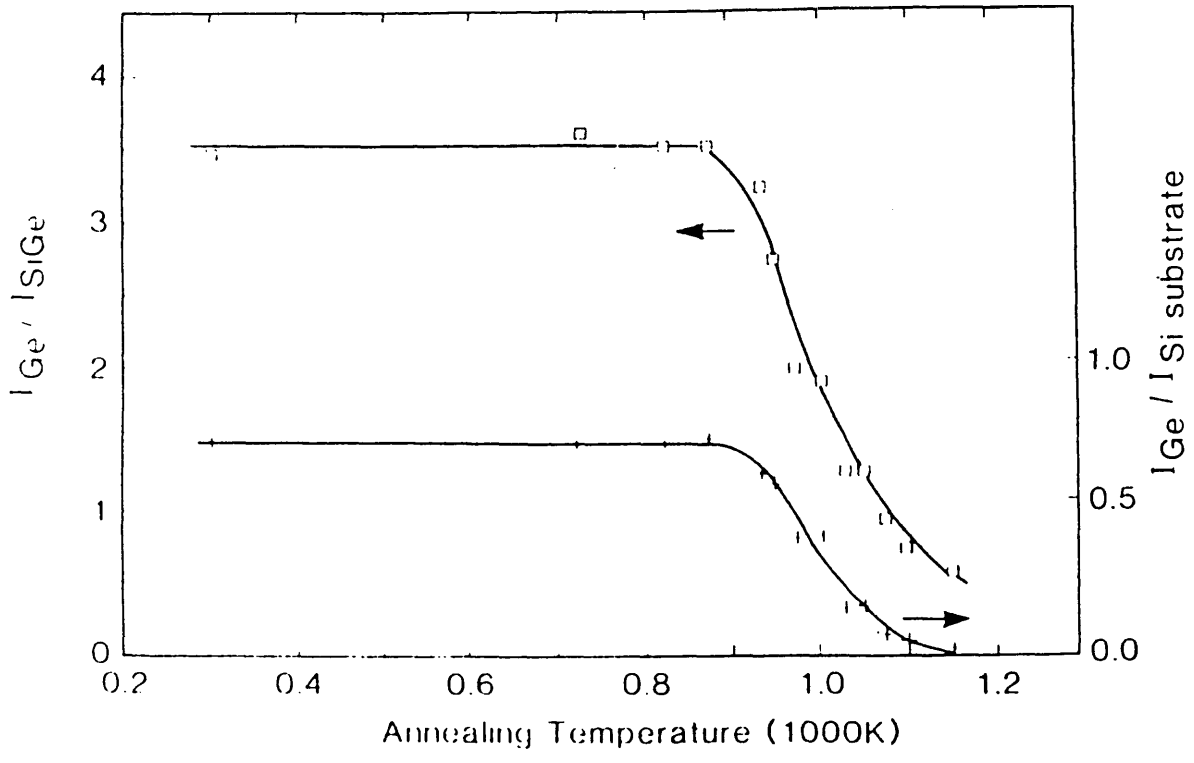


Figure 5.25 Ratio of heights of the Raman peaks for the superlattice Ge-Ge and Si-Ge modes, I_{Ge}/I_{SiGe}, and for the superlattice Ge-Ge mode and the Si-Si mode from the cladding/substrate, I_{Ge}/I_{Si} substrate, as a function of annealing temperature.

Figure 5.23 shows typical Raman spectra for two superlattice samples which have undergone an annealing treatment at 800K, (which is only slightly above the growth temperature) and 1070K. The second confined phonon is very distinct for the sample annealed at 800K. The modes from the sample which has been annealed at a higher temperature are significantly downshifted in energy and intensity. Figure 5.24 shows a spectrum of a sample annealed at 1270K, a temperature above the melting point of pure germanium. Comparing this spectrum with Brya (1973), an alloy of $Si_{0.9}Ge_{0.1}$ is inferred. The ratio of Ge-Ge mode to Si substrate mode and Si-Ge mode to Ge-Ge mode intensities are plotted as a function of annealing temperature and shown in figure 5.25. The Si substrate mode intensity is taken to be independent of annealing temperature. The ratio of peak height of the two superlattice modes remains constant at 3.5 until 900K, when it decreases very rapidly to a value just below unity. The relative strength of the Ge-Ge mode to that of the substrate also remains constant to about 900K but decreases by more than a factor of ten for higher temperatures.

The superlattice mode energies are shown in figure 5.26, and should be compared to Brya's results shown in figure 5.6 with consideration of shifts due to strain. Concentrating on the Ge-Ge superlattice mode, it can be seen that there is a gradual shift down in energy as a function of annealing temperature until 900K when it has a value close to the bulk Ge-Ge mode energy. For temperatures above 900K the decrease is much faster, the mode becoming indistinct at the highest annealing temperatures. The Si-Ge mode decreases monotonically in energy as a function of annealing temperature, unlike the results of Brugger et al. (1988), indicating that the effects caused by annealing are possibly slightly different.

The ratio of Ge-Ge to Si-Ge mode peak heights is used as a qualitative measure of disorder. In the limit of large disorder this ratio will tend to the ratio of the number of Ge-Ge to Si-Ge bonds. The fact that this ratio remains constant up to an annealing temperature of 900K implies that the superlattice remains ordered up to this temperature. This ratio becomes close to unity at a temperature of 1100K but decreases still further until it is almost zero at 1270K. An explanation of this behaviour could be that at 1100K the superlattice has become a $Si_{0.5}Ge_{0.5}$ alloy. However, above 1100K the Si cladding layers act as a reservoir of atoms diffusing in to the 5 period superlattice diluting the concentration of Ge atoms further than just the interdiffusion of atoms within the superlattice period. The reduction of Ge-Ge mode intensity with respect to the Si substrate mode, also indicates loss of superlattice structure, destroying the

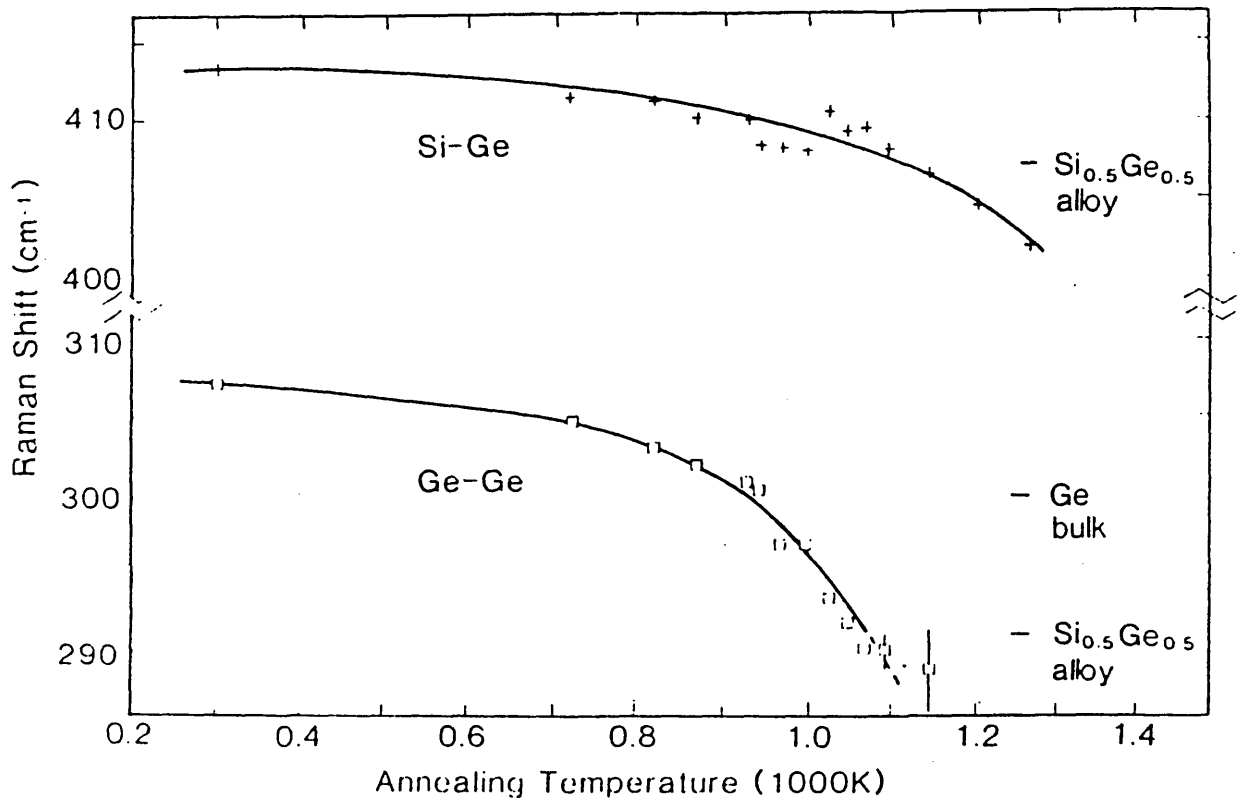


Figure 5.26 Energies of the Ge-Ge and Si-Ge superlattice modes as a function of annealing temperature. The Si-Ge and Ge-Ge mode energies are marked for a relaxed $Si_{0.5}Ge_{0.5}$ alloy, as is the Ge-Ge mode energy for bulk germanium.

critical point on which the scattering is resonant. Whilst critical points in the alloy semiconductors do exist in this vicinity, their strengths are much weaker (Kline et al. (1968)).

The shift in energy of the Ge-Ge mode between 700K and 900K, down to the bulk Ge value could be an indication that the strain in the superlattice is relaxed. Above 900K the intensity and energy changes suggest the regime of interdiffusion. This threshold temperature of 900K is comparable to that observed by Lockwood, Baribeau and Timbrell (1989), although a quantitative comparison is difficult due to the shorter annealing times in their case. The results of Hoeven et al. (1989) are anomalously low but as they point out, can be explained by a more efficient diffusion in the amorphous silicon layers in their samples.

From results on experiments with symmetrically strained Si/Ge (6:4) superlattices, Brugger et al. (1989) propose that diffusion occurs of silicon atoms into the germanium layers, thus giving Ge rich alloy and pure Si regions; their samples have a much thicker superlattice than the sample measured here. The shift in Ge-Ge superlattice mode with annealing temperature in this case, is consistent with the proposal of Brugger et al. (1989). The Si-Si confined mode in the superlattice below the Si substrate mode remains as a shoulder to high annealing temperatures (see figure 5.23), suggesting the Si layers remain intact, evidence which also supports diffusion from the silicon layers to the germanium layers, thus allowing confined modes to exist in the silicon layers. The disappearance of this mode at 1150K is reasonably consistent with the attainment of a $Si_{0.5}Ge_{0.5}$ alloy. The relative weakness of features associated with small diffusions make it difficult to make quantitative claims on atomic kinetics.

(The work presented in this section will appear as a publication: Churchill et al. (1990a).)

5.2.4 Concluding Remarks on the Structural Properties of Si/Ge Superlattices.

Short-period Si/Ge (4:4) superlattices have been analysed using Raman scattering from optic phonons. From the superlattice mode energies and relative intensities, strain and layer ordering can be inferred. Even though there is relatively little superlattice (50Å) compared to the laser probing depth (of about

6000Å), superlattice modes can be seen in single 5 period superlattices. This is mainly because the photon energy of light used is nearly resonant with a critical point in the superlattice. Investigation of resonant scattering has been carried out using the Si substrate mode as a reference intensity. One critical point has been observed at 2.3eV, and another tentatively suggested at about 2.8eV.

The effects of destroying the superlattice layer ordering by annealing samples at temperatures above the growth temperature have been observed. Results are consistent with those of other workers with complementary samples. A temperature of 900K is suggested as a threshold at which the structural properties of the short-period superlattices start to be severely disrupted.

Chapter 6 Optical analysis.

6 Optical Analysis.

The electronic properties of Si/Ge structures were investigated optically. The chosen technique was electro-modulation spectroscopy, a technique used by Pearsall et al. (1985) when looking at other Si/Ge samples. Another optical technique which is popular when looking at electronic transitions in semiconductors is photoluminescence. Abstreiter and co-workers (1989) use photoluminescence to analyse Si/Ge (6:4) superlattices containing large numbers of periods. This technique measures the lowest energy transitions in the band structure and may or may not detect impurities and defects in the samples.

Photoluminescence cannot be used with the samples investigated in the present work. The structures investigated have conduction- and valence-band alignments which are type II with respect to the substrate, Gell (1989). The lowest conduction band valley in the quantum well or superlattice lies above the Si substrate conduction band. Any photo-excited carriers produced in photoexcitation will diffuse to the substrate before recombining. Thus photoluminescence will only give at most information about the substrate band edges and not the superlattice or quantum well. The technique used to study these samples must therefore be an excitation one which overcomes the effects of carriers diffusing to parts of the sample which are not of interest.

Methods for electro-reflectance and electro-transmission spectroscopies were descibed in section 2.2 and chapter 3. These spectroscopies rely on changing the optical response function, (the dielectric constant), by a perturbing electric field. The dielectric function is a bulk property and no documented evidence exists to show it is affected significantly by small numbers of dislocations (typically less than $10^{-9}cm^{-2}$). Thus electro-modulation spectroscopy avoids the possibility of observing effects which could be dominated by defects and impurities in the sample; for example features in photoluminescence spectra seen by Zachai et al. (1990) and Montie et al. (1989a) could be ascribed to defects and impurities decorating dislocations found in Si/Ge strained samples (Weber and Alonso (1989)).

Modulation spectroscopy also has the advantage of being differential in nature, allowing only critical points in the band structure to be detected. With normal reflectivity or absorption, critical points are masked by other transitions between bands of lower energy than the one of interest.

The first section of this chapter investigates electronic states formed by confining electrons and holes within $Si_{1-x}Ge_x$/Si quantum well structures, (outlined in section 2.2.3). The next sections consider a Si/Ge superlattice systems. Firstly the Si/Ge (4:4) superlattice is reported on, this structure has beem widely investigated theoretically and experimentally and is discussed in the review section 2.2.4 and 2.2.8 and in chapter 4. The last section is devoted to investigations of Si/Ge (2:n) superlattices, which are predicted to have a direct band gap. Also considered is a Si/Ge (6:4) superlattice structure which has been investigated by Abstreiter and co-workers (1989).

6.1 Multiple quantum well samples.

In this section electro-reflectance spectroscopy is used to investigate electronic states confined in alloy regions of the quantum well samples QWA,QWB,QWC and QWD. The sample dimensions have been given in chapter 5, along with Raman scattering data which demonstrated sample integrity.

Studies of $Si_{1-x}Ge_x$/Si quantum well structures have been carried out by Pearsall et al. (1986), and Si/Ge quantum wells by Dafesh et al. (1990), using electro-relectance and photo-reflectance spectroscopies. (Photoreflectance spectroscopy is similar to electro-reflectance spectroscopy, see for example Cardona (1969).) The spectra presented all show two characteristics, optical transitions from within the substrate and cladding layers, and optical transitions from the quantum well regions. In these studies, calculations similar to the ones outlined in section 2.3 were used to label spectroscopic features with specific optical transitions within the quantum well band structure. However in contrast to studies on GaAs/GaAlAs quantum wells (Shields et al. (1989)), no effort was made in fitting the spectra with predicted transitions and considerations of the modulation mechanisms of observed spectral line shapes were ignored. This

shortfall, is in part due to the significant number of unknown parameters in the $Si_{1-x}Ge_x/Si$ quantum well system.

For example, considering the sample QWA, a 40Å wide well of $Si_{0.5}Ge_{0.5}$, holes will be confined in the Γ'_{25} band due to the valence band offsets. Using figure 2.13 confinement energies can be determined for the holes. Electrons will be confined in the Γ_7 band, again using figure 2.13 energies can be found. The E_0 transition energy is finally determined by considering the uniaxailly strained band gaps shown in figure 2.12. The resultant transition energies, including E_0 bandgap and confinement energies are summarised in table 2.4. However the analysis in chapter 2 left out the transitions between other bands. Looking at the figure from Kline et al. (1968) reproduced in figure 2.8, it can be seen that the E_1 transition of the alloy well regions will be in the same energy region as the confined E_0 transitions. Unfortunately no confinement effects are calculated for the E_1 transition because effective mass parameters for E_1 transition are difficult to find. The mass is certainly large as the conduction and valence bands run nearly parallel from Γ to L. Thus confinement effects are likely to be small. In addition to the mass parameters for confinement effects, deformation potentials and band offsets are needed for a complete calculation of the quantum well E_1 transitions. Pearsall et al. (1986) calculate transition energies for both E_0 and E_1 transitions; the effective masses are given and band deformations calculated, however it is unclear what band discontinuities were used for the calculations of confinement energies of the E_1 transitions. In the absence of these parameters the best estimate for the confined E_1 states in quantum wells are the bulk values for the transition given by Kline et al. (1968). Care must be taken when assigning transitions to spectral features of $Si_{1-x}Ge_x/Si$ quantum wells, to take into account the E_1 transitions which may lie ontop of the E_0 transitions.

Figure 6.1 shows an example of an electro-reflectance spectrum taken at 90K of a $Si_{1-x}Ge_x/Si$ quantum well sample. In this case sample QWD, the composition is x=0.6 and the well and barrier widths 2.1nm and 12.0nm from table 5.1. The calculated E0 transitions for Γ_2 - heavy hole and Γ'_2 - light hole are 2.80 eV and 2.95 eV respectively. The spectrum contains two features at around 3.4 eV and 2.8 eV. The one at higher energies can be assigned to E_1 and E'_0 transitions in the Si cladding layers and substrate, the lowest direct transitions of silicon. Figure 6.2 shows an electro-reflectance spectrum of a sample with no alloy wells, containing just epitaxial silicon. The line shape of this feature is different from that of the

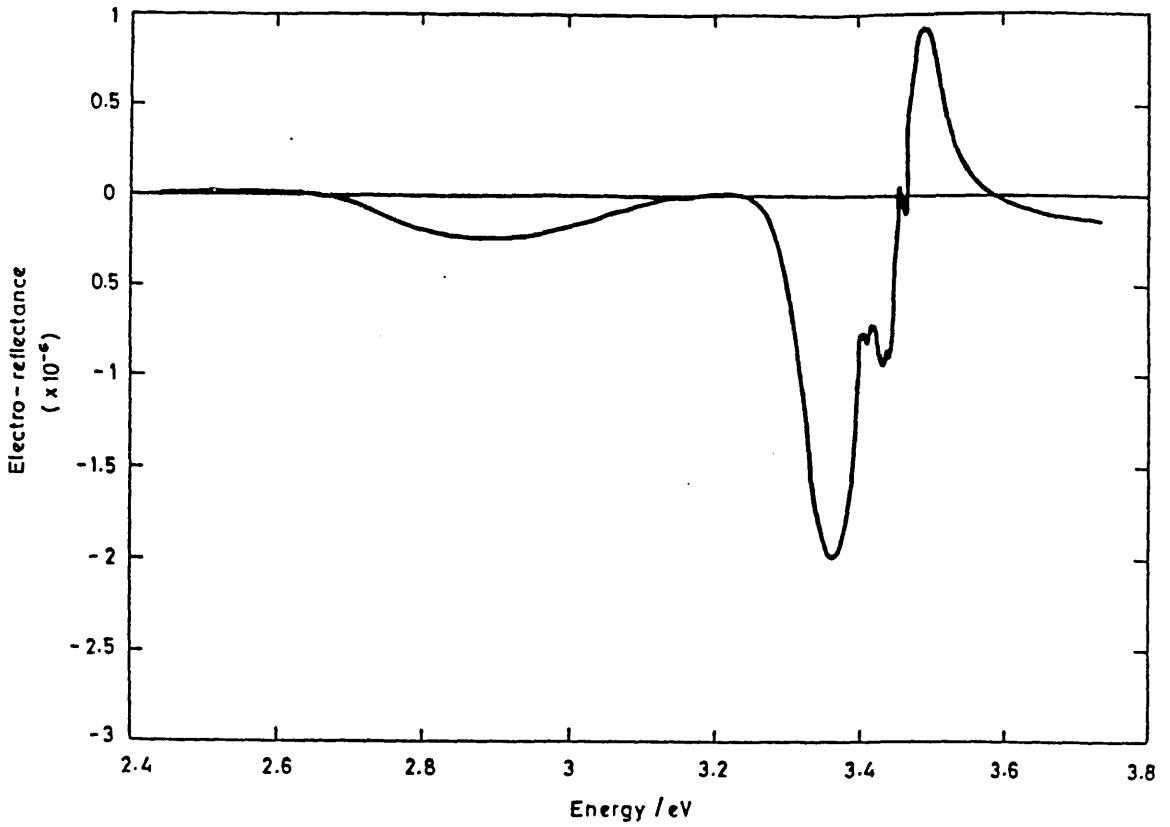


Figure 6.1 Electro-reflectance spectrum of quantum well sample QWD at liquid nitrogen temperatures, showing the E_1/E'_0 transition from the Si cladding layers and a quantum well feature at about 2.7eV.

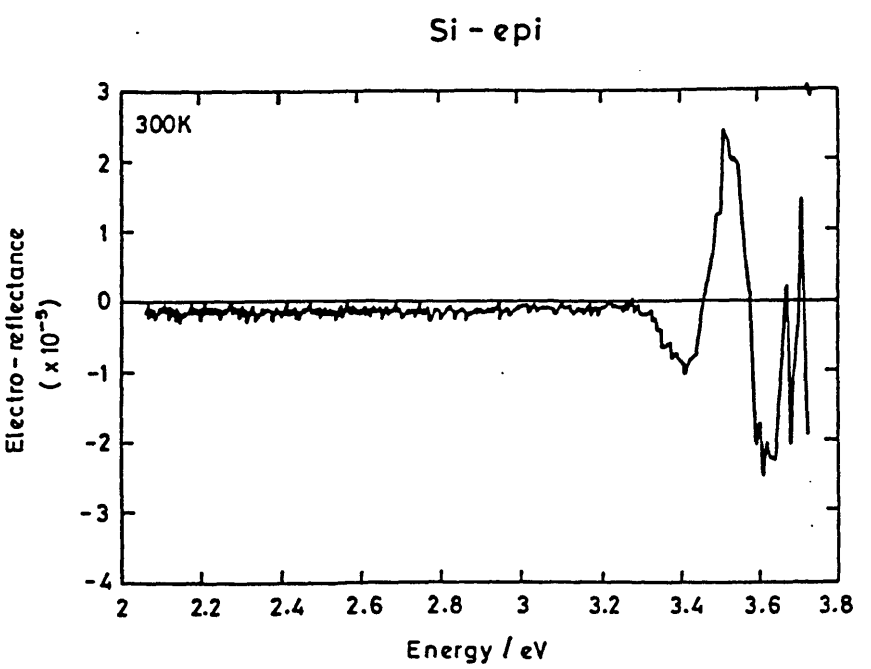


Figure 6.2 Electro-reflectance spectrum of sample Si-EPI, consisting of 0.6μm Si grown on n-type Si(001). (room temperature)

bulk sample shown in figure 3.3 but this can be explained by the different electric field uniformities and strengths in the two samples (Aspnes and Frova (1969)). The important feature of figure 6.1 compared to the control sample figure 6.2 is the new line shape below the Si direct transition, which can only arise from the alloy quantum well transitions. While no specific transitions can be assigned, the calculated E_0 transitions from light and heavy hole valence bands to Γ_2 conduction bands and E_1 and $E_1+\Delta_1$ alloy transitions lie in the middle of this peak (Kline et al. (1968)). The fact that the spectrum shows one broad feature but theories predict atleast four transitions makes the use of experimental data to check parameters used in the calculation of the confined electronic states impossible.

Quantum Well samples QWA, QWB and QWC

Samples QWA to QWC, have a common feature, namely that of the alloy concentration in the well regions. Raman scattering of the optic phonons confirmed that all the samples contain Si0.5Ge0.5 alloy layers which are strained to the Si in-plane lattice constant. However the thickness of the alloy well regions are different: QWA having 40Å, QWB having 20Å and QWC having 10Å thickness. The Si barrier regions are also scaled but are 6 times the well thicknesses. Both the Raman results of Chapter 5 and X-ray diffraction have confirmed these dimensions. The total epitaxial layer is undoped and has a thicknes nominally of about 0.5μm. The substrate is an n^+ type doped Si (001).

Thus the difference in electronic state energies in the well regions for different samples will be determined by the confinement effects due to the layer dimensions and not by properties of the alloy concentration and strain. The predicted E_0 transitions in the wells have been summarised in table 2.4 but are again given in table 6.1 with the sample dimensions. Also shown in table 6.1 are the energies for $Si_{0.5}Ge_{0.5}$ E_1 and $E_1+\Delta_1$ critical points.

The samples were prepared for electro-reflectance spectroscopy with the method described in section 3.3. The incident and reflected light had an angle of 45° to the normal of the sample surface and the light was unpolarised. Figures 6.3, 6.4 and 6.5 show electro-reflectance spectra for the three samples. Figure 6.6 shows the electrical doping level against depletion depth for sample QWA, made with a capacitance-voltage (CV) profiler. The measurement was checked to be frequency independent. The plot shows a

Table 6.1 Predicted optical transitions in samples QWA QWB and QWC

	QWA	QWB	QWC
$Si_{0.5}Ge_{0.5}$ Well thickness (Å)	40	20	10
Si Barrier thickness (Å)	240	120	60
Number of wells	15	30	60
hh-Γ'_2 (eV)	2.79	3.01	3.34
lh-Γ'_2 (eV)	2.8	3.14	3.37
so-Γ'_2 (eV)	3.11	3.33	3.86
E_1 (eV)	2.70	2.7	2.70
$E_1+\Delta_1$ (eV)	2.85	2.85	2.85

Table 6.1 gives the sample dimensions for a set of $Si_{0.5}Ge_{0.5}$/Si quantum wells, also listed are the expected energies of the confined E_0(lh, hh and so), E_1 and $E_1+\Delta_1$ transitions within the alloy well regions.

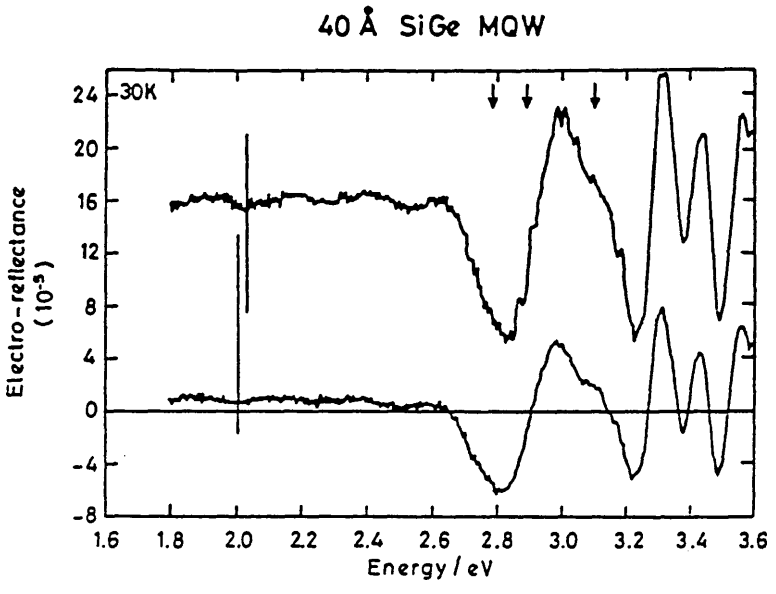


Figure 6.3 Electro-reflectance spectrum of quantum well sample QWA at 30K. The upper trace is taken with an incident light angle of 68°, the lower with an angle of 11°.

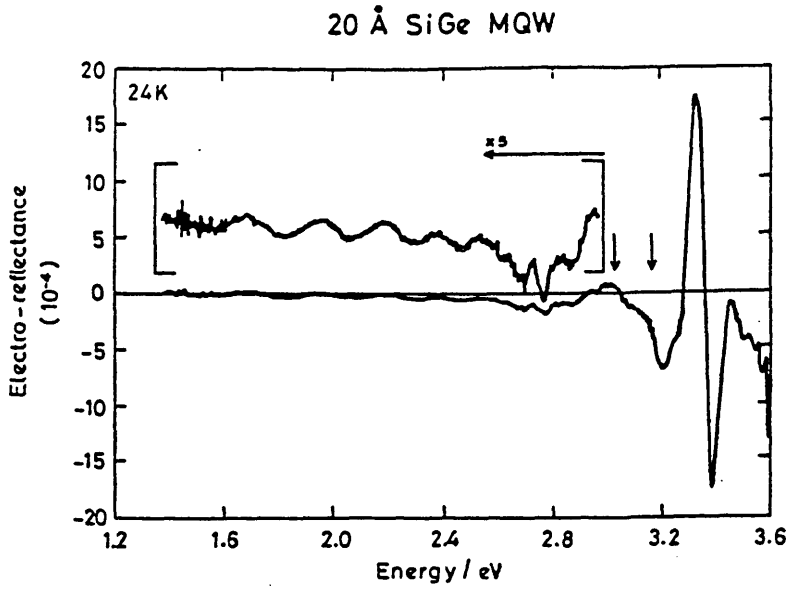


Figure 6.4 Electro-reflectance spectrum of sample QWB at ~25K, with an incident light angle of 45°.

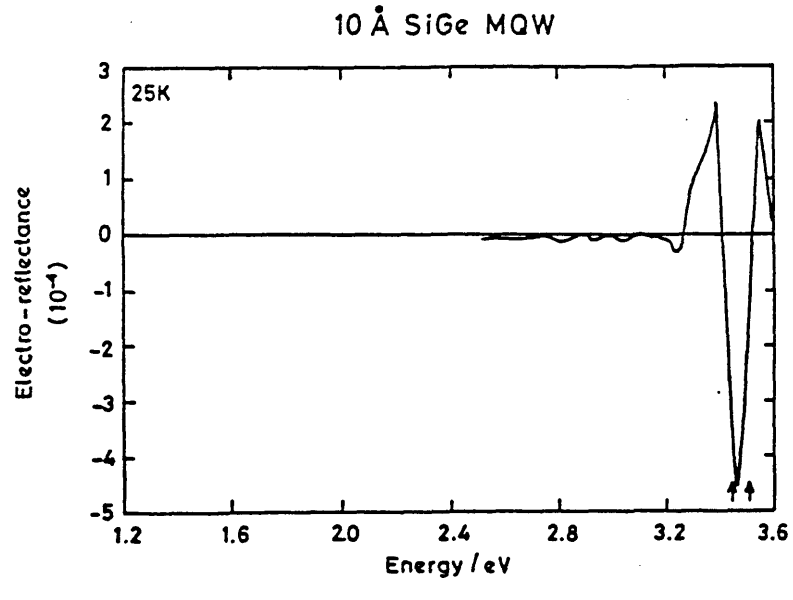


Figure 6.5 Electro-reflecatnce spectrum of sample QWC at 25K, with an incident light angle of 45°.

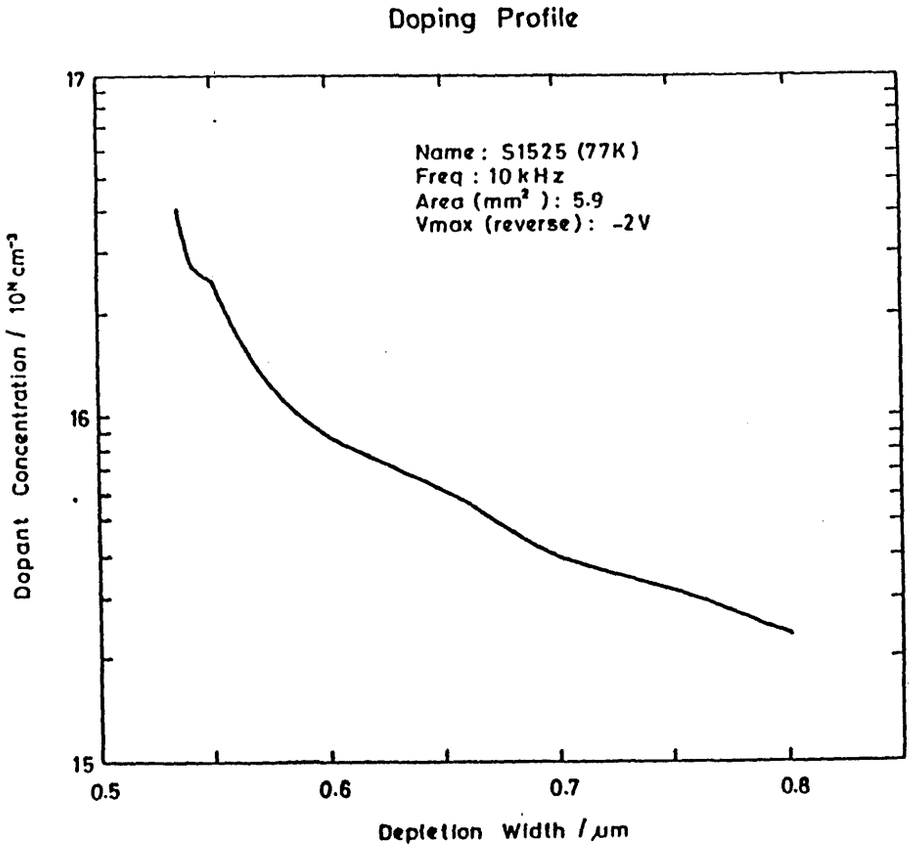


Figure 6.6 A typical doping profile of the quantum well samples investigated (sample QWA) taken at 77K using a CV-procedure on the Ni Schottky diode. (The experimental procedure of R Kumar was used, Imperial College)

depletion depth for the Schottky barrier between 0.5μm and 0.8μm depending on reverse bias voltage. This measurement was typical of all the samples measured. For the electro-reflectance measurements an applied voltage across the reversed biased Schottky barrier had an average value of 1.2V and a peak to peak value of 2.4V. The estimated peak electric field (at 2.4V reverse bias), using the doping profile of figure 6.6, was about 125KV/cm. The electric field extends through the entire epitaxial layer, although the doping profile leads one to believe it is not uniform.

There are several points to note about these spectra. Firstly, all the spectra show a large feature at 3.4eV and above, this can be ascribed to the E_1/E'_0 critical points originating from the Si substrate. Although this feature has a slightly different line shape between sample QWC and the other two, explanation can probably be given by field uniformity (Aspnes and Frova (1969)) and overlayer effects as described in Shields et al. (1989). The second point to note are the additional features below the Si E_1/E'_0 critical points. These features can be assigned to quantum well transitions. Unfortunately the width and unknown line shape of these transitions makes it impossible to assign energies to them. Indicated on the figures, where the energies lie in th figure range, are the calculated E_0 quantum well transitions for light- heavy- and split-off-hole bands, again the presence of additional E_1 states with in the quantum well should be considered aswell.

Electric field modulation of the electronic band structure in quantum wells has been well documented for example by Miller et al. (1984). However use of the quantum confined Stark effect and Lorentzian line shapes for fitting the observed transitions would be futile because of the number of unknown variables.

Another important feature, only observed in samples QWA and QWB, is the oscillatory signal below the quantum well transitions. The period bears no relation to the different quantum well dimensions. Further tests to elucidate the origin of the oscillations have been carried out and are summarised below.

The oscillations observed in a given sample do not change as a function of incident light polarisation. Whilst the intensity of the oscillations changes as a function of peak modulation voltage, the period and phase remain constant. The phase of the oscillation changes, moving the peaks upwards in energy as the incident light angle is increased away from the normal of the sample front. This feature is illustrated on

the spectrum in figure 6.3, the lower trace has an incident light angle of 11°, the upper trace an angle of 68°, the oscillations on the upper trace have moved up very slightly in energy. The line shape of the quantum well and substrate transitions remains unchanged.

Oscillations in electro-reflectance spectra have been reported for bulk semiconductors (Cardona (1969)), however the explanation normally given is that of the Franz-Keldysh effect (section 2.2.7), which has a period dependent on electric field. In this case such an explanation cannot be used. Evidence of incident light angle dependence of the oscillations leads to the conclusion that the oscillatory signal is due to some form of interference effect. Indeed this kind of effect could easily arise in a low finesse Fabry-Perot etalon formed by two low reflectivity mirrors and a dielectric cavity and has been observed elsewhere (Thorn et al. (1989), Pearsall et al. (1989) and Schmid et al. (1990)). If the dielectric is modulated by an electric field then the effective etalon thickness will be changed, leading to periodic changes in the reflectivity of the etalon system. Thorn et al. (1989) have shown that a small reflection (~10^{-4}) at the back of an epitaxial layer, allows the electro-reflectance spectrum to take the character of the electro-absportion spectrum. Figure 6.7 depicts a schematic of the proposed etalon model that could account for oscillations in the electro-reflectance spectra of the quantum well samples. The period of the interference fringes will be a function of the Fabry-Perot etalon thickness, for non-dispersive dielectric cavities this can be obtained from geometric considerations giving the relation [6.1]: (Derived from Pearsall (1989), note there is an error in Eqn (2) of this paper.)

$$\delta_{cavity} = \frac{1.24}{2n\Delta E} \qquad [6.1]$$

where ΔE is the period of the oscillations in electron Volts and n the dielectric refractive index, and δcavity the etalon thickness in microns. For these particular samples the refractive index must be estimated as an average over the energy range of the oscillations. The energies at which the oscillations are observed are near the critical points of the quantum wells and Si cladding layers and the cavity becomes dispersive making a good estimate difficult (Aspnes (1988)). For photon energies below any critical points in the well and cladding regions, the values of refractive index from the dielectric constants of Si (11.9) and Ge (16) can be used. These figures are taken from Sze (1985). An average refractive

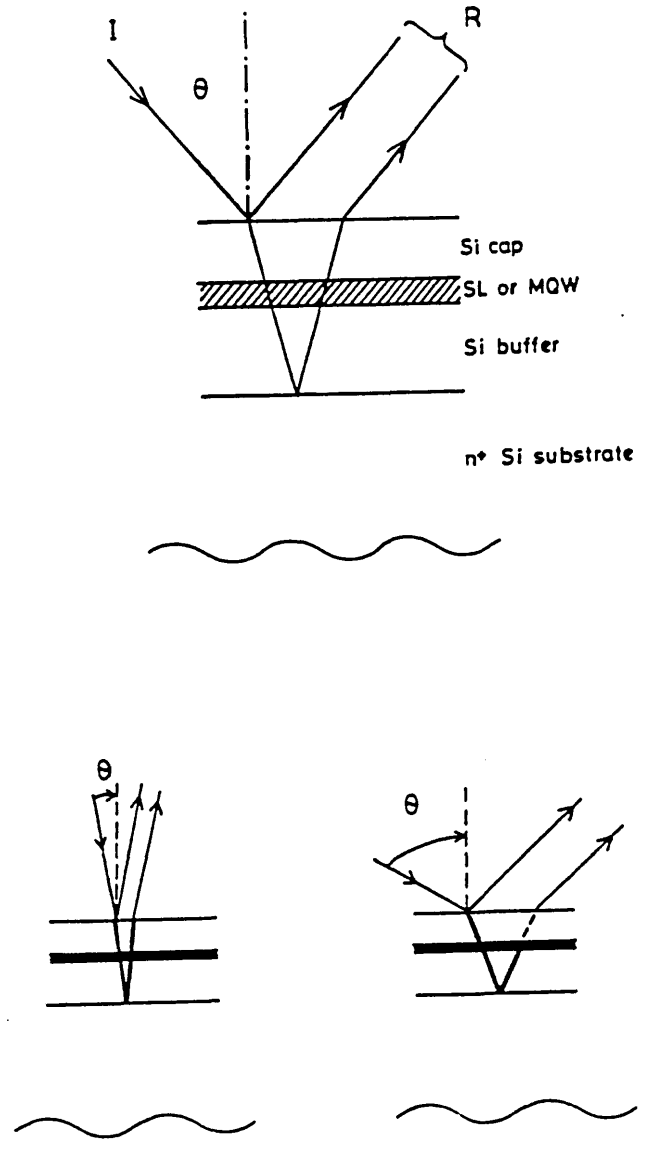


Figure 6.7 Upper: A schematic of a Fabry-Perot Etalon observed in the epitaxial samples, formed from reflection from the front sample surface and the epitaxial/substrate interface. Lower: The effects on the optical path of reflected rays as the incident angle is changed.

index for the quantum well layers can be found, an estimate of the cavity thickness is then made made and is found to be about 0.6μm. Whilst the total thickness of the multiple quantum well region is 420nm, the samples also contain a buffer of Si. The Si buffer is estimated to be about 100nm in thickness by the grower. So to within 20% the etalon would seem to be the whole epitaxial layer (the entire depletion depth). However it is unclear why a reflection can occur at a Si buffer-Si substrate interface, perhaps some surface contamination is present.

The observation of Fabry-Perot cavity effects in electro-reflectance spectra require that the cavity can have its refractive index modulated by the electric field. The origin of this modulation could be due to a perturbation of the electronic states in the quantum well region. The spectrum of the Si epitaxial layer control sample, figure 6.2 compared to the spectra of the quantum wells supports this argument: the spectrum of Si epitaxial material grown on a Si substrate (figure 6.2) show no sign of interference effects, however the quantum well samples do. A test sample, without any quantum wells but with a $Si_{1-x}Ge_x$ alloy, was measured to confirm this idea. Figure 6.8 shows an electro-reflectance spectrum of sample ALY25, 0.6μm of $Si_{0.75}Ge_{0.25}$ alloy grown on a Si buffer on a Si (001) substrate. The weak germanium content in the alloy allows light to penetrate to the epitaxial/substrate interface. A similar experimental set-up for the tests with quantum well samples was used. This spectrum contains a spectral feature at 3.1eV, which is the E_1 transition for a 25% alloy, mixed with the Si E_1/E'_0 substrated transitions, however importantly this sample also shows weak oscillations between 2 and 2.5eV, below the direct transitions within the alloy. The period is calculated to arise from an etalon of 0.83μm and corresponds well to the entire epitaxial layer thickness, which is estimated to be about 0.8μm when a Si buffer of 0.2μm is included. Thus the presence of interference oscillations is not necessarily connected with the states within the quantum well. The evidence so far described, suggests that the interference effect observed in electro-reflectance spectra is connected to the alloy layers within the samples, since the sample without any alloy showed no oscillations in its electro-reflectacne spectrum but the alloy samples do. However, observation of the interference effect requires reflections from the front and back surfaces of the epitaxial layer, at present the origins of the back reflector are not understood, so a definitive conclusion as to the origin of the interference effect cannot be made.

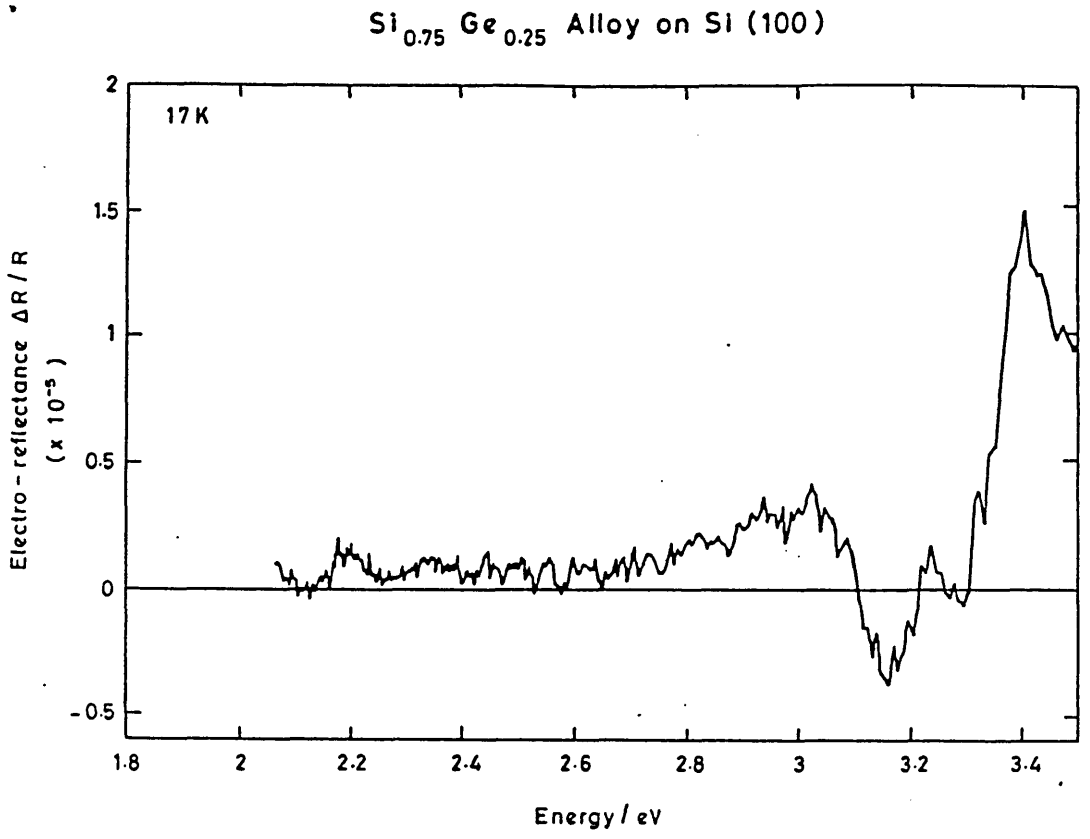


Figure 6.8 Electro-reflectance spectrum of ALY25 an epitaxial $Si_{0.75}Ge_{0.25}$ relaxed alloy on Si(001) taken at 17K, 45° incident light angle. The E_1 critical point from the Si buffer mixed with the E_1 critical point of the alloy layer is observed at 3.2-3.5eV, oscillations are observed below 2.4eV.

Similar interference effects have been observed in GaAs doping superlattices by Thorn at al (1989), however the cavity forming the etalon in this case was from the front and back surfaces of the semiconductor-air interfaces. For these samples the mechanisms for modulating the optical cavity could be ascribed to two phenomena, firstly the Franz-Keldysh effect for the GaAs band edge critical points, as described in section 2.2.7 and secondly the linear electro-optic effect (Yariv (1985)) both induced by the high fields in the doping superlattice. Whilst the applied electric field in the Si samples is large, the results presented here show that the interference effect extends to energies far below any transitions. Thus indicating that the Franz-Keldysh or Quantum Confined Stark Shift effects are not the mechanism behind the observed electro-optic effect. Considering the linear electro-optic effect, Yariv (1985) points out that Si, Ge and $Si_{1-x}Ge_x$ random alloys have centro-symmetric lattices which do not allow the linear electro-optic effects and generally allow only small effects from the higher order electro-optic effects. Some evidence suggests, however that although an epitaxial $Si_{1-x}Ge_x$ alloy should have a random ordering and no centro-symmetry, long range ordering exists (LeGoues et al. (1990)); if the epitaxial layers do contain some additional ordering to that of the diamond structure then electro-optic effects dependent on the additional crystal symmetry, may exist. These effects can be tested, as Yariv (1985) suggests, by optical polarisation effects shown by the electro-optic media, unfortunately no polarisation effects have been observed in any of the samples.

One suggestion for the observation of interference effects together with the absence of substantial proof to thier origin may be that an ordered alloy does exist but in random domains thoughout the epitaxial layer. Implying that an aggregate observation would cancel linear electro-optic polarisation effects but allow a quadratic electro-optic effect, which displays no polarisation effects (Yariv (1985)). However, X-ray diffraction by the grower of these particular samples displays no ordering or smearing from such random ordered-domains.

Summary of Quantum Well Results

New quantum confined transitions have been observed in strained quantum well samples formed from thin layers of $Si_{1-x}Ge_x$ alloys clad with Si. Unfortunately it has been impossible to check material parameters by accurately measuring confinement energies, because the width of these transitions are larger

than the expected shift due to confinement. The poor spectra could be due to poor structural integrity of the samples. In chapter 5 it was demonstrated that as the well width reduced in the sample series, the Raman scattered of folded phonons became less distinct, perhaps indictating some form of interface roughness.

An important electro-optical effect has been observed in $Si_{1-x}Ge_x$/Si quantum well samples and alloy $Si_{1-x}Ge_x$ epitaxial layers, which has not been documented previously. A Fabry-Perot optical cavity is set up between the sample front surface and the epitaxial-substrate interface. The epitaxial layer forming the cavity can be modulated over a large range of photon energy by an electric field, the effects of which were observed in electro-reflectance spectra. The extact mechanism of the modulation away from the critical points in the semiconductors is not presently understood.

6.2 Short-period superlattices (4 monolayer Si: 4 monolayer Ge).

Interest in superlattice samples consisting of 4 monolayers of Si and 4 monolayers of strained Ge began when Pearsall et al. (1987) published an electro-reflectance spectrum of a (4:4) Si/Ge superlattice sample showing large signals between 1 and 3 eV. Since then Pearsall et al. (1989) and Hybertson et al. (1988) have published additional electro-reflectance and photo-current measurements for the (4:4) structure and numerous theoretical predictions have been made for optical transitions from the structure, (see section 2.2.4).

The superlattices investigated here consisted of 5 periods of 4 monolayer Ge, 4 monolayer Si grown on Si(001) buffers of various thicknesses. Just as bulk properties of semiconductors can be reflected by layers 5-6 monolayers in thickness; just 5 periods or 50Å of superlattice (the maximum which can be grown commmensurately on Si(001)) can display the full properties of the superlattice electron band structure. A full description of the sample dimensions is given along with structural integrity in section 5.2. The structures are shown in figure 5.14. Table 6.2 gives the buffer and capping layer thickness for each sample. All the epitaxial layers were nominally undoped and grown on doped n^+ (001) Si substrates.

Table 6.2 Structural dimensions of the Si/Ge (4:4) superlattices

Sample	Buffer thickness (μm)	Capping thickness (μm)	Total thickness (μm)	Electro-refl. determined (μm)
S44A	0.57	0.09	0.66	0.69
S44B	0.67	0.09	0.76	0.79
S44C	1.0	0.02	1.02	1.19
S44D	0.1-0.2	0.1	0.2-0.3	0.18
S44E	0.1	0.02	0.12	N/A
S44M	0.02	19 x 0.012	0.35	N/A

Total thickness of the layers are estimated from growth rate and TEM measurements (Stobbs (1988)) for S44C, S44E and S44M, and SIMS depth profiling (Skevington (1988)) for S44A and S44B. Optical thickness determination, used interference oscillations between 1 and 2eV (except for S44C which was determined between 2 and 3eV).

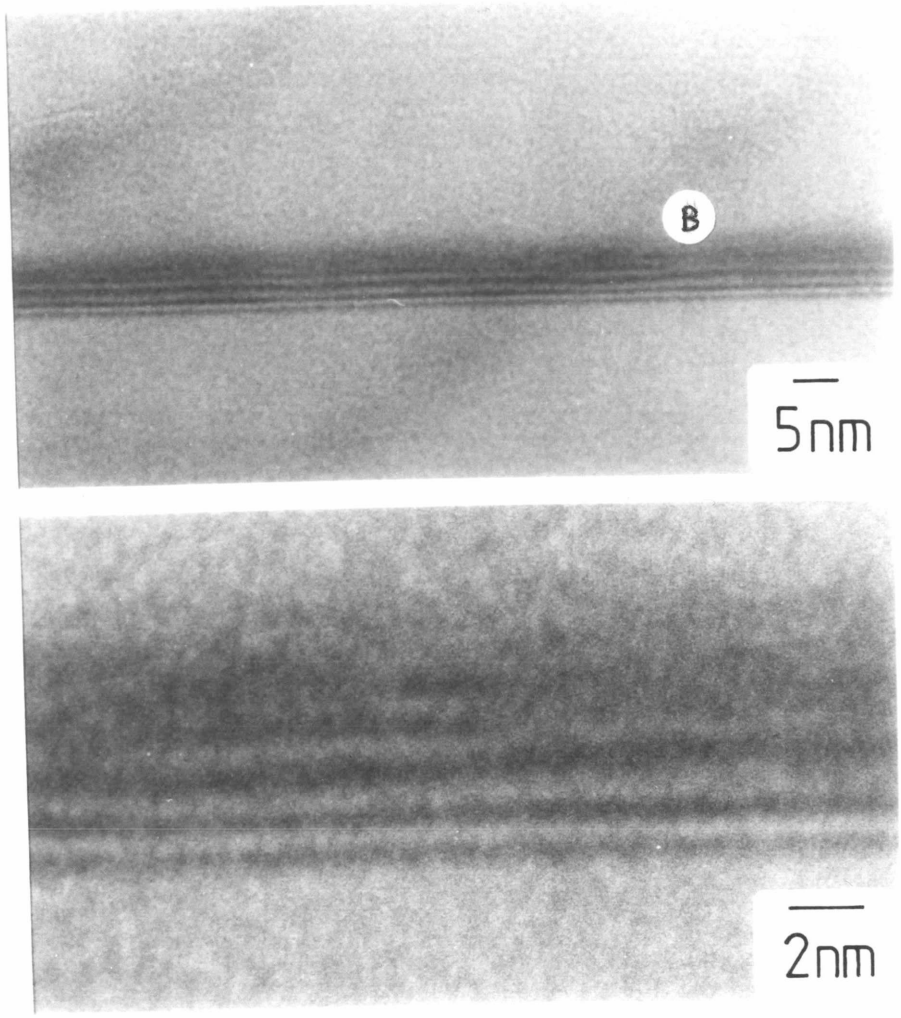


Figure 6.9 High resolution Transmission Electron Micrograph of sample S44B. (Stobbs (1988))

It can be concluded from Raman scattering data in section 5.2 that all the samples have ordered Si and Ge layers where the Ge layer has nominally taken the in-plane lattice constant of the Si substrate. In addition to that structural charaterisation, some samples have been investigated with Transmission Electron Microscopy (TEM). Figure 6.9 shows a TEM micrograph of sample S44B, clearly showing an ordered superlattice (Stobbs (1988)). A slight roughening is observed near the top of the structure. This has the effect in TEM of making the layers look thicker and diffuse. These effects appear when a slightly undulating layer is looked at edge on, making the layer look disordered, when in fact the local ordering is very good. Secondary Ion Mass Spectroscopy (SIMS) depth profiling analysis was undertaken (Skevington (1988) see section 2.1.2), indicating the presence of Ge in the vicinity of the superlattice layers. Concentrations of around 1 - 2 x $10^{17}cm^{-3}$ of carbon and 3 - 5 x $10^{17}cm^{-3}$ of oxygen throughout the epitaxial layer were found. However, the SIMS profile also showed peaks in carbon and germanium concentrations at the interface between the substrate and the epitaxial layer. Whilst the carbon contamination could easily be accounted for by the insitu pre-growth cleaning in the MBE system, the presence of germanium at the epitaxial/substrate interface is not immediately obvious. The presence of Ge at the sample surface prior to growth originates from a small flux of Ge which can find its way past the Ge evaporator shutter after multiple reflections from the chamber walls. Subsequent samples (described in section 6.3) do not suffer from this problem, as Ge sources were only heated when necessary.

6.2.1 Epitaxial layer thickness effects.

Electro-reflectance was carried out on samples S44A to E, using the procedure described in section 3.2. The electric fields were generated typically with a reverse bias of half the peak to peak modulation voltage, so that the applied voltage was from 0V to close to the breakdown voltage of the Schottky barrier. As with the quantum well samples the doped substrate and undoped epitaxial layer implies that the depletion region for the Schottky barrier diodes extends throughout the entire epitaxial layer (This was confirmed with a CV-profile). Initially the angle of incident and reflected light were 45° to the normal of the sample front. As a comparison with Schottky barrier electro-reflectance, electron beam electro-reflectance spectrum was taken of sample S44B. In the electron beam electro-reflectance technique, instead of a metal-semiconductor contact, an electric field is applied perpendicular to the epitaxial layers by an electron beam with an oscillating current. The two spectra of S44B obatined by the different

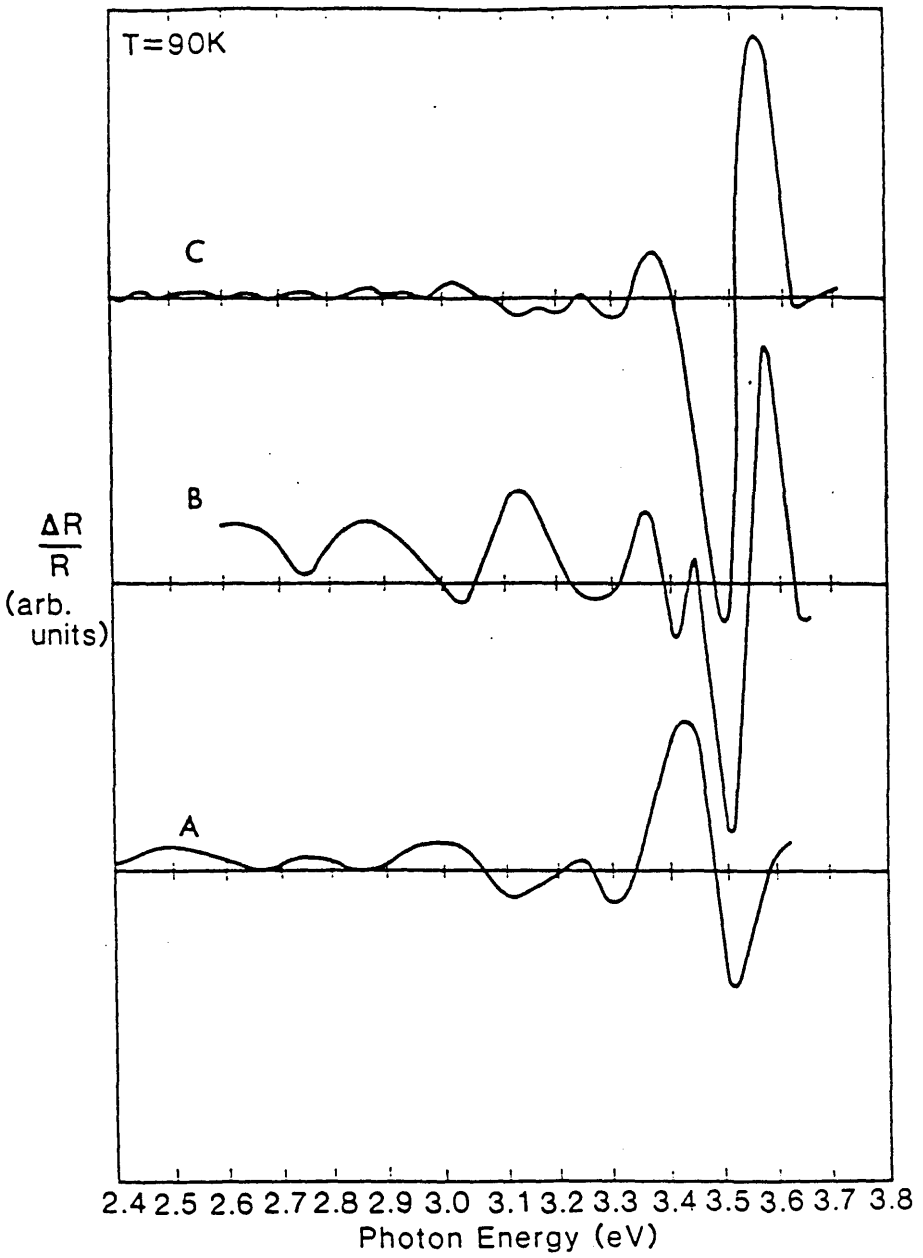


Figure 6.10 Comparison of electro-reflectance spectra for samples S44A, S44B and S44C at 90K.

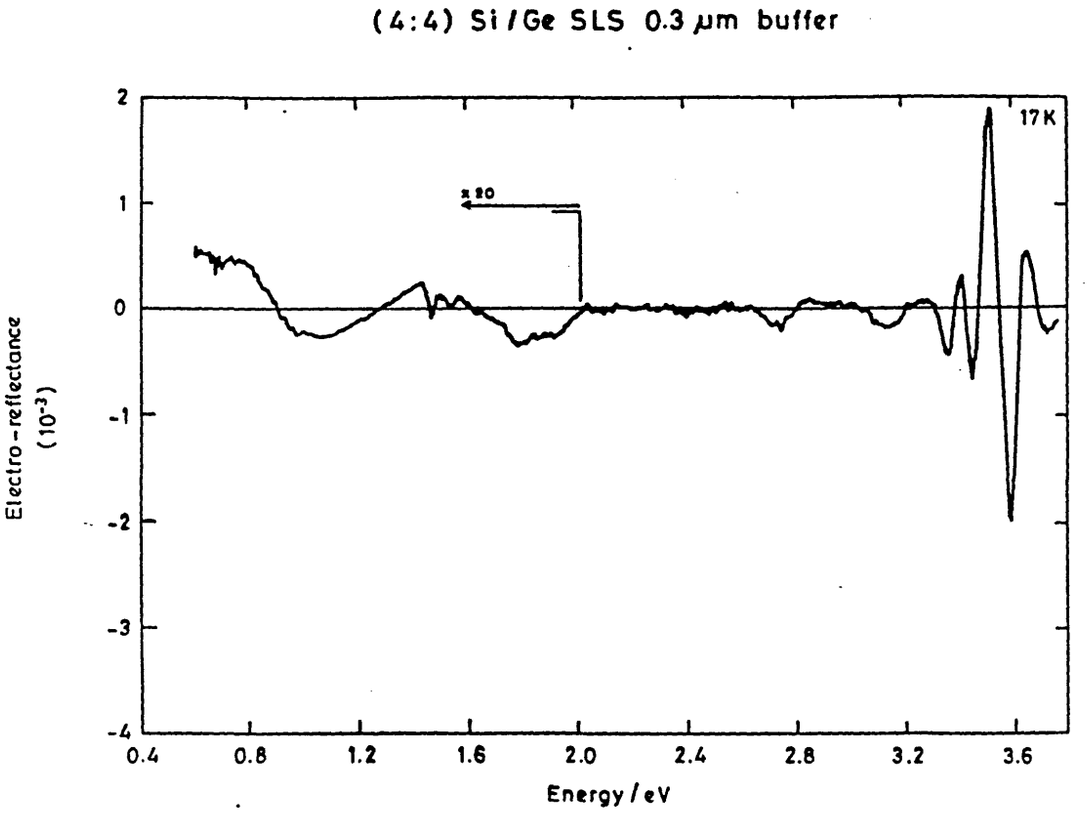


Figure 6.11 Low temperature electro-reflectance spectrum of sample S44D at 17K, with an increase in sensitivity of 20x to show interference oscillations below 2eV.

methods are almost identical and are discussed by Gell (1990c). This provides additional evidence that any effects seen in Schottky barrier electro-reflectance are not functions of the measuring techniques.

Figure 6.10 shows electro-reflectance spectra for three of the samples, S44A, S44B and S44C taken at 90K and unpolarised light was used. As with the results from the quantum well samples, a strong spectral line is observed between energies of 3.4-3.6eV This is due to the E'_0/E_1 critical points in the Si cladding and substrate layers. Again the variability in the electric field because of the unknown doping levels within the samples could explain the slightly different line shapes for the individual samples (Aspnes and Frova (1969)). Comparing with the sample just containing epitaxial Si (figure 6.2) described in section 6.1, the extra features below the Si direct transition can be ascribed to the presence of the superlattice. However although each sample has nominally the same superlattice structure no spectrum is identical. Instead an oscillatory spectrum is observed which scales inversely with epitaxial thickness. Figure 6.11 shows a low temperature electro-reflectance for a sample S44D, the spectrum also shows oscillations with constant period in the spectral region below 2eV. (Note a change in scale below 2eV) The data of Aspnes (1988) gives the refractive index of Si to be dispersionless below about 2eV.

On further examination of samples S44A and S44B in the spectral region between 1 and 2eV, electro-reflectance spectra also showed oscillations that were regular in period. Figure 6.12 shows a spectrum of sample S44A between 1 and 2eV, and figure 6.13 shows the full electro-reflectance spectrum for sample S44B from 0.6 to 4eV both taken at about 90K.

The reciprocal relationship between the oscillation period and epitaxial layer thickness would suggest the presence of an optical etalon, similar to the one found in the quantum well samples. Indeed using expression of [6.1] for epitaxial layer thickness, refractive index data for Si from Aspnes (1988) and the periods in figure 6.10, reasonable agreement of the specified layer thickness is found. However even better agreement is found for samples S44A, S44B and S44D when using the period of oscillations taken from the spectral region 1 - 2eV, far away from critical points in the band structure, where the refractive index of Si is mainly constant. This spectral region gives S44A a thickness of 0.69μm and S44B a thickness of 0.79μm. Subsequent SIMS analysis confirms these sample thicknesses to within 5%. Table 6.2 summarises the epitaxial layer thicknesses, determined optically. A secondary confirmation that these

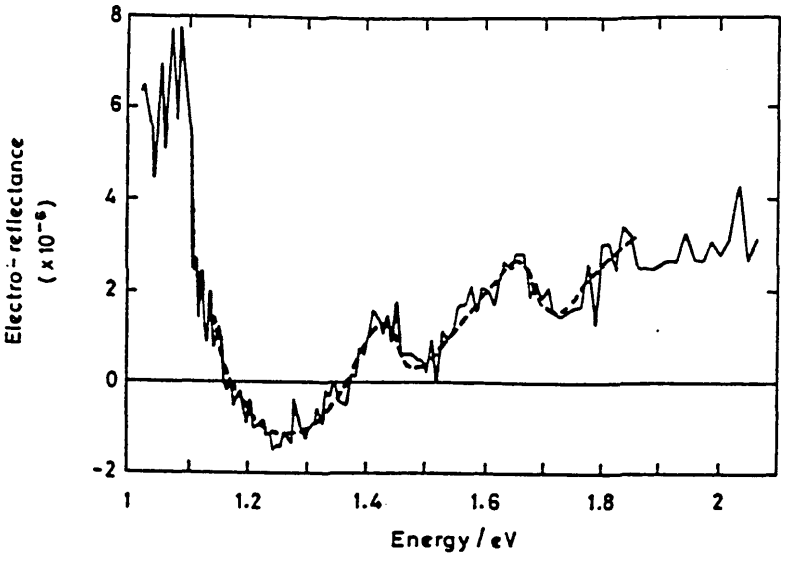


Figure 6.12 Electro-reflectance spectrum of sample S44A in an energy range of 1-2eV, taken at liquid nitrogen temperatures. Interference effects are observed corresponding to formation of an etalon in the epitaxial layer.

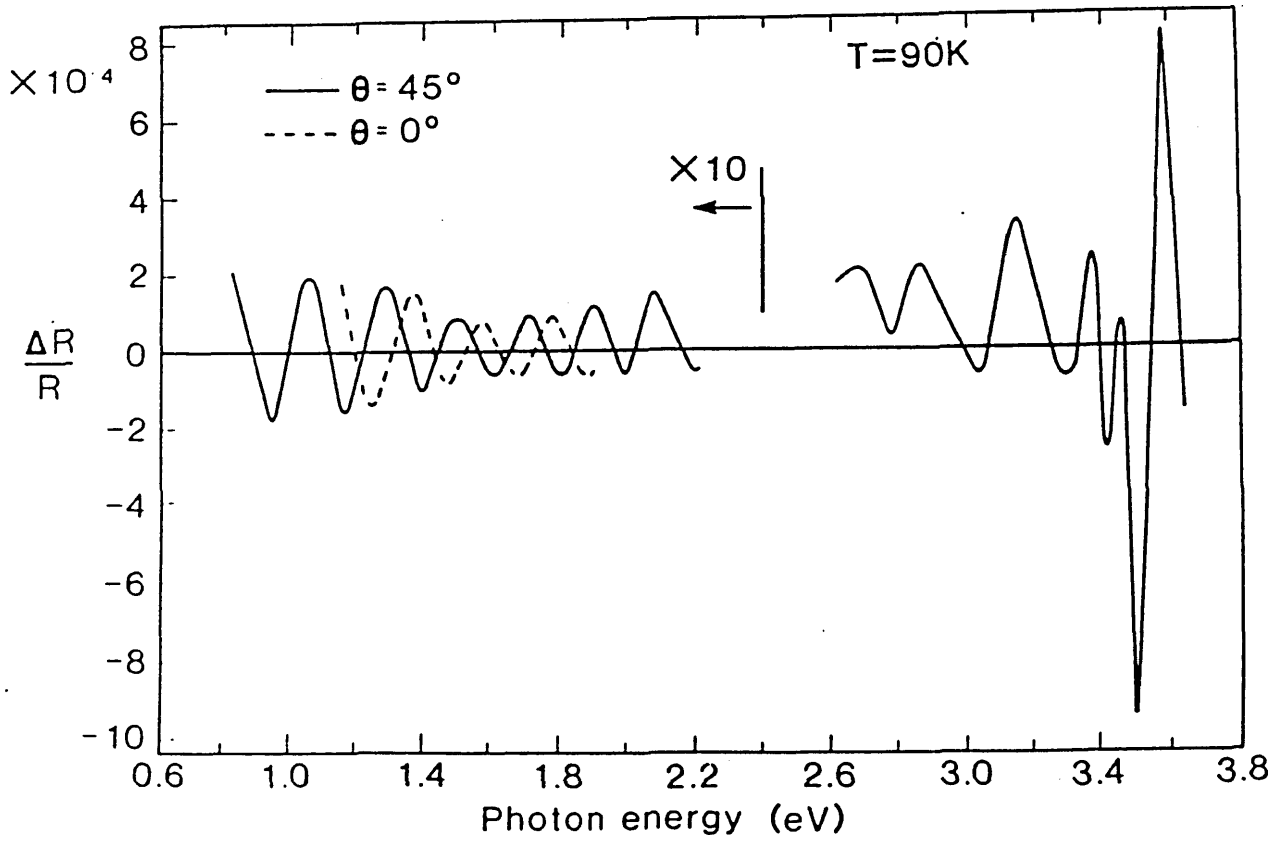


Figure 6.13 Electro-reflectance spectrum of sample S44B between 0.6 and 3.8eV at 90K. In the low energy region, spectra are plotted for 0 and 45° angles of incidence.

effects are truly interference fringes, can be made by changing the optical path difference of the light in the etalon cavity, a test used in confirming the interference effects of the quantum well samples. This can be done by changing the angle of incident and reflected light. An increase in incident angle decreases the optical path within the cavity, moving the Fabry-Perot resonances to shorter wavelengths. This is indeed observed in figure 6.13.

As with the case of the oscillations observed in the quantum well samples, no changes in period or phase were observed when the average electric field bias was changed suggesting that the observed effect is not a Franz-Keldysh effect. Likewise no change in the effect was observed when the incident light polarisation was changed, also suggesting that the effect is not a linear electro-optic one (Yariv (185)).

The effect of interference fringes in electro-reflectance spectra has also been observed by other workers: Pearsall et al. (1989), (note however the period which they observe corresponds to a Fabry-Perot structure of about 7μm thickness and not 400μm as stated in their paper). However looking at the other samples measured by Pearsall et al. (1989) and Hybertson et al. (1988) an example of which is given in figure 2.20, the period of oscillations does not tally with the growers' specified epitaxial layer thickness (nominally given as ~0.3μm). Thus Hybertson et al. and Pearsall et al. may be justified in ignoring etalon effects within the samples. However spectra of similar (4:4) structures taken independently from their publications are very dissimilar, even allowing for 180° phase ambiguity within the setting of the Lock-in amplifiers used to record the spectra, but these workers still assign the same calculated optical transitions to their data. Schmid et al. (1990) have recently investigated short-period superlattices with a rotating polariser ellipsometer, their spectra also suffer from interference effects below 2eV. As Shields et al. (1989) have pointed out, even if the epitaxial layer does not behave as a Fabry-Perot etalon, interference effects are still important when unravelling electronic transitions from electro-reflectance spectra.

It can perhaps be inferred from the presence of the oscillations in the superlattice samples and absence in the Si epitaxial sample, that the oscillations arise because the superlattice is present. However the presence of the reflecting surface at the epitaxial/substrate interface is an important factor in the observation of the interference effect and it is not at present clear why this reflection occurs and whether it

occurs in all epitaxial samples. Raman scattering of the superlattice samples, discussed in section 5.2, together with TEM measurements would imply that the superlattices are well ordered compared to a random alloy of the same average composition. Thus the mechanism which modulates the optical etalon cavity may be somewhat different from the mechanism which causes the interference effects found in the samples of section 6.1, which contain alloys. Measurements of GaAs doping superlattices performed by Thorn et al. (1989), also show interference effects in the vicinity of the E_0 critical point of GaAs. In that case the authors show that the envelope of the oscillations closely follows the electro-absorption. This is because the reflection at the backplane of the cavity forces light to pass twice through the active region of the sample, before emerging from the sample. Thus the intensity of light which emerges from the sample is modulated by the electro-absorption of the active layer. Hence the amplitude of the interference oscillations is enhanced near critical points of the active region. In this case figure 6.13 shows the oscillations increase towards energies of 0.8eV, suggesting a critical point in the superlattice at this energy. Indeed, Gell (1988) predicts superlattice critical points at about 0.8 - 1.0eV.

6.2.2 Evidence for superlattice induced electronic states.

In the above section, electro-reflectance has demonstrated that the presence of a Si/Ge (4:4) short-period superlattice in Si epitaxial material affects the electro-optical properties of the sample. However confirmation of the critical points seen with resonant Raman scattering (section 5.2.4) in the repeated Si/Ge (4:4) superlattice (S44M) has not been made. In addition no firm confirmation has been made of predicted transitions in the superlattice that should occur around 1eV. In this section photo-current spectroscopy is used to look for the weak transitions around 1eV, and a special sample designed to eliminate interference effects is used to confirm higher lying critical points in the (4:4) superlattice band structure.

From the discussion in section 6.2.1, it can be seen that any electro-reflectance spectrum of a sample grown with an epitaxial layer comparable to the wavelength used for the spectral study, will suffer from interference effects. Thus sample S44E was designed to overcome this problem. The sample consists of

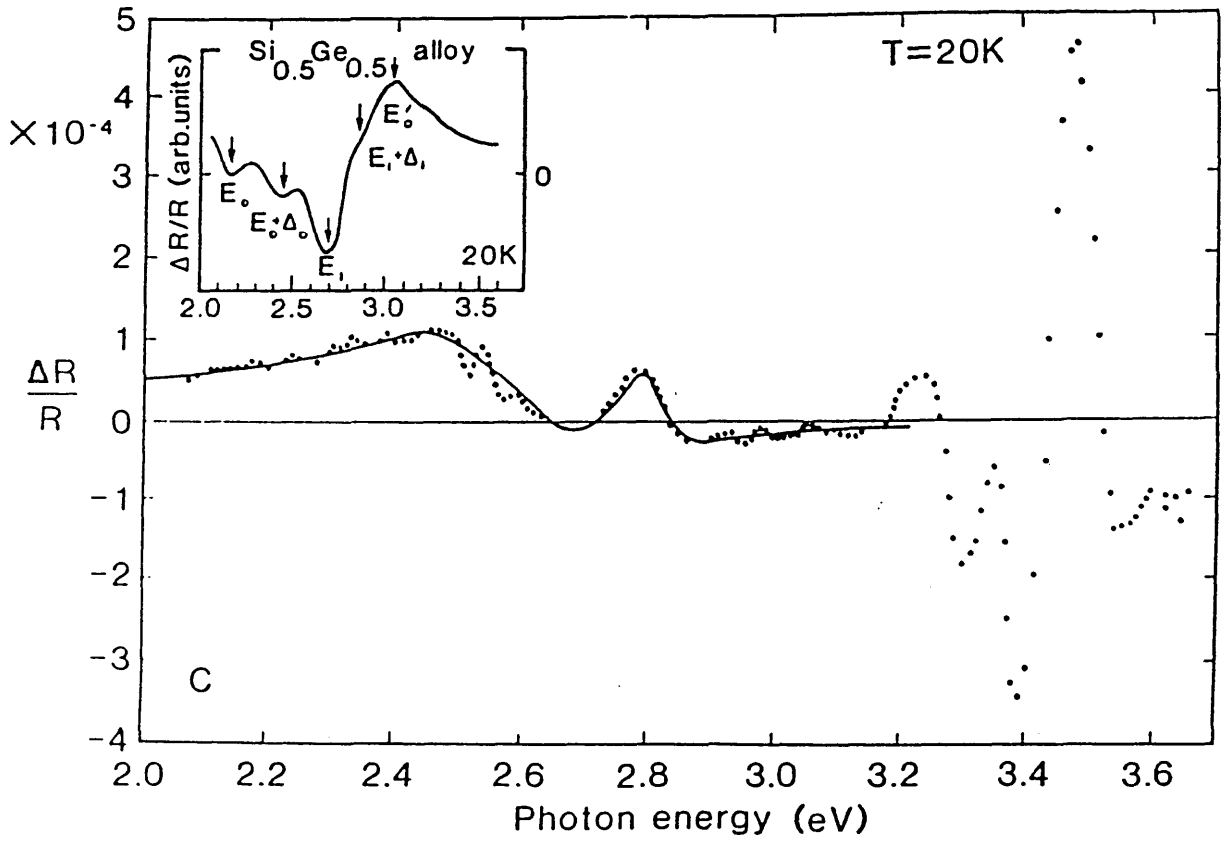


Figure 6.14 Electro-reflectance spectrum for sample S44E between 2 and 3.8eV at 20K. Inset shows spectrum at 20K for the alloy sample ALY50.

a Si/Ge (4:4) short-period superlattice grown on a very thin buffer (1000Å) of Si on a Si n^+doped (001) substrate. A capping layer of 200Å protected the superlattice. The entire thickness of the epitaxial layer corresponds to a wavelength in Si of about 350nm (a photon energy of 3.5eV). An electro-reflectance spectrum for this sample taken at 17K is presented in figure 6.14. A theoretical Lorentzian line, descibed in section 3.4, has been fitted to the lower part of the spectrum, as a guide to the eye. Two transtions fitted having energies at about 2.4 - 2.5 and 2.8eV. The electro-reflectance signal below 2eV is very small and is not shown. Also shown in figure 6.14 is an electro-reflectance spectrum of sample ALY50, 0.2μm of $Si_{0.5}Ge_{0.5}$ on a Si(001) substrate, for comparison with a sample containing the same average composition as the superlattice. As with the other spectra of (4:4) superlattices the features around 3.4-3.6eV of figure 6.14 can be assigned to E_1/E'_0 transitions within the Si cladding layers. However the spectrum is different from the other superlattices looked at so far and no oscillatory interference effects are seen in the spectrum. The two other features at energies below the Si feature are significantly different from the structure observed in the 50% random alloy and can be assigned to the superlattice. In the spectral region between 2 and 3eV the alloy produces features arising from a mixture of E_0 and E_1 transitions, the superlattice sample however, shows only two distinct transitions. The transition energies compare well to the resonant Raman measurements, allowing for a difference in energy (~0.1eV) due to difference in measurement temperature for the two experiments. Figure 6.14 is in contrast to the results of Pearsall et al. (1987), which show oscillatory structure in the electro-reflectance spectra of a Si/Ge (4:4) superlattices from 2 to 3.5eV. Pearsall et al. manage to fit Lorentzian line shapes for transition energies of 3.06, 2.81 and 2.54 eV. The fitted line shapes have much larger width than the ones in figure 6.14.

Unfortunately no direct comparison of resonant Raman and electro-reflectance spectroscopy has been made. Sample S44E used for electro-reflectance, although characterised by Raman scattering, cannot be used for resonant Raman scattering as the Raman signal from the superlattice is too small for a realistic measurement. Likewise the repeated superlattice used for Raman scattering is too thick and stratified for unambiguous electro-reflectance studies. However the independent measurement of critical points in two quite different samples is confirmation that these transitions do indeed exist in short-period superlattices.

Gell (1988) predicts the strength of transitions at 2.8eV to be very similar to the Si E'_0 transition, table 2.6 section 2.2.4 (0.6 times the strength of the E'_0 transition). In S44E the ratio of volume of superlattice to Si cladding layers in the electric field is about 50/1200. From this a predicted strength of 3% of the Si E'_0 transition is found. The actual strength is somewhat larger than this figure (~10%), but the simple calculation shows that the strength is the correct order of magnitude. Other Γ related superlattice states at lower energy (0.8-2eV) are predicted to be 1-2 orders of magnitude below the 2.8eV transition. Thus it is unwise to hope that these transitions can be seen in electro-reflectance or resonant Raman scattering, and absorption measurements should be done.

The state at 2.4 - 2.5eV is predicted to arise from the X points of the superlattice Brillouin zone and cderives from the L related E_1 transitions in the Si and Ge host crystals. Again a volume scale factor can be used to compare this transitions strength to the E_1 critical point of Si.

Turning to the investigation of weaker superlattice transitions, photo-current measurements were needed and are now discussed below. Photo-current spectroscopy is often carried out as an analogue to absorption spectroscopy, particularly when absorption in the epitaxial layer is masked by absorption in a substrate which is difficult to remove from the sample. (See for example Rogers et al. (1984)). Section 3.2.3 describes how the measurements were carried out. The Schottky barrier samples of the preceding section were used, light was absorbed under the Schottky barrier and photo-created carriers were collected by the contacts, helped by the Schottky barrier electric field.

Figure 6.15 shows the photo-current spectrum for sample S44M, containing the repeated superlattice structure. The peak in the spectrum at 1.4eV, orginates from a filter cutting off at shorter wavelengths to remove effects from second order diffracted light from the spectrometer. Extra absorption is observed in the superlattice below 1eV. This should be compared with figure 3.7, which shows Si and $Si_{0.5}Ge_{0.5}$ alloy photo-current spectra in which no absorption occurs below the band edges at 1.1eV and 1eV respectively for Si and the alloy. Above 1.1eV the photo-current signal is expected to have components from both superlattice and Si cladding layers. All the superlattice samples showed evidence for absorption below the Si indirect band edge, ie below 1.1eV.

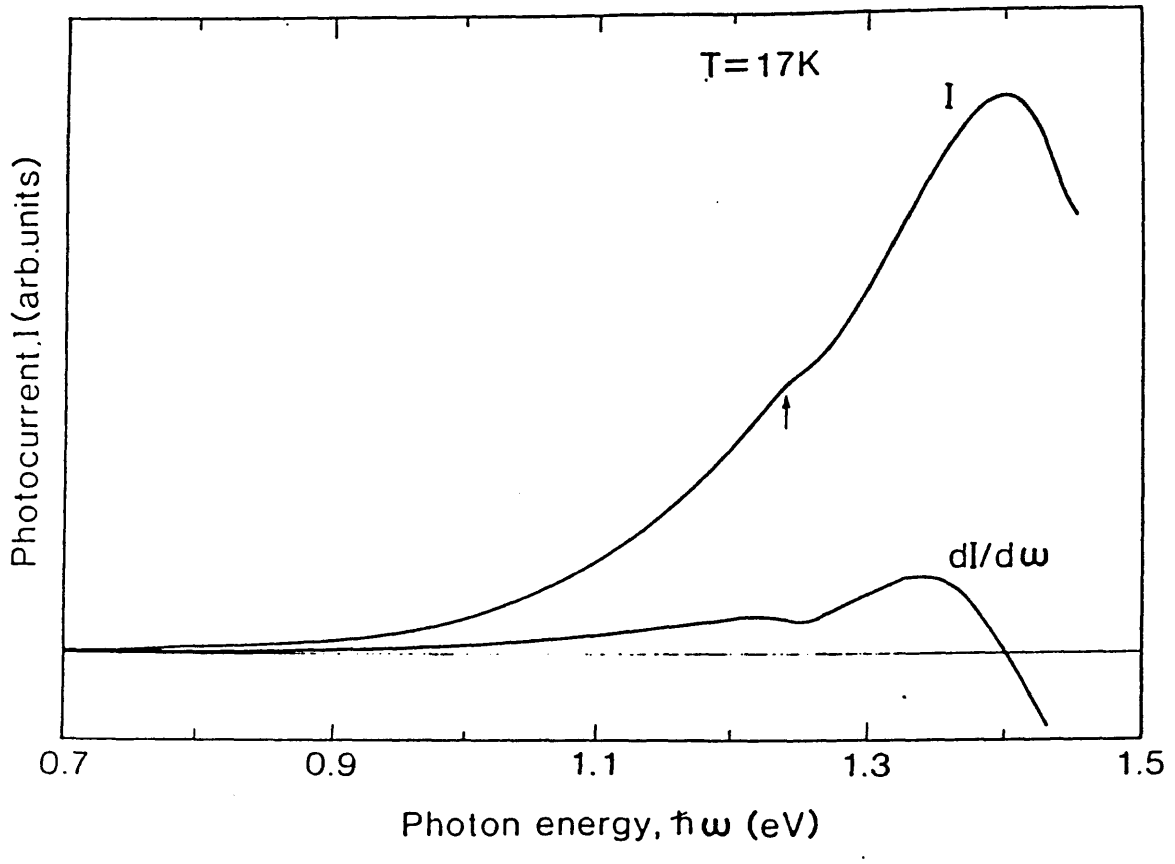


Figure 6.15 Photo-current spectrum at 17K of sample S44M, a repeated Si/Ge (4:4) superlattice, showing absorption below the band edge of Si.

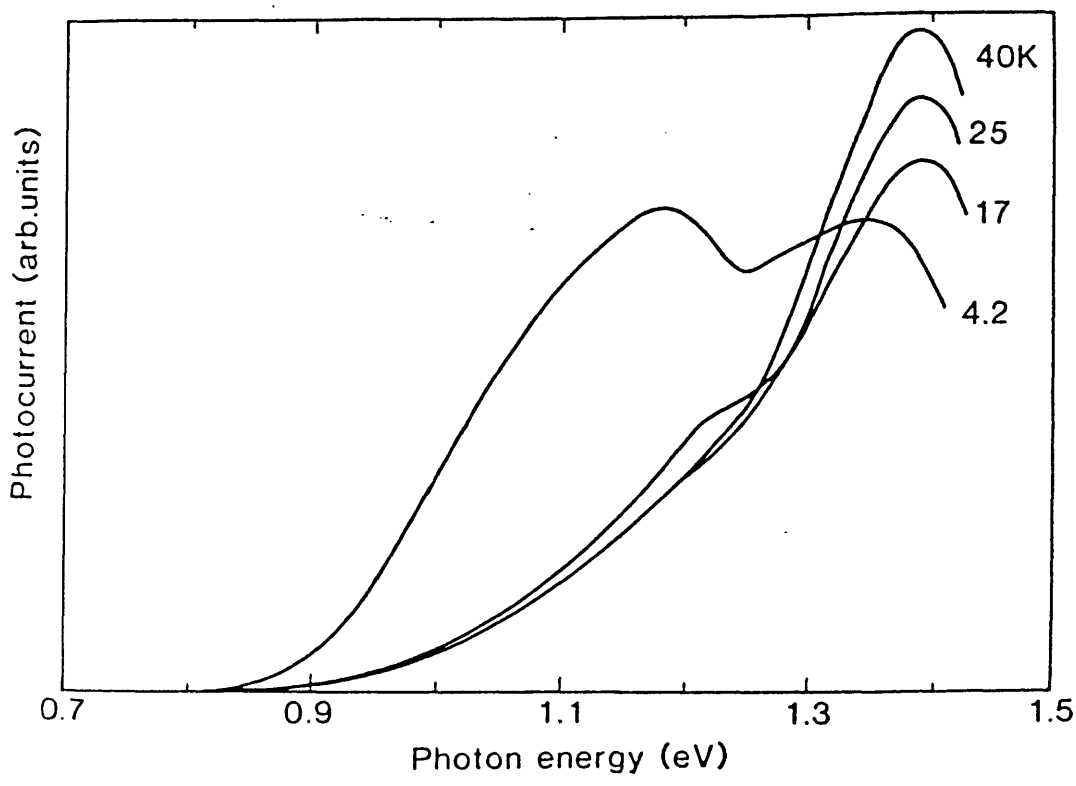


Figure 6.16 Photo-current spectra for sample S44B between 40 and 4.2K using a gold Schottky barrier. The photo-current units of the 4.2K spectrum are not the same as for the other spectra.

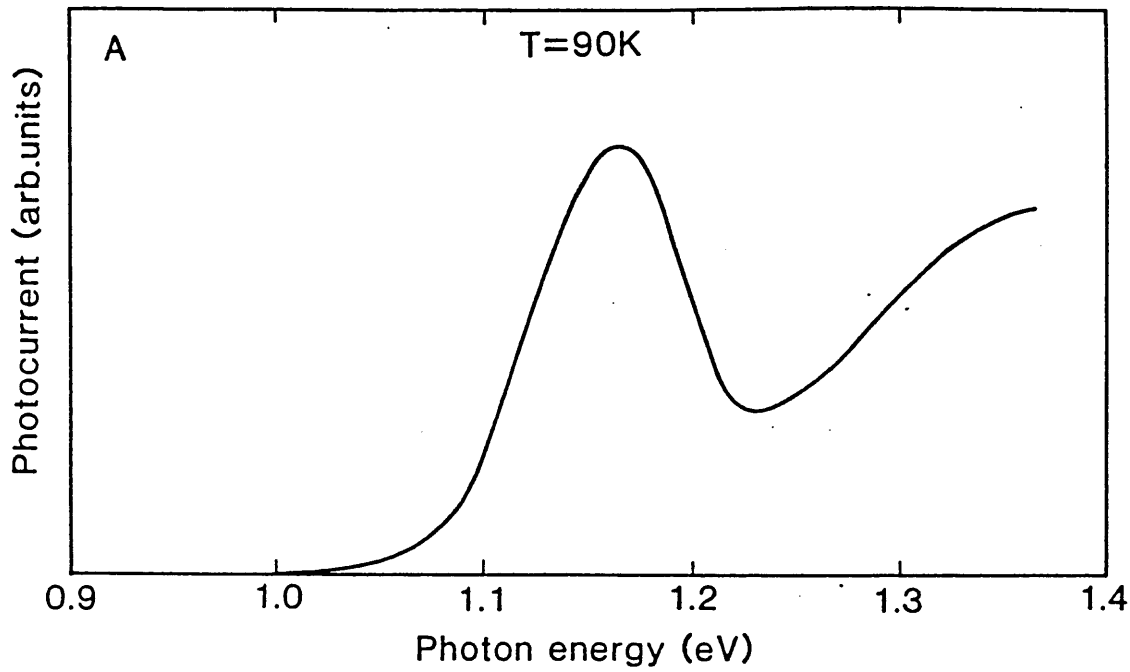


Figure 6.17 Photo-current spectrum of sample S44A at 90K, showing anomalously high absorption at 1.2eV.

In addition to the absorption down to energies of 0.8eV, an inflexion is observed at 1.2eV, (the derivative of the spectrum is also plotted in figure 6.15 to show this feature). The temperature dependence for this feature in sample S44B is plotted in figure 6.16. In this figure it can be seen that the feature remains strong in comparison to the silicon band edge absorption at higher energies which decreases as a function of temperature. This effect can be explained if the Si indirect band edge absorption decreases with temperature due to a reducing phonon population, but the feature at 1.2eV is due to a direct superlattice transition. Gell predicts such a transition at 1eV corresponding to transitions at Γ from superlattice bands V1/V2 to C2. Higher energy transitions, are also predicted but are masked by absorption of the Si indirect edge. Figure 6.17 shows a similar photo-current spectrum of sample S44A, this time at 90K, showing an anomalously large peak at 1.2eV, this feature also varied in magnitude for light absorbed at various places across the Schottky barrier. The latter result might suggest the peak is dependent on the sample and not intrinsic to the superlattice. As carrier life times can sometimes produce similar effects in photo-current measurements, ultimate assignment of the peak must be made with reservations, however this peak was not measured in the $Si_{0.5}Ge_{0.5}$ epitaxial layer sample which has similar epitaxial layer thickness, superlattice average composition, substrate and doping levels.

Assignment of the lower energy absorption tail can be made to the indirect transitions in the superlattice predicted to have a band edge at 0.8eV (Gell (1988), Gell and Churchill (1989)).

The strengths of the optical absorption below the Si edge can be compared to Gell's (1988) predicted strengths for transitions between V1/V2-C2 transitions which should occur at 1.0eV. Gell calculates a ratio in strength of 0.0025 to that of the Si direct edge. The measured strength of the Si E_1/E'_0 observed in electro-reflectance is 0.001 (from figure 3.5). Making the V1/V2-C2 transition a predicted strength of about 10^{-6} if measured in electro-reflectance. This strength is comparable with the Si Γ_{25}-Δ_1 indirect edge observed in electro-reflectance. (Alibert (1988) has observed the Si indirect edge in electro-reflectance spectroscopy. Its strength is about $5x10^{-6}$ and the sample used was a commercial Si photo-diode with about 300V peak to peak applied across it). Thus the weak photo-current signal below 1.1eV which has similar size to the indirect band edge of the cladding layer absorption at higher energies is consistent with Gell's predictions. (Gell (1990a)).

Regardless of the anomalous peaks in the photo-current spectra, the existence of photo-current below the edge observed in $Si_{0.5}Ge_{0.5}$ alloy samples, suggests that the superlattice has optical transitions with a band edge of 0.8eV. It should be noted that these samples do contain dislocations and defects ($\sim 10^9 cm^{-2}$), but most electronic effects associated with defects in Si are related to the indirect conduction band valleys in Si and hence have long life times and corresondingly small strengths (Davies (1989)). So to observe defect related effects, it is usual to use a relaxation type of measurement eg. photoluminesence and not an excitation measurement such as electro-reflectance or photo-current spectroscopy (Weber and Alonso (1990)). Thus the photo-current measurement of an absorption edge can represent an intrinsic effect associated with the band edge in the superlattice.

6.2.3 Summary of results for Si/Ge (4:4) superlattice samples.

Electro-reflectance spectroscopy, a technique well suited to analysis of critical point transitions within semiconductors, has been used to investigate Si/Ge (4:4) short-period superlattices. Initial analysis showed that the spectra of various samples contained interference effects from reflections from the front and epitaxial-substrate interface surfaces similar to the ones observed in epitaxial alloy and quantum well samples. The mechanism causing the electro-modulation of the etalon cavity is unknown. However, it is thought to be different from similar spectral effects observed in the alloy and quantum well samples of the preceding section, which with present evidence, seemed to be connected with the presence of the alloy.

A thin sample, which allowed the Fabry-Perot interference effects to be suppressed, showed critical point structure at 2.8eV and 2.4 - 2.5eV, in addition to structure related to the Si cladding layers. This result confirms the critical point already observed in (4:4) superlattices by resonant Raman scattering. Photo-current spectroscopy of the superlattice samples shows a signal below the indirect band edge of Si, suggesting that superlattice states are present from 0.8eV and above. Additional features in the photo-current spectra, can be assigned to the V1/V2-C2 critical point transition within the superlattice. The strengths of the transitions observed compare well to theoretically predicted strengths for the (4:4) superlattice structure by Gell (1988) and are summarised in table 6.3.

Table 6.3 The Si/Ge (4:4) short-period superlattice

Transition	Predicted		Observed	
	Energy (eV)	Strength (Si E'_0)	Energy (eV)	Strength (Si E'_0)
Γ-Γ(bulkSi)	3.4-3.37	-	3.45	1
$\Gamma_{v1/v2}$-Γ_{c5}	2.6-2.7	0.16	2.8	2.2
$X_{v1/v2}$-X_{c3}	2.8	~Si E_1		
$X_{v1/v2}$-$X_{c1/c2}$	2.3-2.45	~Si E_1	2.42	"
$\Gamma_{v1/v2}$-Γ_{c3}	1.6	0.025	-	
$\Gamma_{v1/v2}$-Γ_{c2}	1.0	0.0025	1.2	0.001
$\Gamma_{v1/v2}$-M_{c1}	0.8	~Si indirect	0.8	~Si indirect

(Measured strengths include volume scale factors)

The electro-reflectance results presented do not agree with the results of Pearsall (1987). It is tentatively suggested that Pearsall's spectra are masked by interference effects, and that sample quality and design plays an important part in whether the superlattice transitions are present or masked by interference effects (Pearsall (1990b)).

Although the Si/Ge (4:4) superlattice has not displayed a direct band gap, indirect transitions can be seen from 0.8eV and above, and zone folded superlattice critical points can be seen at 1.2eV, 2.8 eV and 2.4-2.5 eV (from the X and X' states).

(The work presented in this section will appear as a publication by A C Churchill, P C Klipstein, C J Gibbings, M A Gell, M E Jones and C G Tuppen (1990b).)

6.3 Short-period superlattices (2 monolayer Si: n monolayer Ge).

In this section electro-reflectance and electro-transmission spectroscopies are used to investigate superlattices consisting of Si/Ge (2:n) where n = 6,8 or 10 monolayers of Ge. These superlattices contain bi-atomic layers of Si in their period and are predicted to have a lowest conduction band valley at Γ. Hence they are direct band gap superlattices as opposed to the Si/Ge (4:4) superlattice which is indirect.

The superlattices are clad in $Si_{0.25}Ge_{0.75}$ alloy in order that the conduction band of the superlattice lies below that of the surrounding semiconductor; making the superlattice a type-I quantum well structure. This alloy has a similar average composition to the superlattice and thus masks Raman signals from the superlattice layers. Making Raman scattering analysis for structural integrity too difficult. No distinct strained superlattice and relaxed alloy modes were observed, however unresolved splittings of alloy and superlattice modes resulted in a broad set of Ge-Ge, Si-Ge and Si-Si modes. The ratio of intensities suggested a $Si_{0.3}Ge_{0.7}$ alloy. It would be too optimistic to hope that a line fit to each of the Raman modes would give structural details of any value.

The superlattice is symmetrically strained and contains 51 periods, this number was set by the mechanical limitations of the MBE system. (The Si and Ge flux rates were about 0.3Å/second, to ensure that the solenoid operated shutters opened and closed reliably for the entire superlattice, the driving force was very high and thus there was a risk of breakage, thus the superlattice was restricted to a limited number of preiods). The epitaxial layers were grown on Si (001) n^+ doped substrates, which are much cheaper, more readily available and easier to clean than the alternative of Ge substrates. A buffer layer of Ge was grown before the superlattice in order to obtain a good growth surface for the alloy buffers and superlattices.

Before using electro-reflectance and electro-transmission spectroscopy to investigate the (2:n) superlattices, an investigation is described about a superlattice, proposed by Abstreiter et al. (1989), containing a Si/Ge (6:4) superlattice, also thought to possess a direct band gap.

6.3.1 The Si/Ge (6:4) Superlattice.

The superlattice containing 6 monolayers of Si and 4 monolayers of Ge, has been investigated by Abstreiter et al. (1989) and other co-workers Zachai et al. (1988) and Eberl et al. (1987). The structures are predicted to have direct band gaps because the 10 monolayer period of the superlattice folds the 0.8X conduction band minima of Si in the growth direction to the Brillouin zone centre (Zachai et al. (1990)). However, no full band structures have been calculated for these superlattices, thus no prediction about the strength of the optical transitions has been made. Optical transition energies have been calculated using the effective mass approximation and zone folding effects. Photoluminescence spectra reveal optical transitions associated with the superlattice at 0.85eV (Zachai et al. (1990)) although at the present time it is unclear whether this luminescence arises from the superlattice band structure or defects associated with the dislocations in these samples. Pearsall et al. (1989b) have investigated similar superlattices to Zachai et al. but with electro-reflectance spectroscopy. However, unlike Zachai et al. who looked at superlattices grown on $Si_{1-x}Ge_x$ buffers on Si(001) substrates, the superlattices of Pearsall et al. were grown on Ge (001) substrates of an unspecified doping level. Thus Pearsall's spectra are dominated by the E_0 critical point of germanium. Pearsall et al. do not observe any spectral feature at 0.85eV, but they account for this by a symmetry argument for the states involved in that transition. Pearsall et al. do observe subtle features on the Ge E_0 line shape which they ascribe to high energy bands in the superlattice. However, these effects could be due to doping impurities or inhomogeneities in the applied electric field, which they observe with their control samples. Thus no firm evidence exists to support the idea of direct band gap in the Abstreiter et al. Si/Ge (6:4) superlattice.

For completeness two Si/Ge (6:4) samples were measured with electro-reflectance spectroscopy. One sample S64, is specified nominally to contain the Abstreiter et al. Si/Ge (6:4) superlattice ~0.4μm thick grown on 30nm of $Si_{0.6}Ge_{0.4}$ alloy buffer. The other, S64CL contained an alloy instead of the superlattice and acts as a control. Both samples were uncapped and nominally undoped. They were grown on Si (001) n^+ doped substrates. Raman scattering from the optic phonons was not able to characterise these samples, but TEM measurements confirmed the presence of a superlattice in sample S64 (Stobbs (1988)).

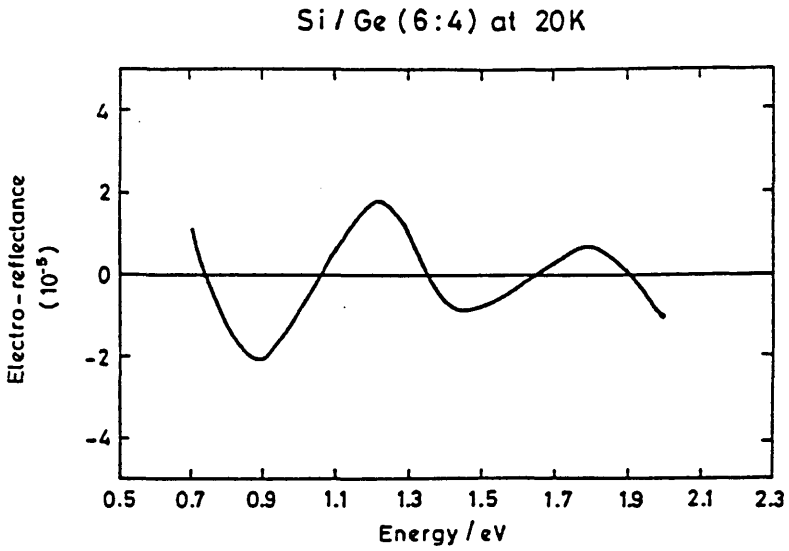


Figure 6.18 Electro-reflectance spectrum of sample S64 at 20K.

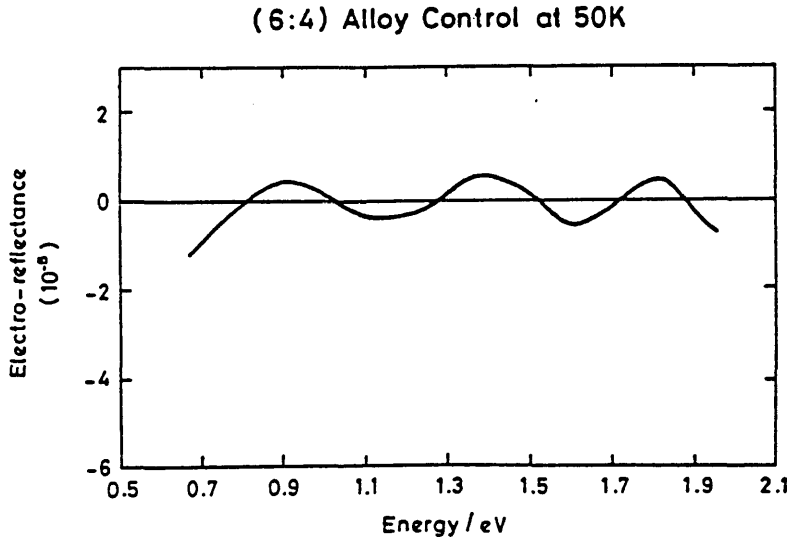


Figure 6.19 Electro-reflecatnce spectrum of sample S64CL at 50K.

Figure 6.18 and 6.19 show electro-reflectance spectra of the superlattice sample and its control sample, both spectra were taken with unpolarised light incident 45° to the sample in a similar fashion to the other electro-reflectance measurements in sections 6.1 and 6.2. The spectra are very similar to each other, and no specific critical point is observed in the energy region of the luminescence that is observed by Zachai et al. (1990). However, the sample containing the superlattice has a larger signal than the control sample.

Both spectra exhibit oscillations similar to the ones observed in the quantum well and epitaxial alloy samples of section 6.1. Taking the refractive index of the $Si_{0.6}Ge_{0.4}$ alloy as 3.64 (ie. an average of Si and Ge), expression [6.1] gives a layer thickness of 0.39μm for the control sample and 0.3μm for the superlattice sample. This is in reasonable aggreement with nominal epitaxial layer thicknesses. Whilst it is not clear why these oscillations appear, they have a very similar character to the ones found in quantum well and (4:4) superlattice samples.

In conclusion, samples containing short-period Si/Ge (6:4) superlattices have been grown. Electro-reflectance spectroscopy reveals oscillatory behaviour but no distinct superlattice transitions. The sample containing the superlattice, had a larger electro-reflectance signal than that of the control sample. As these results are different from the ones of Pearsall et al. (1989) and Zachai (1990), no real conclusions can be made about the optical transitions in the (6:4) Si/Ge superlattice.

6.3.2 Electro-reflectance measurements.

Figure 6.20 shows a schematic of the Si/Ge (2:n = 6,8,10) superlattices under initial investigation, these were denoted S26A, S28B and S210C. 51 periods of superlattice are grown on to a 1000Å $Si_{0.25}Ge_{0.75}$ alloy buffer, which is in turn grown on a 1μm thick Ge buffer in a (001) orientation. The samples were capped with 1000Å $Si_{0.25}Ge_{0.75}$ alloy. TEM measurements on S26A indicated the layering was present, however an image of the bi-atomic sheet of Si could not be obtained (Stobbs (1988)). Another

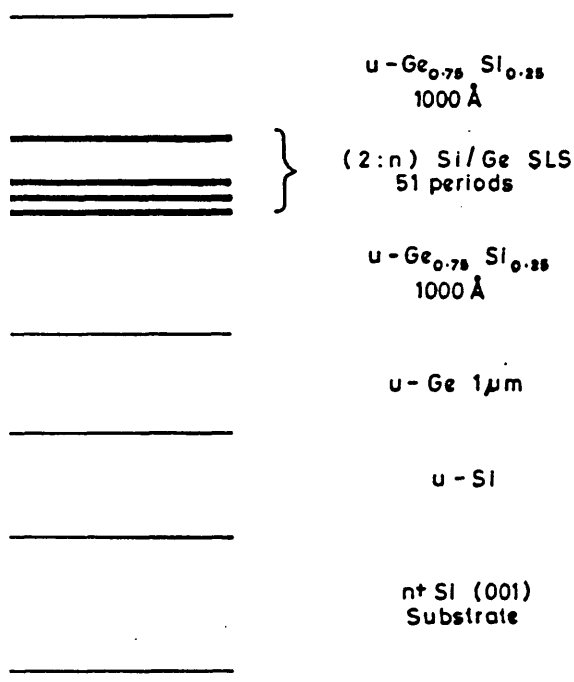


Figure 6.20 Schematic of the sample structures for S26A, S28B and S210C.

sample, S26CL1 was grown at the same time as the superlattice samples using similar fluxes and substrate temperatures, however this sample consisted of 700Å of $Si_{0.25}Ge_{0.75}$ alloy grown on an undoped Ge in turn grown on an undoped Ge (001) substrate. Thus both alloy thickness and the substrate are different from the superlattice samples, but the sample allows some independent verification of the alloy concentration. Figures 6.21-6.23 show electro-reflectance spectra of sample S26A, S28B and S210C. Figure 6.24 shows an electro-reflectance spectrum of the control sample S26CL1. The experimental geometry was similar to previously described experiments, using unpolarised light incident at 45° on the Schottky barrier. A PbS photo-detector was used. Electric fields were estimated to be about 50kV/cm across the entire epitaxial layer, from C-V profiling data.

The spectrum of the control sample shows two features, both originate from the Ge layers in the sample, coming from the E_0 and $E_0+\Delta_0$ transitions of bulk Ge, (see figure 3.3 in section 3.2). The extra oscillations to higher energies on the spectral peaks are a manifestation of the Franz-Keldysh effect described in section 2.2.8. To understand the spectra of the superlattice structures it is necessary to remember that the samples contain several reflecting surfaces: the front sample/air interface has a reflectivity of 35% and the Ge buffer/Si substrate interface a reflectivity of 0.3%. As in the (4:4) superlattice samples these two interfaces dominate the optical spectra, producing interference effects from a Fabry-Perot etalon structure. The period of oscillations corresponds well to an etalon thickness of about 1.2μm, approximately the nominal epitaxial layer thickness.

The results from the (2:n) superlattices should be compared with the other electro-reflectance measurements of Si/Ge epitaxial samples. All samples, except the pure Si epitaxial sample, show interference effects arising from an electro-optic phenomenon in the layers and reflections from the front and back epitaxial interfaces. Whilst a definitive conclusion to the origin of these effects cannot be made, it seems that if a sample contains epitaxial alloy layers, then interference effects will be observed in electro-reflectance spectra. Careful inspection of figures 6.21, 6.22 and 6.23 shows that unlike the interference oscillations seen between 1 and 2eV in the previous samplesof section 6.2, the oscillations are not sinusoidal and have extra irregularities at 0.7 and 0.9 eV. These features are most clear in figure 6.21.

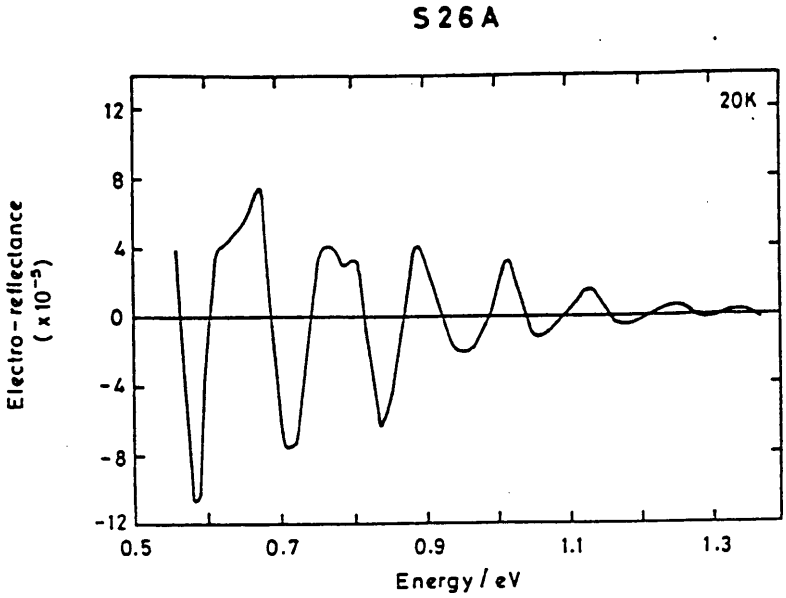


Figure 6.21 Electro-reflectance spectrum of sample S26A at 20K, oscillations in the spectrum arise because of a Fabry-Perot etalon effect.

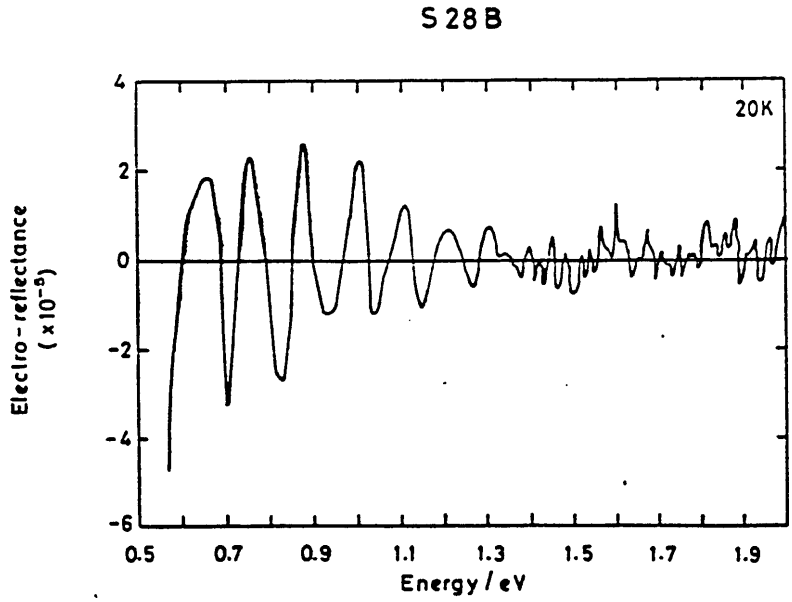


Figure 6.22 Electro-reflectance spectrum of sample S28B at 20K, oscillations in the spectrum arise because of a Fabry-Perot etalon effect.

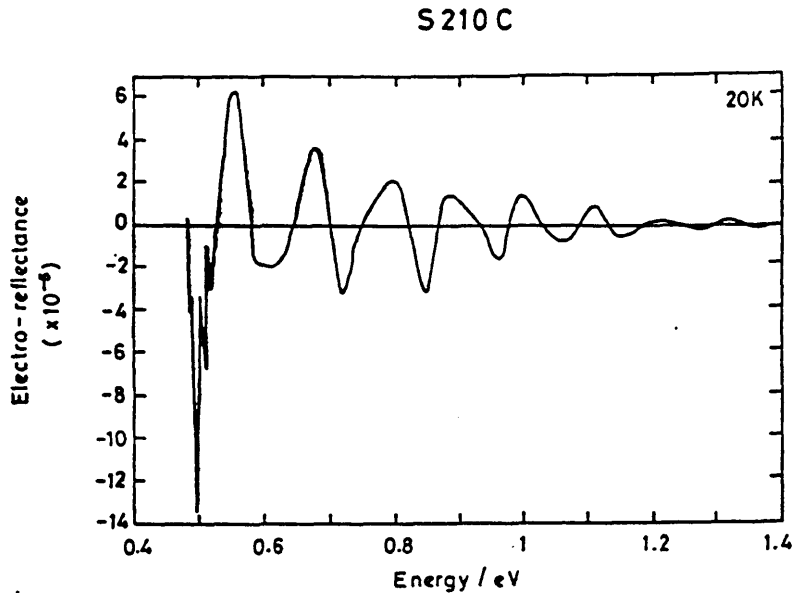


Figure 6.23 Electro-reflectance spectrum of sample S210C at 20K, oscillations in the spectrum arise because of a Fabry-Perot etalon effect.

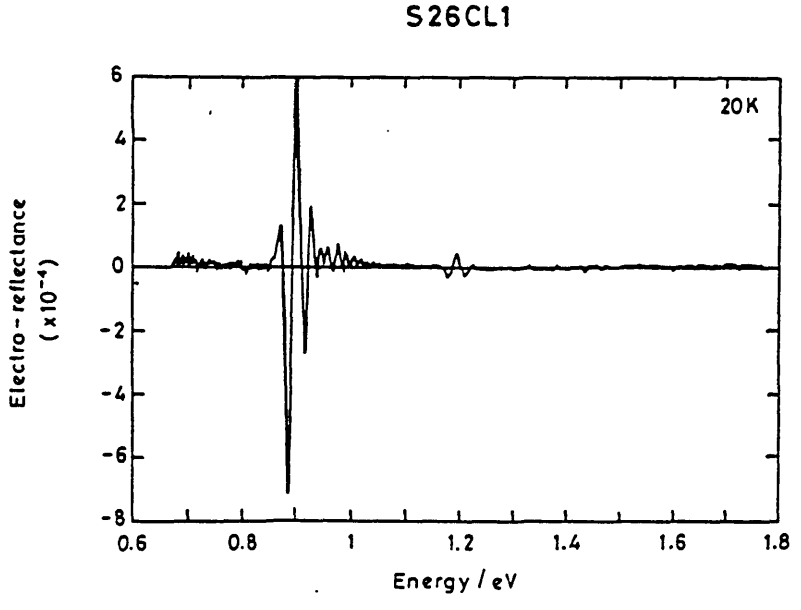


Figure 6.24 Electro-reflecatnce spectrum of control sample S26CL1 at 20K, The line shapes observed arise from the Ge E_0 and $E_0+\Delta_0$ transitions modulated by the Franz-Keldysh effect.

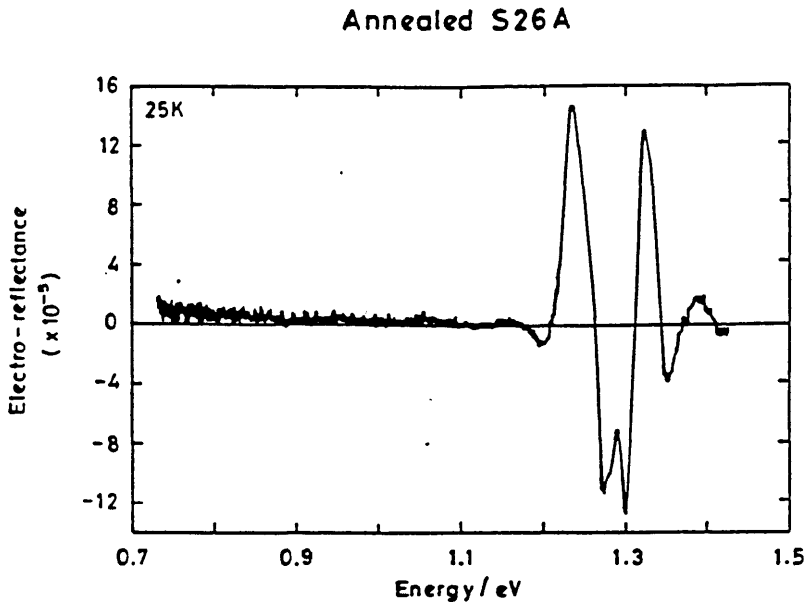


Figure 6.25 Electro-reflectance spectrum of sample S26A, as in figure 6.21 but with the sample annealed at 950°C for 3hrs.

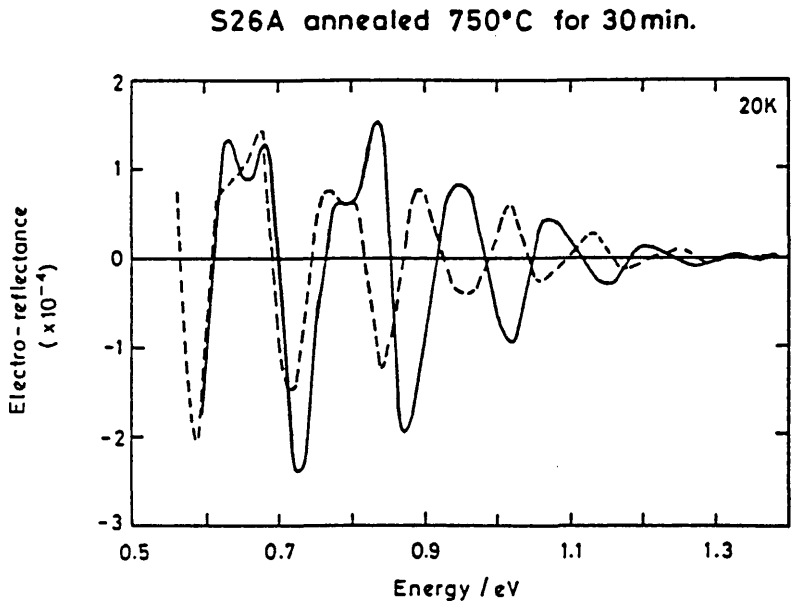


Figure 6.26 Electro-reflectance spectrum of sample S26A annealed at 750C for 30 minutes (——), figure 6.21 is placed on top for comparison (- - - -).

The results of section 5.2.3 showed that annealing samples above temperatures of 700°C can destroy layer ordering in (4:4) superlattices. An experiment was carried out in the hope of elucidating the features seen in sample S26A at 0.7 and 0.9eV. Pieces of S26A were annealed at 750°C for 30 minutes and 900°C for 360 minutes. The lower temperature anneal was performed in the hope that the superlattice layers would interdiffuse but the alloy buffer layers would remain intact. Figure 6.25 shows an electro-reflectance spectrum of the sample annealed at 900°C. No interference oscillations are observed, a feature at 1.25 eV is seen. This can be ascribed to the E_0 and $E_0+\Delta_0$ transitions of a random $Si_{0.2}Ge_{0.8}$ alloy (Kline et al. (1968)). Clearly the higher annealing temperature has severely disrupted both superlattice and buffer layers. Figure 6.26 shows an electro-reflectance spectrum of the sample after the weaker anneal. Superimposed on the figure is a copy of a spectrum of the unannealed sample from figure 6.21. The oscillations are still present in this spectrum. However comparing both spectra, a phase change appears at 0.9 eV. This could indicate that if the irregularity in figure 6.21 at 0.8eVwas produced by a superlattice critical point, the disappearance of it in figure 6.26 might be caused by disruption the superlattice. Unfortunately no Raman scattering can be used to analyse the superlattice ordering in these samples. However, the results of section 5.2.3 suggest annealing a Si/Ge superlattice at 750°C will cause disruption of its layering structure; so the effect observed in figure 6.25 may be attributed to the superlattice.

6.3.3 Electro-transmission measurements.

Transmission measurements were carried out in the hope of overcoming the effects of multiple reflections within the (2:n) samples which produce oscillations in the electro-reflectance spectra. Reflectance measurements are very susceptible to weak reflections within the sample caused by interface effects. Thorn et al. (1989) removed the substrates on their samples allowing transmission measurements to be carried out and have shown transmission measurements can reduce this problem. Transmission measurements can be made on the superlattice samples, without the need to remove the substrate, if the spectral region is restricted to energies below the Si substrate absorption edge ie. below 1.1eV. (Free carrier absorption from the n-type doping is negligible.)

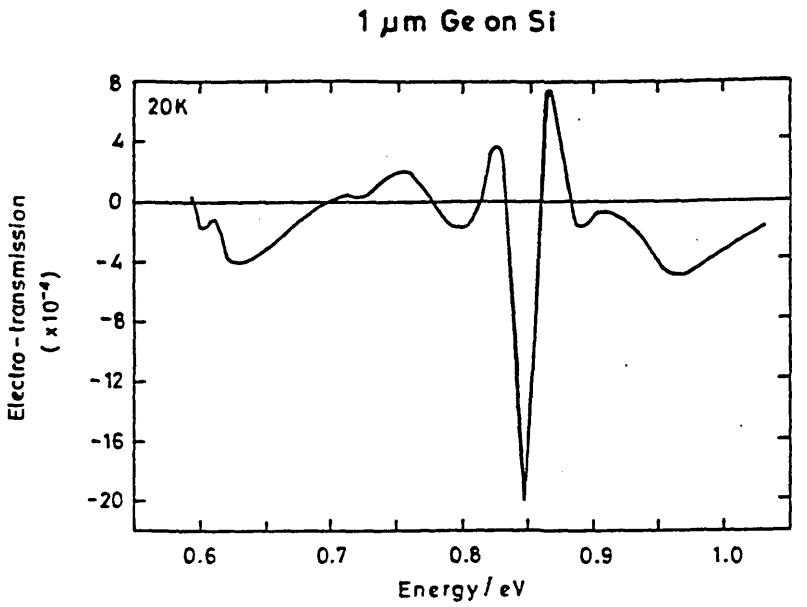


Figure 6.27 Electro-transmission spectrum of 1μm epitaxial Ge grown on Si(001) at 20K.

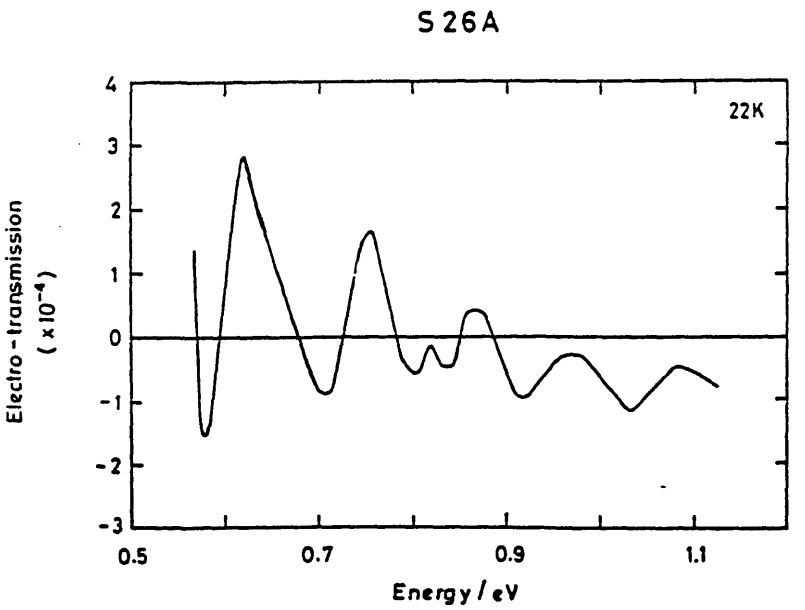


Figure 6.28 Electro-transmission spectrum of sample S26A at 22K for energies below the absorption edge of Si.

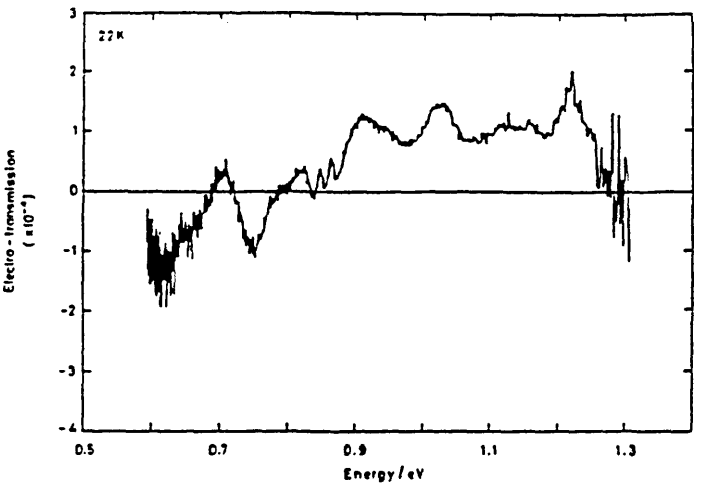


Figure 6.29 Electro-transmission spectrum of sample S28B at 22K for energies below the absorption edge of Si.

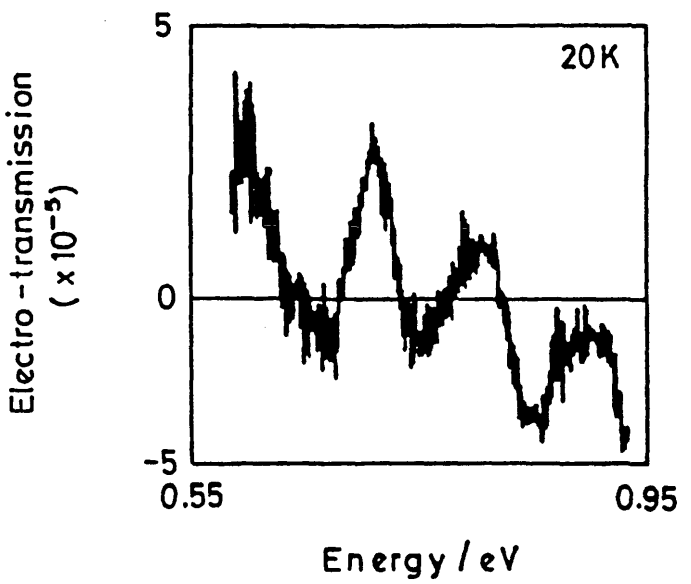


Figure 6.30 Electro-transmission spectrum of sample S210C at 20K, for energies below 1.2eV.

The samples (S26A, S28B and S210C) were prepared for electro-transmission measurements using procedures that were used for the electro-reflectance samples, described in section 3.3. However, first of all, the back surface of the samples was polished to increase specular transmission. Initially the back of the Wacker substrate was polished with 10μm diamond grit, then 3μm grit. At this stage specularly reflected light could be seen from the substrate back. The samples were then cleaned and contacts formed according to section 3.3.

A similar experimental set-up to the electro-reflectance measurement system was used. A $1mm^2$ spot of light was focused at normal incidence on to the Schottky barrier, and photo-currents were used to optimise the final spot placement. The transmitted light was then collected with f/4 optics and a PbS photo-detector. Similar electric fields to the ones used in the electro-reflectance measurements were applied.

As a comparison, a sample containing 1μm of unstrained Ge grown on a Si n^+ doped (001) substrate was also prepared. This sample is equivalent to the superlattice samples without the alloy and superlattice layers. Figure 6.27 shows an electro-transmission spectrum of the Ge, for energies below the absorption edge of the Si substrate. The E_0 critical point is clearly observed. Figures 6.28, 6.29 and 6.30 show the electro-transmission of samples S26A, S28B and S210C respectively, (normalised by the non-modulated transmission). As with the electro-reflectance spectra, all show oscillations from the Fabry-Perot etalon region within the epitaxial layer. However sample S28B shown in figure 6.29, clearly shows a feature at 0.9eV. The feature has several oscillations with much smaller period than the interference oscillations.

Reflection from an interface between two media of different refractive indices can be minimised by using polarised light at the Brewster angle (Pain (1983)). This phenomenon may be used to reduce the interference effect. Reflected light polarised parallel to the plane of incidence can be reduced to zero at an angle θ_B given by:

$$\tan \theta_B = \frac{n_1}{n_2} \qquad [6.2]$$

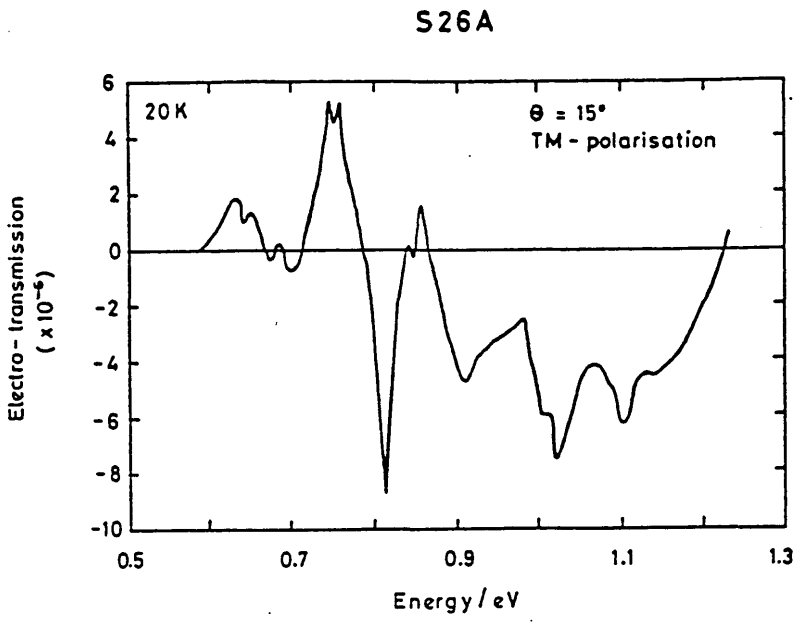


Figure 6.31 Electro-transmission spectrum of sample S26A with the incident light angle 15 and polarised to the plane of the sample. (520K)

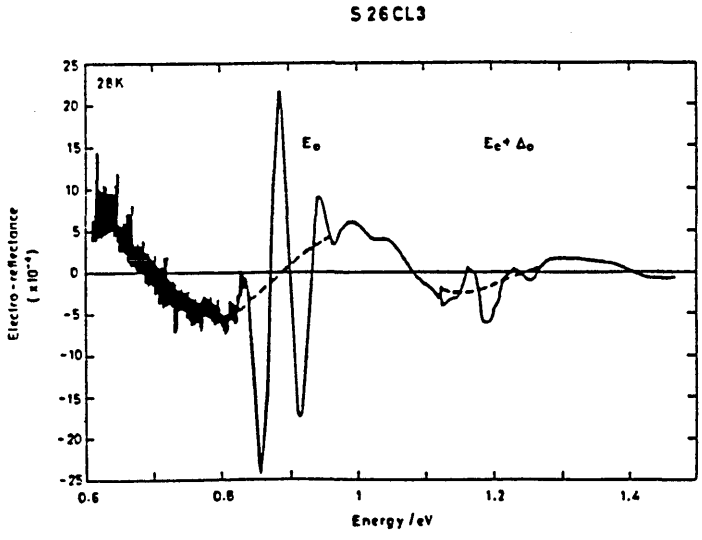


Figure 6.32 Electro-reflectance spectrum of control sample S26CL3, spectrum shows transitions from Ge (E_0 and $E_0+\Delta_0$) on top of a periodic interference effect probably originating from an electro-optic effect from the alloy contained in the sample.

where n_1 and n_2 are the refractive indexes of the materials, in this case n_1=1 for air. Thus assuming $Si_{0.25}Ge_{0.75}$ has a refractive index of 0.25x3.6+0.75x4.0, then the superlattice samples with this average composition will have θ_B=75.5°. Of course experimentally this angle is impossible to realise; rotating the sample so the incident light angle is 75.5°, causes most of the sample to move away from the focal plane of the incident light spot. The spot defocuses and covers a much larger area than the Schottky barrier, decreasing the modulated signal intensity. Figure 6.31 shows a normalised electro-transmission spectrum of sample S26A, measured with light polarised parallel to the plane of incidence and rotated from the normal towards the Brewster condition by 15°. It can be seen that the intensity of interference oscillations has decreased, and a sharp feature at about 0.8eV has appeared. This feature is perhaps also associated with the superlattice.

Due to the sample design the features observed in electro-reflectance and -transmission measurements between 0.8 and 0.9 eV cannot be unambiguously assigned to either the superlattice or the Ge buffer layers. Both predicted superlattce and Ge critical points fall in the same energy region. The large interference oscillations have a period which can only arise from the 1μm thick Ge buffers in the samples. These oscillations not only mask any critical points in optical spectra but indicate that both superlattice and Ge layers are being probed by the incident light. A new set of samples were grown with much thinner Ge buffers, in order hopefully to eliminate these interference problems.

The samples are denoted S26D, S26CL2 and S26CL3. S26D contained 51 periods of Si/Ge (2:6) superlattice and 20nm $Si_{0.25}Ge_{0.75}$ alloy buffer grown on only 200nm of Ge on a Si n^+ doped (001) substrate. Two control samples denoted S26CL2 and S26CL3 contained a $Si_{0.25}Ge_{0.75}$ alloy instead of the superlattice, all samples are capped with 80nm of $Si_{0.25}Ge_{0.75}$ alloy. Samples S26D and S26CL1 have doped buffer layers to make sure the electric field applied with the Schottky barrier is only significant across the superlattice region. Electro-reflectance measurements were carried out on all the samples. Figure 6.32 shows a spectrum of S26CL3, showing features from the Ge E_0 and $E_0+\Delta_0$ critical points superimposed on oscillations caused by a Fabry-Perot cavity. The cavity is probably modulated optically by the effect observed in the previous samples. Figures 6.33 and 6.34 show both electro-reflectance and -transmission spectra for samples S26D and S26CL1 respectively. No oscillations are seen in the spectra, and the observed features can be assigned to the Ge E_0 and $E_0+\Delta_0$ critical points.

Figure 6.33 Electro-reflectance and electro-transmission spectra of sample S26CL2 at 20K (not to scale) showing that one is the Kramers-Kronig transform of the other.

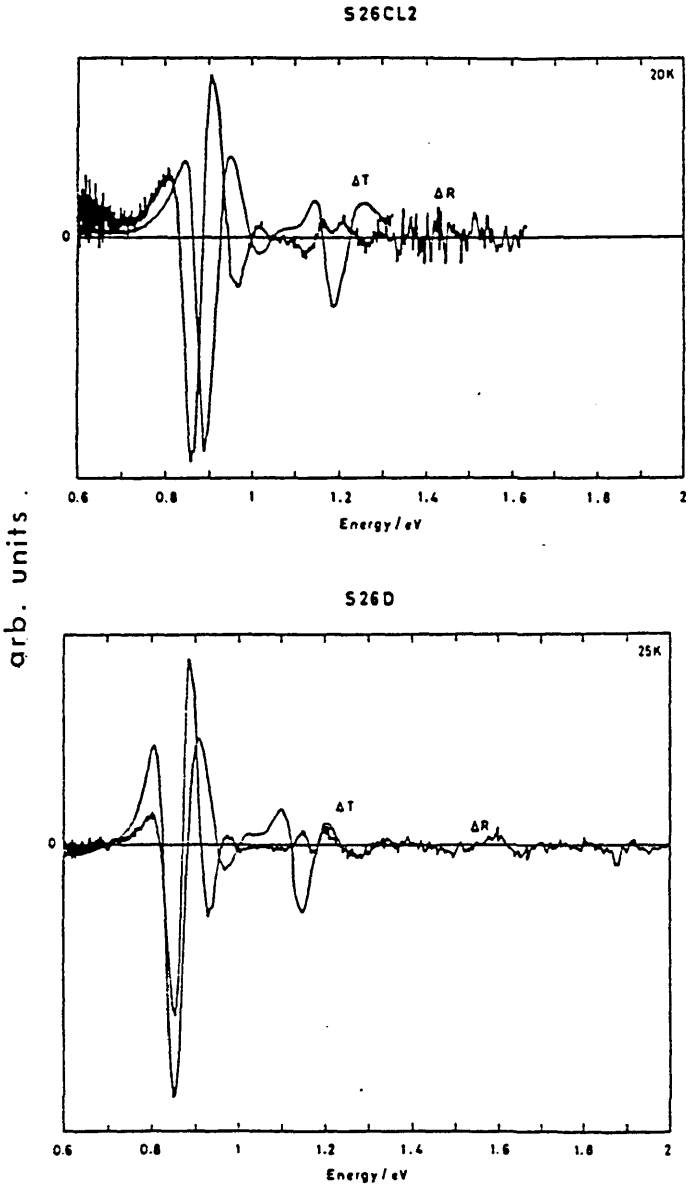


Figure 6.34 Electro-reflectance and electro-transmission spectra of sample S26D at 25K (not to scale) showing the lowest transition in the sample.

It is interesting to note that the reflectance signal is the Kramers-Kronig transform of the transmission signal, ie. a peak or valley in one of the signals corresponds to a zero crossing in the other. This phenomenon is expected for band edge transitions, where the reflected light is proportional to the real part of the dielectric function and the transmitted light proportional to the imaginary part of the dielectric function (Cardona (1969)). However, importantly there is no difference between the superlattice sample and the alloy control sample, and all spectra resemble the transitions found in bulk Ge (figure 3.4). A possible explanation might be that the superlattice critical points are weaker than Ge critical points and they are superimposed on the Ge spectrum, but too weak to be observed.

The unambiguous assignment of states to the superlattice can only be made with spectra from samples that do not contain spurious critical point transitions in the energy vicinity of interest. Thus a measurement needs to be carried out on a sample that contains no Ge. One further measurement on such a sample has been performed. In this case 100 periods of Si/Ge (2:6) superlattice was grown on a 1μm thick undoped buffer $Si_{0.3}Ge_{0.7}$, which in turn was grown on a 15μm thick linear buffer of $Si_{1-x}Ge_x$ for x=0.0 to 0.7. The substrate was a n^+ doped Si(001). Unfortunately no control sample was grown with this sample, and no structural characterisation has been carried out. Figure 6.35 shows a schematic of the sample dimensions. A Schottky barrier sample was prepared and initially a photo-current spectrum was taken at room temperature. Figure 6.36 shows the photo-current spectrum between energies of 0.7 and 1 eV. A line is drawn on the figure representing the indirect band edge of a $Si_{0.3}Ge_{0.7}$ alloy. No features which can be ascribed to a direct or indirect band edge of the suplerlattice are observed below an energy of 0.95eV.

Electro-reflectance spectroscopy was carried out at room temperature, with unpolarised light at an incident angle of 45° to the sample. Figure 6.37 shows an electro-reflectance spectrum between energies of 0.7 and 1.0 eV using a PbS photo-detector, and figure 6.38 from 1.0 to 2.1 eV using a Si photo-detector. The spectral resolution in the latter spectrum is about 20meV, compared to 4meV for figure 6.37. The feature at 1.7 eV observed in figure 6.38 originates from the $Si_{0.3}Ge_{0.7}$ alloy, the energy corresponding well to the E_0 critical point (Kline et al. (1968)). In figure 6.37 two features are observed, the first is a broad transition at about 1.1 eV, the second is an oscillatory interference pattern increasing for energies below 1.0 eV. The period of the interference effect pattern corresponds to a thickness of about 19μm,

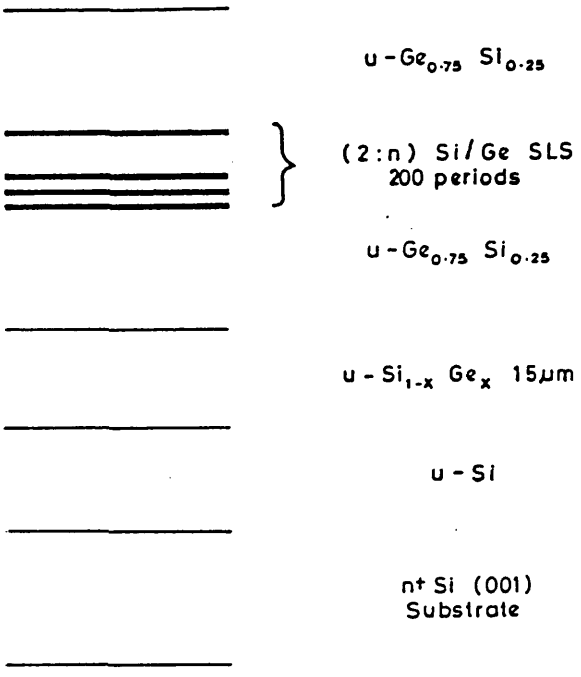


Figure 6.35 A schematic of the S26E sample structure.

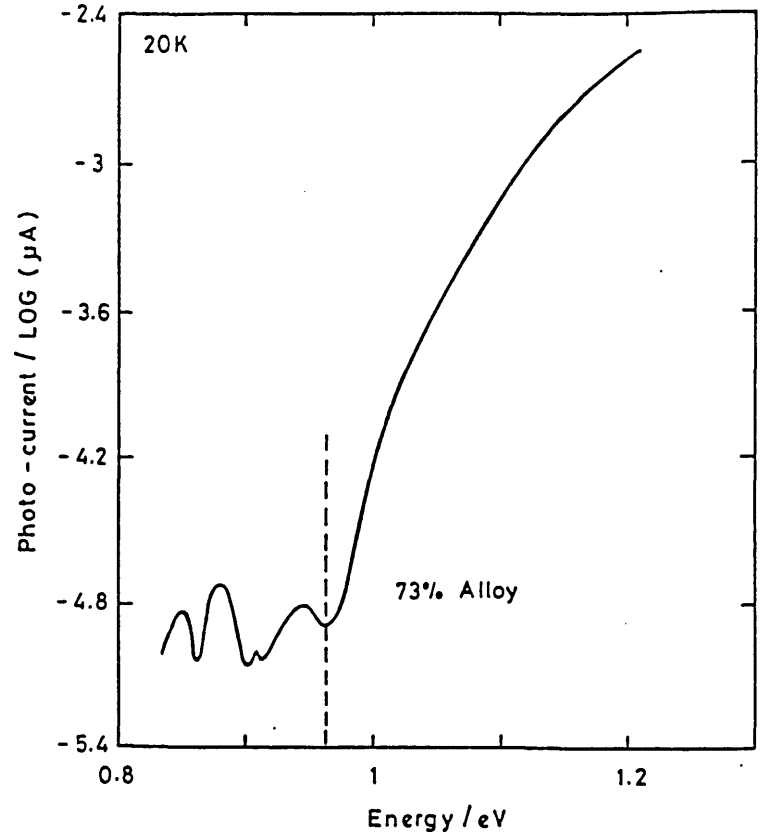


Figure 6.36 A photo-current spectrum of sample S26E at 20K A line indicates the band edge of a $Si_{0.27}Ge_{0.73}$ alloy.

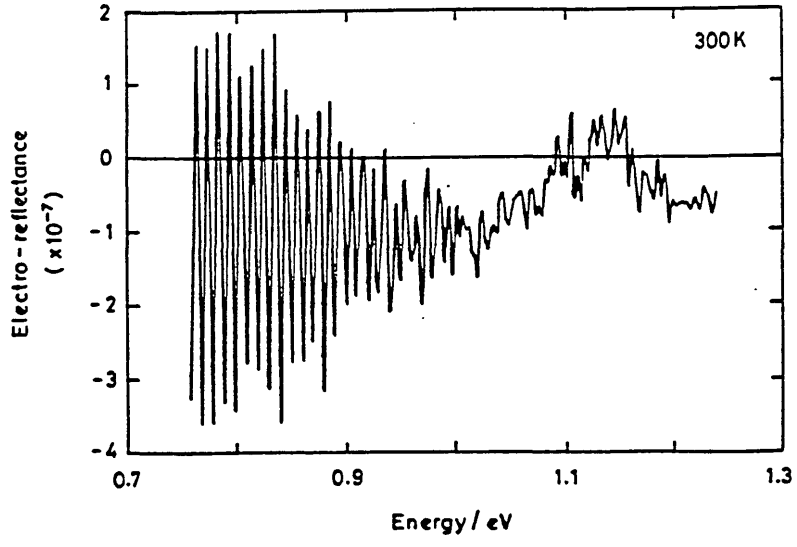


Figure 6.37 Electro-reflectance spectrum of sample S26E at 300K, using a PbS detector between 0.6 and 1.4 eV.

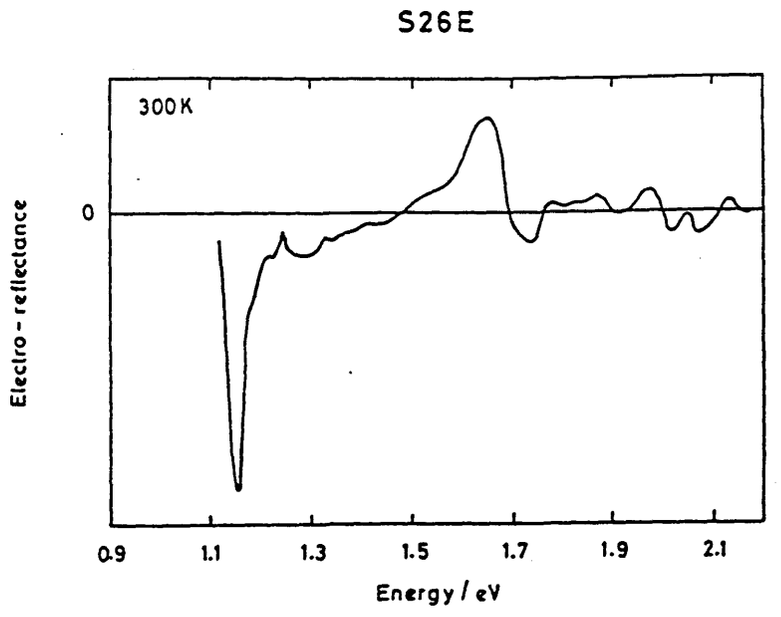


Figure 6.38 Electro-reflectance spectrum of sample S26E at 300K using a Si photo-diode detector between 0.9 and 2.1 eV.

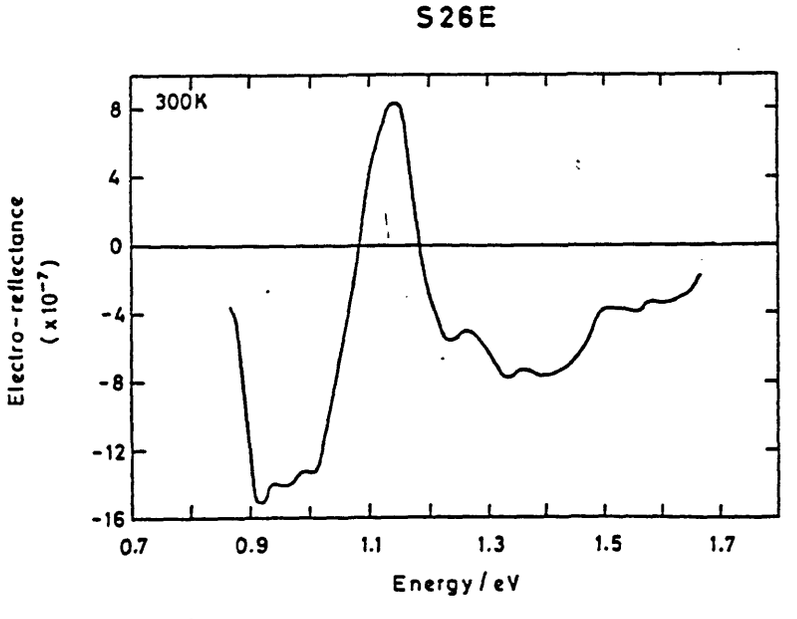


Figure 6.39 A smoothed spectrum of figure 6.38, electro-reflectance spectrum of sample S26E at 300K, removing interference oscillations below 1eV and showing a weak feature thought to be associated with the Si/Ge (2:6) short-period superlattice. The spectral window used for averaging is about 30meV wide.

approximately the entire thickness of the epitaxial layer. This period is calculated assuming refractive index of an alloy taken to be an average composition of the graded buffer layer. Figure 6.39 shows a spectrum where the interference feature has been removed by averaging the signal displayed in figure 6.37, with a spectral window of about 30meV. The feature at 1.1eV still remains, but more clearly defined. This feature probably originates from the superlattice, in the absence of any other plausible assignment. No annealing experiments were carried out in this sample, unlike the (4:4) and the other (2:6) superlattices, as the annealed structure would no doubt contain alloys of many compositions, leading ot dubious interpretations.

6.3.4 Conclusions.

An attempt has been made to measure samples nominally containing the so called 'direct gap' superlattices proposed by Gell (1989). The samples contain short-periods made from bi-atomic sheets of Si and even numbers of Ge monolayers. Optical assessment has been undertaken using electro-reflectance and electro-transmission. Interference effects in the epitaxial layers are seen, which are very similar to the effects observed in other Si/Ge samples, and probably the mechanism for producing this effect is the same.

Spectral features were seen in samples S26A and S28B between 0.8 and 0.9 eV, however these features could not be isolated from interference oscillations in the spectra. At most when a sample was annealed, a phase change in the interference oscillations could be observed in an electro-reflectance spectrum. Alternatively a small feature was observed when using plane polarised light in electro-transmission measurements. However, such effects cannot be distinguished from the Ge buffer found in the samples, the presence of which is necessary, to produce a growth surface of sufficient quality for the superlattice. A final investigation uses sample S26E to overcome this problem. S26E incorporates a large compositionally graded $Si_{1-x}Ge_x$ buffer and no layers of pure Ge. Unfortunately due to the difficulty of growing such a thick epitaxial layer no control sample was grown, so although a feature is observed at 1.1 eV, assignment to the superlattice is difficult.

The lack of evidence for superlattice transitions in (2:n) structures, for which critical point strengths are predicted to be as strong as pure Ge, could be due to the exact layer thickness in the periods being incorrect. Gell (1989,1988) predicts that the optical transition strengths could reduce by an order of magnitude if the bi-atomic sheet of Si was either 1 or 3 monolayers thick. Whilst average layer thicknesses of monolayer precision can be grown in MBE systems, interface roughness (a property not normally measured in TEM) can probably cause local fluctuations in layer thickness far larger than that which can be tolerated by the superlattice structures.

Chapter 7 Conclusions from electro-optic and Raman measurements.

7 Conclusions from Electro-optical and Raman measurements.

This thesis contains optical analyses of $Si_{1-x}Ge_x/Si$ quantum well structures and Si/Ge short-period superlattices. Sources of samples with good structural quality are limited, which has meant that all the samples investigated have been grown in one MBE system. Thus the effects observed in these samples may not be universal for all Si/Ge MBE grown samples. However the samples are among the best available in the field of Si/Ge MBE.

7.1 Multiple Quantum well and indirect band gap superlattice structures.

The samples containing strained $Si_{1-x}Ge_x/Si$ quantum wells and Si/Ge (4:4) short-period superlattices were investigated in response to reports of electro-reflectance measurements by Pearsall et al. (1986 and 1987). Pearsall et al. observed strong optical signals for superlattice samples at energies near the indirect band edge of Si.

When investigated quantum well samples gave electro-reflectance spectra of similar character to the results of Pearsall et al. (1986). However, by using a series of samples containing quantum wells with different confinement effects but the same material composition, effects from strain deformation and electron confinement could be isolated. It was found that assignment of the individual electron states is not as straight forward as Pearsall et al. suggest. Electro-reflectance features can be observed in the expected energy vicinity but they are broad, thus fine structure cannot be resolved definitively. In addition to the quantum well states, periodic oscillations were observed. It is thought that the oscillations arise from interference effects within the sample. Application of an electric field across the alloy or quantum well samples modulates the optical properties of an etalon cavity. The etalon cavity is formed by the front and back surfaces of the epitaxial layer. The front reflector is formed by the large dielectric mismatch between the air and semiconductor. The reflector at the epitaxial/substrate interface is of unknown origin, but contamination of the substrate surface before growth could cause a reflection. The reflection need not be large for the observed effect. This effect has been observed in samples containing $Si_{1-x}Ge_x$ epitaxial alloys but not in a sample containing just Si, suggesting that it could be connected with the presence of a

$Si_{1-x}Ge_x$ alloy. Ultimate assignment of the mechanism of the interference effect is difficult, since its observation is dependent on reflections at the front and back surfaces of the epitaxial layer, something which the observer has no control over.

Following the experimental observations of the multiple quantum well samples, short-period superlattice samples were investigated. Various structures, for example Si/Ge (6:4) and Si/Ge (4:4) superlattices, have been looked at by Abstreiter et al. (1989) and Pearsall et al. (1987). These superlattices show evidence of electronic transitions below the indirect band gap of Si. Looking at the (4:4) structures, careful study showed that like the quantum well samples interference effects were present in the electro-reflectance spectra. However, although the interference effects occur because of reflections from the front and back of the epitaxial layers, not enough evidence exists to say whether the oscillations seen in the short-period superlattices have the same mechanism as the ones observed in alloy and quantum well samples. Pearsall et al. (1989) also observe an interference effect in some of their samples but ignore the possibility that its effect could muddle their interpretation of the spectra. A specially designed sample, to suppress interference effects was measured with electro-reflectance. Distinct superlattice critical points were observed at about 2.8eV and 2.4eV. Using photo-current spectroscopy, lower energy transitions from 0.8eV similar in strength to indirect band gap absorption were observed. A peak in the photo-current spectrum was observed at 1.2eV, this could be a specific superlattice critical point predicted by Gell (1988). Resonant Raman scattering was also used to verify the uppermost superlattice critical points, this technique also allowed assignment of critical point transitions to phonons connected with specific parts of the superlattice period. The strength and energy of the observed optical transitions and critical points compare well to existing theories (Gell (1988)). It is not clear what the origin of the signal at 0.7 - 1.2eV reported by Pearsall et al. (1987) is. Their measurements are too strong to be attributed to intrinsic superlattice critical points, according to present theories.

Raman scattering spectroscopy of phonons was used to check the structural integrity of both quantum well and (4:4) superlattice samples grown on Si(001). Phonons associated with the Ge layers, interface bonds and Si layers were observed. In addition confined modes were seen in the Si layers of (4:4) superlattices. For the superlattice samples it was noted that there seems to be an inverse relationship between the Si-Ge mode height (relative to the Ge-Ge mode height) and the up-shifted Ge-Ge mode energy

due to inbuilt strain. A simple annealing experiment of the (4:4) superlattice showed strain relaxation at annealing temperatures of 600 °C and complete superlattice disruption at greater than about 750 °C.

7.2 Direct band gap superlattice structures.

The final section of the thesis investigated short-period superlattices, which theory predicts to have strong critical points at energies less than 1 eV. Samples consisted of Si/Ge (2:6,8 and 10) superlattices grown on $Si_{1-x}Ge_x(001)$ buffers. Both electro-reflectance and electro-transmission spectroscopies were used. All the samples showed optical interference effects supposedly caused by the alloy present in the samples and strong reflecting interfaces at compositional heterojunctions. By annealing one sample and possibly destroying the superlattice, a phase shift was observed at 0.9eV in the interference oscillations in an electro-reflectance spectrum. However, all of the samples contained Ge, thus ambiguous identification of superlattice states from those of bulk Ge (which has a critical point at 0.89eV at 4K) is difficult and no firm conclusions can be made. One final sample investigated, was grown on a compositionally graded alloy buffer, avoiding any layers of pure Ge. The electro-reflectance spectrum showed interference effects from the alloy, but also a weak feature at 1.1 eV, which could not be readily assigned to the alloy. Optical transitions from the alloy occur at higher energies.

7.3 Further work required.

The work contained in this thesis, describes theoretical and some experimental verification of electronic transitions within Si/Ge heterostructures. The ultimate aim is to find a Si/Ge structure which allows strong optical transitions to occur at near band edge energies in silicon. Theories have been formulated which suggest that such structures do exist, however at present no such transitions have been observed. If we are to confirm the theoretical predictions, then the absence of strong optical transitions arises because the technology is not available to make Si/Ge structures of sufficient quality. Molecular beam epitaxy is a very good technique for making layered semiconductor structures, for example the GaAs quantum well

and associated optical devices. However there is a difference between making GaAs heterojunctions and Si/Ge short-period superlattices. For GaAs and Si1-xGex transport devices, the MBE technique is used to break a symmetry in one direction within the crystal lattice, producing a confinement effect. The size of these devices is usually much larger than the roughness of the layered interface. For the short-period superlattices we are relying on MBE to create a new symmetry in the lattice and thus make a new band structure, the dimensions of the superlattices are very close to the values of interface roughness currently found in MBE samples. Thus, although average layer thicknesses can be very precise, local variations can completely change the structure of the superlattice. It is this difference between breaking and creating symmetry within the crystal lattice which will ultimately decide the viability of Si/Ge MBE for optical devices. Destroying symmetry, of course is always easier than creating it.

If the technology is improved such that Si/Ge structures can be fabricated to produce new transitions below the indirect band gaps of Si and Ge, the further task exists to make the structures emit light. This requires the absence of dislocations and impurities which can have more efficient luminescent or carrier recombination paths. Once all these problems are solved then formulations of device structures, which contain the superlattice, can be made. Of course this step is also not straight forward, as Si/Ge heterostructures have more sensitive thermal properties than bulk semiconductors (as shown in section 5.2.3).

The next step in Si/Ge optical device research needs to include studies on the growth of symmetrically strained structures, followed by further investigations into high quality low dislocation density growth of superlattices. The ultimate aim in superlattice growth will be to produce dislocation free structures having monolayer precisions and very low interface roughness. When this is achieved the symmetry properties that the 'band structure engineers' rely on can be fulfilled.

Clearly even if it is not possible to create new well defined optical transitions in the superlattices, a substantial amount of physical and chemical research is needed to understand the electro-optic effects observed in this thesis in $Si_{1-x}Ge_x$ epitaxial alloys and short-period superlattices. Not only are more samples required from the MBE system which supplied the samples investigated for the thesis but sources of other $Si_{1-x}Ge_x$/Si structures would help obtain a overall view of the electronic properties of the

epitaxial layers. X-ray and other structural probes should be used in an attempt to correlate optical properties with sample integrity and microscopic ordering. The covalent nature of the bonds in the crystal makes this system rather different to other epitaxial semiconductor systems. However the different lattice constants of Si and Ge, allow internal strain to appear within the unit cell of alloy and superlattice crystals. Both these effects make $Si_{1-x}Ge_x/Si$ epitaxial layers an exciting field of study, of which this thesis has just scratched the surface.

References.

Abstreiter G, Brugger H, Wolf T, Jorke H and Herzog H-J (1985): Phys. Rev. Lett. **54** 2441.

Abstreiter G, Eberl K, Friess E, Mencziger V, Wegschider W and Zachai R (1989): J. of Crystal Growth **95** pp431-438. or

Abstreiter G, Eberl K, Friess E, Mencziger V, Wegschider W and Zachai R (1989): Nato Meeting 1989 Venedig, *'Spectroscopy of semiconductor microstructures'* eds. G Fasol, A Fasolino and P Lugli. NATO ASI series, Plenum Publishers, New York.

Alonso M I and Winer K (1988): Phys. Rev. B **39** 10056.

Alonso M I, Cerdeira F, Niles D and Cardona M (1989): J. Appl. Phys. **66**(11) 5645.

Anastassakis E, Pinczuk A, Burstein E, Pollak F H and Cardona M (1970): Solid State Comm. 8 pp133-138.

Aspnes D E (1966): Phys. Rev. **147**(2) 554.

Aspnes D E (1972): Phys. Rev. Lett. **28** 168.

Aspnes D E and Frova A (1969): Sol. Stat. Comm. **7** 155.

Aspnes D E (1988): EMIS Data review series 4 (INSPEC IEE).

Basca W, v. Kanel H, Mader K A, Ospelt M and Wachter P (1988): Superlattices and Microstructures 4(6) 717-721.

Bassani F and Pastori-Parravicini G (1975): *'Electronic States and Optical Transitions in Solids'* Pergamon Press, Oxford

Bastard G and Brum J A (1986): IEEE J of Quantum Electronics **QE22** (9) (Sept).

Bean J C and Sadowski A (1982): J. Vac. Sci. & Technol. **20** 137.

Bean J C (1985): Science **230** 4722 (127) (11 October 1985).

Bean J C (1987): *'MBE 1986'* Editors T Foxon and J Harris North-Holland, London.

Brantley W A (1973): J. Appl. Phys. **44**(1) 534.

Brey L and Tejedor C (1987): Phys. Rev. Lett. **59**(9) 1022.

Brugger H, Friess E, Abstreiter G, Kasper E and Kibbel H (1988): Semiconduct. Sci. and Tech. 3 pp1166-1170.

Brugger H, Abstreiter G, Jorke H, Herzog H -J, and Kasper E (1986): Phys. Rev. B **33** 5928.

Brya W J (1973): Solid State Comm. **12** 253-257.

Cardona M (1969): *'Modulation Spectroscopy'* (Solid State Physics Supplement), Academic Press, New York.

Cardona M (1982): *'Light Scattering in Solids II'*, Topics in Applied Physics Vol. **50**, Eds. M Cardona and G Guntherodt, Spinger-Verlag, Berlin.

Cardona M and Christensen N L (1987): Phys. Rev. B **35**(12) 6182.

Cerdeira F, Buchenauer C J, Pollak F H and Cardona M (1972): Phys. Rev. B 5(2) 580.

Cerdeira F, Pinczuk A, Bean J C, Batlogg B and Wilson B A (1984): Appl. Phys. Lett. **45**(10) 1138.

Cerdeira F, Pinczuk A and Bean J C (1985): Phys. Rev. B 31(2) 1202.

Cerdeira F, Alonso M I, D Niles, Garriga M, Cardona M, Kasper E and Kibbel H (1989): Phys. Rev. B 40(2) 1361.

Chandrasekhar M and Pollak F H (1977): Phys. Rev. B 15(4) 2127.

Chang S J, Huang C F, Kallal M A, Wang K L, Bowman R C and Adams P M (1989): Appl. Phys. Lett. 53(9) 1835

Chelikowsky J R and Cohen M L (1976): Phys. Rev. B 14 556, (see also M L Cohen and J R Chelikowsky: *'Electronic Structure and Optical Properties of Semiconductors'* No.75 Springer Series in Solid State Sciences ed. M Cardona, Springer-Verlag, Berlin (1985)).

Churchill A C, Klipstein P C, Gibbings C J, Gell M A, Jones M E and Tuppen C G (1990a): to appear in Semiconductor Science and Technol.

Churchill A C, Klipstein P C, Gell M A, Gibbings C J, Jones M E and Tuppen C G (1990b): to be submitted.

Cohen M L and Heine V (1970): Solid State Phys. Vol 24 1970, Academic Press, New York.

Dafesh P A, Arbet V and Wang K L (1990): Appl. Phys. Lett. 56(15) 1498.

Davies G (1989): Phys. Rep. 176 83-188.

Dharma-Wardana M W C, Aers G C, Lockwood D J and Baribeau J -M (1990): Phys. Rev. B 41(6) 5319.

Duke C B and Alferieff M E (1966): Phys. Rev. 145(2) 583.

Eberl K, Krotz G, Zachai R and Abstreiter G (1987): Modulated Semiconductor Structures 3, Montplelier. (J de Physique 46 C5)

Esaki L and Tsu R (1970): IBM Res. Develop. 14, 61.

Frank F C and Van der Merwe J H (1949): Proc. Roy. Soc. (London) A 198 216.

Franz W (1958): Z Naturf A13 484.

Freidel P, Hybertson M S and Schluter M (1989): Phys. Rev. B 39(11) 7974.

Friess E, Brugger H, Eberl, Krotz G and Abstrieter G (1989): Solid State Comm. 69(9) pp899-903.

Friess E, Eberl K, Mencziger V and Abstreiter G (1990): Solid State Comm. 73(3) 203.

Fritz I J (1987): Appl. Phys. Lett. 51(14) 1080.

Froyen S, Wood D M and Zunger A (1988): Phys. Rev. B 37(12) 6893.

Gaillard S, Joullie A M, Monteil E and Alibert C (1973): J. of Phys E: Sci. Instruments 6 1129.

Gell M A and Herbert D C (1987): Phys. Rev. B 35(18) 9591.

Gell M A (1988): Phys. Rev. B 38(11) 7535.

Gell M A (1989): Phys. Rev. B 40(3) 1966.

Gell M A and Churchill A C (1989): Phys. Rev. B 39(14) 10449.

Gell M A (1990a): Semicond. Sci. Technol. in press.

Gell M A (1990b): Phys. Rev. B 41 7611.

Gell M A, Herman M H, Ward I D, Gibbings C J, Jones M E, Tuppen C G, Churchill A C and Klipstein P C (1990c): Proc. 11th Int. Vac. Congress/7th Int. Conf. on Solid Surfaces. (to appear in Vacuum)

Ghanbari R A and Fasol G (1989): Solid State Comm. **70**(11) p1025-1029.

Gilat G (1972): Journal of Comp. Phys. **10** 435-465.

Hensel J C and Feher G (1963): Phys. Rev. **129** 1041.

Hesegawa H (1963): Phys. Rev. **129** 1029.

Hoeven A J, Aarts J and Larsen P K (1989): J. Vac. Sci. Technol. **A7** 5.

Holland L (1956): '*VacuumDeposition of Thin Films*' Chapman Hall, London.

Hollinger G (1987): '*Photoelectron Spectroscopies: Probes of Chemical Bonding and Electronic Properties at Semiconductor Interfaces*', p210, Semiconductors and Interfaces: Formation and Properties, Eds G. Lelay, J Derrein and N Boccara, Spinger-Verlag, Berlin.

Houghton D C, Gibbings C J, Tuppen C G, Lyons M H and Halliwell M A G (1990): Appl. Phys. Lett. **56**(5) 460.

Hybertson M S and Schluter M (1987): Phys. Rev. B **36**(18) 9683.

Hybertson M S, Schluter M, People R, Jackson S A, Lang D V, Pearsall T P, Bean J C, Vandenburg J M and Bevk J (1988): Phys. Rev. B **37**(17) 10195.

de Jong T, Douma W A S, Smit L, Korablev V V and F W Saris (1983): J. Vac. Sci. Technol. **B1**, 808.

Kasper E, Herzog H J and Kibbel H (1975): Appl. Phys. **8** 199-205 (Springer-Verlag 1975).

Kasper E, Kibbel H, Jorke H, Brugger H, Fiess E and Abstreiter G (1988): Phys. Rev. B 38(5) 3599.

Kasper E (1989): Silicon Molecular Beam Epitaxy (Si-MBE) in '*Semiconductor Silicon*' Springer Series in Material Science Vol. 13 Eds: GC Harbeke and MJ Schulz. Springer-Verlag, Berlin.

Keldysh L V (1958): Sov. Phys. JETP **7** 788.

Kittel C (1987): '*Quantum Theory of Solids*' John Wiley & Sons, New York.

Kittel C (1976): '*Introduction to Solid State Physics*' John Wiley & Sons, New York.

Klein M V (1986): IEEE J. of Quantum Electrincs **QE22**(9) 1760.

Kline J S, Pollak F H and Cardona M (1968): Helv. Phys. Acta. **41** 968.

Klipstein P C and Apsley N (1986): J. Phys. C: Solid State Phys. **19** 6461.

Kohama Y, Fukuda Y and Seki M (1988): Appl. Phys. Lett. **52**, 380.

Kondo K and Moritani A (1977): Il Nouvo Cimento **39** 2 387.

Kunc K, and Gomes Dacosta P (1985): Phys. Rev. B **32**(4) 2010.

Lang D V, People R, Bean J C, and Sargent A R (1985): Appl. Phys. Lett. **47**(12) 1333.

LeGoues F K, Kesan V P, Iyer S S (1990): Phys. Rev. Lett. **68**(1) 40.

Lepselter M P and Andrew J M (1969): '*Ohmic Contacts to Semiconductors*' Ed. Schawtz, Electro-Chemical Society, New York.

Lockwood D J, Dharma-wardana M W C, Baribeau J-M and Houghton D C (1986): Phys. Rev. B 34(4) 3034.

Lockwood D J, Dharma-wardana M W C, Baribeau J-M and Houghton D C (1987): Phys. Rev. B 35(5) 2243.

Lockwood D J, Baribeau J-M and Timbrell P Y (1989): J. Appl. Phys. **65** 3049.

Luttinger J M and Kohn W (1955): Phys. Rev. **97**(4) 869.

Luttinger J M (1956): Phys. Rev. **102**(4) 1036.

Luyri S, Kaastalsky A and Bean J C (1984): IEEE Trans. Electron Devices ED31 p1135.

Mahowald P H, List R S, Spicer W E, Woicik J and Pianetta P (1985): J. Vac. Sci. Technol. **B3**, 1252.

Manasevit H M, Gergis I S and Jones A B (1983): J. of Elec, Materials **12** (4).

Matthews J W and Blakeslee A E (1974): J. of Crystal Growth **27** 118-125.

Menendez J, Pinczuk A, Bevk J and Mannaerts J P (1988): J. Vac. Sci. Tech. B6(4) 1306.

Merlin R, Colvard C, Klein M V and Gossard A C (1980): Phys. Rev. Lett. **45** 298.

Merzbacher E (1970): *'Quantum Mechanics'*, John Wiley & Sons, New York.

Meyerson B S (1989): Chemical and Physical Considerations in the Chemical Vapour Deposition Process in *'Semiconductor Silicon'* Springer Series in Material Science Vol. **13** Eds: GC Harbeke and MJ Schulz. Springer-Verlag, Berlin.

Miller D A B, Chemla D S, Damen T C, Gossard A C, Wiegmann W, Wood T H and Burrus C A (1984): Phys. Rev. Lett. **53**(22) 2173.

Molinari E and Fasolino A (1989): Appl. Phys. Lett. **54**(13) 1220.

Montie E A, van ser Walle G F A, Gravesteijn D J, van Gorkum A A, Cosman E C, Fredriksz C W and Bulle-Lieuwma C W T (1989a): E-MRS conference, Strasbourg 1989, paper A-X9.

Montie E A, van der Walle G F A, Gravesteijn D J, van Gorkum A A, and Teesselink W J O (1989b): Semiconductor Sci. and Tech. **4** 899.

Moriarty J A and Krishnamurthy S (1983): J. Appl. Phys. **54**(4).

Morrison I and Jaros M (1988): Phys. Rev. B **37**(2) 916.

Neuberger M (1971): *'Group IV Semiconducting Materials'* Plenum, New York.

Pain H J (1983): *'The Physics of Vibrations and Waves'* John Wiley & Sons, New York.

Pearsall T P, Pollak F H, Bean J C and Hull R (1986): Phys. Rev. B 33(10) 6821.

Pearsall T P, Bevk J, Feldman L C, Bonar J M, Mannaerts J P and Ourmazd A (1987): J. Vac. Sci. Technol. **B5**(4) 1274. or

Pearsall T P, Bevk J, Feldman L C, Bonar J M, Mannaerts J P and Ourmazd A (1987): Phys. Rev. Lett. **58**(7) 729.

Pearsall T P, Bevk J, Bean J C, Bonar J M, Mannaerts J P and Ourmazd A (1989a): Phys. Rev. B 39(6) 3741.

Pearsall T P, Vandenburg J M, Hull R, and Bonar J M (1989b): Phys. Rev. Lett. **63**(19) 2104.

Pearsall T P (1990a): To appear in J. of Luminescence.

Pearsall T P (1990b): Private communication.

People R (1985): Phys. Rev. B **32** 1405.

People R (1986a): Phys. Rev. B **34**(4) 2508.

People R (1986b): IEEE J of Quantum Electronics **QE22** No9 (Sept).

People R and Bean J C (1985): Appl. Phys. Lett. **47** 322.

People R and Bean J C (1986): ibid **49** 229.

People R and Jackson S A (1987): Phys. Rev. B **36** 1310.

Pollak F H and Cardona M (1968): Phys. Rev. **172**(3) 816.

Press W H, Flamery B P, Teukolsky S A and Vettering W H (1987): *'Numerical Recipes: The Art of Scientific Computing'*, Cambridge University Press, Cambridge.

Prutton M (1983): *'Surface Physics'*, Oxford University Press, Oxford.

Renucci J B, Renucci M A and Cardona M (1971): Sol. State Comm. **9** 1651-1654.

Rogers D C, Singleton J, Nicholas R J, Foxon C T and Woodbridge K (1984): Phys. Rev. B **34** 4002.

Rohlfing D (1988): Private communication.

Rucker H, Enderlein R and Bechstedt F (1989): Phys. Stat. Sol (b) **153**, 595.

Rytov S M (1956): Akust. Zh. **2** (71), (Sov. Phys. Acoust. **2** (68))

Sakamoto T, Kawai N J, Nakagawa T, Ohta K, Kojima T and Hashiguchi G (1986): Surf. Sci. **174** 651.

Satpathy S, Martin R M and Van der Walle C G (1988): Phys. Rev. B **38**(18) 13237.

Schmid U, Lukes F, Christensen N E, Alouani M and Cardona M (1990): *'Interband Transitions in Strained-Symmetrized Ge4Si6 Superlattices'* Submitted to Phys. Rev. Lett.

Seraphin B O and Bottka N (1966): Phys. Rev. **145** 628.

Shields A J, Klipstein P C and Apsley N (1989): Semicond. Sic. Technol. **4** 476-485.

Shields A J, Klipstien P C, Skolnick M, Whitehouse C and Smith G W (1990): Phys. Rev. B accepted for publication.

Skevington P J (1988): Private communication.

Sood A K, Menendez J, Cardona M and Ploog K (1985a): Phys. Rev. Lett. **54**(19) 2111.

Sood A K, Menendez J, Cardona M and Ploog K (1985b): Phys. Rev. Lett. **54**(19) 2115.

Stobbs W M (1988): Private communication.

Stradling R A and Klipstein P C (1990): *'Growth and Characterisation of Semiconductors'*, Adam Hilger, Bristol.

Stukel D J (1971): Phys. Rev. B **3**(10) 3347.

Sze S M (1981): *'Physics of Semiconducting Devices'* John Wiley & Sons New York.

Tanner B K (1976): *'X-ray Diffraction Topography'*, Pergamon Press, Oxford.

Tatsumi T, Hirayama H and Aizaki N (1989): Appl. Phys. Lett. **52**, 895.

Temkin H, Pearsall T P, Bean J C, Logan R A, and Luyri S (1986): Appl. Phys Lett. **48**(15).

Thorn A P, Klipstein P C and Glew R W (1990): Surface Science **229** 439.

Tinkham M (1964): *'Group Theory and Quantum Mechanics'* McGraw Hill Book Co., New York.

Tuppen C G, Gibbings C J and Hockly M (1989): J Crystal Growth **94** 392.

Tsang J C, Iyrer S S, Pukite R and Copel M (1989): Phys. Rev. B **39**(18) 13545.

Van der Walle C J and Martin R M (1986): Phys. Rev. B **34**(8) 5621.

Wang K L (1985): Solid State Technology (October) p137.

Weber J (1990): Private communication.

Weber J and Alonso M I (1989): Phys. Rev. B **40**(8).

White J, Fasol G, Ghanbari R A, Gibbings C J and Tuppen C G (1989): Thin Solid Films, **183** 77.

Wong K B, Jaros M, Morrison I and Hagon J P (1988): Phys. Rev. Lett. **60**(21) 2221.

Yariv A (1985): *'Optical Electronics"* Holt, Rinehart and Winston.

Yin M T and Cohen M L (1982): Phys. Rev. B **25**(6) 4317.

Yu E T, Croke E T, McGill T C and Miles R C (1990): Appl. Phys. Lett. **56**(6) 569.

Zachai R, Friess E, Abstreiter G, Kasper E and Kibbel H (1988): 19th International Conference on the Physics of Semiconductors, Warsaw.

Zachai R, Eberl K, Abstreiter G, Kasper E and Kibbel H (1990): Phys. Rev. Lett. **64**(9) 1055.

Zhang L R, Hung L S and Mayer J W (1982): Appl.Phys. Lett. **41**(7) 646.

List of Publications.

M A Gell and A C Churchill "Density of states in short-period Si/Ge superlattices" Phys. Rev. B 39 No14 p10449, May 1989

M A Gell, M H Herman, I D Ward, C J Gibbings, M E Jones, C G Tuppen, A C Churchill and P C Klipstein, "E-beam electro-reflectance of short-period Si/Ge Superlattices" Proc. 11th Int. Vac. Congress/7th Int. Conf. on Solid Surfaces. To appear in Vacuum.

A C Churchill, P C Klipstein, C J Gibbings, M A Gell, M E Jones and C J Tuppen. "Optical etalon effects and electronic structure in electro-reflectance and photo-current studies of Silicon-Germanium 4 monolayer:4 monolayer strained superlattices", to appear in Semiconductor Science and Technology. Presented at the IOP conference for Solid State Physics (Warwick (1990)), NATO ASI for Low Dimensional Semiconductor Structures (Toulouse, France (1989)) and the 20th International Conference on the Physics of Semiconductors (Thessaloniki, Greece (1990)).

A C Churchill, P C Klipstein, M A Gell, C J Gibbings, M E Jones and C J Tuppen. "Raman measurements of the effect of annealing short-period Si/Ge superlattcies grown on silicon": to be submitted.